From single to many atoms in a microscopic optical dipole trap

Andreas Fuhrmanek

LABORATOIRE CHARLES FABRY
INSTITUT D'OPTIQUE
CNRS UMR 8501

UNIVERSITÉ PARIS-SUD XI
UFR SCIENTIFIQUE D'ORSAY

THÈSE

Spécialité :
PHYSIQUE QUANTIQUE

présentée pour obtenir le grade de
DOCTEUR EN SCIENCES
de l'Université Paris-Sud XI

par

ANDREAS FUHRMANEK

Sujet:

FROM SINGLE TO MANY ATOMS IN A MICROSCOPIC OPTICAL DIPOLE TRAP

Soutenue le 23 septembre 2011 devant la commission d'examen :

M.	Charles S.	ADAMS	Rapporteur
M.	Antoine	BROWAEYS	Directeur de thèse
M.	Robin	KAISER	Rapporteur
M.	Pierre	PILLET	Examinateur
M.	Yvan	SORTAIS	Co-encadrant de thèse
Mme.	Tatjana	WILK	Examinatrice

Acknowledgements

I have the honor to acknowledge all the people who contributed to the realization of this work. This is the case for all members of the experiment "ASPHERIX" who I had the chance to work with throughout the last three years. This is especially the case for the advisor of this thesis Antoine Browaeys who I had the pleasure to be supervised by. I enormously benefitted from his guidance and motivation together with his daily availability to discuss recent developments.

It is in particular the case for Yvan Sortais, whose profound knowledge and pedagogically worthy explanations have been essential for this work. I very appreciated his enthusiastic and nice character as well as his culinary specialties (Rillettes etc.) enlightening the spirit and stomach of the group.

It is also the case for Philippe Grangier, whose support and help were very important for me.

The research done in the frame of this thesis was overall a result of great team effort. All the PhD and post-doctoral students have left their fingerprints and added a great contribution to the work. I very much thank Charles Tuchendler (together with his guitar) for his introduction to the experiment and his enduring explanations on the setup. I had the pleasure to share the positive attitude of Ronan Bourgain and his support during numerous hours in the lab showing me the real courage of the people of Brittany. Also, the contributions of Andrew Lance were very appreciated.

I would like to thank all docs and post-docs of the Rydberg lab, in particular Charles Evellin, who has been a great companion and moral supporter doing his PhD in parallel, Alpha Gaëtan, Lucas Beguin, Aline Vernier, Sylvain Ravets, Radu Chicireanu as well as all other current and former members of the quantum optics group Remi Blandino, Frank Ferreyrol, Marco Barbieri, Jean Etesse, Imad Agha, Alexei Ourjoumtsev, Rosa Tualle-Brouri, Valentina Parigi, Erwan Bimbard and Gaetan Messin for creating such a wonderful working atmosphere.

The correspondence with members of the atom optics group and the support of Frédéric Morin, André Villing, André Guilbaud, Patrick Roth, Jacky Robin, Florence Fuchs, Benoit Plichon and Carmen Zeques was highly appreciated.

The experience to teach students at the institute has been very valuable for me and I am grateful to the teaching staff, especially Lionel Jacubowiez, Sylvie Lebrun and François Goudail, for giving me this opportunity.

I am happy to have had the support and hospitality of the institute's former and current director Pierre Chavel and Christian Chardonnet. Especially the availability of Pierre Chavel as PhD advisor was astonishing and extraordinary.

I would like to express my gratitude to Robin Kaiser and Charles Adams for their reports and together with Pierre Pillet and Tatjana Wilk, whose kindness I also very appreciated during her PostDoc time in our group, for the evaluation of this work and being part of the examining committee.

Finally, I express a big thank you to my family, in particular my parents and brother, and my girlfriend and friends. Without their support this work would not have been possible.

Contents

Introduction

In the end of the nineteenth century it seemed that all major physical problems were understood and the last issues were about to be clarified. However, two of the most remarkable revolutions in physics were just about to happen, namely the formulation of the theory of relativity and the theory of quantum mechanics. The latter one is so far still inevitable in describing systems on the small scale. Such small scale systems can be semiconductor nanostructures or Josephson junctions as well as the ensemble of nuclei or atoms for example. Important for a study of quantum mechanical laws in all these cases is the requirement for the ensembles to be sufficiently cold as quantum effects are usually more pronounced at low temperatures.

The adaptability of experimental feasible trapping and cooling schemes to atomic gases has proven to be advantageous for fundamental studies using ensembles of atoms and also ions or molecules. For atom gases remarkably low temperatures as low as some hundreds of picoKelvin (Leanhardt *et al.*, 2003) have been reported. These low temperatures enable ultra-cold atoms to be model systems to explore quantum effects.

But ultra-cold atoms also provide ideal conditions for applications such as quantum computation (Ladd *et al.*, 2010) and quantum simulation of many-body systems (Bloch, Dalibard, and Zwerger, 2008; Gerritsma *et al.*, 2010). Together with ions they are the basis of a variety of entangled states that open new and exciting perspectives for quantum metrology (Roos *et al.*, 2006). Furthermore, neutral atoms are considered as forefront candidates for sophisticated quantum operations as one can handily control their interactions (Mandel *et al.*, 2003; Saffman, Walker, and Mølmer, 2010; Wilk *et al.*, 2010; Isenhower *et al.*, 2010). They also provide built-in scalability when placed in optical lattices (Ladd *et al.*, 2010).

However, in the study of ultra-cold many-atom ensembles the focus has so far rather been directed on a macroscopic regime where the atom gases contain millions of atoms. The gases can in this case be well described by a mean-field approach and characterized by thermodynamic quantities as the law of large numbers is very close to be fulfilled (Dalfovo *et al.*, 1999).

Small and dense atom number clouds in optical dipole traps

The last few years have seen a growing interest in the study of mesoscopic systems consisting of typically a few tens of interacting particles. The properties of these

systems usually cannot be described by a mean-field approach and are already too complicated to be calculated from the behavior of each individual interacting particle. These systems can therefore be used to study the applicability of the assumptions of thermodynamic equilibrium when going to small particle numbers. One interesting question in this context would be what superfluidity looks like when only a few atoms are present (Grebenev, Toennies, and Vilesov, 1998).

Dense clouds of ultra-cold atoms provide an ideal test bed to study these mesoscopic systems. The interactions are well-understood at the two-body level and, experimentally, one benefits from the host of tools developed over the years to investigate ultra-cold atomic clouds. Recent demonstrations have been achieved using Bose-Einstein condensates with a few thousand atoms (Orzel *et al.*, 2001; Esteve *et al.*, 2008) and showed their advantages in producing squeezed and entangled states as the produced states become more robust to e.g. decoherence with smaller atom number. For these still rather large numbers of atoms, experiments also show a reduction of the atom-number fluctuations in Bose-Einstein condensates in an optical trap (C.-S. Chuu *et al.*, 2005), in optical lattices (Itah *et al.*, 2010), or in arrays of magnetic micro-traps (Whitlock, Ockeloen, and Spreeuw, 2010). The reduction of atom-number fluctuations with respect to the Poissonian case could for example be useful for atomic interferometry below the standard quantum limit (Wineland *et al.*, 1994).

The clouds could also be used as a source delivering a given number of atoms, as was already demonstrated in the single atom case (Schlosser *et al.*, 2001; Förster *et al.*, 2006; Grünzweig *et al.*, 2010) and in the multi-atom case (McGovern *et al.*, 2011). However, these loading procedures have been probabilistic, meaning that after a fixed time interval the number of atoms is not certain. For bosons protocols for deterministic atom loading in these systems have been proposed using the Rydberg-blockade (Saffman and Walker, 2002; Beterov *et al.*, 2011) for example. Also an extraction of atoms from small Bose-Einstein condensates could be possible (Mohring *et al.*, 2005). Benefitting from the Pauli principle deterministic loading of atom number states has been demonstrated for Fermi gases (Serwane *et al.*, 2011).

Also, producing microscopic atom clouds much smaller than the wavelength of the laser light creates a unique situation for a study of light-induced dipole-dipole interactions. These interactions are usually of short range and would play an important role in strongly confined atom samples. Furthermore, small atom clouds can be exploited to investigate collective effects such as the excitation blockade where only one atom in the ensemble can be excited by resonant laser light, thus creating entangled states such as $(|eggg\ldots\rangle + |gegg\ldots\rangle + |ggeg\ldots\rangle + \ldots)$. One consequence of these states would be the observation of e.g. super-radiance (Gross and Haroche, 1982).

Figure 1: Going to a mesoscopic atom regime. The mesoscopic regime is characterized by a small atom number inside the trap.

Using a single aspheric lens to create a microscopic optical dipole trap

The transition from macroscopic to mesoscopic atom ensembles (see Fig. 1) makes special demands on the geometry of the setup such as a tight trapping confinement and a high imaging resolution for example. Various implementations have already been realized such as arrays of optical tweezers Dumke *et al.* (2002) or of magnetic traps Whitlock *et al.* (2009), double-well potential geometries Albiez *et al.* (2005) and optical lattices (e.g. Mandel *et al.* (2003); Nelson, Li, and Weiss (2007)). Here, we follow the idea of using a high-numerical lens (Sortais *et al.*, 2007) to produce a microscopic optical trap for neutral atoms.

This experimental configuration has been proven to be very fruitful in particular for quantum information science with single neutral atoms. Since the observation of single atom loading (Schlosser *et al.*, 2001) a variety of experiments revealed the high potential of the setup for quantum computation. In this context the controlled emission of single photons from a single atom has been demonstrated (Darquié *et al.*, 2005). The interference between photons emitted from two independently trapped atoms (Beugnon *et al.*, 2006) as well as the scalability of the system has been shown by the control on the distance between several atoms (Beugnon *et al.*, 2007). Additionally, the preparation of the atoms in Rydberg states (Urban *et al.*, 2009; Gaëtan *et al.*, 2009) allowed to control the interaction between the atoms. This enabled the entanglement of neutral atoms and the realization of a quantum gate (Wilk *et al.*, 2010; Isenhower *et al.*, 2010). A first focus of the presented work are experiments devoted to this branch of single atom physics that concentrates on the control and detection of the internal state of the atom.

The experimental configuration serves in this thesis to go beyond the single atom regime and study mesoscopic atom clouds containing just a few atoms. This regime has attracted interest to study ultra-cold atoms in optical lattices where each lattice site usually contains less than ten atoms in the lowest energy states (DePue *et al.*, 1999). Our microscopic trap can be considered as one lattice site where it is possible to manipulate and observe small atom ensembles with high optical resolution. It offers the possibility to observe the atoms individually, not only when the atoms are confined but also when they move or are released from the trap in order to access out-of-equilibrium properties. The second focus of this work is the study of this mesoscopic regime and the production of ultra-cold small atom clouds containing just a few atoms inside the microscopic optical dipole trap.

Outline of the thesis

The thesis is divided into four parts.

- **Part I.** We introduce the main theoretical concepts concerning single and many atom physics. Additionally, we describe our experimental setup and the steps pursued to load atoms inside the optical dipole trap.
- **Part II.** In the second part we focus on purely single atom measurements. We use a single atom to calibrate two independent methods applied to measure the temperature, which is useful to understand the temperature measurement done with many atom ensembles. Furthermore, we use the single atom as a quantum bit and show an efficient state preparation as well as readout measurement without losing the atom.
- **Part III.** The third part focuses on measurements in the range from one to about 30 atoms. In a first experiment, we measure the atom number distribution inside the dipole trap. A second experiment concentrates on light-assisted collisions that interfere in the loading process of the microscopic dipole trap.
- **Part IV.** We discuss our work on microscopic atom clouds containing up to thousand atoms. We present an efficient dipole trap loading from a dense surrounding atom reservoir and apply forced evaporation to cool the atom ensemble to sub μK Kelvin temperatures.

Part I

Theoretical background and experimental setup

Chapter 1

Theoretical notes on single atoms

Contents

We begin by introducing the most important theoretical concepts which set the basis in the description of the experiments carried out in the frame of this thesis. The discussion of specific models used to explain the experimental data can be found along this thesis on the particular subject. In this chapter we focus on theoretical concepts based on a purely single atom nature. The two aspects we want to deal with are the atom's internal structure and its behavior in external light or magnetic fields. We mention that the presence of other atoms can effect the internal atom structure or the light scattering behavior due to interactions between the atoms. Depending

on the strength of the interactions the results obtained here may still be applicable for many atom systems as e.g. in the case of many non-interacting atoms. We will touch the subject on inter-particle interactions in the next chapter.

1.1 Résumé

Les atomes alcalins comme le rubidium 87 ont une structure interne similaire à celle de l'atome d'hydrogène. La présence d'un seul électron de valence rend possible son adressage par des champs externes. La dégénérescence entre les sous-niveaux Zeeman peut être levée à l'aide d'un champ magnétique statique. Un champ électrique oscillant permet d'exercer sur l'atome une force de pression de radiation et une force dipolaire qui varie avec la fréquence de la lumière. La force de pression de radiation est prépondérante lorsque la lumière est quasi-résonante; elle est basée sur le transfert d'impulsions entre le champ électromagnétique et l'atome par absorption et émission de photons. Au contraire, lorsque la lumière est très désaccordée de la transition atomique, c'est la force dipolaire qui est prépondérante. Dans ce cas, la lumière laser exerce une force attractive ou répulsive selon que le laser est désaccordé au rouge ou au bleu de la transition atomique, respectivement. Cette force dipolaire est utilisée pour piéger les atomes.

1.2 Internal atom structure

The internal structure of rubidium 87 can in principle be described by the time-independent Schrödinger equation[1]

$$(H_{kin,p} + H_{kin,e} + U)\Psi = E\Psi \ , \tag{1.1}$$

with

$$H_{kin,p} = -\sum_{i=1}^{Z}\left(\frac{\hbar^2\boldsymbol{\nabla}^2_{\boldsymbol{R}_i}}{2m_p}\right) \quad , \quad H_{kin,e} = -\sum_{i=1}^{Z}\left(\frac{\hbar^2\boldsymbol{\nabla}^2_{\boldsymbol{r}_{ei}}}{2m_e}\right) \ . \tag{1.2}$$

It considers the kinetic energy of the Z electrons with mass m_e and protons with mass m_p at positions $\boldsymbol{r_e}$ and $\boldsymbol{R}$, respectively[2]. U represents the potential energy of the atomic constituents. The atom wave function $\Psi(\{\boldsymbol{R}_i\},\{\boldsymbol{r}_{ei}\})$ is the eigenfunction of the Hamiltonian $H_{kin}+U$ with the energy E as its eigenvalue.

The main component of the potential U is the Coulomb interaction[3] $U_{Coulomb} =$

[1] One usually separates time and position coordinates $\Psi(\{\boldsymbol{R}_i\},\{\boldsymbol{r}_i\},t) = \Psi(\{\boldsymbol{R}_i\},\{\boldsymbol{r}_i\})e^{-iEt}$ to transform the time-dependent equation into the time-independent one.

[2] Vectors will be written as bold letters. Constants such as Planck's constant $\hbar$ are listed in App. A

[3] Additionally, we have to take into account the Coulomb potential between the electrons themselves.

$\sum_{ij} \frac{Ze^2}{|\boldsymbol{R}_i - \boldsymbol{r_e}_j|}$. Most other components are usually smaller and can be treated as perturbations

$$U = U_{Coulomb} + U_{Pertubation} \ . \tag{1.3}$$

In the following we discuss the main atom structure arising from the Coulomb potential and introduce some important perturbations.

1.3 Main atom structure

The eigenvalue problem 1.1 with the Coulomb potential $H_{at} = H_{kin} + U_{Coulomb}$ is analytically solvable only for the one electron hydrogen atom with $Z = 1$ (Landau and Lifshitz, 1981). In this case the time-independent Schrödinger equation can be solved by separating the center-of-mass $\boldsymbol{R_r} = \frac{m_p \boldsymbol{R} + m_e \boldsymbol{r_e}}{m_p m_e}$ from the relative $\boldsymbol{r} = \boldsymbol{R} - \boldsymbol{r_e}$ coordinate $\Psi(\boldsymbol{R}, \boldsymbol{r_e}) = \Psi(\boldsymbol{R_r})\Psi(\boldsymbol{r})$. For the relative component it reads in radial coordinates $\boldsymbol{r} = (r, \vartheta, \varphi)$ as:

$$H_{at}\Psi(\boldsymbol{r}) = -\frac{\hbar^2}{2m_r r^2}\frac{\partial}{\partial r}\left(r^2 \frac{\partial}{\partial r}\right)\Psi(\boldsymbol{r}) + \frac{\boldsymbol{L}^2}{2m_r^2} - \frac{e^2}{4\pi\epsilon_0 r}\Psi(\boldsymbol{r}) = E\Psi(\boldsymbol{r}) \ , \tag{1.4}$$

where $m_r = \frac{m_e m_p}{m_e + m_p}$ is the reduced mass and $\boldsymbol{L}^2 = -\hbar^2\left[\frac{1}{\sin\vartheta}\frac{\partial}{\partial\vartheta}\left(\sin\vartheta\frac{\partial}{\partial\vartheta}\right) + \frac{1}{\sin^2\vartheta}\frac{\partial^2}{\partial\varphi^2}\right]$ the squared angular momentum. Separating the wave function in radial and angular parts $\Psi(r, \vartheta, \varphi) = R_{\mathrm{n,l}}(r)Y_{\mathrm{l,m_l}}(\vartheta, \varphi)$ leads to the solution

$$\begin{gathered} R_{\mathrm{n,l}}(r) = \exp(-\kappa\rho)(2\rho)^{\mathrm{l}}\mathcal{L}_{\mathrm{n,l}}(2\rho) \quad , \quad Y_{\mathrm{l,m_l}}(\vartheta, \varphi) = P_{\mathrm{l,m_l}}(\cos(\vartheta))\frac{1}{\sqrt{2\pi}}\exp(i\mathrm{m_l}\varphi) \\ E_{\mathrm{n}} = -\frac{\mu Z^2 e^4}{(4\pi\epsilon_0)^2 2\hbar^2 \mathrm{n}^2} = -R_y\frac{Z^2}{\mathrm{n}^2} \ . \end{gathered} \tag{1.5}$$

Here, $P_{\mathrm{l,m_l}}(\cos(\vartheta))$ and $\mathcal{L}_{\mathrm{n,l}}$ are the Legendre- and Laguerre-Polynomials, respectively. l ($\mathrm{l} \in \{0, 1, \ldots, \mathrm{n}\}$) is the orbital quantum number for which holds $\boldsymbol{L}^2 Y_{\mathrm{l,m}} = \hbar^2 \mathrm{l}(\mathrm{l}+1)\mathrm{Y_{l,m_l}}$ and $\mathrm{m_l}$ ($\mathrm{m_l} \in \{-\mathrm{l}, \ldots, \mathrm{l}\}$) is the magnetic quantum number for which $\boldsymbol{L}_z Y_{\mathrm{l,m}} = -i\hbar\frac{\partial}{\partial\varphi}Y_{\mathrm{l,m_l}} = \hbar\mathrm{m_l}\mathrm{Y_{l,m_l}}$ holds. $R_y = 13.6$ eV is the Rydberg constant defining the ionization energy as well as the separation between atomic levels with different n. Energy levels with the same l or $\mathrm{m_l}$ are degenerate.

Since the Hamiltonian H_{at} commutes with $\boldsymbol{L}^2$ and $\boldsymbol{L}_z$ we can measure the energy, total angular momentum and its component in z-direction without uncertainty. For the Coulomb potential problem, n, l and $\mathrm{m_l}$ completely describe the internal state of the atom. All quantum numbers belonging to a complete set that describes an atomic state are called good quantum numbers. In the Dirac notation the wave function corresponding to the set of good quantum numbers is denoted as $|\mathrm{n}, \mathrm{l}, \mathrm{m_l}\rangle$.

Rubidium as an alkali atom has a similar atom structure as the hydrogen atom. Its physical properties such as the angular momentum or the spin are mainly gov-

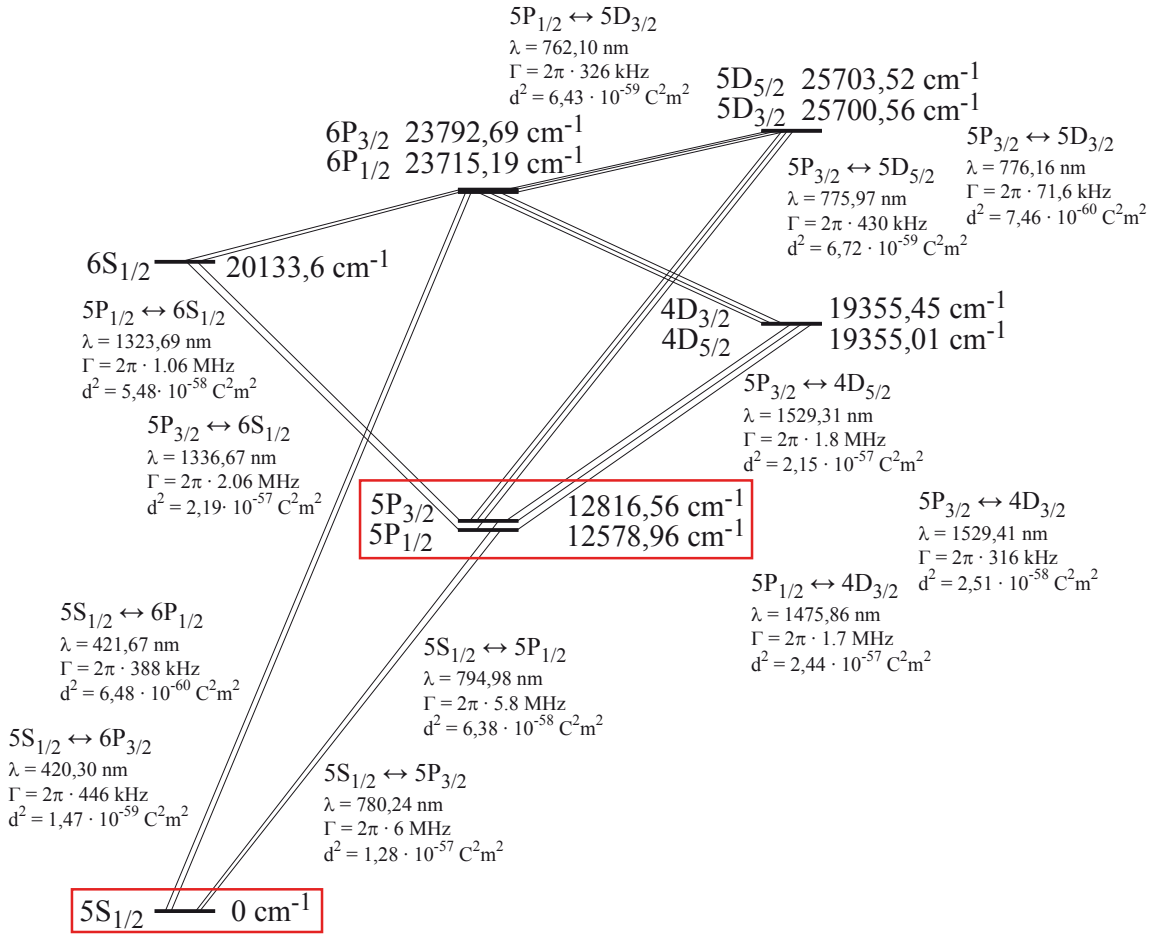

Figure 1.1: Rubidium level structure. The fine-structure of rubidium is shown for the first excited levels. The dipole moment d of each level can be calculated by using the Wigner-Weisskopf formula $d^2_{JJ'} = |\langle J||e\boldsymbol{r}||J'\rangle|^2 = \frac{2J'+1}{2J+1}\frac{3}{8\pi^2}\epsilon_0\hbar\lambda^3_{JJ'}\Gamma_{JJ'}$. The red-framed states are used for our optical transitions.

erned by the valence electron since the angular momentum and spin of the complete inner shells sum up to zero according to Hund's rules. However, while the result for the angular wave function $Y_{\mathrm{l,m_l}}$ stays valid even for atoms with higher Z the radial part and the eigenenergies E_n differ from the ones of hydrogen. They can only be calculated numerically using a self-consistent Hartree-Fock approach which takes into account the Coulomb interaction between protons and electrons as well as electrons themselves. In any case $\mathrm{n, l}$ and $\mathrm{m_l}$ are still good quantum numbers. We will see in the following how other interactions, usually much smaller than the Coulomb interaction and thus allowing perturbation theory to be applicable, can change this situation.

1.3.1 Fine structure

The most important interactions that lead to perturbations are caused by the following:

- **Spin-orbit coupling.** Experimentally the Stern-Gerlach experiment showed that the electron has two possible spin values, which theoretically follows from the relativistic Dirac equation. Analog to the orbital momentum $\boldsymbol{L}$, we can write for the spin $\boldsymbol{S}^2\Psi_\mathrm{s} = \hbar^2\mathrm{s}(\mathrm{s}+1)\Psi_\mathrm{s}$, where $\mathrm{s} = \frac{1}{2}$. The spin is associated to the magnetic moment $\boldsymbol{\mu} = -g_s\mu_\mathrm{B}\frac{\boldsymbol{S}}{\hbar}$, where μ_B is the Bohr-magneton and $g_s \approx 2$ the electron g-factor. In the rest frame of the electron it sees the positive charge of the nucleus orbiting around it. This moving charge creates a magnetic field $\boldsymbol{B}$ proportional to the orbital angular momentum $\boldsymbol{L}$ which the electron spin can align to. The potential energy stocked in the coupling is $U_{so} = -\boldsymbol{\mu}\cdot\boldsymbol{B} \propto -\boldsymbol{S}\cdot\boldsymbol{L}$. It depends on the relative orientation between both vectors. Due to the spin-orbit interaction $\boldsymbol{L}^2$ and $\boldsymbol{L}_z$ do not commute with the Hamiltonian $H_{at} = H_{kin} + U_{Coulomb} + U_{so}$ and thus $\mathrm{n}, \mathrm{l}, \mathrm{m_l}$ are no good quantum numbers any more. We can show that the total angular momentum $\boldsymbol{J} = \boldsymbol{S} + \boldsymbol{L}$ now defines a set of good quantum numbers. Analog to the orbital momentum we define $\boldsymbol{J}^2 |\mathrm{n}, \mathrm{J}, \mathrm{m_J}\rangle = \hbar^2\mathrm{J}(\mathrm{J}+1)|\mathrm{n}, \mathrm{J}, \mathrm{m_J}\rangle$ and $\boldsymbol{J}_z |\mathrm{n}, \mathrm{J}, \mathrm{m_J}\rangle = \hbar\mathrm{m_J}|\mathrm{n}, \mathrm{J}, \mathrm{m_J}\rangle$. We find that $U_{so} \propto -\boldsymbol{S}\cdot\boldsymbol{L} = -\frac{1}{2}(\boldsymbol{J}^2 - \boldsymbol{L}^2 - \boldsymbol{S}^2)$ and thus the energy correction in first order perturbation theory $E_{so} \propto -\hbar^2(\mathrm{J}(\mathrm{J}+1) - \mathrm{l}(\mathrm{l}+1) - \mathrm{s}(\mathrm{s}+1))$. Here, the total angular momentum quantum number J only takes quantized values between $|\mathrm{l}-\mathrm{s}|, \cdots, \mathrm{J}-1, \mathrm{J}, \mathrm{J}+1, \cdots, \mathrm{l}+\mathrm{s}$ (Landau and Lifshitz, 1981).

  The spin-orbit interaction lifts the degeneracy between levels with the same L. For example for rubidium, $s = \frac{1}{2}$, the first excited level with $\mathrm{l} = 1$ splits into two levels having $\mathrm{J} = \mathrm{l} - \mathrm{s} = \frac{1}{2}$ and $\mathrm{J} = \mathrm{l} + \mathrm{s} = \frac{3}{2}$. Levels with the same J are however still degenerate. Typical spin-orbit shifts scale as $\sim 10^{-4}$ eV and are much smaller than the Coulomb interaction $\sim R_y$ justifying the perturbation approach.

- **Relativistic effects.** The kinetic energy has been treated in Eq. 1.2 as $E_{kin} = \sum_{i=1}^{Z}\frac{\boldsymbol{p_i}^2}{2m_e} \rightarrow H_{kin} = -\sum_{i=1}^{Z}\frac{\hbar^2\nabla^2_{\boldsymbol{r_{e_i}}}}{2m_e}$. Treating the kinetic energy relativistically shifts the energy levels and lifts the degeneracy for levels with the same l (Condon and Shortley, 1997).

- **Quantum-electrodynamic effects.** Quantum fluctuations of the vacuum field can perturb the Coulomb force that is seen by the electron orbiting around the nucleus. This perturbation leads to small energy shifts ($\sim 10^{-5}$ eV) called Lamb shift that is most striking for energy levels with small n and depends on l and J (Lamb and Retherford, 1947). For further effects see e.g. Messiah (1999).

The first energy levels for rubidium 87 are illustrated in Fig. 1.1. Due to the interactions $\mathrm{n}, \mathrm{J}, \mathrm{m_J}$ become good quantum numbers now. We denoted the levels according to the rule $\mathrm{n}^{2\mathrm{s}+1}\mathrm{l_J}$. All $\mathrm{m_J}$ levels are degenerate. We follow the convention to use for $\mathrm{l} = 0, 1, 2, ...$ the letters $\mathrm{l} = \mathrm{S}, \mathrm{P}, \mathrm{D}, \ldots$. The ground state of rubidium would then be written as $5^2\mathrm{S}_{1/2}$. The lines indicate single photon transitions that are allowed between the fine levels. They obey the selection rule $\Delta\mathrm{J} = 0, \pm 1 (\mathrm{J} = 0 \nleftrightarrow 0)$ and $\Delta\mathrm{l} = \pm 1$. In the following we focus on the red-framed states as their corresponding D_1

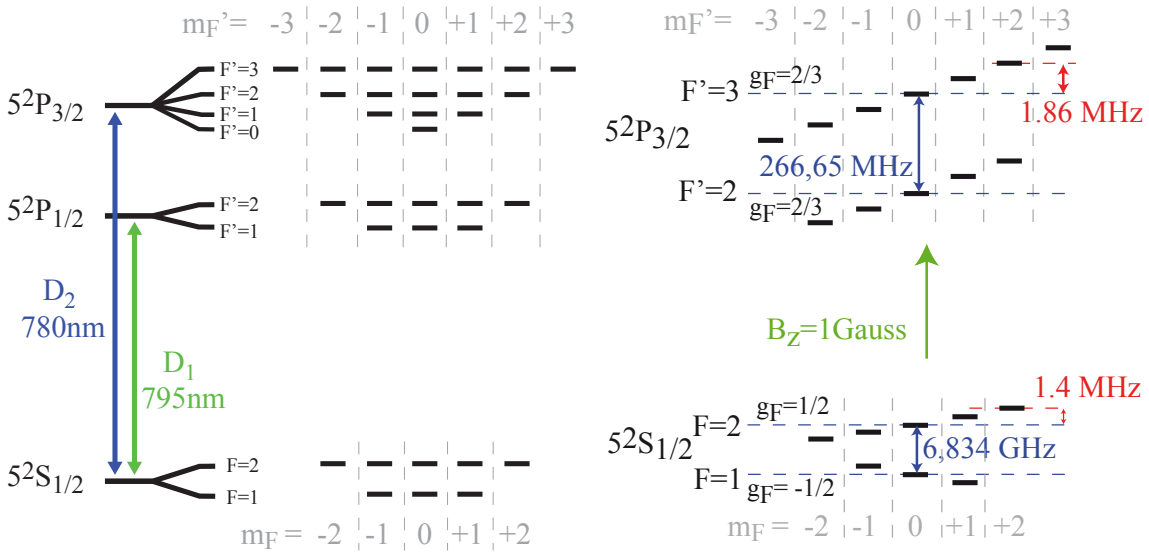

Figure 1.2: Zeeman sub-structure and magnetic field-induced shifts. *left*) Hyperfine and Zeeman level structure of the D_1 and D_2 transitions. *right*) Zeeman level shifts induced by a static external magnetic field along the quantization axis B_z.

($5^2S_{1/2} \rightarrow 5^2P_{1/2}$) and D_2 ($5^2S_{1/2} \rightarrow 5^2P_{3/2}$) transitions are used for our fluorescence measurements.

1.3.2 Hyperfine structure

The fine levels have a further sub structure referred to as the hyperfine structure. It results from a further coupling between the total electron angular momentum $\boldsymbol{J}$ and the nuclear angular momentum $\boldsymbol{I}$. For ^{87}Rb the eigenvalue is $I = \frac{3}{2}$. In analogy to the total electron angular momentum $\boldsymbol{J}$ we introduce a total atomic angular momentum as $\boldsymbol{F} = \boldsymbol{J} + \boldsymbol{I}$, whose quantum number lies in $|\mathrm{J} - \mathrm{I}| \leq \mathrm{F} \leq \mathrm{J} + \mathrm{I}$. The magnetic field of the coupling again leads to a splitting of each level. For instance, for $5^2P_{3/2}$ we find $\frac{3}{2} - \frac{3}{2} = 0 \leq \mathrm{F} \leq \frac{3}{2} + \frac{3}{2} = 3$ and thus four sublevels with $F = 0, 1, 2, 3$. The hyperfine structure for the D_1 and D_2 transition levels is sketched on the left of Fig. 1.2. A more detailed illustration can be found in App. A. The (2F+1) magnetic Zeeman components arise from different orientations of the electron angular distribution of the atom wave function introduced as $\mathrm{m_l}$ in Eq. 1.5. They are all degenerate if no external fields are present.

1.4 Atoms in a static external magnetic field

In the last section we have seen that the internal magnetic field of the atom caused by the electron movement around the nucleus leads to the fine-structure of the atom. Here, we want to describe effects that external fields have on the atom. With an external magnetic field $\boldsymbol{B}$, the Hamiltonian describing the interaction energy is

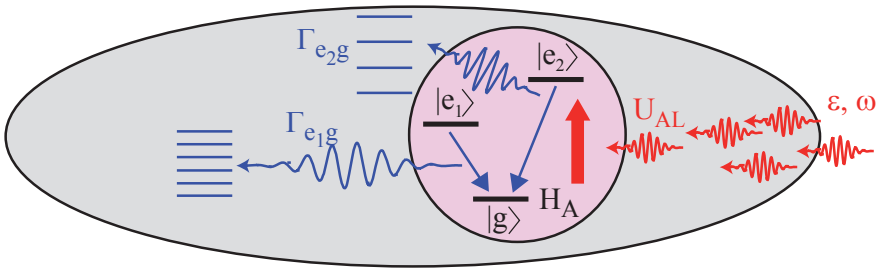

Figure 1.3: Multi level atom in an external light field. The atom couples to the laser field as well as to the electro-magnetic vacuum field.

$$H = \frac{\mu_B}{\hbar}(g_s \boldsymbol{S} + g_I \boldsymbol{I} + g_L \boldsymbol{L}) \cdot \boldsymbol{B} \ , \tag{1.6}$$

g_s, g_I, g_L[4] are the electron spin, nuclear and electron orbit g-factors, respectively (Steck, 2008). In most of our situations the magnetic field shifts the energy levels less than the energy difference between the hyper-fine levels. In this case F as a good quantum number is preserved. With an external magnetic field $\boldsymbol{B}$, the Hamiltonian in Eq. 1.6 is reduced to

$$H_{Zeeman} = \mu_B g_F \boldsymbol{F} \cdot \boldsymbol{B} \ , \tag{1.7}$$

where g_F is the hyperfine g-factor, whose values are shown in the right graph of Fig. 1.2. Assuming our magnetic field to be along the quantization axis z the energy shift in first order perturbation theory is

$$\Delta E_{Zeeman} = \mu_B g_F \mathrm{m_F} B_z \ . \tag{1.8}$$

1.5 Light-atom interaction

So far it has been possible to describe the atom with the time-independent Schrödinger equation as the interactions were of stationary nature. The interaction of the atom with a light field is a dynamic process that is based on the coupling between the atom and the laser field as well as the vacuum field. The coupling of the atom with the laser field can lead to absorption and stimulated emission of photons and the coupling to the vacuum field leads to spontaneous emission, see Fig. 1.3.

We consider transitions between atomic states driven by the electric field of monochromatic laser light

$$\boldsymbol{E}_L(\boldsymbol{r}, t) = \frac{1}{2}\mathcal{E}_L(\boldsymbol{r}) \left(\boldsymbol{\epsilon}_L(\boldsymbol{r}) e^{-i(\omega_L t - \boldsymbol{k}_L \boldsymbol{r})} + \text{c.c.}\right) \ . \tag{1.9}$$

Here, $\mathcal{E}_L$ is the field amplitude, $\boldsymbol{\epsilon}_L(\boldsymbol{r})$ the polarization, ω_L the frequency and $\boldsymbol{k}_L = \frac{2\pi}{\lambda_L}$ the wave vector with λ_L being the wavelength of the light. We are usually dealing

[4] Their values are listed in App. A

with high light intensities that make a quantum-mechanical treatment of the light field unnecessary and a classical description favorable. Possible electric dipole transitions with $\Delta \mathrm{l} = \pm 1$ between the states follow the selection rules

$$\begin{aligned} \Delta F = 0 \quad &\rightarrow \quad \Delta m_F \pm 1 \\ \Delta m_F = \pm 1 \quad &\rightarrow \quad \Delta m_F = \epsilon \ , \end{aligned} \tag{1.10}$$

where $\epsilon = \{0, -1, 1\}$ corresponds to linear, σ^- and σ^+ polarizations. In Sec. 5.4.1 we will use magnetic dipole transitions to drive transitions with $\Delta \mathrm{l} = 0$ for which the theoretical description presented here remains valid.

1.5.1 Interaction Hamiltonian

The Hamiltonian describing the system of one atom interacting with a light field is in principle composed of three terms[5]

$$H_{AL} = H_{kin} + U_{pot} + U_L \ . \tag{1.11}$$

Here, we neglect the electro-magnetic vacuum field $H_R = \sum_n \hbar \omega_n \hat{a}_n^+ \hat{a}_n$ and its interaction with the atom, where $\hat{a}_n^+$ and $\hat{a}_n$ are the creation and annihilation operators of the mode with energy $\hbar \omega_n$. The three essential terms are:

- **Kinetic energy**

$$H_{kin} = \frac{\boldsymbol{P}^2}{2m} \tag{1.12}$$

  We include the kinetic energy of the atom with total mass m, where the atom's center-of-mass momentum is $\boldsymbol{P}$.

- **Internal energy**

$$U_{pot} = \sum_{j=1}^{N_g} \hbar \omega_{g_j} \left| g_j \right\rangle \left\langle g_j \right| + \sum_{l=1}^{N_e} \hbar \omega_{e_l} \left| e_l \right\rangle \left\langle e_l \right| \tag{1.13}$$

  We consider a set of N_g atomic ground $\left| g_1 \right\rangle, \ldots, \left| g_{N_g} \right\rangle$ and N_e excited states $\left| e_1 \right\rangle, \ldots, \left| e_{N_e} \right\rangle$.

- **Atom coupling to the laser field**

  We introduce the dipole matrix $\boldsymbol{\mathcal{D}}(t)$. The matrix elements are defined as

$$\begin{aligned} \boldsymbol{\mathcal{D}}_{g_j e_l}(t) &= \tilde{\boldsymbol{d}}_{g_j e_l} \left| g_j \right\rangle \left\langle e_l \right| e^{-i \delta \omega_{g_j e_l} t} \\ &= \boldsymbol{d}_{g_j e_l} \left| g_j \right\rangle \left\langle e_l \right| \ , \end{aligned} \tag{1.14}$$

  with $\delta \omega_{g_j e_l} = \omega_{e_l} - \omega_{g_j}$. The dipole matrix elements are $\boldsymbol{d}_{g_j e_l} = \left\langle g_j \right| e \boldsymbol{r} \left| e_l \right\rangle$ for which $\boldsymbol{d}_{g_j e_l} = \boldsymbol{d}^*_{e_l g_j}$. The atomic dipole corresponding to the transition $\left| g_j \right\rangle \leftrightarrow \left| e_l \right\rangle$ is

[5] We follow the standard treatment that can be found e.g. in Cohen-Tannoudji, Dupont-Roc, and Grynberg (1988) in a similar way.

$$\boldsymbol{D}_{g_j e_l}(t) = \boldsymbol{d}_{g_j e_l} |g_j\rangle \langle e_l| + \boldsymbol{d}_{e_l g_j} |e_l\rangle \langle g_j| \ . \tag{1.15}$$

The interaction can then be written as

$$\begin{aligned} U_L(\boldsymbol{R}, t) &= -\sum_{j=1}^{N_g} \sum_{l=1}^{N_e} \boldsymbol{D}_{g_j e_l}(t) \cdot \boldsymbol{E}_L(\boldsymbol{R}, t) \\ &= -\sum_{j=1}^{N_g} \sum_{l=1}^{N_e} \frac{1}{2} \mathcal{E}_L(\boldsymbol{r}) (\tilde{\boldsymbol{d}}_{g_j e_l} \cdot \boldsymbol{\epsilon}_L)(\boldsymbol{r}) |g_j\rangle \langle e_l| e^{i((\omega_L - \delta\omega_{g_j e_l})t - \boldsymbol{k}_L \boldsymbol{r})} + \text{h.c.} \\ &= \sum_{j=1}^{N_g} \sum_{l=1}^{N_e} \frac{1}{2} \hbar \Omega_{g_j e_l}(\boldsymbol{r}) |g_j\rangle \langle e_l| e^{i(\omega_L t - \boldsymbol{k}_L \boldsymbol{r})} + \text{h.c.} \ , \end{aligned} \tag{1.16}$$

where $\boldsymbol{R}$ is the position of the atom's center-of-mass and

$$\hbar \Omega_{g_j e_l}(\boldsymbol{r}) = -(\boldsymbol{d}_{g_j e_l} \cdot \boldsymbol{\epsilon}_L) \mathcal{E}_L(\boldsymbol{r}) \ , \tag{1.17}$$

the Rabi frequency[6]. We have applied the rotating-wave approximation including slow oscillating terms $\pm(\omega_L - \delta\omega_{g_j e_l})$ and neglecting fast ones $\pm(\omega_L + \delta\omega_{g_j e_l})$. We have also assumed the atom wave packet to have a dimension much smaller than the laser wavelength λ_L which allows to evaluate the light field at the position of the atom. This assumption is valid for typical laser-cooled atom temperatures of ~ 100 μK for which the thermal de Broglie wavelength $\lambda_{th} = \frac{h}{\sqrt{2\pi m k_B T}} \approx 20$ nm is much smaller than the laser wavelength $\lambda = 780$ nm.

1.5.2 Reduction of the dipole matrix

Information about the dipole matrix element $\boldsymbol{d}_{g_j e_l} = \langle g_j| e\boldsymbol{r} |e_l\rangle$ can be retrieved by measuring the line width or decay rate $\Gamma_{g_j e_l}$ of that transition. As the decay rates $\Gamma_{JJ'}$ between two fine structure levels with J and J' are essentially independent of the hyperfine states involved we define the matrix elements $\langle g_j| e\boldsymbol{r} |e_l\rangle$ as $\sqrt{\frac{2J+1}{2J'+1}} \langle J| |e\boldsymbol{r}| |J'\rangle$ taking into account their level of degeneracy. The dipole matrix elements are then related to the decay rate via the Wigner-Weisskopf equation

$$\Gamma_{jj'} = \frac{8\pi^2}{3\epsilon_0 \hbar \lambda_{JJ'}^3} \frac{2J+1}{2J'+1} |\langle J| |e\boldsymbol{r}| |J'\rangle|^2 \ , \tag{1.18}$$

which can be derived quantum-mechanically from Fermi's golden rule and has a classical analog in the power radiated from a Hertzian dipole (Loudon, 2000). The corresponding matrix elements for the hyperfine levels can be calculated using the Wigner-Eckart theorem (Brink and Satchler, 1994)

[6] The double sum $\sum_{j=1}^{N_g} \sum_{l=1}^{N_e}$ contains all possible combinations between a ground and an excited state that could be driven by a light field. The selection rules are taken into account by the Rabi frequency for which $\Omega_{g_j e_l} = 0$ for not allowed transitions as the dipole matrix element vanishes.

$$\langle F, m_F | \, e\boldsymbol{r} \, | F', m_{F'} \rangle = C^{J,J',I}_{F,m_F,F',m_{F'}} \langle J | \, |e\boldsymbol{r}| \, | J' \rangle \ , \tag{1.19}$$

For the $(5^2S_{1/2}F = 2 \rightarrow 5^2P_{3/2}F' = 2)$ and $(5^2S_{1/2}F = 2 \rightarrow 5^2P_{3/2}F' = 3)$ transitions the Clebsch-Gordon coefficients $C^{J,J',I}_{F,m_F,F',m_{F'}}$ are listed in appendix A.

1.5.3 Semi-classical picture of atom-light interaction

The light-atom interaction has two important effects on the atom: First, it can change the internal energy of the atom and second, it can alter the center-of-mass motion of the atom. The absorption and re-emission of photons leads to changes in velocity of $\Delta v = v_{rec} = \frac{\hbar k_L}{m}$ due to the recoil momentum of the photon. We can thus assume the external parameters to vary on time scales as $t_{ext} \sim \frac{1}{k_L \Delta v}$. The internal evolution takes place at a rate Γ which leads to $t_{int} \sim \Gamma^{-1}$. For the D_1 and D_2 transitions in rubidium we find $t_{int} \ll t_{ext}$ where the internal evolution takes place at much shorter time scales than the external one. In this case it is possible to separate the external evolution related to H_{kin} from the internal evolution $U_{pot} + U_L$ by using an averaged atom position in the light field's phase $\boldsymbol{k}_L \langle \boldsymbol{R} \rangle$. In the following we use a semi-classical description. The external evolution of the atom is treated classically while the interaction with the laser light field is described quantum-mechanically.

1.5.4 Internal atom evolution: Optical Bloch equations

The density matrix

$$\boldsymbol{\rho} = \sum_{j=1}^{N_g} \rho_{g_j g_j} \, |g_j\rangle \langle g_j| + \sum_{l=1}^{N_e} \rho_{e_l e_l} \, |e_l\rangle \langle e_l| + \sum_{j=1}^{N_g} \sum_{l=1}^{N_e} \left(\rho_{g_j e_l} \, |g_j\rangle \langle e_l| + \rho_{e_l g_j} \, |e_l\rangle \langle g_j| \right) \tag{1.20}$$

contains in its diagonal the probabilities $\rho_{g_j g_j}$, $\rho_{e_l e_l}$ for the atom to be in a given internal ground $|g_j\rangle$ or excited $|e_l\rangle$ state and in its off-diagonals the coherence between different states. As we reduce the atom to the valence electron only, it is here possible to write the internal density matrix on a one electron basis. In matrix form we can write

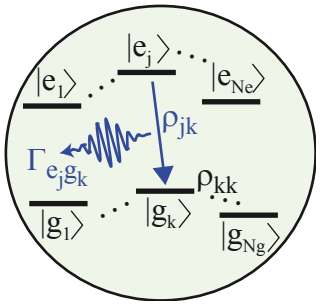

Figure 1.4: Internal structure.

$$\boldsymbol{\rho} = \begin{pmatrix} \rho_{g_1 g_1} & \cdots & \rho_{g_1 g_{N_g}} & \rho_{g_1 e_1} & \cdots & \rho_{g_1 e_{N_e}} \\ \vdots & & \vdots & \vdots & & \vdots \\ \rho_{g_{N_g} g_1} & \cdots & \rho_{g_{N_g} g_{N_g}} & \rho_{g_{N_g} e_1} & \cdots & \rho_{g_{N_g} e_{N_e}} \\ \rho_{e_1 g_1} & \cdots & \rho_{e_1 g_{N_g}} & \rho_{e_1 e_1} & \cdots & \rho_{e_1 e_{N_e}} \\ \vdots & & \vdots & \vdots & & \vdots \\ \rho_{e_{N_e} g_1} & \cdots & \rho_{e_{N_e} g_{N_g}} & \rho_{e_{N_e} e_1} & \cdots & \rho_{e_{N_e} e_{N_e}} \end{pmatrix} . \tag{1.21}$$

The temporal evolution of the density matrix follows from the Liouville equation

$$\dot{\boldsymbol{\rho}} = \frac{d\boldsymbol{\rho}}{dt} = -\frac{i}{\hbar}[\boldsymbol{H}, \boldsymbol{\rho}] + \frac{\partial \boldsymbol{\rho}}{\partial t} = -\frac{i}{\hbar}[\boldsymbol{H}, \boldsymbol{\rho}] + \boldsymbol{\mathcal{L}}_{loss} \cdot \boldsymbol{\rho} \ , \tag{1.22}$$

where $\boldsymbol{H}$ is any Hamiltonian in matrix form and $\boldsymbol{\mathcal{L}}_{loss}$ a function acting on $\boldsymbol{\rho}$ representing the decoherence. The Liouville equation leads to a set of coupled differential equations, see e.g. App. B. For the fast evolving light-atom Hamiltonian parts that govern the internal evolution $U_{pot}+U_L$ from Eq. 1.11 these equations are called optical Bloch equations.

1.5.5 External atom evolution: Light forces

For the external evolution of the atom we calculate the forces governing the equations of motion by averaging over the fast oscillating components

$$\begin{aligned} \langle \boldsymbol{F}(\boldsymbol{R}, t)\rangle_{int} &= -\langle \boldsymbol{\nabla} U_L(\boldsymbol{R}, t)\rangle_{int} \\ &= \left\langle \sum_{j=1}^{N_g}\sum_{l=1}^{N_e} \boldsymbol{\nabla}(\boldsymbol{D}_{g_j e_l}(t) \cdot \boldsymbol{E_L}(\boldsymbol{R}, t)) + \text{h.c.} \right\rangle_{int} \\ &= -\frac{1}{2}\hbar \sum_{j=1}^{N_g}\sum_{l=1}^{N_e} Tr(\boldsymbol{\rho}^{(st)} |g_j\rangle \langle e_l|) \boldsymbol{\nabla}(\Omega_{g_j e_l}(\boldsymbol{R}) e^{i(\omega_L t - \boldsymbol{k}_L \boldsymbol{r})}) + \text{h.c.} \ . \end{aligned} \tag{1.23}$$

The position of the atom's center-of-mass can be inferred by using Ehrenfest theorem $\frac{d}{dt}\langle \boldsymbol{R}\rangle = \langle \frac{\boldsymbol{P}}{m}\rangle$. We add that a second force resulting from the coupling between the atom and the vacuum field due to spontaneous decay averages out over time due to the decay into the entire solid angle. The time-averaged transition probability $\langle |g_j\rangle \langle e_l|\rangle_{int} = Tr(\boldsymbol{\rho}^{(st)} |g_j\rangle \langle e_l|)$ between two states can be calculated using the stationary solution $\boldsymbol{\rho}^{(st)}$ of the optical Bloch equations and tracing out the density matrix. Between two states $|g_j\rangle$ and $|e_l\rangle$ the transition probability

$$Tr(\boldsymbol{\rho}^{(st)} |g_j\rangle \langle e_l|) = \rho_{g_j e_l} = \tilde{\rho}_{g_j e_l} e^{i(\omega_L t - \boldsymbol{k}_L \boldsymbol{r})} \tag{1.24}$$

oscillates with the laser field[7]. If we average over one cycle of the laser field[8] $\langle \boldsymbol{F}(\boldsymbol{R}, t)\rangle_t = \boldsymbol{F}(\boldsymbol{R})$, we obtain

$$\boldsymbol{F}(\boldsymbol{R}) = -\hbar \sum_{j=1}^{N_g}\sum_{l=1}^{N_e} \left(\frac{\tilde{\rho}_{g_j e_l} + \tilde{\rho}_{e_l g_j}}{2} \boldsymbol{\nabla}(\Omega_{g_j e_l}(\boldsymbol{R})) - \frac{\tilde{\rho}_{g_j e_l} - \tilde{\rho}_{e_l g_j}}{2i} \Omega_{g_j e_l}(\boldsymbol{R}) \boldsymbol{\nabla}(\boldsymbol{k}_L \boldsymbol{R}) \right) \ . \tag{1.25}$$

The force in Eq. 1.23 has two two parts: We start with a discussion of the term which is proportional to $\boldsymbol{\nabla}(\boldsymbol{k}_L \boldsymbol{R})$.

[7] For a system with one ground and N_e excited states this is shown in App. B.

[8] Terms with $\langle \cos(\omega_L t - \boldsymbol{k}_L \boldsymbol{R}) \sin(\omega_L t - \boldsymbol{k}_L \boldsymbol{R})\rangle_t = 0$ average to zero while terms with $\langle \cos^2(\omega_L t - \boldsymbol{k}_L \boldsymbol{R})\rangle_t$ equal $\frac{1}{2}$.

1.5.6 Fluorescence scattering

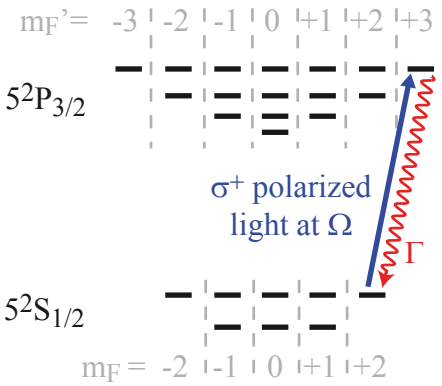

Figure 1.5: Closed cycling transition.

In order to obtain an expression for the term $\propto \boldsymbol{\nabla}(\boldsymbol{k}_L \boldsymbol{R})$ we need to calculate the off-diagonal density matrix elements. For many-level atoms solutions can be quite involved and analytic expressions unhandy. However, there are situations in which the rubidium atom can be considered a two level system. This is the case when σ^+-polarized light near 780 nm will address only the transition between $|g\rangle = \left|5^2\mathrm{S}_{1/2}\mathrm{F}=2, \mathrm{m_F}=+2\right\rangle$ and $|e\rangle = \left|5^2\mathrm{P}_{3/2}\mathrm{F}'=3, \mathrm{m_F}=+3\right\rangle$ as shown by the blue arrow in Fig. 1.5. From $|e\rangle$ the atom will always deexcite back into $|g\rangle$ with the decay rate $\Gamma_{ge}=\Gamma$ and eventually be reexcited by the laser at a rate $\Omega_{ge}=\Omega$. For these two states the differential equations in the slow-rotating reference frame[9] with $\rho_{ge}=\tilde{\rho}_{ge}e^{i(\omega_L t-\boldsymbol{k}_L\boldsymbol{R})}$ follow from Eq. 1.22

$$\begin{gathered}\dot{\rho}_{gg}=i\frac{\Omega}{2}(\tilde{\rho}_{ge}-\tilde{\rho}_{eg})+\Gamma\rho_{ee} \quad , \quad \dot{\rho}_{ee}=i\frac{\Omega}{2}(\tilde{\rho}_{eg}-\tilde{\rho}_{ge})-\Gamma\rho_{ee} \ , \\ \dot{\tilde{\rho}}_{ge}=i\frac{\Omega}{2}(\rho_{gg}-\rho_{ee})-(\frac{\Gamma}{2}+i\Delta)\tilde{\rho}_{ge} \ ,\end{gathered} \tag{1.26}$$

for which the conditions $\rho_{gg}+\rho_{ee}=1$ and $\tilde{\rho}_{ge}=\tilde{\rho}^*_{eg}$ hold. $\Delta=\omega_L-(\omega_e-\omega_g)=\omega_L-\delta\omega_{eg}$ is the detuning between the laser frequency and the atomic transition. The stationary $\dot{\rho}=0$ solution (Loudon, 2000) is

$$\rho^{(st)}_{gg}=1-\rho_{st,ee} \ , \quad \rho^{(st)}_{ee}=\frac{1}{2}\frac{2\left(\frac{\Omega}{\Gamma}\right)^2}{1+2\left(\frac{\Omega}{\Gamma}\right)^2+4\left(\frac{\Delta}{\Gamma}\right)^2} \ , \quad \tilde{\rho}^{(st)}_{ge}=\frac{i\frac{\Omega}{\Gamma}+\frac{2\Delta\Omega}{\Gamma^2}}{1+2\left(\frac{\Omega}{\Gamma}\right)^2+4\left(\frac{\Delta}{\Gamma}\right)^2} \ . \tag{1.27}$$

For the light pressure force we obtain

$$\boldsymbol{F}_{pr}(\boldsymbol{R})=\hbar\boldsymbol{k}_L\Omega\frac{\tilde{\rho}^{st}_{ge}-\tilde{\rho}^{st}_{eg}}{2i}=\hbar\boldsymbol{k}_L\Gamma\rho^{st}_{ee}=\hbar\boldsymbol{k}_L R=\hbar\boldsymbol{k}_L\frac{\Gamma}{2}\frac{s(\boldsymbol{R})}{1+s(\boldsymbol{R})+4\left(\frac{\Delta}{\Gamma}\right)^2} \ , \tag{1.28}$$

where we used

$$s(\boldsymbol{R})=2\left(\frac{\Omega}{\Gamma}\right)^2=\frac{I_L(\boldsymbol{R})}{I_{sat}} \ . \tag{1.29}$$

For the second step we replace Ω by its definition in Eq. 1.17 and introduce the laser intensity $I_L(\boldsymbol{R})=\frac{1}{2}\epsilon_0 c\mathcal{E}_L(\boldsymbol{R})^2$ to obtain

$$I_{sat}=\frac{c\epsilon_0\hbar^2\Gamma^2}{4\left|\boldsymbol{\epsilon}_L\langle g|\,e\boldsymbol{r}\,|e\rangle\right|^2}=16.693\ \mathrm{W/m^2} \ . \tag{1.30}$$

[9] The matrix form of the Hamiltonian and its transformation into the slow-rotating reference frame are shown in App. B for a generalized situation of one ground and N_e excited states

For the chosen levels we can replace the matrix element

$$\begin{aligned} |\langle g|\, e\boldsymbol{r}\, |e\rangle|^2 &= \left|\left\langle 5^2\mathrm{S}_{1/2}\mathrm{F}=2, \mathrm{m_F}=+2\right|\, e\boldsymbol{r}\, \left|5^2\mathrm{P}_{3/2}\mathrm{F}'=3, \mathrm{m_F}=+3\right\rangle\right|^2 \\ &= \frac{2J'+1}{2J+1}\left|C^{1/2,3/2,3/2}_{2,+2,3,+3}\,\langle J|\,|e\boldsymbol{r}|\,|J'\rangle\right|^2 = \frac{3}{8\pi^2}\frac{\epsilon_0\hbar\lambda^3}{\Gamma} \end{aligned} \tag{1.31}$$

by the Wigner-Weisskopf expression in Eq. 1.18. This finally leads to

$$I_{sat} = \frac{2\pi^2\hbar c\Gamma}{3\lambda^3}\ . \tag{1.32}$$

The light pressure force is a dissipative force. It is based on the photon absorption from the laser field, see Fig. 1.6. Spontaneous emission does not lead to a net force on average as the emission goes into the entire solid angle. The force has a Lorentzian shape centered around the atomic transition frequency with line width Γ. Its width is given by the natural line width Γ and is broadened by the probe laser intensity $\frac{I_L}{I_{sat}}$. The maximal photon scattering rate is $\Gamma/2$ when the saturation is infinite $s\to\infty$. In this situation the atom stays in the excited state with probability one-half $\rho_{ee}=\frac{1}{2}$.

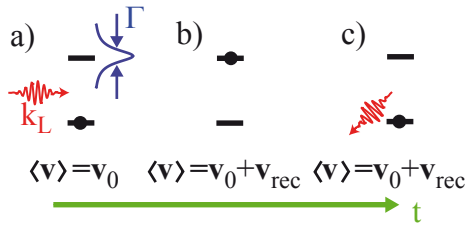

Figure 1.6: Light pressure due to near-resonance light.

1.5.7 Dipole force

The other term of the force $\propto \boldsymbol{\nabla}(\Omega_{g_j e_l}(\boldsymbol{R}))$ corresponds to the dispersive part. On a two-level basis this conservative force equals

$$\boldsymbol{F}_{dip}(\boldsymbol{R}) = -\hbar\Delta\frac{2\left(\frac{\Omega}{\Gamma}\right)^2}{1+2\left(\frac{\Omega}{\Gamma}\right)^2+4\left(\frac{\Delta}{\Gamma}\right)^2}\frac{\boldsymbol{\nabla}(\Omega(\boldsymbol{R}))}{\Omega(\boldsymbol{R})} \tag{1.33}$$

and vanishes for laser frequencies near the atomic transition resonance as it is proportional to Δ and for plane waves for which $\boldsymbol{\nabla}\Omega(\boldsymbol{R})=0$. This on the other hand means that the atom feels the force only for larger detunings. In a classical picture the electric field of the laser leads to an induced dipole moment of the atom which in turn interacts with the laser field.

The large laser detuning of the dipole trap ($\Delta\sim 70-170$ nm in our case) has the consequence that the probability for the atom to be in the ground rather than the excited state is high $\rho_{gg}\gg\rho_{e_ie_i}$. This assumption can be used to calculate the force on a many-level atom. As an example, we calculate the force for a linear laser polarization if the atom is in the ground state $|g\rangle=\left|5^2\mathrm{S}_{1/2}\mathrm{F}=2, \mathrm{m_F}=-2\right\rangle$. If we restrict ourselves to wavelengths used in our experiment of around $850-950$ nm the strongest coupling is with states (see left graph on Fig. 1.7) $|e_1\rangle=\left|5^2\mathrm{P}_{1/2}\mathrm{F}'=2, \mathrm{m}'_\mathrm{F}=-2\right\rangle$, $|e_2\rangle=\left|5^2\mathrm{P}_{3/2}\mathrm{F}'=2, \mathrm{m}'_\mathrm{F}=-2\right\rangle$ and $|e_3\rangle=\left|5^2\mathrm{P}_{3/2}\mathrm{F}'=3, \mathrm{m}'_\mathrm{F}=-2\right\rangle$ as $\mathrm{m_F}=\mathrm{m}'_\mathrm{F}$ for a linear polarization. For other higher

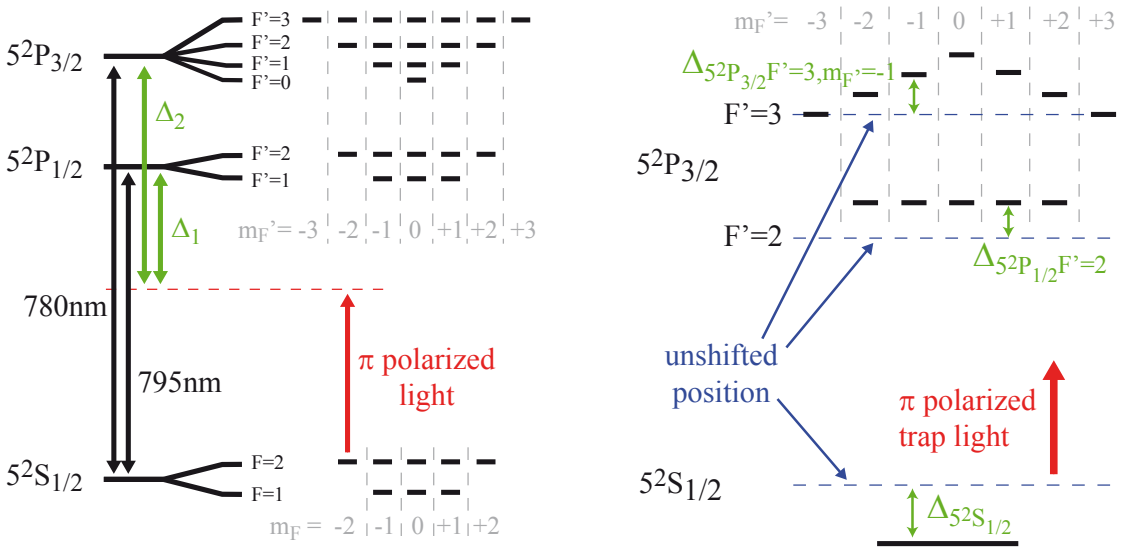

Figure 1.7: Light shifts for far-off resonance detuned π-polarized light. *left*) Far-off resonance detuned laser light can couple different Zeeman sub-levels with each other. The laser detuning is denoted as Δ_1 and Δ_2 for the D_1 and D_2 transition, respectively. *right*) We illustrate the light-shift on each Zeeman sub-level of the $5^2P_{3/2}F'=2$ and $F'=3$ hyperfine levels. All Zeeman sub-levels of $5^2S_{1/2}$ are shifted by the same quantity.

lying levels the coupling becomes much smaller as the detuning increases significantly. The Bloch equations for the four level system are a special case of the one shown in App. B. In steady state we can derive a simple analytical expression by using $\rho_{e_ie_i}^{(st)} \ll \rho_{gg}^{(st)} \approx 1$. As the laser does not couple two excited levels we neglect coherence terms of the form $\tilde{\rho}_{e_ie_j}$ in Eq. B.6c and find

$$\tilde{\rho}_{ge_i}^{(st)} = i\frac{\Omega_{ge_i}/2}{\frac{\Gamma_{ge_i}}{2}+i\Delta_{ge_i}} = \frac{\Omega_{ge_i}\Delta_{ge_i}/2 + i\Omega_{ge_i}\Gamma/4}{(\Gamma_{ge_i}/2)^2+\Delta_{ge_i}^2} \quad , \quad \frac{\tilde{\rho}_{ge_i}^{(st)}+\tilde{\rho}_{e_ig}^{(st)}}{2} = \frac{\Omega_{ge_i}}{2\Delta_{ge_i}} \ . \tag{1.34}$$

The total force on the many-level atom then follows as

$$\boldsymbol{F}_{dip}(\boldsymbol{R}) = -\hbar\sum_{i=1}^{3}\frac{1}{4\Delta_{ge_i}}\boldsymbol{\nabla}(\Omega_{ge_i}^2(\boldsymbol{R})) \ . \tag{1.35}$$

For a laser frequency much smaller than the atomic transition frequency $\Delta_{ge_i} < 0$ (red-detuning) the force becomes attractive. The atom moves to the point of highest laser intensity. For $\Delta_{ge_i} > 0$ (blue-detuning) the light is repulsive and pushes the atom away from the point of highest intensity. This dipole force can be used to trap atoms. In our experiment we use red-detuned light with wavelengths $\lambda_{dip} \approx 850 - 950$ nm to trap the atom at the point of highest laser intensity. In principle it would also be possible to trap an atom by using blue-detuned light where it can act as a potential barrier as it pushes the atom away from the point of highest intensity. In this case the atom is trapped at a point of no laser intensity and needs to see potential barriers in all three dimensions. Otherwise it would escape into the direction with no potential barrier (Puppe *et al.*, 2007).

Dipole potential and light shift

The dispersive force corresponds to a conservative dipole potential $-\boldsymbol{\nabla} U_{dip} = \boldsymbol{F}_{dip}(\boldsymbol{R})$. For the atom in state $5^2\mathrm{S}_{1/2}\mathrm{F}=2, \mathrm{m_F}=+2$ it equals to

$$\begin{aligned} U_{dip}(\boldsymbol{R}) &= \frac{\hbar\Gamma^2 I_L(\boldsymbol{R})}{8 I_{sat}} \left(\frac{1}{3\Delta_{ge_1}} + \frac{2}{6\Delta_{ge_2}} + \frac{2}{6\Delta_{ge_3}} \right) \\ &= \frac{\hbar\Gamma^2 I_L(\boldsymbol{R})}{8 I_{sat}} \left(\frac{1}{3\Delta_1} + \frac{2}{3\Delta_2} \right) , \end{aligned} \tag{1.36}$$

where we set $\Gamma = \Gamma_{ge_i}$ for $i = 1, 2, 3$ as the decay rate is essentially the same for all hyperfine levels[10]. For the D_1 transition we use $\Delta_{ge_1} = \Delta_1$ and for the D_2 transition $\Delta_2 = \Delta_{ge_2} \approx \Delta_{ge_3}$. Note that we still apply the rotating wave approximation $\omega_L - \delta\omega_{ge_i} \ll \omega_L + \delta\omega_{ge_i}$, which is valid for our dipole trap laser wavelength $850 - 950$ nm.

The potential energy U_{dip} induced by the $\pi-$polarized laser light corresponds to a shift in the energy levels of the atom $\hbar\Delta_{dip}$. Fig. 1.7 illustrates the effect of the laser light on the energy levels. All Zeeman states of the two hyperfine ground states $5^2\mathrm{S}_{1/2}\mathrm{F}=1$ and $5^2\mathrm{S}_{1/2}\mathrm{F}=2$ are subject to the same light shift. The excited energy levels are shifted to the opposite direction. While the $5^2\mathrm{P}_{3/2}\mathrm{F}'=2$ Zeeman states are uniformly displaced, we find a Zeeman-dependent shift for the $5^2\mathrm{P}_{3/2}\mathrm{F}'=3$ levels. Here, the extreme states $5^2\mathrm{P}_{3/2}\mathrm{F}'=3, \mathrm{m_{f'}}=\pm 3$ belonging to the closed cycling transition are not shifted. The state $5^2\mathrm{P}_{3/2}\mathrm{F}'=3, \mathrm{m_{f'}}=0$ experiences the largest light-shift which is equal to about half of the light-shift of the ground state for large detunings (Darquié, 2005).

$$\begin{aligned} \Delta_{5^2\mathrm{P}_{3/2}\mathrm{F}'=3,\mathrm{m_{f'}}=0} &= -\frac{\Gamma^2 I_L(\boldsymbol{R})}{8 I_{sat}} \left(\frac{3}{5\Delta_2} \right) \\ \Delta_{5^2\mathrm{P}_{3/2}\mathrm{F}'=3,\mathrm{m_{f'}}=\pm 1} &= -\frac{\Gamma^2 I_L(\boldsymbol{R})}{8 I_{sat}} \left(\frac{8}{15\Delta_2} \right) \\ \Delta_{5^2\mathrm{P}_{3/2}\mathrm{F}'=3,\mathrm{m_{f'}}=\pm 2} &= -\frac{\Gamma^2 I_L(\boldsymbol{R})}{8 I_{sat}} \left(\frac{1}{3\Delta_2} \right) \\ \Delta_{5^2\mathrm{P}_{3/2}\mathrm{F}'=3,\mathrm{m_{f'}}=\pm 3} &= 0 \end{aligned} \tag{1.37}$$

$$\Delta_{5^2\mathrm{P}_{3/2}\mathrm{F}'=2} = -\frac{\Gamma^2 I_L(\boldsymbol{R})}{8 I_{sat}} \left(\frac{1}{3\Delta_2} \right) \tag{1.38}$$

$$\Delta_{5^2\mathrm{S}_{1/2}} = \frac{\Gamma^2 I_L(\boldsymbol{R})}{8 I_{sat}} \left(\frac{1}{3\Delta_1} + \frac{2}{3\Delta_2} \right) \tag{1.39}$$

The light shifts depend on the trap polarization ϵ as the light couples different atomic levels. For the ground state (Grimm, Weidemüller, and Ovchinnikov, 2000) a formula describing the polarization-dependent light-shift can be derived

[10] A complete list of the Clebsch-Gordon coefficients can be found in e.g. Steck (2008).

$$\Delta_{5^2S_{1/2}}(\epsilon) = \frac{\hbar\Gamma^2 I_L(\boldsymbol{R})}{8I_{sat}}\left(\frac{1-\epsilon g_F m_F}{3\Delta_1} + \frac{2+\epsilon g_F m_F}{3\Delta_2}\right) . \tag{1.40}$$

The terms that scale with ϵ are called vectorial light shifts. As we have seen above, the dipole potential experienced by the atom depends on its internal state. If the atom experiences the light field of a near-resonant laser its internal state is steadily altered. In steady state the effective dipole potential

$$U_{dip}(\boldsymbol{R}) = \rho_g^{(st)} U_g(\boldsymbol{R}) - \rho_e^{(st)} U_e(\boldsymbol{R}) \tag{1.41}$$

takes this fact into account. For instance, if the atom stays on average some time in the excited state, the dipole potential is effectively lower than if it would stay in the ground state only.

Scattering rate and dipole laser induced Raman transitions

The effect of the dipole force on the atom has been derived on the assumption that the population in the excited states $\rho_{e_ie_i}$ is small. Using the result in Eq. 1.34 and Eq. B.6b we find the rate of total number of photons scattered on the atom to be

$$R = \sum_{i=1}^{3} \Gamma\rho_{e_ie_i} = \frac{\Gamma^3 I_L(\boldsymbol{R})}{8I_{sat}}\left|\frac{1}{3\Delta_1^2} + \frac{2}{3\Delta_2^2}\right| . \tag{1.42}$$

The total scattering rate R is composed of two parts. First, the coherent Rayleigh scattering R_{Rayleigh} does not change the internal state. Second, there is a incoherent Raman scattering R_{Raman}, in which the atom changes the hyperfine or Zeeman level of the ground state $5^2S_{1/2}$ (Beugnon, 2007). The left graph on Fig. 1.8 illustrates the basic idea behind the scattering processus, between which hold the relationships

$$\begin{aligned} R &= R_{\text{Rayleigh}} + R_{\text{Raman}} \quad , \quad R_{\text{Raman}}/R_{\text{Rayleigh}} = 2\left(\frac{\Delta_2-\Delta_1}{\Delta_2+2\Delta_1}\right)^2 , \\ R_{\text{Rayleigh}} &\propto \frac{1}{9}\left(\frac{\Delta_2+2\Delta_1}{\Delta_1\Delta_2}\right)^2 \quad , \quad R_{\text{Raman}} \propto \frac{2}{9}\left(\frac{\Delta_2-\Delta_1}{\Delta_1\Delta_2}\right)^2 . \end{aligned} \tag{1.43}$$

1.5.8 Harmonic dipole potential

The dipole potential is characterized by the form of the laser intensity distribution $I_L(\boldsymbol{r})$ as can be seen in Eq. 1.36. For Gaussian laser beams the intensity distribution is

$$I_L(\boldsymbol{r}) = \frac{2P}{\pi w_x w_y}\frac{1}{1+\left(\frac{z}{z_R}\right)^2} e^{-2\left(\frac{x^2}{w_x^2}+\frac{y^2}{w_y^2}\right)/\left(1+\left(\frac{z}{z_R}\right)^2\right)} . \tag{1.44}$$

P is the laser power, w_x and w_y are the laser beam waists in x and y direction and $z_R = \pi w^2/\lambda_{dip}$ is the Rayleigh length. The maximal intensity $I_L(0) = \frac{2P}{\pi w_x w_y}$ is

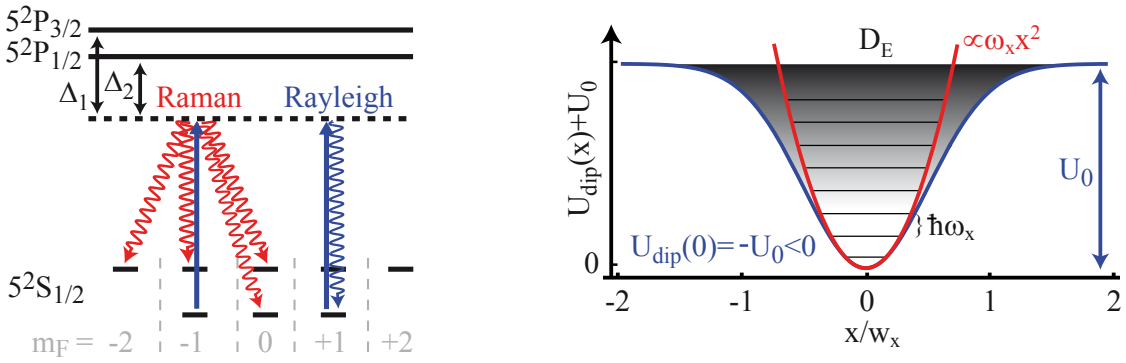

Figure 1.8: Difference between Raman and Rayleigh scattering. Gaussian dipole trap potential *left*) Rayleigh scattering does not change the internal state of the atom while Raman scattering changes the internal state. *right*) Gaussian dipole trap profile with harmonic approximation for an attractive potential.

chosen such that the integrated laser intensity at $z=0$ corresponds to the laser power $P=\int_{x'=-\infty}^{\infty}\int_{y'=-\infty}^{\infty} I_L(x',y',0)dx'dy'$. We are free to add the constant potential $U_0=-U_{dip}(0)>0$ to Eq. 1.36 in order to shift the origin of the energy scale to the bottom of the potential ($x=y=z=0$) as shown in the right graph of Fig. 1.8. The bottom part of the dipole trap can be considered to be harmonic,

$$U_{harm}(\boldsymbol{r})=\frac{1}{2}m(\omega_x^2x^2+\omega_y^2y^2+\omega_z^2z^2)\ . \tag{1.45}$$

Developing the exponential function in Eq. 1.44 and comparing with Eq. 1.45 gives expressions for the trap frequencies that completely describe the harmonic trap

$$\omega_x=\sqrt{\frac{4U_0}{mw_x^2}}\quad,\quad \omega_y=\sqrt{\frac{4U_0}{mw_y^2}}\quad,\quad \omega_z=\sqrt{\frac{2U_0}{mz_R^2}}\ . \tag{1.46}$$

The eigenenergies of the harmonic potential are equidistant

$$E_{n_x,n_y,n_z}=\hbar(\omega_x(\frac{1}{2}+n_x)+\omega_y(\frac{1}{2}+n_y)+\omega_z(\frac{1}{2}+n_z))\ . \tag{1.47}$$

A difference with the real Gaussian laser trap potential appears for higher energies. For the real Gaussian potential the energy spacing decreases going to higher energies and eventually becomes a continuum. In the special case of one atom in the ground state $n_x=n_y=n_z=0$ its wave function is

$$\begin{aligned}\phi_0(\boldsymbol{r})&=\left(\frac{m}{\pi\hbar}\right)^{3/4}(\omega_x\omega_y\omega_z)^{1/4}e^{-\frac{m}{2\hbar}(\omega_x x^2+\omega_y y^2+\omega_z z^2)}\\&=\frac{1}{\pi^{3/4}\sqrt{a_xa_ya_z}}e^{-(x^2/2a_x^2+y^2/2a_y^2+z^2/2a_z^2)}\ ,\end{aligned} \tag{1.48}$$

where we used the size of the wave function for $i=x,y,z$

$$a_i=\sqrt{\frac{\hbar}{m\omega_i}}\ , \tag{1.49}$$

1.6 Conclusion

Alkali atoms such as rubidium 87 are in its internal structure similar to the hydrogen atom. Due to the completeness of the inner-shell electrons we can uniquely address the valence electron with external fields. Static magnetic fields lift the degeneracy between the Zeeman levels. Dynamic electric fields lead to the radiation pressure force and to the dipole force depending on the light frequency. The first prevails for near-resonance light which excites the atom to higher lying states. Near-resonance light leads to the radiation pressure force based on the recoil momentum transfer between the photon field and the atom by absorption and emission. The dipole force dominates for far-off-resonance laser frequencies so that the excitation to higher levels is much lower. In this case the laser light exerts an attractive or repulsive force for red or blue detuned laser light, respectively. This dispersive dipole force will be used to trap atoms.

Chapter 2

Theoretical background on many-body physics

Contents

The properties of a physical system containing many atoms are essentially governed by the interactions between the atoms. The interactions lead to marvelous effects such as the melting of solids to liquids or the condensation of gases to liquids. These interactions are based on the electro-magnetic force and characterize the collisional behavior between the atoms.

We begin by introducing the theoretical basis which describes the collision processes between two atoms. For this we classify collisions being elastic or inelastic. Elastic collisions are responsible for the redistribution of energy between the atoms in the gas and can bring the gas to thermal equilibrium. Inelastic collisions generally lead to loss of both scattering partners from the dipole trap. In the last part we discuss how we can macroscopically describe the atom gas in a harmonic trap in thermal equilibrium. Here, we use the grand-canonical ensemble and thermodynamic

quantities such as atom number, temperature and chemical potential to characterize the gas.

2.1 Résumé

Quand plusieurs atomes sont présents dans le piège l'interaction entre les atomes peut changer les caractéristiques introduites dans le dernier chapitre, qui étaient basées sur un calcul à une seule particule ou plusieurs particules indépendantes. Ici, nous discuterons les effets les plus importants pour nos expériences, notamment les collisions élastiques et inélastiques. Pour les collisions inélastiques nous différencierons entre collisions en présence de lumière et collisions en absence de lumière. Nous introduirons également les propriétés statistiques que seront utilisées pour décrire les nuages d'atomes dans notre piège optique.

2.2 Scattering theory

The scattering process between two atoms is based on the following idea: The incoming atom described as a plane wave with wave vector $\boldsymbol{k}_{at}$ ($|\boldsymbol{k}_{at}| = k_{at}$) and energy $E = \frac{\hbar^2 k_{at}^2}{2m_r}$ sees the potential of the scattering center in the form of the second atom, where m_r is the reduced mass. One assumes the outgoing atom wave to be composed of an unscattered part as a plane wave and a radially scattered part as a spherical wave

$$\Psi(r,\vartheta,\varphi) = e^{ik_{at}z} + f(\vartheta,\varphi)\frac{e^{ik_{at}r}}{r} \ , \tag{2.1}$$

where $f(\vartheta,\varphi)$ is the scattering amplitude. It can be calculated by solving the equivalent Schrödinger equation $E\Psi(\boldsymbol{r}) = (\boldsymbol{p}^2/2m_r + U(r))\Psi(\boldsymbol{r})$. For an isotropic scattering center $U(r)$ the associated potential only depends on the radial coordinate r. Analog to the hydrogen atom problem in Sec. 1.3 we treat the wave function in spherical coordinates $\Psi(\boldsymbol{r}) = \sum_{\mathrm{l}=0}^{\infty} A_{\mathrm{l}} R_{\mathrm{l,k_{at}}}(r) P_{\mathrm{l}}(\cos\vartheta)$ with summation amplitudes A_{l}. The radial part $R_{\mathrm{l,k_{at}}}(r)$ then follows from

$$\frac{1}{r^2}\frac{d}{dr}\left(r^2\frac{d}{dr}R_{\mathrm{l,k_{at}}}(r)\right) + \left(k_{at}^2 - \frac{\mathrm{l}(\mathrm{l}+1)}{r^2} - \frac{2m_r}{\hbar^2}U(r)\right)R_{\mathrm{l,k_{at}}}(r) = 0 \ . \tag{2.2}$$

The effective ground state potential $U(r) = U_{\mathrm{IA}}(r) + U_{\mathrm{CF}}(r)$ is composed of the interatomic potential $U_{\mathrm{IA}}(r)$, usually a repulsive short range Lennard-Jones plus an attractive longer range van-der-Waals potential $U_{\mathrm{IA}}(r) = C_{12}/r^{12} - C_6/r^6$, and the potential arising from the centrifugal barrier $U_{\mathrm{CF}}(r) = \frac{\hbar^2 \mathrm{l}(\mathrm{l}+1)}{2m_r r^2}$. For $\mathrm{l} > 0$ the centrifugal barrier can prevent the atoms from colliding if their initial energy is smaller than the height of the barrier, see Fig. 2.1.

It can be shown (Landau and Lifshitz, 1981) that for the solution of Eq. 2.2 to equal Eq. 2.1 the summation amplitudes obey $A_{\mathrm{l}} = \frac{1}{2k_{at}}(2\mathrm{l}+1)\mathrm{i}^{\mathrm{l}}\mathrm{e}^{\mathrm{i}\delta_{\mathrm{l}}(\mathrm{k})}$ and the scattering amplitude follows as

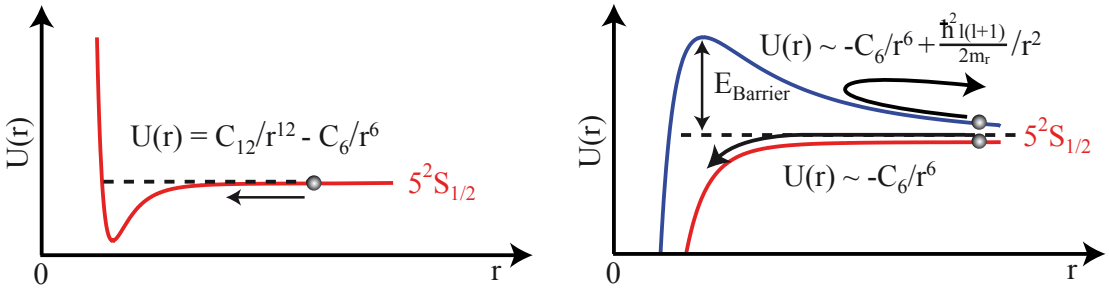

Figure 2.1: Ground state potential with centrifugal barrier. *left*) Ground state potential without centrifugal part $\mathrm{l}=0$ (s-wave scattering). The colliding atoms do not see any centrifugal barrier. *right*) An atom with $\mathrm{l}>0$ does not collide with another atom if its kinetic energy is lower than the centrifugal barrier E_{Barrier}.

$$f(\vartheta) = \frac{1}{2ik_{at}} \sum_{\mathrm{l}=0}^{\infty} (2\mathrm{l}+1)(\mathrm{e}^{2\mathrm{i}\delta_{\mathrm{l}}(\mathrm{k_{at}})} - 1)\mathrm{P_l}(\cos\vartheta) \ , \tag{2.3}$$

where $\delta_{\mathrm{l}}(k_{at})$ are the phase shifts of the scattered waves with respect to the incoming plane wave. For further evaluation we distinguish collisions between identical and non-identical particles:

- **Identical.** Fig. 2.2 shows how it is impossible to decide which of the two atoms are scattered which way. In this case all odd partial waves interfere destructively while even partial waves interfere constructively. Since we sum over two scattering amplitudes with scattering angle difference π we only integrate over half of the solid angle. The total scattering cross-section σ_{tot} then reads[1]

$$\begin{aligned} \sigma_{tot} &= \int_{\Omega/2} |f(\vartheta) + f(\pi-\vartheta)|^2 \, d\Omega = 2\pi \int_0^{\pi/2} |f(\vartheta) + f(\pi-\vartheta)|^2 \sin(\vartheta) d\vartheta \\ &= \frac{8\pi}{k_{at}^2} \sum_{\substack{\mathrm{l}=0 \\ l \ even}}^{\infty} (2\mathrm{l}+1)\sin^2\delta_{\mathrm{l}}(\mathrm{k_{at}}) \ . \end{aligned} \tag{2.4}$$

- **Non-identical.** The analog treatment can be done for non-identical particles as encountered e.g. in samples where the atoms are in the same hyperfine ground state but occupy different m_f Zeeman levels. Here, all partial waves add up which leads to

$$\sigma_{tot} = \int_{\Omega/2} f(\vartheta)^2 d\Omega = \frac{4\pi}{k_{at}^2} \sum_{\mathrm{l}=0}^{\infty} (2\mathrm{l}+1)\sin^2\delta_{\mathrm{l}}(\mathrm{k_{at}}) \ . \tag{2.5}$$

[1] We use the relationship $\int_0^{\pi} P_{\mathrm{l}}^2(\cos\vartheta)\sin(\vartheta)d\vartheta = 2/(2\mathrm{l}+1)$.

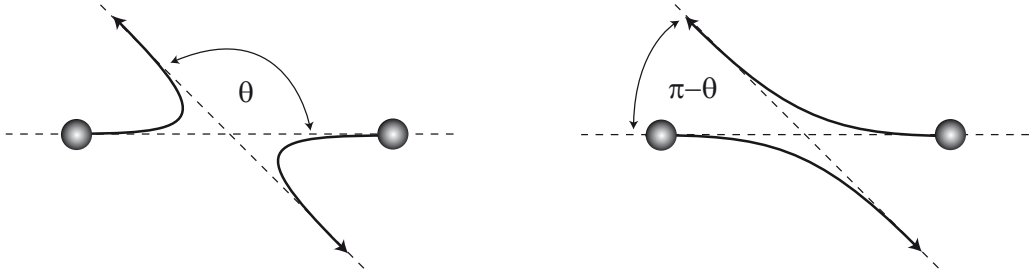

Figure 2.2: Scattering between two identical particles. We cannot tell which of the two scattering atoms goes which way after the scattering.

2.2.1 Elastic collisions

The atoms in our dipole trap usually have temperatures below one milliKelvin so that s-wave scattering with $l=0$ plays the dominant role (left of Fig. 2.1). The elastic collision is governed by a van der Waals potential $U(r)=-C_6/r^6$, where C_6 is a constant. One usually models this potential as a box potential

$$U(r)=\begin{cases} -U & \text{for} \quad r<R \\ 0 & \text{for} \quad r\geq R \end{cases} \quad . \tag{2.6}$$

For this potential and low energies $k\to 0$ we find $\sin^2\delta_0(k_{at})\propto k_{at}^2$ and the elastic collision rate for non-identical particles can be written as

$$\sigma_{el}=4\pi a^2 \quad , \quad a=-\lim_{k_{at}\to 0}\frac{\delta_0(k_{at})}{k_{at}} \ , \tag{2.7}$$

The scattering length for rubidium 87 has been measured to be $a=5.24$ nm (Marte *et al.*, 2002). It is responsible for a redistribution of energy, see thermalization process in Sec. 2.3.1, between the atoms at a rate given by

$$\gamma_{el}=n\sigma_{el}v=n8\pi a^2 v \ , \tag{2.8}$$

where n is the atom density and $v=\sqrt{\frac{8k_BT}{\pi m_r}}=\sqrt{\frac{16k_BT}{\pi m}}$ the mean velocity of the reduced mass of the atom pair.

2.2.2 Inelastic collisions in the absence of light

We will consider inelastic loss due to one-, two- and three-body collisions, for which the collision loss rates are γ, β and L, respectively. The collision-induced atom loss[2] leads to a decrease in atom density over time as

$$\frac{dn}{dt}=-\gamma n-\beta n^2-Ln^3 \ . \tag{2.9}$$

Using fluorescence imaging we do not measure the density directly but infer it by measuring the atom number N and the physical volume V occupied by the atoms.

[2]Elastic collisions also lead to atom loss but will not be considered here.

The number of trapped atoms N inside the dipole trap varies over time as

$$\frac{dN}{dt} = -\gamma N - \beta' N^2 - L' N^3 \ , \tag{2.10}$$

where γ, β' and L' are the associated loss constants[3]. They are related to the loss rates by

$$\beta = \beta' V \quad , \quad L = L' V^2 \ . \tag{2.11}$$

Working with low atom numbers there exists a phenomenological equation describing the atom loss

$$\frac{dN}{dt} = -\gamma N - \beta' N(N-1) - L' N(N-1)(N-2) \ . \tag{2.12}$$

The scattering cross-section σ_{inel} for two-body collisions can be inferred by using

$$\beta = v \sigma_{inel} \ . \tag{2.13}$$

Theoretically it can in principle be calculated using the framework in Sec. 2.2. However, one needs to include the internal structure of the atom to properly describe the inelasticity of the scattering process (Sakurai, 1993).

One-body

The one-body loss rate γ does not depend on the number of rubidium atoms inside the dipole trap. It is typically due to collisions with the background gas. There are mainly two types of collisions. The first is due to collisions between a trapped rubidium atom and another rubidium atom coming from the rubidium source. The second is due to collisions with hydrogen molecules H_2 that make up the major part of the residual vacuum pressure. Assuming the arriving atoms to be in their ground state the van-der-Waals $U(r) = -C_6/r^6$ interaction describes the scattering process. As the background gas atoms are at room temperature (300 K) the scattering process can be described classically. The energy passed to the trapped atom during a collision is usually much higher than typical trap depths of around 1 mK. The scattering rate has been calculated to be $\sigma = 295$ Å^2 for $Rb - H_2$ and $\sigma = 2500$ Å^2 for $Rb - Rb$ (Bali *et al.*, 1999). This leads to loss rates $\gamma/n_p = 4.9 \cdot 10^{-9}$ cm^{3}s^{-1} for $Rb - H_2$ and $\gamma/n_p = 6.3 \cdot 10^{-9}$ cm^{3}s^{-1} for $Rb - Rb$, where n_p is the density of the background gas. A measure of the rate γ and a discussion about other one-body loss sources that do not depend on collisions with the background gas is given in Ch. 5.3.

Two-body

In contrary to one-body loss the two-body loss depends on the number of rubidium atoms inside the trap. Without any near-resonant light present the main two-body loss is given by hyperfine-changing collisions. This collision occurs between two atoms

[3] We discuss the limitations of this equation in Sec. 8.5 and App. D in the particular case of two-body losses.

in different hyperfine states $5^2S_{1/2}F=1$ and $5^2S_{1/2}F=2$. During the collision a spin-flip can occur where the atom in $5^2S_{1/2}F=2$ ends up in $5^2S_{1/2}F=1$. The amount of energy released in such a collision corresponds to the ground state splitting of 6.8 GHz and about 100 times higher than typical trap depths of 1 mK or several tens of MHz. The loss rate for thermal clouds with a mixture of Zeeman levels is of the order of $\beta=10^{-11}$ cm^{3}s^{-1} (Gensemer *et al.*, 1997, 2000). It can be avoided by preparing all atoms in the $F=1$ manifold. Trap-induced Raman transition however lead to a population in $F=2$ and subsequent spin-flip collisions (see Sec. 9.3.4).

Three-body

Three-body recombination creates molecules that are e.g. responsible for the condensation of a gas to a solid. They become important for densities of $\sim 10^{15}$ cm^{-3} which can be reached in our microscopic dipole trap. Typical loss rates for rubidium 87 are on the order of $\sim 10^{-29}$cm^{6}s^{-1} (Burt *et al.*, 1997; Söding *et al.*, 1999). The scattering cross-section for three-body collisions is usually hard to calculate. For ultra-cold atom gases an intuition on the process has been given by Fedichev, Reynolds, and Shlyapnikov (1996), who show under certain hypothesis a dependence of the loss rate L on the fourth power of the elastic scattering length a. We will measure the three-body loss rate in our dipole trap in Ch. 10.

2.2.3 Inelastic collisions in the presence of light

The scattering potential between two atoms in their ground state $5^2S_{1/2}$ is a van der Waals $V(r)=-C_6/r^6$ potential. In the presence of light one has to treat the case where the atom pair absorbs a photon and excites into $5^2S_{1/2}+5^2P$. In this case the potential is of dipolar nature $U(r)=-C_3/r^3=-3\hbar\Gamma/4(kr)^3$, where $k=2\pi/\lambda$ with $\lambda\sim 780$ nm. Depending on the frequency of the excitation or probe laser one can distinguish three cases.

Radiative escape collisions

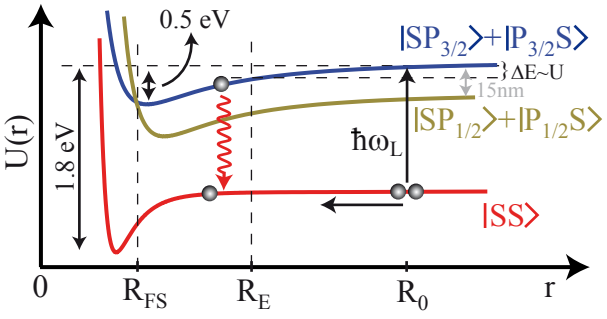

Figure 2.3: Light-assisted collision.

We focus on the case where the probe laser is near resonance with the level $5^2P_{3/2}$ and neglect the hyperfine structure. The formalism is the same for an excitation into $5^2P_{1/2}$. In this situation the atom pair in $5^2S_{1/2}+5^2S_{1/2}$ denoted as $|SS\rangle$ can be excited into $5^2S_{1/2}+5^2P_{3/2}$ denoted as [4] $|SP_{3/2}\rangle+|P_{3/2}S\rangle$. The two atoms accelerate towards each other due to the dipolar potential curve which has a longer

[4] There also exists a repulsive potential curve corresponding to the eigenstate $|SP_{3/2}\rangle-|P_{3/2}S\rangle$ that we do not consider here.

range than the van der Waals potential, see Fig. 2.3. The acceleration takes place until the excited atom pair emits the photon and both atoms see the short range van der Waals potential. If the gain in kinetic energy is greater than the trap depth U the atom pair is expelled from the trap. Assuming the atom to be excited at a distance R_0 from its partner it must at least accelerate until it reaches the escape radius $kR_E \sim \left(-\frac{\hbar\Gamma}{U}\right)^{1/3}$ to gain enough energy. For a trap depth of e.g. 50 MHz we find $R_E \sim 60$ nm. If it emits the photon before reaching R_E it stays trapped. Also, the probability to pass R_E once, bounce off the potential barrier and pass R_E a second time to leave the escape region is here negligibly small in contrast to magneto-optical traps for example. We follow the approach introduced by Gallagher and Pritchard[5] (Gallagher and Pritchard, 1989).

We assume the atom to have initially zero kinetic energy. The probability to survive the distance $\overline{R_0 R_E}$ without emitting the photon is

$$\gamma_{surv} = \exp(-2\Gamma t(R_0)) \ , \tag{2.14}$$

where 2Γ corresponds to the lifetime of the excited atom pair and $t(R_0)$ is the time the atom needs to reach R_E starting from R_0. The flight time can be calculated

$$t(R_0) = \sqrt{\frac{m_r}{2}} \int_{R_E}^{R_0} \frac{dr}{\sqrt{\frac{\hbar\Gamma}{(kr)^3} - \frac{\hbar\Gamma}{(kR_0)^3}}} \tag{2.15}$$

where we used $U = \frac{\hbar\Gamma}{(kR_E)^3} - \frac{\hbar\Gamma}{(kR_0)^3}$. The probability per time to be excited follows from Eq. 1.27 and can be written as

$$P_E(R_0) = \Gamma\rho_{ee}^{(st)} = \frac{I_L}{\hbar\omega_L}\frac{3\lambda^2}{2\pi}\frac{1}{1 + \frac{I_L}{I_{sat}} + \left(\frac{\Delta}{\Gamma} + \frac{1}{(kR_0)^3}\right)^2} \ . \tag{2.16}$$

In this equation we used the fact that the atomic transition frequency depends on the position as $\omega_L - \omega_A(r) = \omega_L - (\omega_A - \frac{\Gamma}{(kr)^3}) = \Delta + \frac{\Gamma}{(kr)^3}$. The probability to be excited and pass the escape radius R_E equals the loss rate β

$$\beta = \frac{1}{2}\int_0^\infty 4\pi R_0^2 P_E(R_0)\exp(-2\Gamma t(R_0))dR_0 \ . \tag{2.17}$$

For typical values of the trap depth 3 mK and the excitation laser saturation $s = 0.5$ resonant with the atom in free space we find a collision loss rate $\beta = 1.1 \cdot 10^{-10}\mathrm{cm}^3\mathrm{s}^{-1}$. The deexcitation of the atom pair can lead to an energy release $\gg 1$ K which results in the loss of both atoms. We measure the radiative escape in Ch. 9.

The described situation is a case for which the laws derived on a single atom basis in the last chapter cannot be simply applied to many atom samples. If one atom is excited by resonant laser light the excited level of N other atoms inside a sphere of $\lambda/2\pi$ are shifted by $V/\hbar \sim \Gamma$ due to the shape of the excited potential curve. The probability for them to scatter photons is much reduced in this case which inhibits a

[5] Other more accurate but also more complex approaches have been developed, see e.g. Weiner *et al.* (1999).

simple scaling of the photon scattering rate $R_{tot} = NR_{\text{single}}$. This excitation blockade could be used to study e.g. super-radiance effects (Gross and Haroche, 1982).

Fine changing collisions

For the radiative escape mentioned above we focused on an atom pair to be excited into the state $5^2S_{1/2} + 5^2P_{3/2}$. Rubidium 87 has a second fine level, namely $5^2P_{1/2}$. As shown in Fig. 2.3 it happens that both dipolar potential curves cross at a distance R_{FC}. The atom pair excited into $5^2S_{1/2} + 5^2P_{3/2}$ can change the fine level into $5^2S_{1/2} + 5^2P_{1/2}$ at R_{FS}. If it deexcites into $5^2S_{1/2} + 5^2S_{1/2}$ it can gain kinetic energies as high is the level spacing between the P states of 15 nm corresponding to ~ 170 K even if $r \gg R_{FS}$. For rubidium 87 R_{FS} is on the order of 0.8 nm. This loss can theoretically be described analog to radiative escape and becomes important for far-off red-detuned lasers. For near-resonance laser light the atom usually deexcites back into the ground state before reaching R_{FS} so that no fine-changing process occurs.

Photoassociation

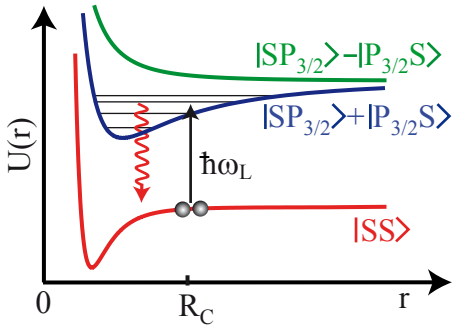

Figure 2.4: Photoassociation of two rubidium atoms to bound molecular state.

Photo association is the mechanism where the atom pair absorbs a photon and excites to a bound molecular state. The atom pair is initially in its ground state. The photon can now couple the two ground state atoms to a bound molecular state if the photon energy $\hbar\omega_L$ corresponds to a bound molecular state energy (Jones *et al.*, 2007) at the Condon point R_C, $\lesssim 15$Å for rubidium, see Fig. 2.4. The production of molecules leads to the loss of the atom pair as the molecules' deexcitation releases energies much greater than typical trap depths. Experimental measurements for a thermal rubidium gas shows a clear excitation spectrum between ~ 800 nm and ~ 860 nm (Miller, Cline, and Heinzen, 1993). For our many atom experiments we work at a dipole trap wavelength of 945 nm to avoid any photoassociation loss. Fig. 2.4 also shows the existence of a repulsive potential curve which does not have any bound molecular states.

2.3 Atoms in a harmonic dipole trap

During an elastic collision the participants exchange energy in such a way that on average the total energy is partitioned equally on both participants. In an ensemble of many atoms elastic collisions lead to a redistribution of energy between all atoms. For our finite trap depth U_0 this redistribution of energy comes along with a loss of atoms as atoms with energy $E > U_0$ are not trapped any more. The gas thermalizes by losing the hottest atoms while cold atoms remain trapped. The total energy of the gas decreases until the gas reaches its equilibrium. With increasing total energy

of the gas higher energy levels in the harmonic trap are occupied. We work in the grand-canonical ensemble and distinguish between three regimes: The thermal regime in which many high lying energy levels are occupied and the atoms can be described classically; The quasi-degenerate regime where the lower energy levels are occupied and the condensed regime where a macroscopic population of the ground state is present.

2.3.1 Atoms in thermal equilibrium

The probability for an energy level inside the trap to be occupied is given by the phase-space distribution function $f(E)$. Considering s-wave collisions it can be shown by using the Boltzmann transport equation (Luiten, Reynolds, and Walraven, 1996) that the phase-space distribution function in thermal equilibrium for a finite trap U_0 is a truncated Boltzmann distribution

$$f_{th}(E) = e^{-E/k_B T}\theta(U_0 - E) \ , \tag{2.18}$$

where $\theta(x)$ is the Heaviside step function with $\theta(x) = 1$ for $x \geq 0$. In the classical case the position and momentum change continuously and the total energy is $E(\boldsymbol{r}, \boldsymbol{p}) = \boldsymbol{p}^2/2m + U_{harm}(\boldsymbol{r})$ with the harmonic potential given in Eq. 1.45. The atom density n follows from

$$n(\boldsymbol{r}) = \frac{n_0}{V_p} \int f_{th}(E) d\boldsymbol{p} = n_0 e^{-m(\omega_x^2 x^2 + \omega_y^2 y^2 + \omega_z^2 z^2)/2k_B T} \ , \tag{2.19}$$

where n_0 is the peak density and $V_p = (2\pi m k_B T)^{3/2}$ the normalization volume. The peak density is given by

$$n_0 = N/V = N/((2\pi)^{3/2}\sigma_x\sigma_y\sigma_z) \qquad \text{with} \qquad \sigma_i = \sqrt{\frac{k_B T}{m\omega_i^2}} \ , \tag{2.20}$$

where the number of atoms N follows from

$$N = \frac{n_0}{V_p} \int\int f_{th}(E(\boldsymbol{r}, \boldsymbol{p})) d\boldsymbol{r} d\boldsymbol{p} = N \int D_s(E) f_{th}(E) dE \ . \tag{2.21}$$

In the last step we assumed that the phase-space distribution of the atoms only depends on the energy so that we can transform the position and momentum integrals into one integral over the total energy using the energy density of states $D_s(E)$. $D_s(E)$ is a measure of how many possibilities there are for $\boldsymbol{r}, \boldsymbol{p}$ to obtain a fixed total energy $E(\boldsymbol{r}, \boldsymbol{p})$. For a harmonic potential the density of states can be calculated with Eq. 1.45 to be

$$D_s(E) = \frac{1}{V \cdot V_p} \int\int \delta(E - U_{harm}(\boldsymbol{r}) - \boldsymbol{p}^2/2m) d\boldsymbol{r} d\boldsymbol{p} = \frac{1}{2(kT)^3} E^2 \ . \tag{2.22}$$

It can handily be used to calculate the internal energy for example

$$E_{int} = \int E D_s(E) f(E) dE = 3N k_B T \ . \tag{2.23}$$

Figure 2.5 shows the truncated Boltzmann distribution times the energy density of states $D_s(E) f_{th}(E)$ for two different temperatures. For temperatures $k_B T \lesssim U_0$ a significant part of the distribution has an energy higher than U_0. All atoms belonging to this part are lost from the trap as their energy is greater than the trap depth. For high temperatures we also need to question the harmonic approximation which is only valid for the bottom of the trap. As the hot atoms are lost the gas rethermalizes and ends up with a colder temperature until the equilibrium regime is reached. In optical traps this regime has been found to be reached for $\eta = U_0/k_B T \gtrsim 10$ as the thermalization process usually becomes very slow beyond this point (Adams *et al.*, 1995). At these lower temperatures the truncated part of the Boltzmann distribution can be neglected. Our Gaussian dipole trap can then be considered to be harmonic and the here derived quantities are valid.

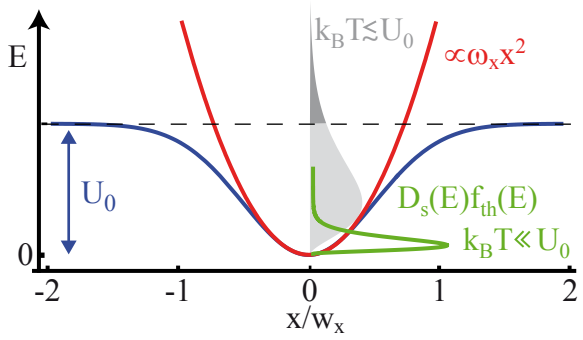

Figure 2.5: Boltzmann distribution in a harmonic dipole trap.

2.3.2 Atoms in a quasi degenerate regime

As the gas reaches a critical temperature T_C the ground state of the trapping potential starts to populate macroscopically. In this still thermal regime we use a semi-classical approach. For the phase-space distribution function we use a Bose-Einstein distribution

$$f_{BE}(E) = \frac{1}{e^{(E-\mu)/k_B T} - 1} \ , \tag{2.24}$$

where μ is the chemical potential. For the total energy we still use the classical expression $E(\boldsymbol{r}, \boldsymbol{p}) = \boldsymbol{p}^2/2m + U_{harm}(\boldsymbol{r})$ with $\boldsymbol{r}$ and $\boldsymbol{p}$ varying discretely now and find for the density and the atom number (see e.g. Dalfovo *et al.* (1999))

$$\begin{aligned} n(\boldsymbol{r}) &= \sum_{\boldsymbol{p}} f_{BE}(E(\boldsymbol{r}, \boldsymbol{p})) = \sum_{\boldsymbol{p}} \sum_{l=1}^{\infty} e^{-(E(\boldsymbol{r},\boldsymbol{p})-\mu) l/k_B T} \\ &= \frac{1}{h^3} \sum_{l=1}^{\infty} \int e^{-(E(\boldsymbol{r},\boldsymbol{p})-\mu) l/k_B T} d\boldsymbol{p} = \lambda_{th}^{-3} g_{3/2}(e^{(\mu - U_{harm}(\boldsymbol{r}))/k_B T}) \end{aligned} \tag{2.25}$$

$$N = \sum_{\boldsymbol{r},\boldsymbol{p}} f_{BE}(E(\boldsymbol{r},\boldsymbol{p})) = \frac{1}{h^3}\int\int f_{BE}(E(\boldsymbol{r},\boldsymbol{p}))d\boldsymbol{r}d\boldsymbol{p}$$
$$= \int D_s^{sc}(E) f_{BE}(E) dE = g_3(e^{\mu/k_\mathrm{B}T})\left(\frac{k_\mathrm{B}T}{\hbar\bar{\omega}}\right)^3 , \tag{2.26}$$

where $g_k(z) = \sum_l \frac{z^l}{l^k}$ and $\bar{\omega} = (\omega_x\omega_y\omega_z)^{1/3}$. In a first step the sum over $\boldsymbol{r},\boldsymbol{p}$ can be transformed into an integral assuming that each combination of $\boldsymbol{r},\boldsymbol{p}$ occupies a volume of h^3 in phase-space. The volume is assumed to be small enough for the passage from the discrete sum to the continuous integral to be justified. It is also based on the assumption that the level spacing $\hbar\bar{\omega}$ becomes much smaller for $N \to \infty$. In order to transform the space and momentum integral into an energy integral as has been done in the classical case we introduce in a second step the phase-space density in the semi-classical picture

$$D_s^{sc}(E) = \frac{1}{h^3}\int\int \delta(E - U_{harm}(\boldsymbol{r}) - \boldsymbol{p}^2/2m) d\boldsymbol{r}d\boldsymbol{p} = \frac{1}{2\hbar^3\omega_x\omega_y\omega_z}E^2 . \tag{2.27}$$

2.3.3 Atoms in a Bose-Einstein condensate

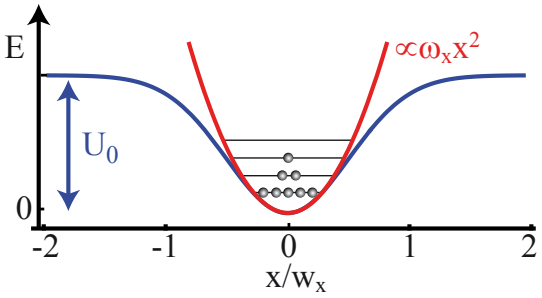

Figure 2.6: The condensed gas has a macroscopic ground state population.

As the temperature decreases for a given N, the gas condenses and the ground state becomes macroscopically populated. In this case we need to treat the total energy quantum-mechanically. For s-wave scattering lengths much smaller than the typical distance between the atoms, the gas can be described by using the Gross-Pitaevskii equation (see e.g. Dalfovo *et al.* (1999))

$$i\hbar\frac{\partial}{\partial t}\Phi(\boldsymbol{r},t) = -\frac{\hbar^2\boldsymbol{\nabla}^2}{2m}\Phi(\boldsymbol{r},t) + U_{dip}(\boldsymbol{r})\Phi + \frac{4\pi\hbar^2 a}{m}|\Phi(\boldsymbol{r},t)|^2\Phi(\boldsymbol{r},t) . \tag{2.28}$$

The time dependence of the function $\Phi(\boldsymbol{r},t) = \Phi(\boldsymbol{r})e^{-i\mu t}$ can be separated by using the chemical potential, in analogy to the separation of time and position coordinates for the hydrogen atom in Sec. 1.2. We can distinguish two cases: One where the potential energy is dominant and a second where the s-wave scattering interaction is dominant.

Ideal free Bose gas

If the potential energy becomes more dominant than the interaction energy, atoms can be considered to behave as free particles. In this case we can neglect the interaction term in Eq. 2.28. Most atoms N_0 are in the ground state. Their atom wave function $\Phi(\boldsymbol{r}) = \sqrt{N}\phi_0(\boldsymbol{r})$ is just the harmonic oscillator result given in Eq. 1.48 with $\mu =$

$\frac{1}{2}\hbar(\omega_x+\omega_y+\omega_z)$. It corresponds to a Gaussian density profile $n(\boldsymbol{r})=|\Phi(\boldsymbol{r})|^2$ with spatial dimensions a_i given in Eq. 1.49. Further quantities can be calculated analog to the previous case but using the quantum-mechanical energies for the harmonic oscillator from Eq. 1.47. For the atom number N we find

$$\begin{aligned} N-N_0 &= \sum_{n_x,n_y,n_z\neq 0} f_{BE}(E_{(n_x,n_y,n_z)}) = \sum_{n_x,n_y,n_z\neq 0} \frac{1}{e^{\hbar(\omega_x n_x+\omega_y n_y+\omega_z n_z)/k_\mathrm{B}T}-1} \\ &= \int_0^\infty\int_0^\infty\int_0^\infty \frac{1}{e^{\hbar(\omega_x n_x+\omega_y n_y+\omega_z n_z)/k_\mathrm{B}T}-1} dn_x dn_y dn_z \\ &= \int_0^\infty\int_0^\infty\int_0^\infty \sum_{l=1}^{\infty} \frac{e^{-\hbar(\omega_x n_x+\omega_y n_y+\omega_z n_z)l/k_\mathrm{B}T}}{l} dn_x dn_y dn_z \\ &= g_3(1)\left(\frac{k_\mathrm{B}T}{\hbar\bar{\omega}}\right)^3 , \end{aligned} \tag{2.29}$$

where we separate out the condensed fraction N_0 in the ground state. The same result can again be obtained by transforming the integrals over the occupation number into one integral over the energy $\int_0^\infty \frac{D_s^{sc}(E)dE}{e^{E/k_\mathrm{B}T}-1}$. We note that the result is identical to the one obtained in the semi-classical calculation in Eq. 2.26 setting $\mu=0$. The transition temperature is defined as the temperature at which there is not yet any markable occupation in the ground state $N_0\sim 0$ so that

$$k_\mathrm{B}T_C = g_3(1)^{-1/3}\hbar\bar{\omega}N^{1/3} = 0.94\hbar\bar{\omega}N^{1/3} . \tag{2.30}$$

In combination with Eq. 2.29 we find the relationship

$$\frac{N_0}{N} = 1-\left(\frac{T}{T_C}\right)^3 . \tag{2.31}$$

Eq. 2.30 can also be written as

$$1.202 = N\left(\frac{\hbar\bar{\omega}}{k_\mathrm{B}T_C}\right)^3 = \rho(T_C) . \tag{2.32}$$

The quantity ρ is called the phase-space density. At the critical temperature T_C it roughly equals one and indicates the set in of condensation. It can be shown that it is equivalent to $2.61=n_0\lambda_{th}^3$, where n_0 is the peak density of a quasi-degenerate gas.

Interacting Bose gas

In this case known as the Thomas-Fermi limit we can neglect the kinetic energy in Eq. 2.28. The atomic wave functions and eigenenergies can only be calculated numerically. For the density however we can directly solve the equation for $|\Phi|^2$

$$\begin{aligned} n(\boldsymbol{r}) = N|\Phi|^2 &\propto N max\left(\frac{\mu-U_{dip}(\boldsymbol{r})}{4\pi\hbar^2 a/m},0\right) \\ &\propto \frac{N}{a_{x,c}a_{y,c}a_{z,c}} max\left(1-\frac{x^2}{a_{x,c}^2}-\frac{y^2}{a_{y,c}^2}-\frac{z^2}{a_{z,c}^2},0\right) , \end{aligned} \tag{2.33}$$

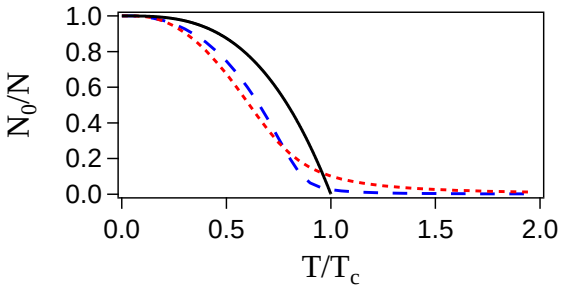

Figure 2.7: Finite size effect on BEC phase transition. Fraction of atoms in the Bose-Einstein condensate versus temperature of the atom sample. We compare the phase transition for three different situations: Thermodynamical limit $N \to \infty$ (black line), $N = 100$ (blue dashed) and $N = 10$ (red dots).

where $a_{i,c} = \sqrt{\frac{2\mu}{m\omega_i^2}}$ for $i = x, y, z$. Eq. 2.32 can also be used to describe the onset of condensation for the interacting gas.

2.3.4 Finite size effects

Our experiments are carried out with ensembles containing only a few hundred atoms. The question in this case is if a grand canonical ensemble and the transformation from a sum to an integral done in Eq. 2.25, Eq. 2.26 and Eq. 2.29 are still justified. We can numerically solve the sum instead of integrating the equation and study the effect of the finite size of the system (Grossmann and Holthaus, 1995). Fig. 2.7 shows how the BEC transition changes going from the thermodynamical limit $N \to \infty$ according to Eq. 2.31 to finite N. We observe a smearing out of the phase transition which becomes remarkable for atom numbers as small as $N \sim 100$ (Ketterle and van Druten, 1996b; Haugerud, Haugset, and Ravndal, 1997).

2.4 Conclusion

The properties of atom gases are governed by the interactions between the atoms and characterize their collision behavior. Elastic collisions manifest themselves as a redistribution of the internal energy between the atoms. Inelastic collisions lead to an increase of kinetic energy and a subsequent loss of both collision partners from the trap.

Depending on the internal energy of the atoms the occupation distribution of the energy levels of a harmonic trap changes. For high temperatures at which higher lying energy states are occupied the occupation distribution inside the trap can be described by a Boltzmann distribution. When the atoms reach lower lying levels the levels are occupied according to a Bose-Einstein distribution. At very low temperatures the inset of Bose-Einstein condensation leads to a macroscopically populated ground state. The phase transition governing this condensation smears out when going to small atom numbers.

Chapter 3

From a solid piece of rubidium to single atoms in an optical dipole trap

Contents

This chapter introduces the main experimental stages that rubidium atoms initially present as a solid go through to end up trapped inside our microscopic dipole trap in form of a dilute gas. The key tool of this process is laser cooling that can be applied to decrease the temperature of atomic gases many orders of magnitude down to typically a few micro Kelvins. We start by reviewing the main idea on which the experimental setup is based on. Afterwards, we discuss the experimental realization and focus on the trap loading process.

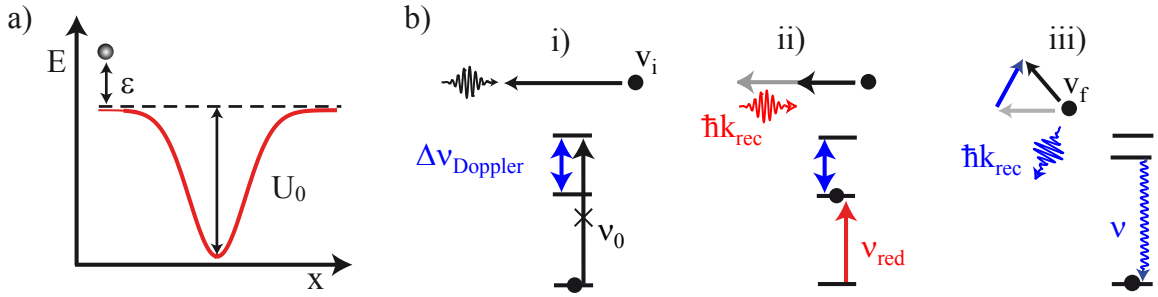

Figure 3.1: Principle of trap loading and laser cooling. *a)* x cross-section of the dipole trap potential. *b)* Principle of laser cooling based on the Doppler-shift, photon absorption and reemission processes.

3.1 Résumé

La partie principale de notre dispositif expérimental est une lentille asphérique qui permet de focaliser le laser de piégeage dipolaire au niveau de $\sim 1\ \mu$m. Il est possible de charger le piège dans deux régimes différents: l'un dans lequel un atome et un seul peut être piégé, et l'autre dans lequel en moyenne plusieurs atomes peuvent être chargés.

3.2 Naive view of dipole trap loading via laser cooling

There are two main requirements to be fulfilled in order to load an optical dipole trap. First, we need to create a reservoir of atoms around the dipole trap from which they are attracted by the dispersive dipole force discussed in Sec. 1.5.7. The dipole force creates a conservative potential with depth U_0 (Fig. 3.1 a)). Atoms with total energy $E > U_0$ falling into the potential well will subsequently exit, leaving their total energy unchanged. As a second requirement we therefore need a friction force to slow down the atoms that entered the trap until their total energy is smaller than the trap depth $E < U_0$.

Both requisites can beautifully be fulfilled using the technique of laser cooling proposed in the seventies (Hansch and Schawlow, 1975; Wineland and Dehmelt, 1975). The idea behind the cooling principle is illustrated in Fig. 3.1 b) and relies on the dissipative force discussed in Sec. 1.5.6. Consider an atom with an initial velocity $\boldsymbol{v}_\mathrm{i}$. Counter propagating photons that are resonant with the atom at rest ν_0 would be absorbed if the atom was not moving. The moving atom on the other hand sees the photons blue shifted due to the Doppler-shift $\Delta\nu_\mathrm{Doppler}$. Depending on the frequency shift the probability of the photons to be absorbed by the moving atom can be much reduced according to Eq. 1.28 (Fig. 3.1 b,i)). One can now detune the laser frequency to the red (to lower frequencies $\nu_\mathrm{red} < \nu_0$) such that photons become resonant with the atom in its moving frame. The atom can now absorb the photon and it loses one photon energy $h\nu_\mathrm{red}$ in kinetic energy and reduces its momentum by $\hbar k_{rec}$. In

exchange the atom is transferred to the excited level (Fig. 3.1 b,ii)). Eventually the excited atom spontaneously decays emitting a photon with higher frequency in a random direction (Fig. 3.1 b,iii)). Averaging over many cycles and emission directions in the entire solid angle the atom's kinetic energy can be significantly reduced. It can be shown that the atom's energy is reduced by $\sim E_{\mathrm{rec}}$ per cycle on average (Foot, 2005). The crucial point for laser cooling to work is therefore that the cooling laser frequency is smaller than the atom's rest resonance frequency.

We now describe our experimental setup, which is based on these ideas of laser cooling and is at the heart of loading our dipole trap from a reservoir of laser cooled atoms.

3.3 Experimental realization

The experimental system is qualitatively illustrated in Fig. 3.2. The vacuum chamber is divided into two parts. The part on the left contains a small solid sample of rubidium, which can be heated by some heating wires winded around the oven. With increasing temperature more rubidium atoms evaporate from the solid sample and increase the pressure in this part of the chamber. The increase in pressure leads to a beam of atoms passing through a differential pumping into the second part of the vacuum chamber. All laser frequencies are chosen to address transitions in ^{87}Rb. ^{85}Rb atoms in the atom beam will not be addressed by the laser light. We use a Zeeman slower to initially slow down a part of ^{87}Rb in the atom beam. A fraction of these slowed ^{87}Rb atoms is then trapped using a typical optical molasses or magneto-optical trap (MOT) configuration with six counter-propagating laser beams near resonance at 780 nm. The created atom cloud (~ 150 μK) serves as an atom reservoir from which the dipole trap can be loaded. The dipole trap consists of a far-off red-detuned ($850 \lesssim \lambda_{trap} \lesssim 950$ nm) laser beam focused into the atomic vapor using an aspheric lens ($NA = 0.5$) that is placed inside the vacuum chamber. The high numeric aperture allows to focus laser beams with wavelengths around 850 nm down to waists of ~ 1 μm. The dipole laser light creates an attractive potential and pulls atoms from the laser-cooled atom cloud to the point of highest laser intensity. We can prove the existence of atoms inside the optical dipole trap by imaging their fluorescence light onto a CCD camera and an avalanche photodiode. This is done by illuminating the atoms with near resonant light at 780 nm and collecting the scattered photons with the same aspheric lens. After the lens, the fluorescence light at 780 nm is separated from the dipole trap laser light by using a dichroic mirror. After this mirror the light is split by a polarizing beam splitter (PBS). One path leads onto a light intensifier used to amplify incoming photons before the CCD camera. The other path leads to a single mode fiber, which directs the photons onto an avalanche photo diode (APD) operating in single photon counting mode.

In the following we give some detailed information on the essential parts of the setup such as the laser system, the oven, the Zeeman slower, the optical molasses/MOT and the imaging system.

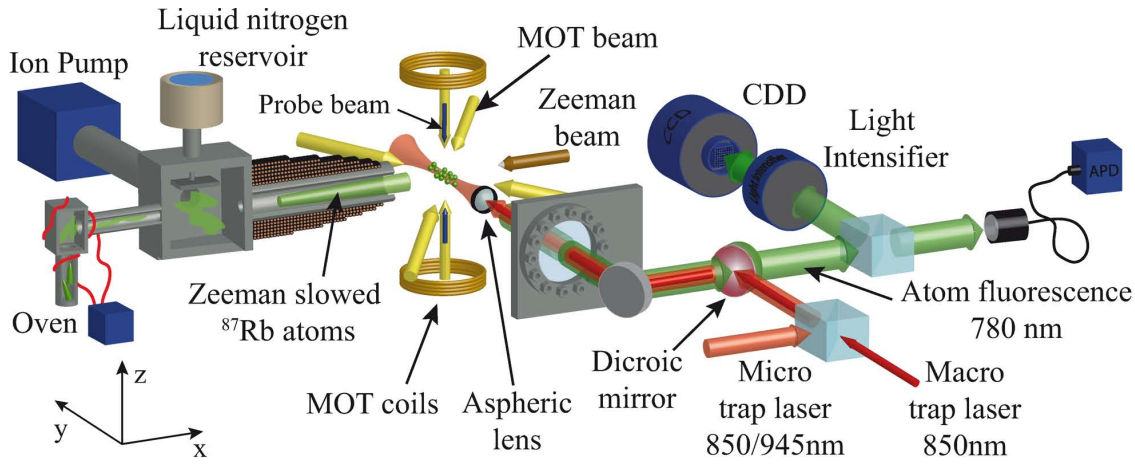

Figure 3.2: Experimental setup. In a first step ^{87}Rb atoms are slowed down to about 1 K using the Zeeman slowing technique. The atoms are further cooled to around 150 μK using standard 3D laser-cooling techniques. A dipole trap laser, whose frequency is far-off red detuned to the Rb transition at 780 nm, is focused by an aspheric lens into this atom cloud. The same lens is used to image the fluorescence light emitted by the atoms onto a CCD camera and an avalanche photodiode.

3.3.1 Laser System

All laser beams used in the experiment can be categorized in three classes. The first class contains all beams coming from a laser diode that is frequency-locked onto the crossover transition $F = 2 \rightarrow F' = 1 \times 3$ at 780 nm for ^{87}Rb by using standard Doppler-free saturation spectroscopy[1]. Acousto-optical modulators (AOM) can then be used to shift from the crossover to the atomic transitions, i.e. $5^2S_{1/2}F = 2 \rightarrow 5^2P_{3/2}F' = 2$ (pumper) or $5^2S_{1/2}F = 2 \rightarrow 5^2P_{3/2}F' = 3$ (MOT, probe, Zeeman). A second class contains all repumper beams. The repumper laser diode is locked onto the crossover transition $F = 1 \rightarrow F' = 1 \times 2$ (MOT repumper, probe repumper, Zeeman repumper). AOMs are again used to shift the laser frequency to the transition $5^2S_{1/2}F = 1 \rightarrow 5^2P_{3/2}F' = 2$. Finally, we group all lasers that are used to create the optical dipole trap. Due to the large detuning with respect to the rubidium transition frequencies, a frequency-lock is not necessary as small drifts in frequency have negligible influence on the atom.

All laser beams are prepared in a similar way: Directly after the laser output an optical isolator is used to suppress possible back reflections into the laser that could otherwise lead to multi-mode behavior. Acousto-optical modulators (AOM) are then used to shift the laser frequency to its final value. Depending on the frequency the beam is more or less deviated from its original path after the AOM (see Fig. 3.3 a)). The deviated beam is coupled into an optical fiber and directed to the vacuum chamber. Switching off the AOM, the laser beam passes the AOM straight. It is thus decoupled from the optical fiber which permits to switch on and off the laser

[1]The diode laser is locked on a crossover transition as its signal is much higher than normal transition signals.

class	Laser type	λ/nm	P_{out}/mW	Used as
1	Cavity grating stabilized diode laser (Toptica DL100)	780	150	optical molasses/ MOT Probe Zeeman Pumper
2	Cavity grating stabilized diode laser (Toptica DL100)	780	120	Rep. MOT Rep. probe Rep. Zeeman
3	Free diode laser Free diode laser Verdi TiSa cavity ring laser	850 945 532 850 – 950	250 300 6000 700 – 200	dipole trap dipole trap pump laser for TiSa dipole trap

Table 3.1: Laser system parameters. .

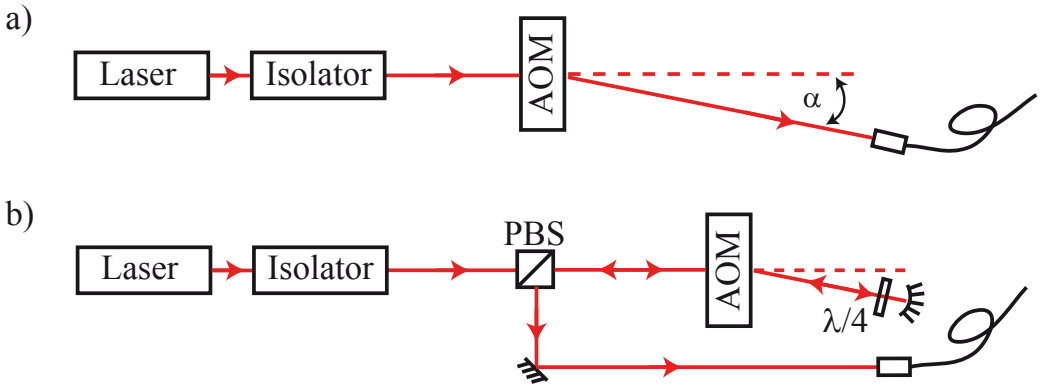

Figure 3.3: Optical laser beam path. Typical preparation of laser beams before they are sent into the vacuum chamber. a) Single pass AOM setup serves as a rapid optical switch: When the AOM is switched off, the laser beam follows the dashed line and is not coupled into the fiber. b) In the double pass configuration a curved mirror retro-reflects the laser beam into the AOM even for different deflection angles α. The light is therefore not decoupled from the optical fiber if the frequency is slightly changed.

beam very fast ($\sim$100 ns from 10 % $\rightarrow$ 90 %). For the MOT and the probe beams a double path AOM setup is used (see Fig. 3.3 b)). In this configuration the beam is retro-reflected after the AOM and passes the AOM a second time. A $\lambda/4$-plate is used to turn the beam's polarization and to separate the returning beam from the incoming one by using a polarizing beam splitter (PBS). The advantage of this setup is that it is now possible to change the frequency over a range of $\sim$50 MHz without having the laser beam decoupled from the optical fiber. This allows frequency scans with small intensity variations.

3.3.2 Oven and vacuum chamber setup

Approximately 1 g of rubidium (^{85}Rb+^{87}Rb) is provided in a small glass ampoule. Just before being placed inside the vacuum chamber one end of the ampoule is broken

off to ensure that the rubidium can leak out. At room temperature the sample is in a solid phase. It is placed inside a vacuum tube directly connected to the left side of the vacuum chamber according to the illustration in Fig. 3.4. Depending on the temperature of the oven T_{oven} a certain quantity of atoms evaporates from the sample and creates a vapor inside the tube. The temperature can be varied by heating wires tied around the tube, in which the solid sample has been placed. While heating the sample we make sure that the upper part of the tube is also heated at least above the rubidium melting temperature $T_{tube} > 38.9°\mathrm{C}$ to avoid clogging of the tube. Atoms of the vapor start to leak into the first chamber. The flux of atoms Fl_1 leaking out of the tube can be estimated via

$$Fl_1 = \frac{1}{4} n v A \ , \tag{3.1}$$

where $n = \frac{P}{k_\mathrm{B} T_{oven}}$ is the atomic density inside the tube, $v = \sqrt{\frac{8 k_\mathrm{B} T}{\pi m}}$ is the average Boltzmann velocity and $A = \pi \left(\frac{d_{tube}}{2}\right)^2$ the aperture of the tube with $d_{tube} = 5$ mm (Ramsey, 1990). We used the ideal gas law with the Boltzmann constant k_B and the atomic mass m. P is the vapor pressure, which can be estimated using the law $P(T) \approx 10^{(9.318 - 4040/T)}$ (Steck, 2008). For oven temperatures of $T_{oven} = 273 + 120$ K we find a flux of $Fl_1 = 3 \cdot 10^{16}$ s^{-1} just after the hole. The atoms spreading into the first chamber create a residual vapor. An ion pump is used to keep this residual pressure at typically $\sim 10^{-10}$ mbar. Additionally, a finger with a copper surface inside this part of the chamber is cooled via thermal contact with a reservoir of liquid nitrogen at 77 K on the outside. This leads to absorption of some rubidium atoms of the atom vapor and helps to avoid a rapid saturation of the ion pump. The part of the vacuum chamber containing the oven is separated from the part where the actual manipulation of the rubidium atoms takes place by the Zeeman slower tube with length $l_{Zee} = 70$ cm and diameter $d_{Zee} = 2 r_{Zee} = 15$ mm. This leads to ultra-high vacuum conditions $\sim 10^{-11}$ mbar on the right side of the vacuum system. The lower pressure corresponds to a much lower residual gas in this part of the chamber and reduces e.g. the rate at which the atoms in the dipole trap undergo background gas collisions.

The higher vacuum pressure due to the Zeeman slower tube is at the expense of the atomic flux. After the tube the atom flux Fl_2 goes into the solid angle $\Omega_\alpha = \frac{\pi}{4}\alpha^2 = \frac{\pi}{4}(d_{Zee}/l_{Zee})^2$. We use

$$Fl_2 = Fl_1 \frac{\Omega_\alpha}{4\pi} \ . \tag{3.2}$$

to estimate the net flux of atoms arriving at the dipole trap and find a reduction of nearly a factor 10^5 to $Fl_2 = 8.8 \cdot 10^{11}$ s^{-1}. The velocity probability distribution of the atoms in the atomic beam follows the distribution $\frac{m^2}{2(k_\mathrm{B} T_{oven})^2} v^3 \exp\left(-\frac{m v^2}{2 k_\mathrm{B} T_{oven}}\right)$. The average velocity for $T_{oven} \sim 400$ K is 368 m/s (right side of Fig. 3.4). The capture range of typical optical molasses is of the order of one Kelvin corresponding to ~ 16 m/s which means that only a small fraction of $\sim 10^{-5}$ atoms are effectively used for its production. To increase the fraction of captured atoms we use the Zeeman slower

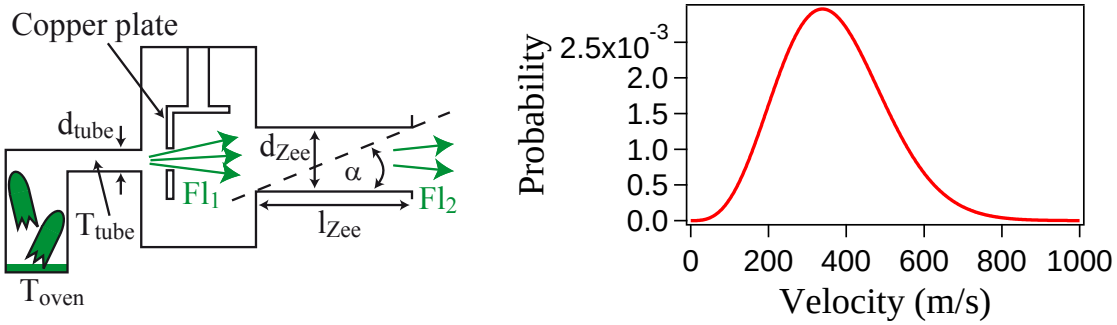

Figure 3.4: Rubidium oven and velocity distribution. *left*) Sketch of the first part of the vacuum chamber with the rubidium oven. *right*) Velocity distribution of the atoms passing the differential pumping into the ultra-high vacuum chamber at 400 K.

technique explained in the next paragraph.

3.3.3 Zeeman slower

The Zeeman slower (Phillips and Metcalf, 1982) is based on the laser cooling principle introduced in Sec. 3.2. It is used in our experiment to slow down a fraction of the atoms coming from the oven. To do so we counter propagate to the atomic beam in x-direction a σ^+ polarized laser beam. The laser is $\Delta\nu_{red} = -133$ MHz red-detuned from the vacuum transition frequency ν_0 of $5^2S_{1/2}F = 2 \rightarrow 5^2P_{3/2}F' = 3$, i.e. $\nu_{red} = \nu_0 + \Delta\nu_{red} = \nu_0 - 133$ MHz and is unchanged throughout the slowing process. Additionally, a repumper laser is superimposed to bring all atoms that deexcite from $5^2P_{3/2}F' = 3$ to $5^2S_{1/2}F = 1$ back into $5^2S_{1/2}F = 2$. Due to the circular polarization of the laser the atoms will quickly be pumped into the closed transition $5^2S_{1/2}F = 2, m_F = +2 \rightarrow 5^2P_{3/2}F' = 3, m'_F = +3$. The Doppler shift for atoms at $v_{x,i} \simeq 300 \frac{m}{s}$ is $\Delta\nu_{Doppler,i} = -\frac{v_{x,i}}{\lambda} = -385$ MHz. In order for the laser frequency to be resonant with the atom one introduces an additional level shift induced by an external magnetic field of $\Delta\nu_{B,i} = \Delta\nu_{red} - \Delta\nu_{Doppler,i} = 252$ MHz, see left side of Fig. 3.5. This Zeeman shift for $F = 2, m_F = +2 \rightarrow F' = 3, m'_F = +3$ in first order follows from Eq. 1.8 and equals $\Delta\nu_B/B = 1.4$ MHz/Gauss. This means that to be resonant with the atom at 300 m/s we need a magnetic field along the laser direction of $B_i = 180$ Gauss.

Nevertheless, there is one difficulty that has to be dealt with. If the atom is slowed down only 10 m/s, the reduced Doppler shift drives the resonance further away from the laser frequency by $\sim 2\,\Gamma/2\pi$. The cooling process becomes less efficient since less photons are absorbed and it eventually stops. The main idea is now to adjust the magnetic field along the atom's direction of propagation x such that the laser stays on resonance with the Doppler-shifted atomic transition for velocities ranging from 300 m/s to 5 m/s. For 5 m/s the maximal Doppler shift is $\Gamma/2\pi$, so that the atom stays resonant with the laser even if further cooled. To derive the dependence of the magnetic field on the position of the atom x we assume that the atom loses on average one recoil momentum k_{rec} per photon absorption event

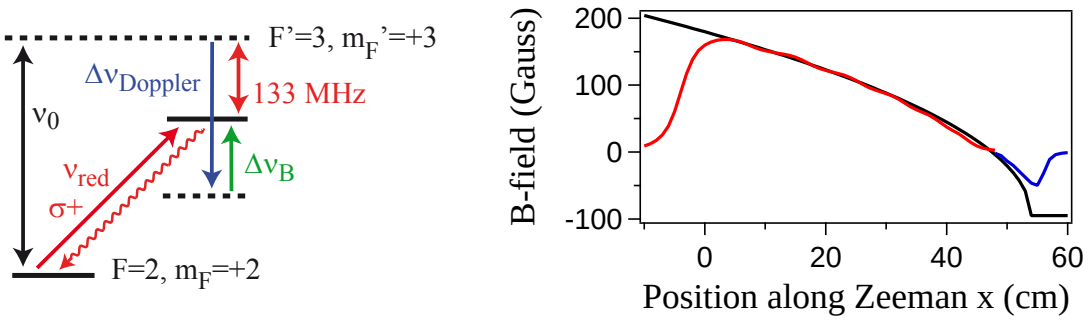

Figure 3.5: Zeeman slower principle. *left*) ^{87}Rb levels considered in the Zeeman slower. *right*) Theoretical magnetic field (black line) versus the position inside the Zeeman tube. Two arrays of solenoids are adjusted to create a magnetic field (red and blue line) that matches the theoretically calculated field.

along the propagation direction x. On resonance the absorption and reemission take place at a rate $\frac{\Gamma}{2}\frac{s}{1+s}$ depending on the laser saturation s. The atom thus decelerates according to $a = v_{rec}\frac{\Gamma}{2}\frac{s}{1+s}$. The position and velocity of the atom follow the equations of motion $v_f = v_i - at$ and $x = v_i t - \frac{1}{2}at^2$. Replacing t in the second equation we can calculate the length $x = L = \frac{v_i^2 - v_f^2}{2a} \approx \frac{v_i^2}{2a}$ $(v_i \gg v_f)$ over which the magnetic field has to be varied. In our case we find $L = 54$ cm assuming[2] $s \sim 3$. For the resonance condition $\Delta\nu_B = \Delta\nu_{red} - \Delta\nu_{Doppler}$ to be fulfilled the magnetic field has to vary as

$$B(x) = \frac{h}{\mu_B \Delta g_F m_F}\left(\Delta\nu_{red} - \Delta\nu_{Doppler}\right) = \frac{1}{\mu_B}\left(\Delta\nu_{red} + \frac{v_i}{\lambda}\sqrt{1 - x/L}\right) , \qquad (3.3)$$

where we use $\Delta(g_F m_F) = g_{F'=3} m_{F'} - g_{F=2} m_F = 1$. In our case we use two arrays of six solenoids to reproduce the theoretical curve shown as the black curve on the right of Fig. 3.5. The first array consists of six consecutive solenoids each having a length of $(11.1, 9.8, 8.6, 7.3, 6, 4.7)$ cm with $(330, 250, 180, 105, 60, 25)$ windings. It follows the resonance until the Doppler-shift equals the laser frequency detuning $\Delta\nu_{red} - \Delta\nu_{Doppler} = 0$. After this point the magnetic field has to switch direction. The second array of solenoids is therefore built in reverse. The coil lengths are $(2, 1.6, 1.3, 0.9, 0.5, 0.2)$ cm and each coil has $(2, 10, 20, 30, 80, 100)$ windings. The magnetic field created by the first (red) and second (blue) array are shown on the right side of Fig. 3.5.

We introduced the cooling principle with one atom having initially a fixed velocity $v_i \simeq 300$ m/s. The situation is slightly more complex when there is a distribution of many velocity classes present. On the right side of Fig. 3.4 we show the velocity distribution of the atomic beam at 400 K with a mean velocity 368 m/s. We adjusted the magnetic field to slow down all atoms with an initial velocity $v_i = 300$ m/s. All atoms with higher velocity cannot be slowed down since higher magnetic fields would be needed. The capture range of the slower is thus fixed at 300 m/s. Atoms initially

[2] Although the laser beam has an intensity well above $s = 3$, we cannot ensure that this is the saturation actually seen by the atom due to alignment error etc.. We therefore take a saturation of $s \sim 3$ to not overestimate the real saturation of the atom.

being in the lower tail of the Boltzmann distribution $v < v_i$ do not see the laser light in the beginning. But they become resonant with the laser light at a point along x at which the difference between their Doppler-shift and magnetic Zeeman shift equals again the laser frequency. All atoms having velocities smaller than v_i are thus slowed down as well (33 % of entire velocity distribution). The final velocity in x direction is close to zero and limited by the laser light diffusion. The Doppler-temperature in 1D is $T_D = \frac{\hbar\Gamma}{2k_B} = 137\ \mu$K corresponding to an average velocity of 0.2 m/s. We note that a detailed measurement of these values has not been done so far on this experiment.

We end this paragraph with some remarks. The Zeeman slower cools the atoms in one dimension, namely along x whereas the photon emission in the solid angle leads to a transverse heating of the beam. The transverse root-mean-square (rms) velocity after having passed the slower is $\Delta v = v_{rec}\sqrt{\frac{N_{ph}}{3}}$ (Joffe *et al.*, 1993) and depends on the number of scattered laser photons N_{ph}. In our case we find $N_{ph} \approx \frac{v_i}{v_{rec}} = 51000$ and consequently a transverse rms velocity of 0.8 m/s. This heating results in a radial rms deviation of the beam by $\Delta r = \frac{2}{3}\frac{v_{rec}}{\Gamma}N_{ph}^{3/2} = 1.2$ mm.

3.3.4 Optical molasses and magneto-optical trap

The Zeeman slower is able to reduce the velocity of the atoms in the beam largely below 10 m/s but does not confine or trap atoms. In this paragraph we briefly discuss how a magneto-optical trap can be used to create an atom reservoir which the dipole trap can be loaded from. Depending on how many atoms we want to load into the dipole trap we work in two configurations: For a low atom number ~ 10 we use an optical molasses while for higher atom numbers we use a magneto-optical trap (MOT) as it leads to higher densities in the atom reservoir.

Optical molasses

To confine the atoms slowed down by the Zeeman slower in three dimensions we superimpose on the dipole trap three pairs of counter-propagating laser beams having opposite polarization ($\sigma^+ - \sigma^-$) in all three spatial dimensions (Fig. 3.6 a)). The pair of beams in z-direction are orthogonal to the pair of beams in the $x-y$ plane. Both pair of beams in the $x-y$ plane enclose an angle of $\sim 50°$ with each other. Larger angles are not possible due to the large NA aspheric lens that would otherwise clip the laser beams. The laser beam waist is with $w = 2\sigma_{mol} = 2$ mm relatively small and also limited by the mechanical mount of the aspheric lens. The laser frequency is kept fixed at $\Delta\nu_{MOT} = -3.5\Gamma$ to the cycling transition. The laser power is ~ 2 mW per beam which results in an atom saturation of $s \sim 100$. A repumper laser is additionally superimposed with all six beams to bring atoms that fall into the $5^2S_{1/2}F = 1$ manifold back into $5^2S_{1/2}F' = 2$. It has the same waist and a laser saturation of $s \sim 30$. The rather high saturation parameters increase the volume of the atom reservoir as atoms away from the center of the beams by $2\sigma_{mol}$ still see a saturation $s \sim 1$. This helps for the alignment of the reservoir around the optical dipole trap and improves

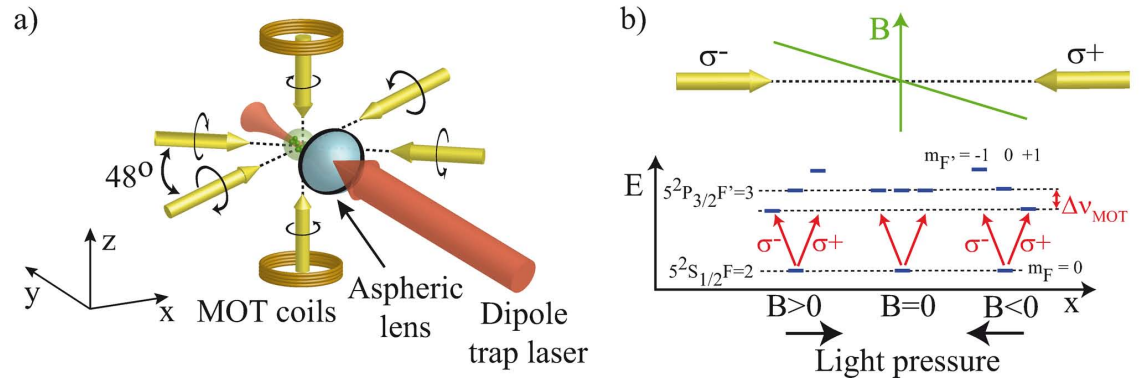

Figure 3.6: Magneto-optical trap (MOT). *left*) Experimental MOT configuration. *right*) Principle of a MOT for an atom with three Zeeman levels.

the atom loading into the dipole trap.

The configuration described above leads to a cooling in 3D, where temperatures around the Doppler limit $T_D = \frac{\hbar\Gamma}{2k_B}$ ($T_D \sim 145$ μK for rubidium) can be reached. It was experimentally shown that this Doppler limit can be passed and Sub-Doppler temperatures can be obtained (Lett *et al.*, 1988). The explanation of this phenomenon is referred to as polarization gradient cooling (Dalibard and Cohen-Tannoudji, 1989). It works best when the magnetic field is well-compensated in the molasses region.

We want to add two remarks: First, for the chosen laser detuning atoms initially not faster than 16 m/s can be confined with this configuration. We calculate that the Zeeman slower increases the fraction of atoms captured by the molasses out of the atomic beam by a factor $\sim 7 \cdot 10^4$ to 33 %. It accelerates the loading of the molasses and thus the duty cycle of the experiment. Second, the molasses has a cooling but no trapping effect. There is no force pulling the atoms back into the center of the molasses after they have been slowed down. The next section will show how such a restoring force can be created.

Magneto-optical trap

Our magneto-optical trap configuration consists of an optical molasses combined with a magnetic field gradient, as shown in Fig. 3.6 b). It leads to a restoring force. The force is simply the radiation pressure force which this time depends on the position of the atom. The position dependence can be created using a pair of coils operating in anti-Helmholtz configuration. This creates a magnetic field that is approximately linear around the center and induces a Zeeman shift of the level. If the atom is now on the right with positive magnetic field it will be resonant only with the σ^- laser which pushes the atom to the left. The contrary works for the atom on the left so that effectively a force pointing to the center of the MOT has been created. The restoring force helps to increase the atom cloud density.

The magnetic field is created by two coils in anti-Helmholtz geometry with $R =$

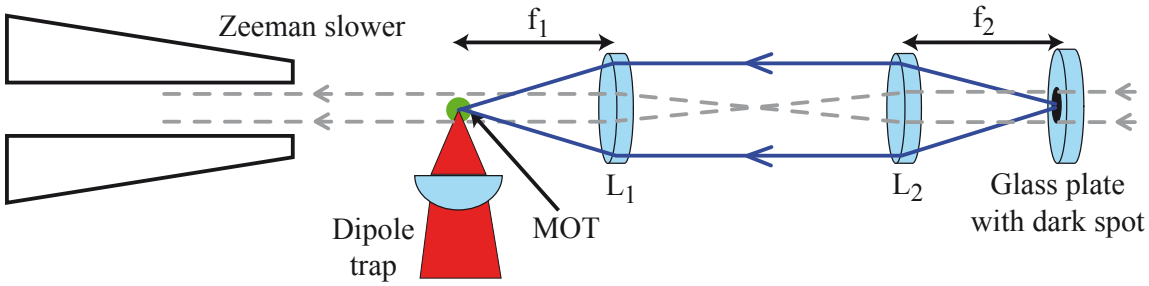

Figure 3.7: Imaging of a dark spot into the Zeeman beam. The lenses L_1 and L_2 have focal lengths of $f_1' = 750$ mm and $f_2' = 750$ mm, respectively.

8.5 cm. Each coil has $n = 81$ windings and can support up to 10 A. To create the MOT we operate the current in the coils at 4.5 A. This leads to magnetic gradients of ~ 5 Gauss/cm in the center of the trap. We use a CCD camera to measure the MOT fluorescence. Knowing the collection efficiency and photon scattering rate of the atoms ($\Gamma/2$) we deduce about 10^7 atoms in the MOT, which has a nearly Gaussian shape with rms width of 330 μm. This corresponds to a peak atom density on the order of 10^{10} cm^{-3} that is mainly limited by the small laser beam waists. The actual MOT density around the dipole trap can only be vaguely inferred since we do not have a precise enough diagnostic to measure the position of the dipole trap with respect to the MOT.

The MOT needs to be aligned with the Zeeman beam to ensure an efficient loading of the MOT. In our setup this is done by aligning the six MOT beams on the axis of the Zeeman slower. The Zeeman slowed atoms thus arrive directly into the cross-section of all MOT beams. Since the Zeeman laser passes right through the MOT the radiation force pushes the MOT towards the Zeeman slower. To avoid any perturbation of the Zeeman laser on the MOT we image a dark spot onto the position of the MOT. The dark spot has a diameter of ~ 1 mm and is imaged onto the MOT as illustrated in Fig 3.7. While this leads to no Zeeman light illuminating the MOT center light still passes into the Zeeman slower and slows down the atoms inside the slower.

3.3.5 Dipole trap and imaging system

The center part of the imaging system is the aspheric lens. The lens has a diameter $D = 8$ mm and a focal length $f' = 8$ mm, which leads to a collection solid angle of $\Omega/4\pi = 0.067$ and a numerical aperture of $NA = 0.5$. The working distance is 5.71 mm. This property permits to focus laser beams at 850 nm down to a spot size of 1 μm FWHM (Sortais *et al.*, 2007). We use the same lens to image the fluorescence light coming from the atoms onto an APD and a light-intensified CCD camera [3].

[3] A discussion of the light intensifier is given in Ch. 4

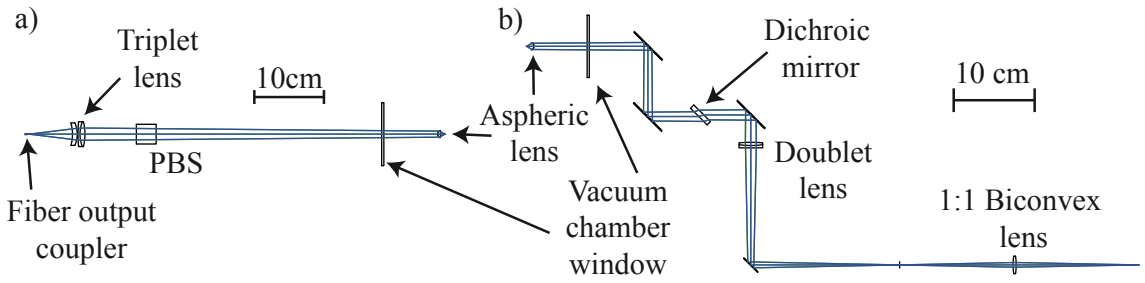

Figure 3.8: Micro trap beam path and imaging system. a) Beam path of the micro trap laser between the optical fiber and the aspheric lens. The calculated axial magnification is $g_x = 1/g_y^2 = 1/4.2^2$. b) Imaging system used to collect atom fluorescence by the aspheric lens and detect it on a CCD and APD. The calculated radial magnification is $g_y = 26 \pm 2$.

Dipole trap setup

A PBS before the vacuum chamber is used to independently produce two dipole traps at the same time into the vacuum chamber. One trap has a waist of ~ 1 μm while the second is slightly bigger with a waist of 3.8 μm. The small trap created by the strongly focused laser beam will be referred to as the micro trap in the following. We refer to the bigger trap as the macro trap.

Micro trap

The optical path for the micro trap after the optical fiber is shown in Fig. 3.8 a). To create spot sizes of 1 μm we have to illuminate the lens with a nearly collimated laser beam. Coming out of the optical fiber, the Gaussian laser beam passes a triplet lens ($f' = 60$ mm), which focuses the beam onto the aspheric lens. After the triplet lens we use a PBS to superimpose the micro trap with the macro trap. The beam then passes the vacuum chamber window and impinges on the aspheric lens. We pursue the calculations for a trap wavelength of $\lambda_{dip} = 850$ nm.

The laser beam before the lens has a Gaussian shape with a waist of $w_i = 3.6$ mm. The lens diameter is $D = 8$ mm so that we unavoidably cut off the outer part of the Gaussian beam. It is therefore not certain that the laser beam after the lens will still have a Gaussian shape. The radial field $E(r)$ resulting from the conjugation of the incident dipole trap beam $E_i(r) \propto \exp -r^2/w_i^2$ by the lens can in the far field be calculated from

$$E(r,z) = \frac{-i}{\lambda_{dip} z} e^{\frac{ik_{dip} r^2}{2z}} e^{ik_{dip} z} \int_0^{2\pi} \int_0^{D/2} E_i(\rho) e^{-\frac{ik_{dip}\rho^2}{2f'}} e^{\frac{ik_{dip}\rho^2}{2z}} e^{\frac{ik_{dip}\rho r\cos(\theta)}{z}} \rho d\rho d\theta \ , \quad (3.4)$$

with $k_{dip} = 2\pi/\lambda_{dip}$. At the focal point $z = f'$ we find

$$E(r,f') = \frac{-i}{k_{dip} f'} e^{\frac{ik_{dip} r^2}{2f'}} e^{ik_{dip} f'} \int_0^{D/2} E_i(\rho) J_0\left(\frac{k_{dip}\rho r}{f'}\right) \rho d\rho \ , \quad (3.5)$$

where J_0 is the Bessel function. The normalized intensity $I(r) = |E(r,f')/E(0,f')|^2$ (red line) is shown in Fig. 3.9 and is in good agreement with a Gaussian fit (dashed

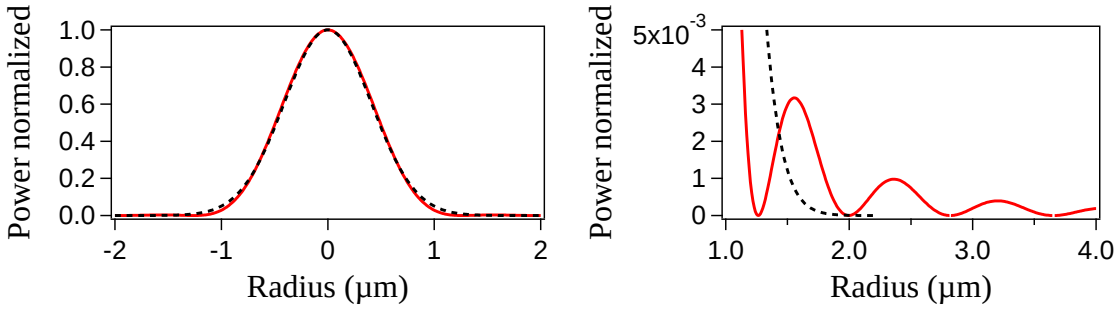

Figure 3.9: Micro trap profile. *left*) The normalized intensity created by the dipole trap in the focal plane of the aspheric lens. *right*) A zoom onto the wings of the profile shows the presence of Airy rings. These are very small and have a height of only $\sim 3 \cdot 10^{-3}$.

black line). A zoom on the side of the curve (right image in Fig. 3.9) reveals small differences between the actual intensity profile and a Gaussian shape. These differences are mainly due to the presence of Airy rings. The height of the first Airy ring with respect to the center peak is $\sim 3 \cdot 10^{-3}$ and can safely be neglected.

Macro trap

The macro trap has a beam waist of $w_{M,i} = 0.57$ mm before the lens. This is much smaller than the diameter of the lens so that the beam is not clipped. We deduce a waist of the macro trap after the lens of $w = \lambda_{dip} f'/(\pi w_{M,i}) = 3.8$ μm.

Detection of the atom fluorescence

In all experiments we use the fluorescence technique to visualize the atoms that are trapped inside the optical dipole trap. The fluorescence can be induced by using the molasses and repumper molasses lasers. Also, we can use the in z-direction $\sigma^+ - \sigma^-$ counter-propagating probe and repumper probe laser beams (see Fig. 3.2). For the molasses and probe lasers the fluorescence is induced on the $5^2S_{1/2}F = 2 \rightarrow 5^2P_{3/2}F' = 3$ transition. The repumper laser stays on resonance with the atom vacuum transition $5^2S_{1/2}F = 1 \rightarrow 5^2P_{3/2}F' = 2$ for all experiments while the molasses and probe laser frequency can be frequency shifted around the $5^2S_{1/2}F = 2 \rightarrow 5^2P_{3/2}F' = 3$ transition using to the double path AOM setup (see Fig. 3.3 b)). The induced fluorescence photons are partially collected by the aspheric lens. They are separated from the dipole trap light using a dichroic mirror. Afterwards they pass an optical bandpass filter centered at 780 nm with a bandwidth of 10 nm. The light is then divided into two paths. One leads to a single-mode fiber that is connected to an APD and the other goes to a light-intensified CCD camera. The proportion of light going in each path can be tuned using a $\lambda/2$-plate and is set to[4] ~ 50 %. The optical imaging path is illustrated on the right side of Fig. 3.8. We align the imaging system such that light coming from the dipole trap center is directly imaged onto the CCD

[4] The fluorescence light coming from the atoms has been measured to be elliptically polarized. The percentage of light in each path can be changed between 50 % – 50 % and 20 % – 80 % by turning the $\lambda/2$-plate.

Loss cause	Efficiency/ %
Solid angle	6.7
Optics	90
Dichroic mirror	90
Filter	70
PBS	50/50 (+95)
APD single-mode fiber coupling	60 ± 20
APD quantum efficiency	50
Light intensifier in front CCD camera	10 ± 1

Table 3.2: Detection efficiency budget for light at 780 nm.

camera and at the same time is coupled into the APD fiber. We will discuss a detailed calibration of the imaging system in part II.

Detection efficiency

All elements that influence the fluorescence collection efficiency η of our imaging system are listed in Table 3.2. The solid angle covered by the aspheric lens is 6.7 % of the whole solid angle. All glass surfaces due to mirrors, vacuum chamber etc. make up 90 % of the transmission. The dichroic mirror has a transmission at 780 nm of 90 % and the filter to further reduce light components different from 780 nm has a transmission of 70 %. Up to the PBS separating the fluorescence to the CCD camera and the APD we capture 3.8 % of the total amount of fluorescence emitted from the center of the dipole trap. The measurement of the detection efficiency of the APD is given in Ch. 7. We find APD detection efficiencies of 0.6 ± 0.2 % which is typical of systems using high numerical aperture lenses (Darquié *et al.*, 2005) (see Sec. 7.4.3). For the intensified CCD camera we calculate $1.9 \pm 1 \cdot 10^{-3}$ which is experimentally confirmed in Sec. 6.2.2 and Sec. 8.3.3.

3.4 Dipole trap loading

The last step to single atoms or small atomic ensembles trapped inside the dipole trap is the implementation of an efficient loading. The number of atoms attracted by the laser light obviously increases with the surrounding atom density. The density around the focal point can experimentally be changed by varying e.g. the temperature of the oven, the MOT laser intensities or the MOT magnetic field gradient. The number of atoms entering the dipole trap per second is referred to as the loading rate R. It depends on many factors, most importantly the MOT density around the trap and the efficiency of the Doppler cooling mechanism. Without cooling the atoms would just see a conservative potential and not stay inside the trap. The loading rate R would then be zero[5].

[5]We neglect self trapping mechanisms such as collisions between two or more atoms that could remove enough energy from an entering atom to be trapped.

The number of atoms that can maximally be loaded into the trap is limited by the trap losses. Of all loss mechanisms described in Sec. 2.2 we limit ourselves to the two most important loss mechanisms that govern the dipole trap loading from a MOT: One-body losses and light-assisted collisions induced two-body losses. Including the loading rate R into Eq. 2.12 the number of trapped atoms N follows

$$\frac{dN}{dt} = R - \gamma N - \beta' N(N-1) \ . \tag{3.6}$$

Note that in this equation N cannot be strictly associated with the mean number of atoms $\bar{N}$ (see Sec. 8.5 and App. D). It can however be used to obtain an approximation of the mean-value (first order moment) of the atom number. For the stationary case $\frac{dN}{dt} = 0$ we can distinguish between two regimes: The single and the multi atom regime.

3.4.1 Single atom regime

For all single atom experiments presented in this thesis the atom is directly loaded from the optical molasses. To work in the single atom regime we usually reduce the loading rate $R \ll \gamma$ by switching off the Zeeman and repumper Zeeman beams. Additionally the temperature of the oven is held between room temperature and $\sim 90°$C in order to reduce the atomic flux from the oven. During the single atom loading the dipole trap depth is $U/k_B \sim 3$ mK ($U/h \sim 60$ MHz). It happens that while an atom enters the dipole trap it is also Doppler cooled inside the trap by the molasses light. During this process the atom steadily scatters photons that are partially captured by the aspheric lens and coupled to the single-mode fiber connected to the APD. Light coming from surrounding molasses atoms is much less coupled to the fiber and contributes to the background level.

Let us estimate if a clear difference can be made between light coming from an atom in the center of the dipole trap and the surrounding atom reservoir. We assume the atom to scatter with $s \sim 50$ (see below) inside the trap of 60 MHz. Near the bottom of the trap the atom sees a total laser detuning[6] $\sim 13.5\Gamma$ and therefore fluoresces at the rate $\frac{\Gamma}{2}\frac{50}{1+50+4\cdot 13.5^2} \sim \Gamma/40 = 1 \cdot 10^6$ photons/s. We estimate the number of detected photons during a detection time of 1 ms to be on average 5 photon/ms knowing the detection efficiency to be 0.6 %. Assuming a Poisson distribution for the detection process the signal is subject to $\Delta_{sig} = \sqrt{5} \sim 2.2$ photon/ms fluctuations. Having estimated the signal contribution we need to consider the noise contributions next. We measure a constant background noise contribution of typically $\Delta_{bkgd} \sim 1$ photon/ms which is mainly due to APD dark counts and the residual molasses fluorescence. The total noise is thus $\Delta_{bkgd} = \sqrt{\Delta_{sig}^2 + \Delta_{bkgd}^2} \sim 2.4$/ms. This leads to a signal-to-noise ratio (SNR) of only 2.1 which would make it difficult to distinguish between the real atom fluorescence and the background contributions. A possible solution is to

[6] The detuning is composed of the light shift induced by the dipole trap and the initial red detuning -3.5Γ of the molasses laser.

integrate the fluorescence over a sufficiently longer time interval. If we increase the integration period by a factor 10 to 10 ms we find a background noise amplitude of $\sqrt{10} \sim 3$ photon/10 ms and a signal of 50 ± 7 photon/10 ms. We find a SNR of 6.6 which should allow a reliable detection of a single atom.

The estimations made above are roughly confirmed by measuring the molasses laser-induced atom fluorescence (left in Fig. 3.10), where each data point is the accumulation of 10 ms fluorescence integration. In the single atom regime we observe characteristic fluorescence steps on the APD, which can be explained by the following mechanisms. Each time an atom enters the trap, its scattered light is coupled to the fiber and detected by the APD. In this case we detect ~ 50 photons during the 10 ms integration period which corresponds to the previously made estimations. We note that the difference in calculated molasses laser saturation $s = 100$ and the observed case $s \sim 50$ is due to the fact, that the trap is not well centered on the molasses and hence does not see the entire molasses laser intensity.

If a second atom enters the trap light-assisted collisions can lead to a gain in kinetic energy much greater than the trap depth and both atoms are immediately[7] ejected. The loss of the atoms manifests itself in a drop of the fluorescence signal to the background level (here ~ 5 photons/10 ms). After a while the next atom enters the trap and the procedure repeats itself. This leads to the characteristic single atom steps on the APD. The experimental evidence of single atom loading into an optical dipole trap has been first shown in 2002 (Schlosser, Reymond, and Grangier, 2002). It is remarkable that in this situation the atom number distribution inside the trap is sub-Poissonian ($\Delta N^2/\overline{N} = 0.5$) as only zero or one atom is present with nearly 50 % chance. This sub-Poissonian behavior completely relies on the two-body loss as one-body loss alone leads to Poissonian loading. Poissonian loading ($\Delta N^2/\overline{N} = 1$) could be reached for loading rates R much smaller than the one-body loss γ. In this case the probability to have two atoms inside the trap is negligibly small. The steady state atom number $N_{st} = \frac{R}{\gamma} \ll 1$ follows from Eq. 3.6 neglecting the two-body loss term[8]

Triggered single atom loading

Observing the single atom steps implies a loading rate smaller than $1/10\text{ms} = 100\ \text{s}^{-1}$. In this case the atom stays long enough in the trap to detect a sufficient amount of photons in order to decide on its presence. In practice we trigger on a single atom if the fluorescence level of three consecutive time bins with 10 ms duration is higher than ~ 50 % of the single atom fluorescence signal. For the case shown in Fig. 3.10 the trigger threshold would be set to ~ 25 photons/10 ms. If the trigger condition is fulfilled we know that a single atom is inside the trap (N=1,$\Delta N = 0$). In this case we can switch off the molasses laser beams and avoid the fast loss of the atom due to a

[7] Two atoms stay inside the trap for ~ 1 ms, see Sec. 9

[8] Further details are discussed in Sec. 8.5.

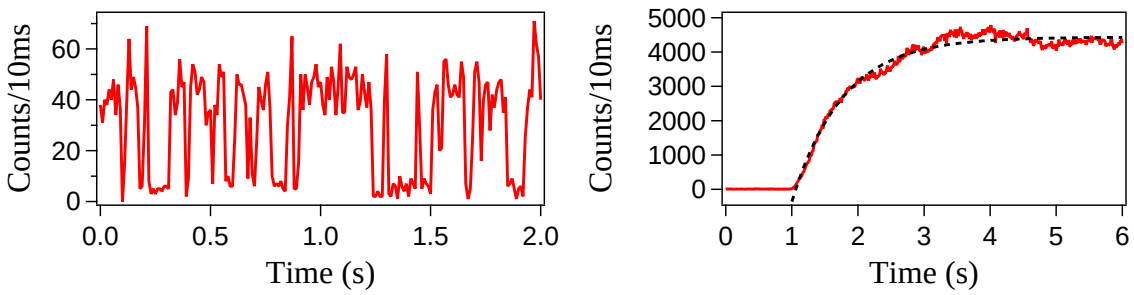

Figure 3.10: Atom and MOT fluorescence on the APD. *left*) The molasses-induced single atom fluorescence shows characteristic intensity jumps between ~ 5 and ~ 45 photon counts/10 ms over time. Each data point is averaged over 10 ms. *right*) Starting the MOT loading at $t = 1$ s the fluorescence shows an exponential increase over time. The loading time is 1.3 s after which the fluorescence level can reach values 100 times higher than for the single atom.

light-assisted collision with another atom. Switching off the molasses light helps in two ways. First, it leads to a loading rate $R = 0$ so no further atoms enter the trap. Second, since no light is present, no collisions assisted by this light can be triggered.

There are however several reasons for which the triggering is not 100 % efficient. We could imagine that during the three 10 ms trigger bins, we detect by chance most of the photons during the first half of the 5 ms. Just afterwards a second atom enters and leads to the loss of both atoms. The trigger condition in this case is still fulfilled but no atom is trapped. We measure a probability for this to happen of ~ 0.6 % ($T_{oven} = 90°$). It can be reduced by decreasing the loading rate R at the expense of the experimental duty cycle, which is usually on the order of 2 Hz.

The energy distribution of a single atom inside the dipole trap is a thermal Maxwell-Boltzmann distribution[9] (see Sec. 2.3.1) which has been experimentally shown by Tuchendler *et al.* (2008). From a theoretical point of view it can be shown that the molasses cooling can be described by a Fokker-Planck equation, which in a linearized form is solved by a Gaussian distribution corresponding to a thermal energy distribution (Parkins and Zoller, 1992).

Single atom detection

To check whether the single atom is still present in the dipole trap, we switch on again the molasses laser beams. The atom begins to be Doppler cooled while scattering photons. We can now check if the fluorescence level still exceeds the level set for triggering. If this is the case we know that the atom is present, otherwise it has been lost. In the experiment we use two time bins of 10 ms over which the fluorescence level must be higher than the trigger threshold.

[9] We assume the atom to be in higher energy levels of the harmonic trap.

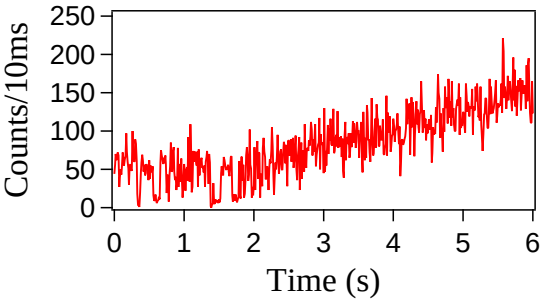

Figure 3.11: Beyond the single atom regime. For low trap loading rates in the beginning we observe the single atom steps. With increasing loading the fluorescence rises without showing a two step characteristic anywhere. Each point is the fluorescence integration over 10 ms.

3.4.2 Multi atom regime

The second regime is governed by a high loading rate R for which it is more probable to have more than one atom inside the trap. Light-assisted collisions are then much more likely to occur than one-body losses. If we neglect one-body losses in this case we find a steady state atom number $N_{st} \sim \sqrt{\frac{R}{\beta'}}$ using Eq. 3.6. It is an equilibrium based on the fact that the loss due to light-assisted collisions is compensated by new atoms loaded into the trap.

To reach this regime we need to increase the loading rate R which is usually done by increasing the oven temperature to $\sim 120°C$. Additionally, we load the trap from the MOT which itself is loaded by the Zeeman slower. On the APD we see an exponential increase in detected fluorescence photons when switching on the MOT beams (right in Fig. 3.10). The rising time of the fluorescence signal is 1.3 s and determines together with the length of the experimental sequence the duty cycle of the experiment. However, the loading time of the MOT highly depends on the alignment of the MOT laser beams which are subject to change over time. In this example the fluorescence level is ~ 100 times higher than the single atom level. It is composed of the fluorescence coming from the atoms inside the dipole trap and the background fluorescence coming from the atoms inside the MOT.

For all many-atoms experiments presented in this thesis we trigger on this fluorescence level. For example, if we set a trigger level of 2000 photons/10 ms, each sequence is launched when the fluorescence reaches this threshold. Assuming a MOT density proportional to the observed fluorescence this triggering procedure ensures a roughly stable atom loading rate R for each sequence. However, we measure that the atom number inside the dipole trap fluctuates ($\Delta N \neq 0$) and shows a sub-Poissonian behavior as in the single-atom case (see Sec. 8.5).

Why is the multi-atom loading probabilistic?

Triggering on a fixed fluorescence level does not lead to a fixed number of atoms inside the dipole trap. In fact, only the average number of atoms can roughly be fixed in this way. To understand this point we look at a very slow dipole trap loading rate as shown in Fig. 3.11. In the beginning we see the single atom steps as before.

After about two seconds the loading increases and with it the fluorescence level starts to rise. We do not observe any double or higher order steps that would correspond to two or more atoms inside the trap. There are two main reasons for this. Firstly, the inefficient photon detection of our setup or the rapidity of the loading and loss processes inhibit such an observation. As the fluorescence has to be averaged over 10 ms to clearly see the single atom steps, we lose all information on the processes at shorter timescales. Consequently, we do not know how many atoms entered and left the dipole trap during the 10 ms time bin when the loading rate is much higher than 100 Hz. We measure an averaged fluorescence rate resulting from atoms entering and leaving the trap at timescales much shorter than 10 ms. In this case the APD signal cannot be used to deterministically trigger on a fixed atom number. Secondly because the height of the steps itself decreases due to light-induced dipole-dipole interactions that shift and broaden the atomic line (Morice, Castin, and Dalibard, 1995). Due to the random nature of the two-body losses during the loading this procedure leads to fluctuations in the number of trapped atoms from shot to shot ($\Delta N^2 \neq 0$).

There are however some possibilities to deterministically load many atoms inside the dipole trap. One is based on using a bigger dipole trap to reduce the light-assisted collision rate and detect enough photons to decide how many atoms are trapped (Frese *et al.*, 2000). Another is using a laser tuned to the repulsive dipolar potential which can also slow down the atom loss rate significantly (McGovern *et al.*, 2011). However, it is difficult to apply the methods for atom numbers higher than ~ 5.

Improved dipole trap loading

To increase the number of atoms loaded into the dipole trap we apply a MOT compression phase. After the trigger on the APD fluorescence level the frequency of the MOT laser beams is tuned from $-3.5\ \Gamma$ to $-10\ \Gamma$ during 20 ms. This leads to a compression of the MOT and an increased density (Petrich *et al.*, 1994) around the dipole trap[10]. Due to the increasing detuning the molasses laser beam power reduces by a factor ~ 10 due to the decoupling from the optical fiber.

Additionally to the compression, we switched off the repumper laser after 15 ms in order to limit the number of atoms in level $5^2S_{1/2}, F = 2$ to ~ 10 %. A significant fraction of atoms in $5^2S_{1/2}, F = 2$ would otherwise lead to atom losses due to inelastic spin-changing collisions. On the other hand it does not decrease significantly the atom number loaded into the dipole trap.

3.5 Conclusion

The center piece of the setup is the aspheric lens which permits to focus the optical dipole trap down to microscopic sizes around 1 μm. It is possible to operate in two different regimes: One in which a single atom can be trapped and a second in which

[10] Other techniques to increase the density are discussed in Sec. 10.2.

many atoms can be loaded into the trap. In the case with many atoms inside the dipole trap only the average number of trapped atoms is controlled on our experiment.

Chapter 4

Light intensifier calibration

Contents

Our experiment highly benefits from the use of a charge-coupled device (CCD) camera. Working with small atom numbers and typically low light signals the presence of several noise sources can inhibit a reliable detection, in particular the detection of single photons. There are however some approaches that can overcome the few problems of ordinary CCD technology. Promising devices are EMCCDs, where an electron multiplier (EM) register is used to amplify the single photon signal. Here, typical noise sources can be overcome to a great extent but still affect the detection of very low light levels (Tulloch and Dhillon, 2010). The EMCCD technology has recently been adopted in an experiment where single photons emitted by an atom cloud were detected (Bücker *et al.*, 2009).

In our experiment we use a different approach. We place a light intensifier before the CCD camera (ICCD). This largely intensifies single photon events above all CCD noise levels. The intensifier can additionally be used as a fast and efficient shutter and allows very short exposure times. Its disadvantages lie in the low quantum efficiency that is usually less than the one of EMCCDs as well as the rather high noise generation. Here, we describe the characterization of our light intensifier, which is necessary for a reliable use in practice as well as for understanding our atomic fluorescence signals. First, we study its single-photon response and will later focus on the use with higher light intensities.

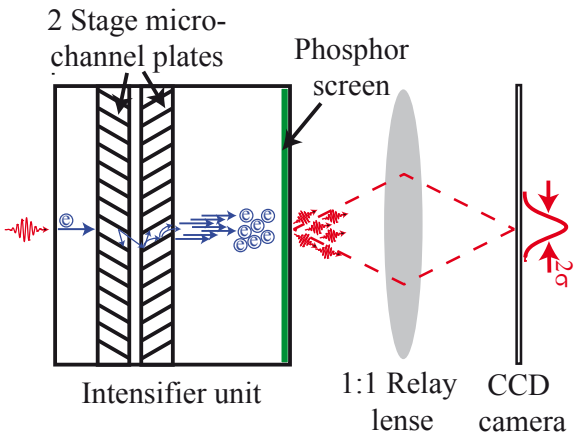

Figure 4.1: Experimental ICCD setup. Photons arriving on the intensifier unit are converted into electrons, which are accelerated towards a double stage microchannel plate. Inside the plate avalanche electron multiplication occurs. The electrons are then accelerated towards a phosphor screen. The phosphor screen is imaged with a 1:1 relay lens onto the CCD camera. The photons coming from the phosphor screen create a spot with a Gaussian profile on the CCD camera.

We inform the reader that this chapter is very technical and relies on many ideas developed for astronomical applications.

4.1 Résumé

Notre système d'imagerie utilise une caméra CCD et un intensificateur de lumière qui a une sensibilité au niveau du photon unique, et permet d'amplifier le rapport signal sur bruit. Nous présentons une analyse de notre système d'imagerie qui servira de calibration pour les expériences effectuées dans ce travail de thèse. Ce chapitre présente un algorithme permettant de compter les événements photoniques détectés sur la caméra CCD. Il présente également la mesure et la compréhension théorique de la réponse de l'intensificateur, notamment son efficacité quantique et sa linéarité.

4.2 ICCD Setup

The ICCD setup is briefly shown in Fig. 4.1. It consists of a light intensifier (Hamamatsu C9016-22) used to amplify single photon events above the noise sources of our CCD camera (Princeton Instruments, Pixis 1024, 16bit, 13 μm pixel size). The CCD noise can be assumed to be white and mainly due to the read-out process (see Fig. 4.2). All other noise sources such as clock induced charges are assumed to be much smaller than the read-out noise and contribute a small fraction to the measured value[1] $\sigma_{RO} = 6$ adu/pixel. The dark current noise can be neglected by operating the CCD chip at[2] $-70°$C. Photons arriving onto the input window of the intensifier are converted into electrons that are accelerated towards a double stage microchannel plate where they create avalanche electrons. Leaving the microchannel plates the electron avalanches are further accelerated onto a phosphor screen where they pro-

[1] 1 adu (analog-to-digital unit) corresponds to the digitization step of the analog signal acquired by the CCD camera. For all measurements the electron-to-adu conversion factor is 1 e^-/adu.

[2] The dark count of the CCD being ~ 0.001 adu/pixel/s is negligible for the parameters of our experiments. The CCD camera does however have a constant dark current offset of some hundreds of adu depending on several aspects such as the exposure time and the size of the readout region.

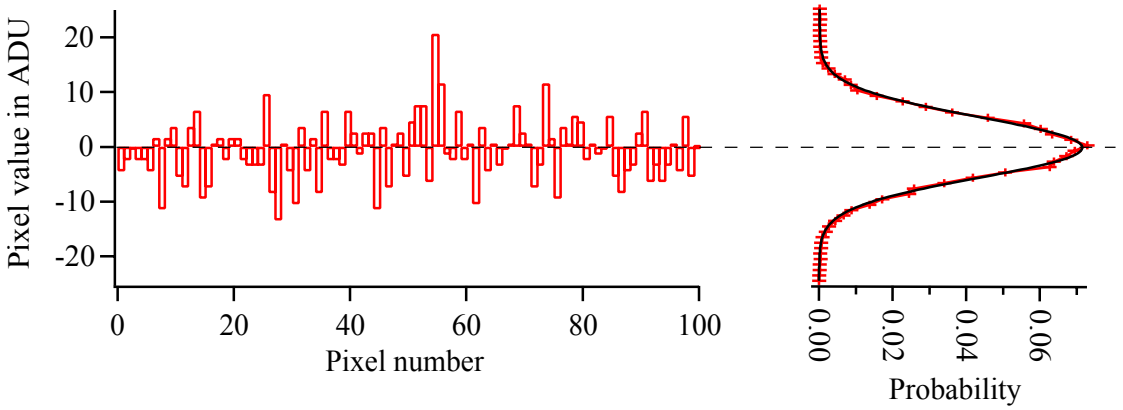

Figure 4.2: CCD noise characteristics. Cross-section through a CCD image of 100 × 100 pixels without any incoming photon event. The noise distribution has a Gaussian shape with a rms width of 5.6 adu. It comprises clock induced charges as well as read-out noise. A constant dark current offset of 622 adu has been subtracted.

duce a shower of photons. The phosphor screen is imaged with a 1 : 1 magnification onto the CCD camera using a relay lens (Nikon A4539). The acceleration gain voltage applied between the input window and the microchannel plates can be varied linearly from 1000 to 1800 V to increase the light amplification by turning a potentiometer. The gain voltage can also be reversed to inhibit electron multiplication. We refer to the gain as it was set on the potentiometer, 0 corresponding to 1000 V and 10 to 1800 V, respectively[3].

We operate the intensifier in a gated mode where it is possible to reverse the internal gain voltage by applying a standard TTL trigger pulse. With no trigger applied, the gain voltage stays in reverse and the intensifier inhibits avalanche creation. It thus prevents photons from falling onto the CCD chip. Applying a trigger pulse switches the internal voltage and enables electron multiplication. Hence, the intensifier can not only serve as a photon multiplicator but also as a fast switch as the voltage can be quickly reversed within 5 ns to disable photon multiplication with a repetition rate of 20 kHz.

Here, we focus on analyzing the photon amplification characteristics of the intensifier at a single photon level. To detect some well-separated single photon spots on the CCD camera we open the intensifier for a time of 1 ms. The intensifier is exposed to a dim light of a 780 nm laser source, which power can be varied to adjust the average number of incoming photons on the CCD camera. The background light level is held much smaller than the laser light so that spurious photon events are negligible. The image size of the CCD camera is fixed to ROI = 300 × 300 pixels over which the illumination is homogeneous. Each time the intensifier is switched off we subsequently read out the CCD camera and obtain one image. We repeat the sequence to obtain some hundred images in order to have sufficient statistics. A typical image for gain

[3]The intensifier is in use for about four years at the time of this analysis. We do not exclude that the measured values are subject to variations with age.

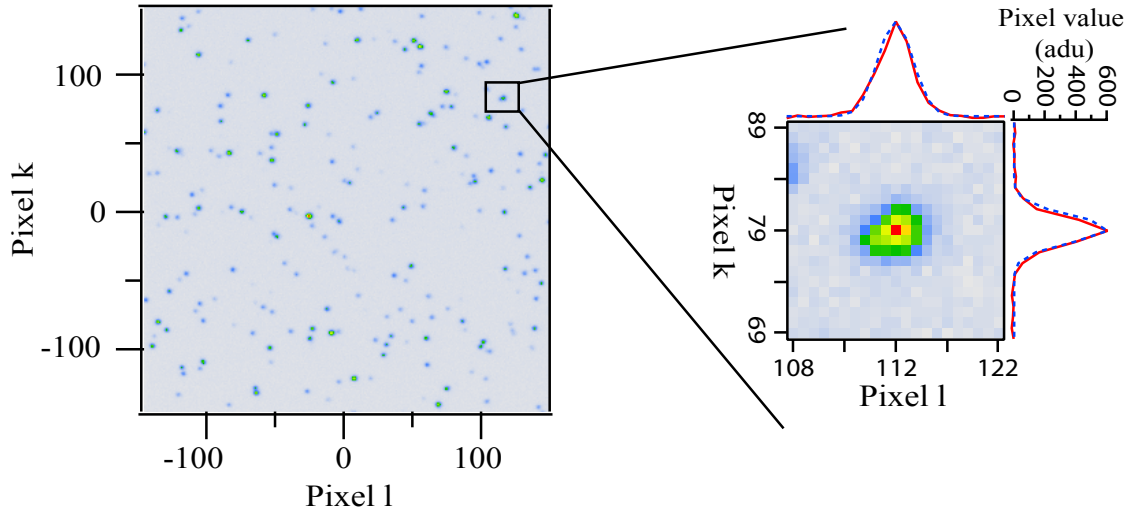

Figure 4.3: Image showing photon events for a gain of 8. A typical image showing photon events for a gain 8. The region of interest corresponding to the image size is ROI = 300×300 pixels. The average number of events per image is $\bar{N}_{\text{events}} \sim 240$. Looking at the cross-sections of one event we see that the event is well fitted by a Gaussian function (blue dashed line) with a rms width of $\sigma = 1.2 \pm 0.2$ pixel.

8 is shown in Fig. 4.3 for which we detect ~ 250 events per image on average. Each event consists of a photon shower coming from the phosphor screen and imaged onto the CCD camera. We want to characterize the shower of photons, in particular its distribution in space and height. To do so we use the following counting algorithm.

4.3 Counting algorithm

To only count real photon events we set a counting threshold of $\epsilon = 6\sigma_{RO} = 36$ adu/pixel. All peaks under this threshold cannot be assured to be real events but can also be due to read-out noise for example. So we only restrict the analysis to events higher than this threshold. We first look at the spatial distribution and discuss the amplitude distribution in Sec. 4.4. Analyzing several hundreds of distinct isolated events above the counting threshold ε, we find that the spot on the CCD and associated with a detected photon, the point spread function (PSF), agrees very well with a Gaussian distribution $H_{k_0,l_0} G(k-k_0, l-l_0) + const$ with H_{k_0,l_0} the height of the center pixel fit and $G(k,l) = \exp\left(-\frac{k^2+l^2}{2\sigma^2}\right)$ a Gaussian shape function (see Fig. 4.3). We measure an average rms width $\sigma = 1.2 \pm 0.2$ pixel which does not significantly depend on the gain (see Tab. 4.1). All events show a small asymmetry between the k and l dimension of ~ 8 %. Note also that by imaging a sharp edge onto the intensifier we find that the rms width of the effective PSF of 1.9 ± 0.3 pixel is larger than the single event PSF by ~ 50 % (see Sec. 4.6).

To measure the amplitude distribution we count all events per image and save

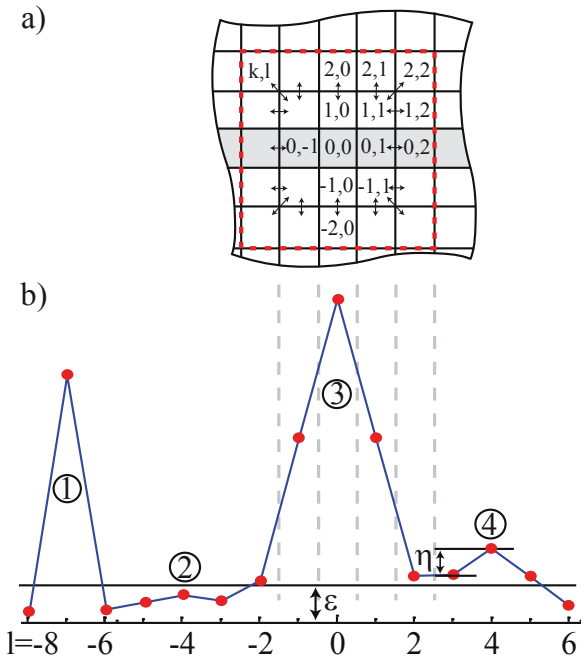

Figure 4.4: Counting procedure. In part a) we illustrate a section of the CCD array centered around one photon event at $(k_0, l_0) = (0, 0)$. The arrows indicate some pairs of pixels that are compared in the counting algorithm to erase this photon event in order to avoid its double counting. The dashed red line indicates a possible EROI region (see text) with $d = 2$ around the center peak. Part b) shows a one-dimensional cut in the $k = 0$ plane (highlighted in gray in part a)). Going away from the center peak ③, the values will decrease unless another peak ④ is present. All peaks like ② below the counting threshold $\varepsilon = 6\sigma_{RO}$ are not counted. False events such as ① can be filtered using the "sharp" value (see text).

the information on their amplitude. To avoid a bias in the overall result we need to make sure that no event is counted more than once. We use the following counting algorithm to avoid double counting:

1. Search for the pixel with the highest adu value on the CCD camera. If there is a pixel higher than the counting threshold ε, it represents the center of a photon event (Pixel (0,0) in Fig. 4.4 a) corresponding to ③ in Fig. 4.4 b)). Otherwise no further events are detected and the search is finished. Events such as ② are below the threshold and are not counted.

2. To avoid double counting, pixels that belong to the same event need to be put to zero (or below the counting threshold ε). To do so we define an event region of interest (EROI), i.e. a square region around the center of an event with side length $2d + 1$ pixel (d depends on the gain and is calibrated below. Its value is given in Tab. 4.1). We now apply the following procedure to decide if a pixel belongs to an event: Moving away from the center pixel we always compare pairs of pixels indicated by the arrows in Fig. 4.4 a) and set the value of the outer pixel to zero if its value is not higher than the inner one. A higher value of the outer pixel is usually a signature of another event so that it cannot be put to zero a priori. We illustrate these steps by looking on a section of a CCD chip with some photon events. Let us focus on the pixel row $k = 0$ in Fig. 4.4 a) which cut is shown in part b). We set pixel (0,1) to zero (or below ε) since it is necessarily smaller than the center peak (0,0) and move one pixel further out. Pixel (0,2) can also be put to zero since it is smaller than pixel (0,1). The situation changes on pixel (0,4) which is higher than (0,3) by an amount of η. Pixel (0,4) is therefore not set to zero and is counted as a new event in the next

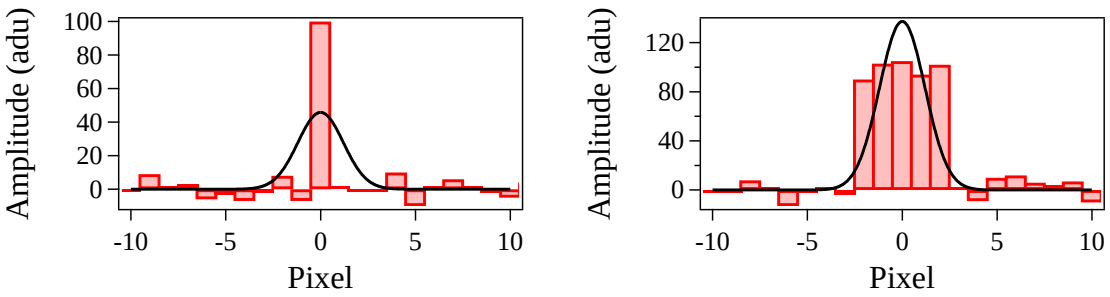

Figure 4.5: Example of non-Gaussian events. *left*) A Gaussian fit (with fixed rms width $\sigma = 1.2$ pixel) of a thin event yields a lower peak height $H_{0,0}$ than the real pixel value $H_{k_0,l_0} < D(k_0, l_0)$. For such peaks the "sharp" value is usually greater than one. *right*) A small "sharp" value $0 \lesssim$"sharp"$\ll 1$ can be found for events that are somewhat broader than the Gaussian function.

search. The number of pixels d we need to move outward from the center peak in each direction depends on the gain and is given in Tab. 4.1.

3. Start again at step one.

Having found a set of possible photon events by using the counting algorithm we make further use of a procedure developed in astronomy to filter out false photon events (Stetson, 1987; Hroch, 1999). The filtering relies on the assumption that possible false photon events will deviate from the symmetric Gaussian shape measured above. Figure 4.5 shows how false events could look like and that a Gaussian fit does not reproduce the shape of the event.

In order to measure the deviation from a Gaussian fit, we first estimate the amplitude H_{k_0,l_0} of each found event. One could do so by fitting a Gaussian function to the event to extract the height. This however can be a time-consuming task when dealing with many thousand events. But even if no fitting procedure is applied one can still estimate the height very fast by the method of linear least squares (Stetson, 1987)

$$H_{k_0,l_0} = \frac{\sum_{k,l=-u}^{u} G(k,l)D(k_0+k,l_0+l) - \frac{1}{n}\sum_{k,l=-u}^{u} G(k,l)\sum_{k,l=-u}^{u} D(k_0+k,l_0+l)}{\sum_{k,l=-u}^{u} G(k,l)^2 - (\sum_{k,l=-u}^{u} G(k,l))^2/n} , \tag{4.1}$$

where $D(k,l)$ is the actual value of pixel (k,l) and $G(k,l)$ the Gaussian function. Each sum $\sum_{k,l=-u}^{u}$ is evaluated over a square with side length $2u+1$ pixel and centered around the event peak center (k_0, l_0). The number of total pixels inside this square is denoted as $n = (2u+1)^2$. Next, we calculate the difference between the value of the center pixel $D(k_0, l_0)$ and the average value of all surrounding pixels in the square

$$I_0 = D(k_0,l_0) - (\sum_{k,l=-u}^{u} D(k_0+k,l_0+l) - D(k_0,l_0))/((2u+1)^2-1) . \tag{4.2}$$

The so called "sharp" value is defined as "sharp"$= I_0/H_{k_0,l_0}$ and can be used to characterize the deviation of events from a Gaussian shape. For events that are thinner than the typical Gaussian intensifier response with rms width $\sigma = 1.2$ pixel (see left graph in Fig. 4.5 or event ① in Fig. 4.4 b)) we find $I_0 \sim D(k_0, l_0)$ since the surrounding pixels have small values. The estimated height H_{k_0,l_0} is smaller than the center pixel value $H_{k_0,l_0} < D(k_0, l_0)$ so that the "sharp" value takes on values above one ("sharp"$\gtrsim 1$). For larger events (see right graph in Fig. 4.5) on the other hand it takes on values close to zero ($0 \lesssim$"sharp"$\ll 1$) (Hroch, 1999). The acceptance range for the "sharp" values for which an event is declared a false event is discussed below.

Another quantity to rule out false events is based on the measurement of their symmetry. If an event is asymmetric above a certain degree we say that it is not a real photon event. To measure the symmetry of an event we calculate the so-called "round" value "round"$= 2\frac{h_y - h_x}{h_y + h_x}$. Here, h_x, h_y are calculated the same way as H_{k_0,l_0} but by using one-dimensional Gaussian distributions $\exp\left(-\frac{k^2}{2\sigma^2}\right)$ and $\exp\left(-\frac{l^2}{2\sigma^2}\right)$ for G in Eq. 4.1. The parameter gives an intuition about the symmetry of the event. Totally symmetric events have "round"$= 0$. The more asymmetric the event the higher the absolute value of the "round" value. For Gaussian events the "round" value lies in the interval between -2 and 2. The highest possible asymmetry of a Gaussian event is indicated by "round"$= \pm 2$. A criteria for which degree of asymmetry an event should be considered a false event is given below.

Counting algorithm calibration

For a calibration of the counting algorithm we need to set the most efficient values for d, u and the acceptance ranges of the "sharp" and "round" values for which an event is declared to be a true one. In the following we categorize all events found by the algorithm described above into three groups:

- **Group 1.** The first group consists of all counted events. With a certain probability some of these events are false events and need to be distinguished from real ones.
- **Group 2.** A first filtering can be done by using the "sharp" and "round" values. All events that survive the filtering process make up the second group of events.
- **Group 3.** A difficulty arises in crowded images, in which some events can overlap. Here, one peak can have several neighbors that can affect the calculation of the "sharp" and "round" values. We build up a third group of events namely those that do not have any neighbors inside a certain area around their center. We choose this area to be the EROI (see below).

We experimentally evaluate the size of the EROI ($(2d+1)^2$) in order to fully erase every event in each direction. We analyze the same set of images several times for increasing d and look at all counted events. For e.g. $d = 0$ only the center part of an event is erased and the surrounding is then counted as other additional events. For increasing d more and more of the event is being erased and less counts are being

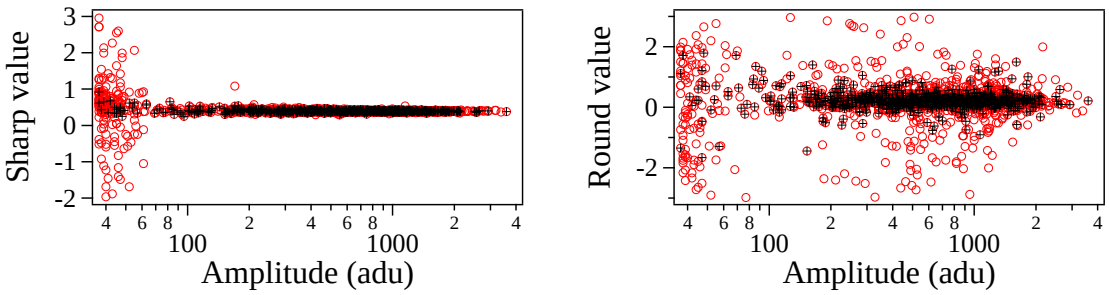

Figure 4.6: "Sharp" and "round" values for gain 9. *left*) We plot the dependence of the "sharp" parameter on the peak amplitude, where we use an area of 3×3 ($u = 1$) pixels around the peak center for the calculation. Isolated events are highlighted as red crosses. *right*) We show the same for the "round" parameter using a 7×7 ($u = 3$) pixels around the peak center.

registered. Tab. 4.1 shows the value of d for which no new counts are registered ensuring that each event is fully erased. Double counting of the same event can thus be avoided. In the algorithm presented here the value of d is fixed for each gain and used for all events.

We now use all events (group 1) and all isolated events (group 3), those with no neighbor inside the EROI, to set the acceptance sets for the "sharp" and "round" values and the conditions for u. Let us begin by looking how the values depend on the amplitude of the events. Fig. 4.6 shows this dependence using for the "sharp" value $u = 1$ i.e. a square of 3×3 pixels around each center pixel k_0, l_0 and for the "round" value $u = 3$. We observe that the values obtained for isolated events (black crosses) spread much less than when using all events (red circles), in particular for small peak heights. As we will see in the next section these small peaks accumulate around bigger events and are false events not originating from real photons. If we assume that all isolated events stem from real photons which we do not want to filter we can set the "sharp" and "round" conditions by minimizing the number of filtered isolated events (group 3) while maximizing the number of filtered events taking all events into account (group 1). Doing so we find optimized values for declaring an event false if "sharp" < 0.2 or "sharp" > 1 keeping $u = 1$ and "round" < -1.5 or "round" > 1.5 keeping $u = 3$.

Isolated events (black crosses) fulfill the "sharp" and "round" conditions ~ 98 % of the time. This also supports the assumption of a Gaussian event shape of the intensifier response that was checked by fitting isolated events with Gaussian distributions as described above. Taking all events (red circles) we filter $\sim (9, 11, 12, 18)$ % for gains of $(6, 7, 8, 9)$, respectively, namely those events whose "sharp" or "round" value (or both of them) exceeds the tolerance boundaries indicating that their shape deviates from a Gaussian. Note that the "sharp" value can become negative and the "round" value can pass its boundaries "round" < -2 or "round" > 2. This is only compatible with negative estimated heights which can occur when small events lie very close to bigger ones. As we will see these small events need to be filtered which can efficiently be done using the "sharp" and "round" values.

Gain	σ_x, σ_y/pixel	d/pixel	g/adu	Δg/adu	κ/%
6	$1.3 \pm 0.2, 1.2 \pm 0.1$	3	40 ± 0.1	40	60 ± 0.2
7	$1.3 \pm 0.1, 1.2 \pm 0.2$	4	136 ± 0.4	136	23 ± 0.1
8	$1.3 \pm 0.2, 1.2 \pm 0.2$	5	369 ± 25	265	6.5 ± 0.7
9	$1.3 \pm 0.2, 1.2 \pm 0.3$	6	822 ± 45	560	1.8 ± 0.3

Table 4.1: Intensifier characteristics. The table summarizes the typical characteristics of the intensifier unit. The photon events with rms widths σ_x, σ_y are totally erased by setting the values of all pixels within a square of side length $2d+1$ pixels centered around the center pixel to zero. The average g and the standard deviation Δg of the event distribution increases with intensifier gain. This decreases the probability κ for photon events to be below the counting threshold $\varepsilon = 6\sigma_{RO} = 36$ adu/pixel.

The advantage of this algorithm is that it is easily implemented and fast in analyzing images since no elaborated fitting procedures with several fit parameters are involved. Information such as the number of events, their positions and their amplitudes are quickly obtained. It works very well for images with a constant background on which the nearly Gaussian events are fairly well separated[4]. For the images used for this characterization this is given as we use images for which the probability of having two events within a radius of 2σ is estimated to be much below 1 %. This estimation relies on a calculation of the density of events $\rho_{\text{events}} = \pi(2\sigma)^2 \bar{N}_{\text{events}}/\text{ROI}$ per image. ρ^2_{events} is an estimator of the probability for two events to overlap in a region of 2σ. We verified our results with a second algorithm, where the images are pre-processed by convolution with the PSF as proposed in the DAOPHOT algorithm (Stetson, 1987). We essentially obtain the same results mostly due to the fact that the PSF can be well described by a Gaussian distribution and the images are not crowded.

There are several drawbacks to our algorithm. It is not capable to distinguish between events that are separated by less than 2σ. Additionally, all events inside the EROI of other bigger events that do not clearly rise in the wings of the bigger event are missed. Erasing pixels belonging to an event is done by comparing only two pixels each time. This can be problematic for small peak heights since here the result can be affected by the readout noise. Furthermore, for a given gain, the EROI is held fixed for all events in the image. Ideally it should be adapted to each individual event as their height and therefore the number of pixels belonging to the event vary.

4.4 Response distribution

We now discuss the characterization of the event height distribution. To model the probability to detect an event with a certain height we use the model developed by Matsuo et.al. (Matsuo, Teich, and Saleh, 1985) for electron multiplication processes[5].

[4] If this is not the case the much more complex DAOPHOT algorithm commonly used in astronomical application could be used instead Stetson (1987)

[5] Knowing that the events are of Gaussian shape and having measured the average width we could also infer the volume of the events instead. We verified that there exists no specific correlations

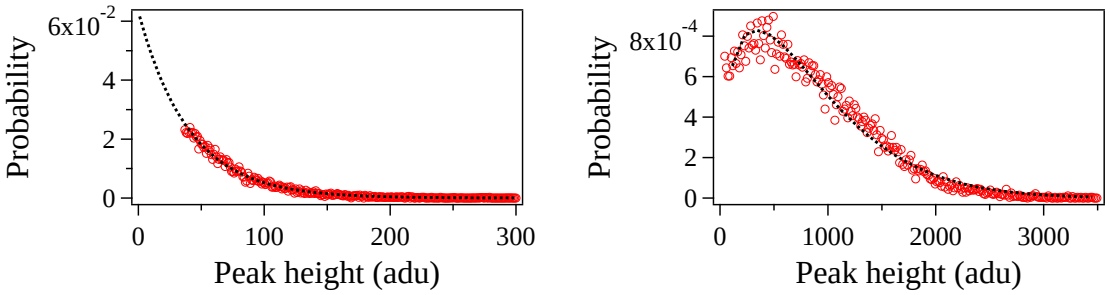

Figure 4.7: Peak histogram for gain 6 and 9. Amplitude distributions for a gain of *left*) 6 and *right*) 9 for isolated events (group 3). The data for gain 9 is binned by 15. The black line corresponds to the theoretical prediction. All events smaller than the threshold ε are not counted.

Ideally every photon impinging on the intensifier creates one electron. Each electron is accelerated and creates secondary electrons which themselves create other electrons leading to an avalanche. Working at low light levels for single photon sensitive measurements we assume these avalanches to be well separated and thus independent of each other. Each electron has a chance P of creating a secondary electron when colliding with the walls of the intensifier microchannel plate. As this probability depends on the electron's velocity it can be varied by setting the electron acceleration in form of the intensifier gain voltage. Assuming that the electron undergoes r collisions, one can derive a recursive set of equations describing the probability $p(x)$ of having a certain number of electrons x at the end of the avalanche process

$$\begin{aligned} p_r(x) &= (1-P)p_{r-1}(x) + \\ &\qquad P\sum_{k=0}^{x} p_{r-1}(x-k)p_{r-1}(k), \quad x, r \geq 1 \\ p_r(0) &= 0, \quad r \geq 1 \\ p_0(x) &= \delta_{1,x} \ . \end{aligned} \tag{4.3}$$

The last line states that the probability for one electron to exit the multiplication stage is one if no collision with the walls occurs[6]. For small probabilities P and high number of collisions r the result of the recursive algorithm can be approximated by an exponential function (Basden, Haniff, and Mackay, 2003)

$$p(x) = g^{-1}\exp(g^{-1}x) \ . \tag{4.4}$$

Here, $g = \langle x \rangle = (1+P)^r$ is the average and also the standard deviation $\Delta g = g$ of the amplitude distribution. We will describe the actual observed event height distribution on the CCD with the electron distribution $p(x)$ leaving the microchannel plates. Both are proportional but not identical for two reasons. First, the phosphor screen transforming electrons into photons is not 100 % efficient but it can be assumed to

between width and amplitude that could bias the volume calculation in such a case.

[6]We neglect the fact of any electron absorption by the walls.

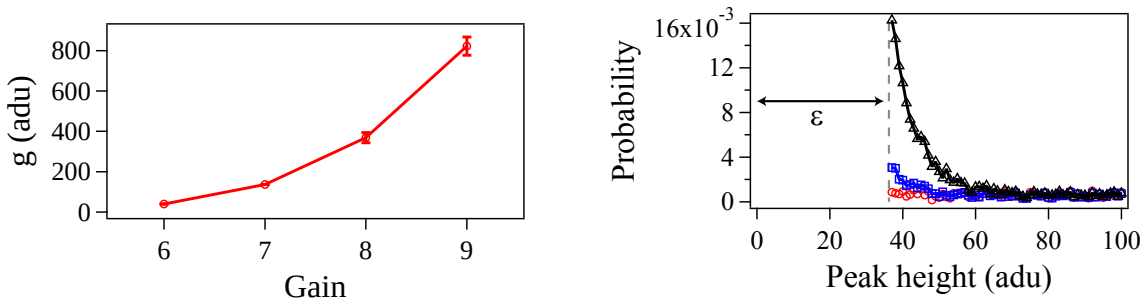

Figure 4.8: Intensifier gain and beginning of histograms for gain 9. *left*) g is plotted for different intensifier gains. The intensifier response is clearly nonlinear. *right*) Initial part of the events histogram for gain 9 in Fig. 4.7. We compare the distributions for isolated (red circles), post-selected (blue squares) and all (black triangles) events for small amplitudes.

be linear for small light intensities (compare Sec. 4.6). Further, the total photon number leaving the phosphor screen is a factor $0.9^{-1} \sim 1.1$ higher than observed on the CCD, since the CCD quantum efficiency over the band of wavelengths emitted by the phosphor screen around 550 nm is about 90 %.

Fig. 4.7 shows the measured normalized event amplitude distribution for gains 6 and 9, respectively. Not to be biased by neighbors, only isolated events from group 3 have been considered for these data. For a gain of 6 the exponential law of Eq. 4.4 fits the data very well. Here, the probability to produce a secondary electron can safely be assumed to be small so that Eq. 4.4 works well. For a gain of 9, the distribution clearly differs from an exponential law. Here, the probability P for second electron generation cannot be assumed to be small any more. We therefore have to use the recursive algorithm to model the data. Being limited by computational power we run the algorithm for a number of $r = 9$ collisions. Even for $P = 1$ this could simulate the data only up to peak heights of $x \leq 2^r = 512$. In order to compare the theory to the data which go up to $x \sim 3000$ for a gain of 9, we scale the theoretical result to higher x. The multiplication factor g is inversely proportional to x for small gains as is directly seen on Eq. 4.4. We assume that this is still true for slightly higher multiplication factors. We find qualitative good agreement between the data and the theory.

For higher gains, where the exponential fit does not work, we extract the mean value of the amplitude distribution by using $g = \langle x \rangle = \sum xp(x)$ and its variance by using $\Delta g^2 = \sum x^2 p(x) - \langle x \rangle^2$ (see Tab. 4.1). The photon multiplication behaves nonlinearly with the applied gain as can be seen on the left of Fig. 4.8. For a gain of 6 for example we find a multiplication factor of 40 ± 0.1, which is enough to enhance the single photon signal above the CCD noise. The Fano-factor $\Delta g^2/g$ ($= 1$ for a Poisson distribution) stays largely above one for all gains and emphasizes a super-Poissonian characteristic. Due to the limited intensifier amplification a percentage of photon events κ listed in Tab. 4.1 stays below the counting threshold ϵ and leads to an underestimation of photon counts. The percentage of missed events decreases with increasing gain.

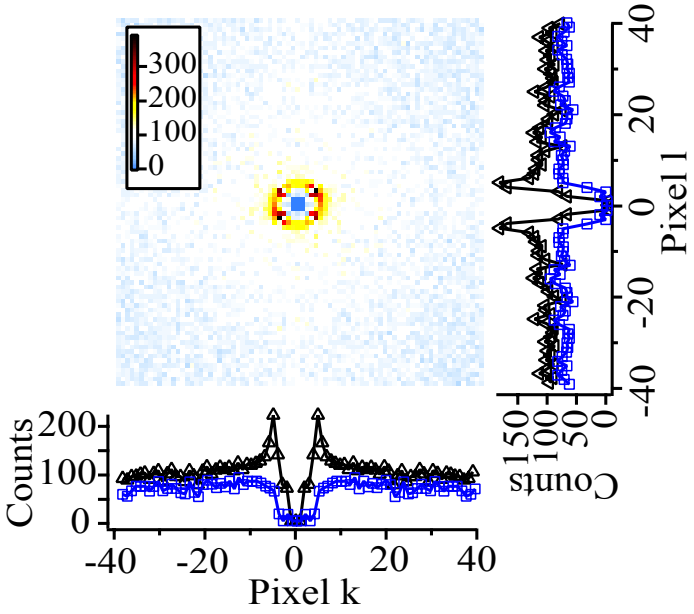

Figure 4.9: Position correlation function. The image shows the center part of the position correlation function $G_2(k,l)$ when all photon events are counted. Cross-sections through the center are plotted on each side (black triangles). By using the "sharp" and "round" values we can efficiently filter out false events. The position correlation function becomes more homogeneous, as shown on the cross-sections (blue squares). $G_2(k,l)=0$ for $|k|,|l|<2\sigma$ since the algorithm cannot distinguish between two or more events in this region.

So far we focused on isolated events only. Our images are not crowded so that the amplitude distribution analysis of all events from group 1 should be essentially the same. As can be seen on the right of Fig. 4.8, this is not entirely true and a clear discrepancy is visible for small peak heights. There seems to be many more small events when taking into account all events (black triangles) than after counting isolated events (red circles) only. To find out where these small events stem from, we take a look at the spatial distribution of all events on the CCD. Fig. 4.9 shows the $G_2(k,l)=\sum_{i,j,i\neq j}\delta(k-(k_{0,i}-k_{0,j}))\delta(l-(l_{0,i}-l_{0,j}))$ position correlation function, where each index of the sum i,j goes over all events with their center position $k_{0,i/j},l_{0,i/j}$. Although the illumination can be assumed homogeneous over the intensifier region, we see that the events tend to accumulate (black triangles in cross sections of Fig. 4.9). Analyzing the accumulation of peaks we find that small events have a tendency to lie close to bigger ones. We attribute this behavior partially to the nature of our counting algorithm as well as to the structure of the microchannel plates where avalanches have a finite probability of separating themselves into side avalanches. These side avalanches are not necessarily Gaussian. In fact, by using the post-selection via the "sharp" and "round" values, we efficiently filter out these false events (group 2) as indicated by the blue squares in the cross-sections. This is also visible in the distribution of filtered events (blue squares) in Fig. 4.7. The number of small events is significantly reduced using the filtering procedure. However, there remains some false events that have a Gaussian shape comparable to the one of real events and seem to be indistinguishable from them. They lead to an overestimation of the real number of photon events by <1 %. It can be estimated by comparing the number of counted neighbors with the theoretical number obtained by evaluating the probability to have two or more events inside the same EROI.

4.5 Intensifier noise

Auto-generated events are a considerable source noise. While there are essentially no events on our timescales (several minutes) when the intensifier is closed and the internal electron-acceleration voltage is in reverse the situation changes when we open the intensifier. Here, we can distinguish between two operating regimes. The first regime is a static regime where the intensifier is opened once for a certain time during which impinging photons can be multiplied. Even if there is no light falling onto the intensifier[7], there are some photon events auto-generated by the intensifier. We open the intensifier for 2 min after which many such auto-generated events form a uniform background on the CCD camera. We then read out the CCD and find an auto-generation rate of $R_{auto} = (8, 29, 87, 243)$ adu/pixel/s for gains of $(6, 7, 8, 9)$, respectively[8]. Knowing the average height g of a photon event we can infer the number of photon events auto-generated to be $R_{auto}/g = (0.2, 0.2, 0.24, 0.3)$ events/pixel/s for gains of $(6, 7, 8, 9)$, respectively.

The second regime is the dynamic regime where we open the intensifier 60000 times for 1 ms during a total of 2 min. We measure the same noise generation rate as found in the static regime. However, we find an increase of the noise generation in the dynamic regime when the time interval during which the intensifier is switched off is much larger than 1 ms. This has for example been observed in the experiment presented in Ch. 8. In that experiment we detect 84 events on the CCD (ROI = 100×100 pixel) when the intensifier at gain 9 is opened for 20 μs and the sequence is repeated 200 times at a rate of around 1 Hz (see Sec. 8.3.4). This translates in a noise generation of 2.1 events/pixel/s, a factor ~ 7 higher than the static noise generation. The noise generation is therefore mainly due to a dynamic effect such as the voltage reversing process for example.

We end this section with two remarks. First, we find that the auto-generated events are indistinguishable from real events and the response histogram containing only auto-generated events does not significantly deviate from the histogram when real photons are impinging on the intensifier. Post-selection is therefore no considerable option. However, to obtain the average real number of photon events in counting experiments one can independently measure these auto-generated events by taking a background image. Subsequently, one subtracts the average number of auto-generated events from the average number of all events. Second, we measured the auto-generation rates in the morning, after the intensifier has been switched off over night, and in the evening having used the intensifier for measurements during the day. We find a decrease in the noise level during typical days of ~ 10 % due to gain ageing of the microchannel plates.

Signal-to-noise ratio in single-photon mode

The amplification of single photon events above the CCD read-out noise leads to an increase of the signal-to-noise ratio (SNR) compared to using a CCD camera only.

[7] We cover the front of the intensifier with a black cap to avoid any light falling onto the cathode.
[8] Here, we assume the static noise generation rate to be constant in time.

We define for the single-photon counting mode

$$\mathrm{SNR_{SP}} = \frac{\#N}{\#B} \ , \tag{4.5}$$

where $\#N$ is the number of photon events detected on the CCD and having come from the observed scatterer and $\#B$ takes into account the number of background events visible on the CCD. Background events originate e.g. from intensifier auto-generated events or photons coming from some background light and not from the observed scatterer. More sophisticated SNR can be used (Tulloch and Dhillon, 2010; Tubbs, 2003) but here the essential is captured by this simple formula.

If we use only a CCD camera we will not be able to observe any individual single photon event due to the read-out noise of the camera exceeding the photon response. This means that $\#N = 0$ and $\mathrm{SNR_{SP}} = 0$ for CCDs. Using the intensifier on the other hand we can observe single photon events on the CCD camera and the gain in SNR, nomatter what the background level $\#B$, is infinite with respect to the case where only the CCD camera has been used. Besides, the intensifier acts as an efficient shutter which is the second reason why we use the light intensifier. For example, measuring the atom number distribution inside the dipole trap (see Ch. 8) would have been impossible without the use of the intensifier.

4.6 Multiphoton detection

So far we focused on the photon amplification characteristics of the intensifier at the single-photon level. Nonlinear effects of the intensifier are negligible in this regime. We now turn to the case of the multiphoton response.

Intensifier quantum efficiency

For convenience we use the laser beam at 780 nm coupled into the trap laser fiber as shown on the left in Fig. 4.10. A small part of the laser beam (~ 10 %) is reflected by the dichroic mirror and passes the aspheric lenses. After the vacuum chamber the beam is retro-reflected and returns into the chamber. It again passes the two lenses and the dichroic mirror before it reaches the intensifier. The laser beam has a waist of $15.2 \pm 3\mu$m at the entrance of the intensifier. We open the intensifier for $\tau = 2$ μs and subsequently read out the CCD camera once. We vary the power of the laser beam $\mathrm{P_L}$ and evaluate the number of photons received by the CCD camera knowing that each integrated photon event contains $2\pi\sigma_x\sigma_y g \sim 8 \pm 3 \cdot 10^3$ adu·pixel^2 for gain 9, as mentioned above. The right side of Fig. 4.10 shows the detected photons as a function of the total incident photon number, which is calculated via $N_{in} = \mathrm{P_L}\tau/h\nu$. The quantum efficiency of the intensifier is evaluated from the slope of the linear dependence to be 10 ± 1 % at 780 nm.

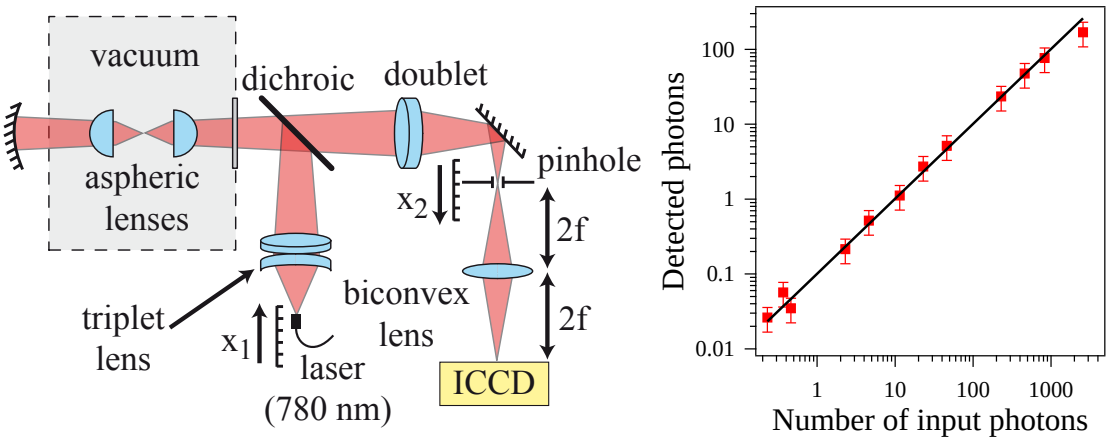

Figure 4.10: Intensifier efficiency and nonlinearity. *left*) Setup for the determination of the intensifier efficiency and its nonlinearity. The laser beam at 780 nm is retro reflected after it passed through the two aspherical lenses, and is then directed towards the intensifier. *right*) Dependence of the number of detected photons by the CCD camera versus the number of photons impinging onto the intensifier. The intensifier quantum efficiency corresponds to the slope and is equal to 10 ± 1 %.

Intensifier nonlinearity

The last data point at 2600 incident photons corresponding to $\sim$330 pW however starts to deviate slightly from the linear behavior and indicates the onset of nonlinearity. We want to have a clearer signature of the nonlinearity. To do so, we change the position of the laser fiber coupler x_1 and thus the laser beam rms width incident on the intensifier. This way we vary the light intensity on the intensifier whilst keeping the laser power constant. For incident photon fluxes below the nonlinearity threshold (28 and 280 photons during 2 μs), we observe no change in the total detected power indicating that the intensifier is linear in this regime (see left side in Fig. 4.11). When increasing the intensity above the threshold we reach the nonlinear regime where we see a drop in the detected power when the beam is maximally focused. The laser beam waist at the intensifier is shown on the right side in Fig. 4.11. The dashed line is a guide to the eye and is used to estimate the axial magnification g_x between the fiber and the aspheric lens. Assuming a perfect symmetric system we find $g_x^{-2} = 4.5 \pm 0.3$, which is compatible with the result in Sec. 3.3.5. Our imaging system does not allow to reduce the rms width of the laser incident onto the intensifier to less than $15.2 \pm 3\mu$m. Taking 330 pW for the nonlinearity threshold we find a threshold intensity of 0.23 ± 0.04 W/m^2 at 780 nm. To estimate how many atoms can be imaged onto the ICCD without being in the nonlinear regime we assume the trapped atoms to scatter at $\Gamma/2$ and estimated the detection efficiency up to the intensifier to be 2 % (Sec. 3.3.5). For probe pulses with a duration 2 μs, the nonlinear behavior (2600 photons on a surface smaller than the resolution limit of our imaging system) becomes important for 3400 atoms in the trap. We usually work with atom

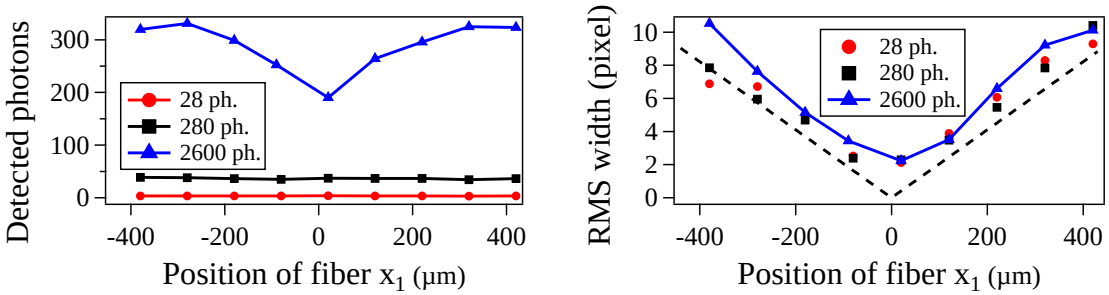

Figure 4.11: Intensifier nonlinearity. *left*) Dependence of the detected power on the CCD camera versus the laser fiber coupler position x_1 for three different incident photon number of 28, 280 and 2600 photons during 2 μs. *right*) Laser beam waist as it appears on the CCD camera versus the fiber coupler position. The dashed line corresponds to the expected defocus.

numbers smaller than 3000 so that the nonlinearity does not play a role[9].

Intensifier effective PSF

We saw that the PSF of single events has a Gaussian shape with rms width of around 1.3 pixel. In the multi photon case we measure the PSF by imaging the sharp edge of a pinhole onto the intensifier using the light of the MOT as a uniform illumination source at 780 nm. The cross-section of the pinhole in the object plane is illustrated on the left of Fig. 4.12. A fit of the edge to the erf-function yields the rms width of the effective PSF. The imaged pinhole has a radius of ~ 50 pixels corresponding to $50 \cdot 13 = 650$ μm and is placed on axis[10]. When moving the pinhole out of the object plane ($x_2 = 0$) the edge smears out as can be seen on the right of Fig. 4.12. A parabolic fit yields the minimum resolution of the intensifier 1.9 ± 0.3 pixel. This rms width of the effective PSF of 1.9 ± 0.3 pixel exceeds the PSF of a single event ~ 1.3 pixel. The increase in the PSF for multiphoton illumination indicates that consecutive photons arriving on the exact same spot on the intensifier can be slightly deviated by the microchannel plate structure, maybe due to high voltage fluctuations. This also leads to an uncertainty on the actual position of the photon event.

Signal-to-noise ratio in multiphoton detection

With the amplitude distribution and the noise characteristics at hand, we can calculate the SNR using the intensifier in the multiphoton regime. The SNR is usually written in the form

$$\mathrm{SNR_{MP}} = \frac{FQt}{\sqrt{(\Delta F^2 + \Delta B^2)Qt + \Delta R_{auto}^2 t + \sigma_{RO}^2}} \,, \tag{4.6}$$

[9]For higher atom numbers one could for example use longer cloud expansion times which increases the intensifier surface the fluorescence photons fall on.

[10]The biconvex lens with $f = 75\ mm, NA = 0.1$ adds a negligible part of $\frac{1.22\lambda}{2NA}\frac{0.35}{13\ \mu\mathrm{m}} = 0.13$ pixel to the diffraction. The universal factor 0.35 is used to transform the airy function width into a Gaussian rms width and originates by fitting a Gaussian to an Airy function as shown in Fig. 3.9.

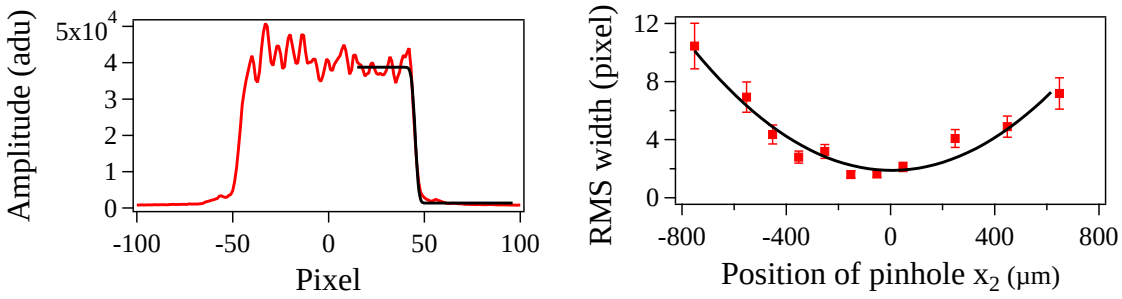

Figure 4.12: Intensifier resolution. *left*) Cross section of the edge as it appears on the CCD camera with the erf-function used as a fit in red. The rms width of the erf-function, corresponds to the effective PSF. *right*) Dependence of the rms width versus the distance x_2 of the sharp edge with respect to object plane. At the minimum the edge is conjugated with the intensifier and has a rms width of 1.9 ± 0.3 pixel.

where $F, \Delta F^2, \Delta B^2, t$ represent the mean photon flux on the CCD camera, its variance, the variance of the background flux and the integration time, respectively. ΔR_{auto} takes into account the noise introduced by the auto-generation event rate of the intensifier. Furthermore we introduce Q as the quantum efficiency of the device. In order to evaluate the impact of the intensifier on the SNR, we calculate the SNR in a concrete case for which we consider a constant incident photon flux $F_{in} = 100$ adu/pixel/s. Assuming $B = \Delta B = 0$, we obtain a $\mathrm{SNR_{MP}}$ of 7.3 in the absence of the intensifier (we take $Q = 78\,\%$ at 780 nm, and $\Delta R_{auto} = 0$, and the incident photon flux to have a Poissonian distribution $\Pi(x, F)$ $(\Delta F^2 = F)$).

Using the intensifier in front of the CCD camera, we have to take into consideration the amplification factor of the intensifier as well as the auto-generation rate. Let us first concentrate on the amplification of the intensifier. The amplification leads to a larger signal and a larger noise on the signal. We first calculate the signal being the mean flux of photons after the intensifier and detected on the CCD. We use the intensifier distribution $p(x, g, \Delta g)$ from Sec. 4.4 where we include the first two moments, namely the mean g and the rms value Δg of the single-photon intensifier response distribution as parameters. When y photons impinge on the intensifier these moments scale approximately as $y \cdot g$ and $\sqrt{y} \cdot \Delta g$ in the linear intensifier regime. As the number of photons y impinging on the intensifier follow a Poissonian distribution $\Pi(y, F)$ we calculate the mean photon flux after the intensifier F_{int} by convoluting both distributions

$$F_{int} = \sum_{x=0}^{\infty} \sum_{y=0}^{\infty} x \cdot \Pi(y, F) p(x, y \cdot g, \sqrt{y} \cdot \Delta g) = \sum_{y=0}^{\infty} \Pi(y, F) \cdot y \cdot g = F \cdot g \ . \qquad (4.7)$$

As expected we find that the mean photon flux after the intensifier is just the mean incoming photon flux multiplied by the intensifier amplification. For gain 9 and including the quantum efficiency of the CCD camera this gives a mean flux $F_{int} = 100 \cdot g \sim 8 \cdot 10^4$ adu/pixel/s. For the noise of the amplified signal we calculate the variance ΔF_{int}^2 of the flux after the intensifier

$$\begin{aligned}\Delta F_{int}^2 &= \sum_{x=0}^{\infty}\sum_{y=0}^{\infty} x^2 \cdot \Pi(y,F) p(x, y\cdot g, \sqrt{y}\cdot\Delta g) - F_{int}^2 \\ &= \sum_{y=0}^{\infty} \Pi(y,F)\left[y\cdot\Delta g^2 + y^2\cdot g^2\right] - F_{int}^2 \\ &= F\cdot\Delta g^2 + F\cdot g^2 + F^2\cdot g^2 - (F\cdot g)^2 = F(\Delta g^2 + g^2)\ .\end{aligned} \tag{4.8}$$

The fluctuations on the detected photon signal are much larger than a Poisson distribution due to the large statistical spread (Δg^2) of the intensifier response. This introduces an additional noise referred to as the multiplication noise (Hollenhorst, 1990).

We now come to the second implication when using the intensifier namely the presence of auto-generated noise. It has been measured in Sec. 4.5 and can be implemented in Eq. 4.6 by using $\Delta R_{auto}^2 = R_{auto}\Delta g^2/g$. For gain 9 we find $\Delta R_{auto}^2 = 93\cdot 10^3 \mathrm{adu}^2/\mathrm{pixel}^2/\mathrm{s}$. As a final result the intensifier leads to a worse signal-to-noise ratio of $\mathrm{SNR}_{\mathrm{MP}} = 2.6$ compared to the case where only the CCD is used.

The lower SNR for intensified cameras is a standard problem for astronomers (Tulloch and Dhillon, 2010; Tubbs, 2003) and could in our case render the observation of small Bose-Einstein condensates difficult, as the condensed and thermal velocity distribution are very similar (see Sec. 11.5) and the intensifier noise is much larger than typical Poissonian noise for CCD cameras. On the other hand the intensifier is crucial for the detection of single photons which is impossible using a CCD camera only (see Sec. 4.5).

4.7 Conclusion

In this chapter we discussed in detail the characterization of the light intensifier unit in the single and multi photon regime. It is a useful device to enhance the single photon response above the CCD camera noise levels. It furthermore serves as an efficient shutter even for high repetition rate applications. Its disadvantages lie in the low efficiency that is usually less than the one of CCDs or EMCCDs and the rather high noise generation. Our image analysis is based on a counting algorithm that is fast and efficient when the background is flat and when the events are well separated. The photon response distribution is well reproduced by the theoretical model based on the description of avalanche processes. We showed that the intensifier has a tendency to produce neighboring peaks which lead to a small overestimation (~ 1 %) of counted photon events.

Part II

Single atom measurements

Chapter 5

Calibration measurements using a single atom

Contents

A single atom inside the optical dipole trap is the ideal object to characterize and calibrate our experimental setup (Darquié, 2005; Beugnon, 2007). In this chapter we discuss some of the experiments that we pursued to retrieve information about quantities such as the depth of the optical dipole trap, residual magnetic fields, collision rate with the background gas etc..

5.1 Résumé

Ce chapitre explique comment nous utilisons un atome unique pour sonder son environnement (mesure de la profondeur du piège dipolaire, mesure du champ magnétique résiduel ... etc) et mesurer le taux de collisions avec le gaz résiduel dans la chambre

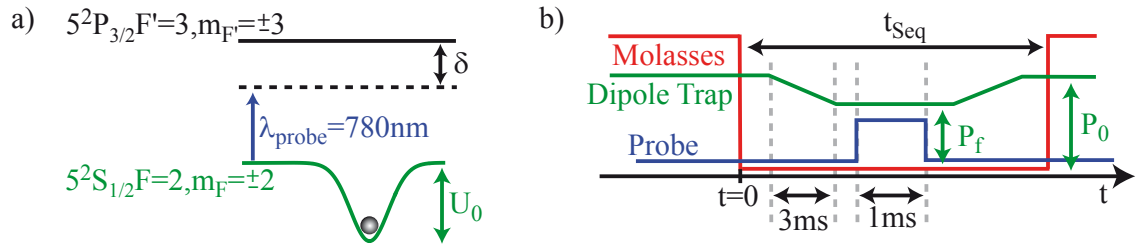

Figure 5.1: Single atom spectroscopy of the cycling transition $5^2S_{1/2}F=2, m_F=\pm2 \leftrightarrow 5^2P_{3/2}F'=3, m'_F=\pm3$. a) The probe frequency is scanned around the transition $5^2S_{1/2}F=2, m_F=\pm2 \leftrightarrow 5^2P_{3/2}F'=3, m'_F=\pm3$ which undergoes a light shift induced by the dipole trap light. b) The sequence begins at $t=0$ when the single atom is loaded. At that point the molasses and molasses repumper lasers are switched off during the entire sequence with length $t_{Seq}=40$ ms. The trap power is ramped from initially $P_0=21.5$ mW to a variable final value P_f in ~ 3 ms. The probe laser is held at $s\sim 0.3$ and is scanned in frequency over a range of 80 MHz during 1 ms. Finally, the trap power is switched back to its initial value.

ultra-vide. La série d'expériences présentées dans ce chapitre montre les possibilités comme les limites de notre système et constitue la base pour les travaux suivants.

5.2 Characterization of the optical dipole trap

Important properties about the dipole trap can be inferred by the following three experiments.

5.2.1 Measurement of trap depth

The trapping laser light induces a light-shift on the atom that shifts the transition frequencies between the ground and the excited states (see Sec. 1.5.7). Measuring the transition frequency can be used to infer the light shift seen by the atom and thus the depth of the trapping potential U. We want to pursue spectroscopy of the closed cycling transitions $5^2S_{1/2}F=2, m_F=\pm2 \leftrightarrow 5^2P_{3/2}F'=3, m'_F=\pm3$ (see Sec. 1.5.6) for which only the ground state experiences a light shift $\Delta_{5^2S_{1/2}}$ given in Eq. 1.39 and illustrated in Fig. 5.1 a). We use the counter-propagating $\sigma^+ - \sigma^-$ probe laser to drive simultaneously both transitions.

The experimental sequence is illustrated in Fig. 5.1 b). A single atom is trapped in our dipole trap at 945 nm having a power of $P_0=21.5$ mW. It is adiabatically ($\sqrt{P}/k_BT \sim \sqrt{U}/k_BT = \text{const}$) ramped to its final value in 3 ms. It is then illuminated by the counter-propagating probe laser for 1 ms; during this time the frequency of the probe laser is scanned over 80 MHz. If the frequency becomes resonant with the light-shifted atom during the scan photons are scattered by the atom and detected on the APD. In the end we ramp back the trap power to its initial value P_0 and switch on the MOT light to trigger on the next atom. The sequence is repeated about 500 times.

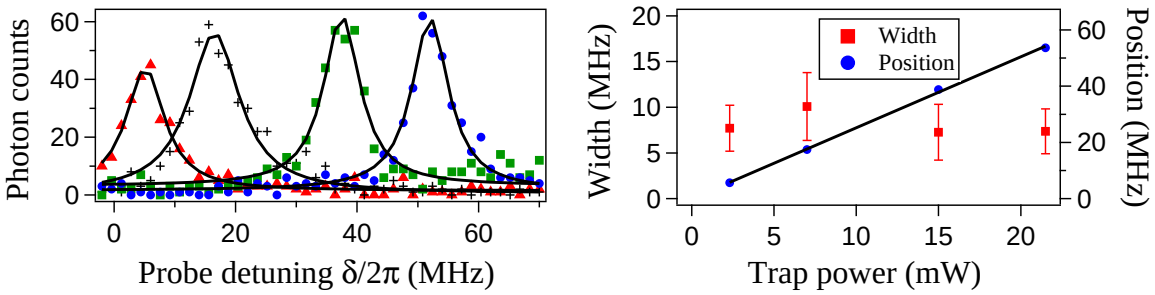

Figure 5.2: Single atom light shifted transition spectra. *left*) Detected photon counts versus the probe laser frequency for different trap depths corresponding to laser powers of $2.3, 7, 15, 21.5$ mW (triangles, crosses, squares, circles) for a trap at 945 nm. The spectra are fitted by a lorentzian profile. *right*) Center position (blue circles) equivalent to the light shift $\Delta_{5^2S_{1/2}}$ and width (red squares) of the lorentzian fit of the spectra versus the trap depth. The linear fit of the position through the origin has a slope of 2.52 ± 0.02 MHz/mW.

Typical spectra for different trap powers are shown on the left of Fig. 5.2. The spectra are well-fitted by a lorentzian function according to Eq. 1.28. To estimate the trap depth we need to take into account possible biases:

- **Residual magnetic fields.** External magnetic fields shift the transition frequency according to Eq. 1.8. In the presence of residual magnetic fields we would measure a biased transition frequency and therefore a biased trap depth. Our magnetic fields are compensated to ~ 50 kHz (see Sec. 5.4.1) so that its influence can safely be neglected.

- **Finite atom temperature.** The initial trap depth U_0 corresponds to the maximal value at the bottom of the trap which the atom sees when it is at position $(x, y, z) = 0$ according to Fig. 1.8. But atoms with high temperatures explore not only the bottom of the trap. The measured trap depth is then a result averaged over a range of positions each corresponding to a different light shift and thus also a different trap depth.

  We can estimate the temperature bias by calculating the probability for the atom to see a certain light shift. The light shift experienced by an atom only depends on its position and thus its potential energy and not on e.g. its velocity. Taking the potential energy probability $f_{th}(E_{pot}(\boldsymbol{r}))$ to be a Boltzmann distribution in Eq. 2.18 (see Sec. 3.4.1) and using the equality mentioned in Sec. 2.3.1

$$\frac{1}{V}\int f_{th}(E_{pot}(\boldsymbol{r}))d\boldsymbol{r} = \int D_s(E_{pot}) f_{th}(E_{pot}) dE_{pot} \tag{5.1}$$

  we solve for the density of states $D_s(E_{pot})$

$$D_s(E_{pot}) = \frac{2}{\sqrt{\pi (k_B T)^3}} \sqrt{E_{pot}} \ . \tag{5.2}$$

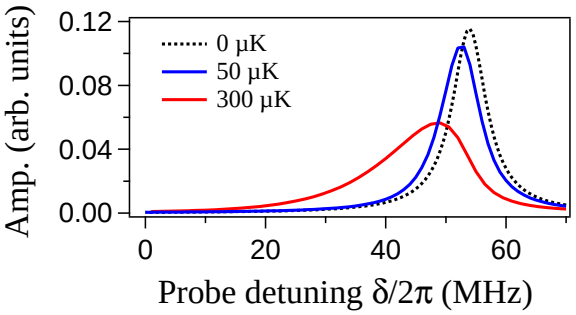

Figure 5.3: Light-shift distribution $D_s(\delta)f_{th}(\delta)$ for a thermal atom in a trap of 2.7 mK. Light shift distribution depending on the potential energy and thus the probe frequency $\delta/2\pi$. For an atom at 0 μK it has a lorentzian shape. For higher temperatures the maximum shifts as $\frac{3}{2}k_BT$ and broadens. The curves are calculated by using a probe saturation of $s = 0.3$.

Fig. 5.3 shows the light-shift distribution $D_s(\delta)f_{th}(\delta)$ for temperatures of 0 μK, 50 μK and 300 μK. For 0 μK we find the lorentzian of the Eq. 1.28 centered around U_0/h. For higher temperatures the lorentzian profile is convoluted by the light-shift distribution. The convolution shifts the center position by $\hbar\delta_{shift} = \frac{3}{2}k_BT$ and broadens the line.

For this measurement here, the atom temperature has been measured to be[1] $T = 50$ μK for a trap power of $P_0 = 21.5$ mW. This corresponds to a peak shift of $\delta_{shift}/2\pi = 1.6$ MHz. The actual trap depth is therefore 1.6 MHz deeper than measured. On the right side of Fig. 5.2 we show the corrected center position of the lorentzian peak as a measure of the light shift $\Delta_{5^2S_{1/2}}$ depending on the trap power. A linear fit fixed at the origin leads to a slope of 2.52 ± 0.02 MHz/mW which corresponds to trap depths of 0.12 mK/mW. The initial trap depth for $P_0 = 21.5$ mW corresponding to a light shift of $\Delta_{5^2S_{1/2}} = 54$ MHz is thus $U_0/k_B = 2.6$ mK. Assuming a Gaussian trapping laser profile and using formula Eq. 1.39 and Eq. 1.44 we can evaluate the product of the beam waists in x and y direction $\sqrt{w_x w_y} = 1.04$ μm.

The width of the lorentzian profiles is 8 ± 2 MHz on average and slightly higher than the natural line width $\Gamma/2\pi \sim 6$ MHz. The broadening can partially be explained by the probe laser saturation $s \sim 0.3$ which leads to a broadening of ~ 1 MHz for 0 μK. An additional broadening is due to the temperature. For 50 μK it increases the width to ~ 7.8 MHz. This broadening should however decrease for lower trap depths as the temperature is adiabatically lowered to ~ 15 μK for 2.3 mW. We do not observe any notable decrease in width which could be due to heating by the probe laser for example. Another source of broadening can be attributed to the probe laser line width[2] ~ 700 kHz.

5.2.2 Measurement of oscillation frequencies

We also measured the oscillation frequency of the single atom inside the dipole trap to obtain an estimate of the individual waists w_x and w_y. The idea (Engler *et al.*,

[1] The measurement of the single atom temperature inside the dipole trap is discussed in Ch. 6.

[2] The laser line width has been estimated to be ~ 700 kHz by measuring the width of the beat note between two identical laser beams.

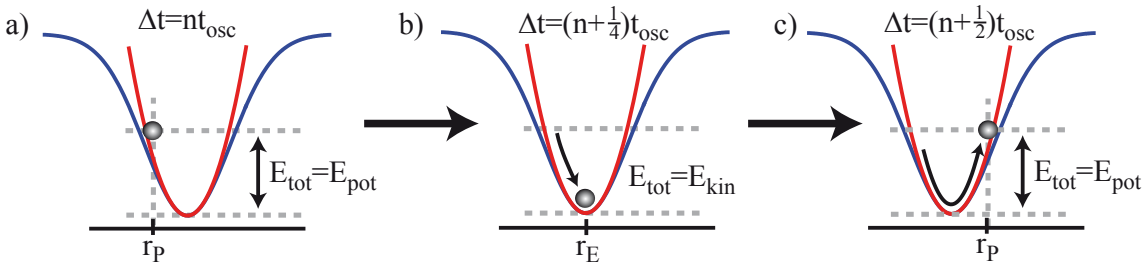

Figure 5.4: Idea of measuring the trap frequencies. a) The atom's total energy is in form of potential energy. b) After one forth oscillation it converts the potential energy into kinetic one. c) The atom reaches another point where its total energy corresponds to the potential energy.

2000) is illustrated in Fig. 5.4. At position r_P the atom has reached its maximal potential energy and has therefore zero velocity. If at this point the trap is switched off for a short duration t_2 the atom does not move (zero kinetic energy) and should stay trapped when switching back on the trap. If we wait for $\Delta t = (n + \frac{1}{4})t_{osc}$, where t_{osc} is the time to undergo one half oscillation and $n = 0, 1, 2, \ldots$, the atom is at position r_E and has totally converted its potential into kinetic energy. If at this point the trap is switched off for t_2 it escapes the trap region quickly and the probability to lose the atom is highest. At times $\Delta t = (n + \frac{1}{2})t_{osc}$ the situation corresponds to $\Delta t = nt_{osc}$ since the kinetic energy equals zero again. By measuring the recapture rate of the atom while varying Δt we should observe oscillations proportional to t_{osc}, which yields the trap frequency $\nu = 1/(2t_{osc})$.

At each position $\boldsymbol{r}_i$ the atom's velocity $\boldsymbol{v}_i$ is defined by the total energy of the atom $E = 3k_B T$. Over many realizations the combination of $(\boldsymbol{r}_i, \boldsymbol{v}_i)$ has a Gaussian distribution in phase space as mentioned in Sec. 2.3.1 for a thermal distribution. Averaging over many different initial positions and velocities corresponding to oscillations having the same frequency but different phases would lead to a smearing of the averaged final result. It can be shown that by switching off the trap for a usually short duration t_1 one can reduce all possible combinations $(\boldsymbol{r}_i, \boldsymbol{v}_i)$ to those having all the same phase (Sortais *et al.*, 2007).

The left side of Fig. 5.5 shows the experimental sequence. We trap a single atom at a trap depth of $U_0/k_B = 2.6$ mK. We switch off the trap a first time for $t_1 = 2$ μs to adjust the atom's phase creating a monopolar mode. We then let the atom oscillate for Δt and switch off the trap again for $t_2 = 8$ μs to check if the atom is at the bottom of the trap with high kinetic energy (atom is lost) or if it has maximal potential energy (atom stays trapped). The trap is switched on again and the molasses beams are used to check if the atom is still present.

On the right side of Fig. 5.5 we show the observed oscillation. We fit the data by the function[3] $f(t) = z + a\sin(2\pi\nu_x' t + \phi_1) + b\sin(2\pi\nu_y' t + \phi_2)$, and obtain $\nu_x = \nu_x'/2 =$

[3]We checked the validity of the function to extract the oscillation frequencies by comparing to the result of a Monte-Carlo simulation.

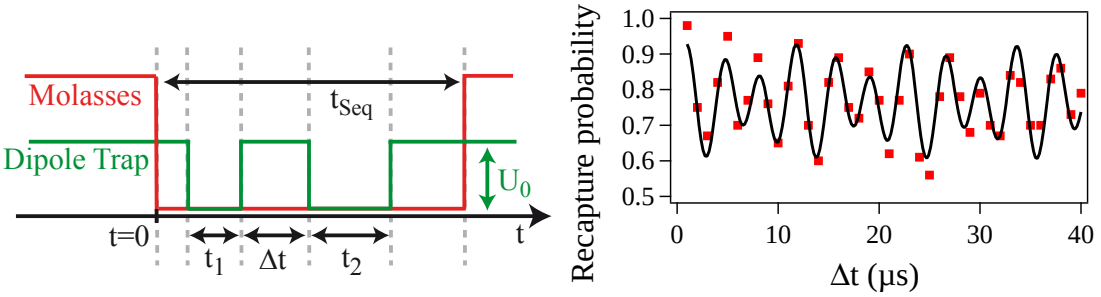

Figure 5.5: Oscillation frequency measurement. *left*) We illustrate the experimental sequence applied to measure the trap oscillation frequency. A first pulse $t_1 = 2$ μs adjusts the atom's phase. After the oscillating time Δt we leave the atom a short period $t_2 = 8$ μs to leave the region of the trap if its kinetic energy is sufficient. The time between the atom trigger and the atom detection is $t_{Seq} = 40$ ms. *right*) The graph shows the recapture probability depending on the oscillation time Δt. The fit (black line) leads to frequencies $2\nu_x = 184 \pm 1$ kHz and $2\nu_y = 274 \pm 2$ kHz.

92 kHz and $\nu_y = \nu_y'/2 = 137$ kHz. We incorporate a factor two due to the fact that the atom swings back and forth and is lost twice during one oscillation period. Possible heating effects coming into play while adjusting the phase for example can bias the measurement and are difficult to estimate. On the other hand the ratio of the frequencies $\nu_x/\nu_y = 1.5$ should be unaffected by a possible heating. Together with the result of the last section $\sqrt{w_x w_y} = 1.04$ μm we can calculate waists of $w_x = 0.9$ μm and $w_y = 1.3$ μm for the x and y directions.

For the dipole trap at 850 nm we find a more cylindrical beam with $\nu_x/\nu_y = 1.1$. This is probably due to a better alignment of the dipole trap laser on the aspheric lens. For a beam waist of $w_x \sim w_y = 1$ μm we deduce a Rayleigh length of 3.6 μm. The oscillation frequency along this axis is much lower ($\nu_z = 30$ kHz) and cannot be measured by this technique due to dephasing and atom loss at longer time scales.

5.2.3 Trap-induced Raman transitions between the hyperfine ground states

We want to measure the spontaneous Raman transition rate induced by the trap light as described in Sec. 1.5.7 as it can lead to a change of the hyperfine ground state (Cline *et al.*, 1994). The experimental sequence to do so is shown in Fig. 5.6 a). We trap a single atom in the dipole trap at 850 nm with $U_0/k_B = 2.7$ mK and prepare it in one of the two hyperfine ground states for which the atom has a temperature of 150 μK. If we leave only the molasses repumper beams on for 4 ms after the trigger at $t = 0$ we can pump the atom into $5^2S_{1/2}F = 2$ with nearly 100 % efficiency. If on the other hand we leave the molasses laser beams on and switch off the molasses repumper beams for 4 ms we prepare the atom in $5^2S_{1/2}F = 1$. Subsequently, the trap is adiabatically ramped to its final value $U_f/k_B = 9.9$ mK and left there for t_{hold}. The atom temperature has changed from 150 μK to 290 μK. During this time the

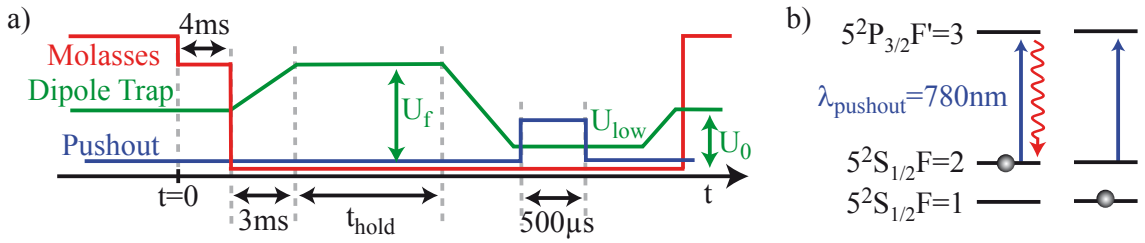

Figure 5.6: "push-out" technique using to measure trap light induced Raman transitions. a) The graph shows the experimental sequence. A single atom is trapped in the 850 nm dipole trap at $U_0/k_B = 2.7$ mK. The trap is adiabatically ramped to $U_f/k_B = 9.9$ mK in 3 ms and left at this value for t_{hold}. The push out is applied at a trap depth of $U_{low}/k_B = 0.29$ mK for 500 μs. Finally, the presence of the atom is checked by switching on the molasses lasers at the initial trap depth $U_0/k_B = 2.7$ mK. b) The uni-directional σ^+ "push-out" laser with $s \sim 5$ drives the closed cycling transition $5^2S_{1/2}F = 2 \rightarrow 5^2P_{3/2}F' = 3$. If the atom is in state $5^2S_{1/2}F = 2$ it will scatter photons and will be heated out of the trap. An atom in state $5^2S_{1/2}F = 1$ is not driven by the "push-out" laser and stays trapped.

Raman transitions induced by the trap light can lead to a change of the hyperfine ground state. If for example the atom is initially prepared in $5^2S_{1/2}F = 1$ it can be pumped during t_{hold} into $5^2S_{1/2}F = 2$. In order to measure in which hyperfine state the atom is we apply a "push-out" pulse. After the "push-out" laser we switch back on the molasses and molasses repumper lasers to check if the atom is still present.

The "push-out" technique based on the state-selective loss of the atom when it is illuminated by a resonant laser can be used to do a state-selective measurement (Kuhr *et al.*, 2003; Yavuz *et al.*, 2006; Jones *et al.*, 2007). The principle is shown in Fig. 5.6 b). We use the σ^+ probe beam as an uni-directional "push-out" laser at high saturation $s \sim 5$. The laser drives the cycling transition between levels $5^2S_{1/2}F = 2, m_F = +2$ and $5^2P_{3/2}F' = 3, m'_F = +3$. If the atom is initially prepared in any Zeeman state in $5^2S_{1/2}F = 1$ it does not scatter any photons and stays trapped. Independent of the initial Zeeman state an atom in $5^2S_{1/2}F = 2$ will quickly be pumped into the cycling transition, scatters photons and will be heated out of the trap. The recapture rate therefore tells us how many atoms were in which hyperfine state. It is important to note that the repumper probe laser is switched off for the "push-out" to work. For some applications however a lossless state detection is favorable. A lossless detection scheme is described in Ch. 7.

To improve the efficiency of the "push-out" technique it is best to work at a low trap depth $U_{low}/k_B = 0.29$ mK for which less photons need to be scattered in order for the atom to be lost. Also the difference in differential light shifts between the excited levels can be held smaller than $\Gamma/2\pi$ so that the "push-out" laser is resonant with all transitions between any two Zeeman states. The "push-out" laser frequency is adjusted to the trap induced light shift of 6 MHz to stay in resonance with the trapped atom. At this trap depth the atom needs to scatter $U_{low}/2E_{rec} \sim 800$ photons, where $E_{rec} = 3.78$ kHz is the recoil energy at 780 nm. At full saturation this takes 42 μs which is largely covered by the length of the 500 μs pulse. Nevertheless, we measure

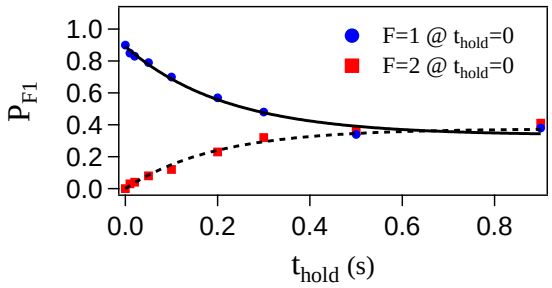

Figure 5.7: Measurement of the trap-light induced Raman transitions. The single atom recapture rate is measured versus the holding time t_{hold}, during which the trap induces hyperfine changing Raman transitions. A fit is used to extract the Raman transition rates for an initial preparation in $5^2S_{1/2}F=1$ (blue circles) and $5^2S_{1/2}F=2$ (red squares).

small detection errors of ~ 0.1 % which can be due to improper laser polarizations. In this case there is a chance that the atom is depumped into $5^2S_{1/2}F=1$ during the "push-out" pulse. The atom stops scattering photons and stays trapped although having been prepared in state $5^2S_{1/2}F=2$. We want to add that a uni-directional beam such as the "push-out" creates a radiation force on the atom[4].

Fig. 5.7 shows the experimental data. If the atom is initially prepared in state $5^2S_{1/2}F=1$, it is recaptured since the "push-out" beam does not lead to any heating. For longer holding times we see an increasing loss due to Raman transitions from $5^2S_{1/2}F=1$ into $5^2S_{1/2}F=2$. To extract a transition rate we set up the following rate equations

$$\begin{aligned} \dot{P}_{F1} &= -R_{\text{Raman}} P_{F1} + \frac{3}{5} R_{\text{Raman}} P_{F2} \\ \dot{P}_{F2} &= -\frac{3}{5} R_{\text{Raman}} P_{F2} + R_{\text{Raman}} P_{F1} \ , \end{aligned} \tag{5.3}$$

where we define P_{F1} and P_{F2} to be the probability to be in state $5^2S_{1/2}F=1$ and $5^2S_{1/2}F=2$, respectively. R_{Raman} is the Raman transition rate introduced in Eq. 1.43. The factor $\frac{3}{5}$ takes into account the number of degenerate Zeeman levels per hyperfine state. The equations are solved by

$$P_{F1} = \frac{1}{8}\left(3 + 5\exp(-\frac{8}{5}R_{\text{Raman}}t)\right) \quad , \quad P_{F2} = \frac{5}{8}\left(1 - \exp(-\frac{8}{5}R_{\text{Raman}}t)\right) \ . \tag{5.4}$$

Fitting the function to the data, we extract $R_{\text{Raman}} = 3.2 \pm 0.3$ s^{-1} and $R_{\text{Raman}} = 2.9 \pm 0.3$ s^{-1} for the atom initially prepared in $5^2S_{1/2}F=1$ and $5^2S_{1/2}F=2$, respectively. The theoretical value is calculated from the set of equations 1.43. At 290 μK the average light-shift that the atom feels is ~ 9.6 mK for which the Raman rate equals $R_{\text{Raman}} = 3.5$ s^{-1} which roughly agrees with the measured values. Note, that for long times the population P_{F1} tends to the calculated final value of $\frac{3}{8}$.

Trap-induced Raman transitions can hamper proper state preparation over longer time intervals. Additionally, it can lead to two-body spin-flip losses (see Sec. 2.2.2) even if all atoms are initially prepared in hyperfine state $F=1$. One solution to lower

[4] Radiation pressure leads to an effective trap depth that is smaller than U_{low} as will be discussed in Sec. 7.2.2

the Raman transition rate is to choose a further red-detuned dipole trap as the rate decreases according to Eq. 1.43. In our case we reduce the Raman rate by a factor ~ 10 by using a trap at 945 nm rather than 850 nm.

5.3 Lifetime of a single atom inside the dipole trap

Another important quantity is the lifetime of a single atom inside the dipole trap. There are several loss mechanisms that could explain the single atom losses:

- **Background gas collisions.** Collisions with the background gas as mentioned in Sec. 2.2.2 can be one cause of the trap loss. They show an exponential decrease at a rate γ.
- **Trap power and frequency fluctuations.** Fluctuations of the trap power or frequency at frequencies that are multiples of twice the radial or axial trapping frequency 2ν can lead to parametric heating of the atom (Savard, O'Hara, and Thomas, 1997). This loss origin can be excluded as power fluctuations are ~ 5 % and we measured that the frequency of the power fluctuations does not have any notable components oscillating at any multiple of the trapping frequencies.
- **Trap laser light absorption.** Even at far-off detuned optical dipole traps the atom does scatter some trap laser photons with rate R as described in Sec. 1.5.7. Every photon absorbed from the trap light and emitted in a random direction leads to an increase of the atom's total energy by two photon recoil energies $2E_{rec}$. We assume the atom to have a thermal distribution $D_s(E)f_{th}(E)$ inside the trap which is completely defined by the atom's temperature T (see Sec. 2.3.1). We further assume that the temperature increases linearly with each absorption and emission process as $T(t) = T_0 + \alpha t$, T_0 being the initial temperature and $\alpha = 2E_{rec}R$ being the heating rate. All atoms that belong to the energy tail of the distribution with an energy higher than the trap depth U_0 are lost as shown in Fig. 2.5. The probability for the atoms to still be trapped can be calculated by integrating the energy distribution

$$P(t) = \int_0^{U_0} D_s(E)f_{th}(E)dE = 1 - \left[1 + \frac{U_0}{k_B T(t)} + \frac{1}{2}\left(\frac{U_0}{k_B T(t)}\right)^2\right] \exp^{-\frac{U_0}{k_B T(t)}}, \tag{5.5}$$

To measure the single atom life time we use the experimental sequence illustrated on the left of Fig. 5.8. We start by trapping a single atom inside the $U_0/k_B = 2.7$ mK deep dipole trap. Its temperature is measured to be $T_0 = 150$ μK initially. We leave the atom in the dark for a time t_{hold} and check if the atom is still there afterwards. Over 100 repetitions we build up the recapture probability depending on the holding time t_{hold}, which is shown on the right of Fig. 5.8. The loss is partially due to collisions with the background gas $\propto \exp(-\gamma t)$ and partially due to Rayleigh scattering of the trap light $P(t)$ given in Eq. 5.5. We fit the function $P_{tot} = P(t)\exp(-\gamma t)$ to the data

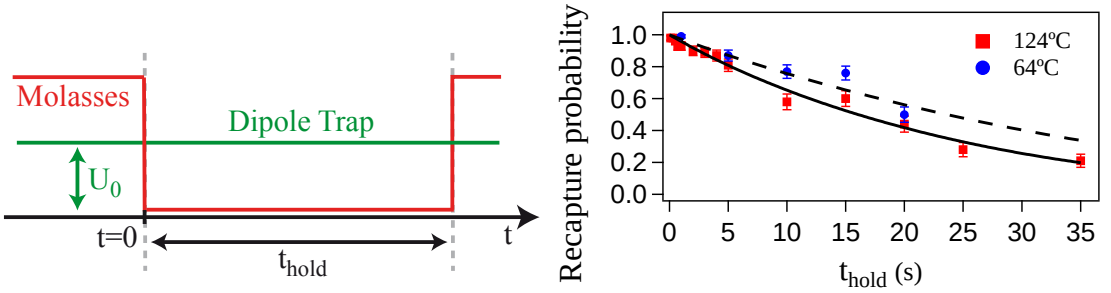

Figure 5.8: Single atom trap lifetime. *left*) At $t=0$ we trigger on a single atom in a dipole trap with wavelength 850 nm and a trap depth $U_0/k_B = 2.7$ mK. After the holding time t_{hold} we check if the atom is still trapped. *right*) Recapture probability versus holding time. We repeat the measurement for two different oven temperatures 64°C and 124°C and find lifetimes of $\tau = 1/\gamma = 36$ s and $\tau = 24$ s, respectively.

and obtain the collision rate $\gamma = 42 \pm 3 \cdot 10^{-3} s^{-1}$ and a heating rate of $\alpha = 11 \pm 8$ μK/s for an oven temperature of 124°C.

The heating rate $\alpha = 11 \pm 8$ μK/s corresponds to a total of ~ 30 photons/s that are absorbed. The theoretical value of $R = 70$ photons/s is about a factor 2 higher and can be explained by the sensitivity of α to slight changes in the initial fit parameters as can be seen on the high error given for α.

For the background gas at room temperature 300 K we find a collision rate $\gamma \sim 10^{-3} s^{-1}$ for Rb and hydrogen given in Sec. 2.2.2, for which the density for the measured vacuum pressure of 10^{-11} mbar can be calculated as mentioned in Sec. 3.3.2. The measured values are about a factor 10 higher than calculated. This could be explained due to a bias measurement of the vacuum pressure or additional background collisions with atoms coming from the atomic beam. We find an indication for these types of collisions by decreasing the oven temperature from 124°C to 64°C, for which the atomic flux is divided by a factor ~ 50. Nevertheless we find a collision rate of $\gamma = 28 \pm 4 \cdot 10^{-3} s^{-1}$ for the same α, which is only about twice as low as for 124°C. The atom beam coming from the oven does therefore only have a small effect on the trap lifetime of the atom.

5.4 Hyperfine-level spectroscopy for magnetic field compensation

We use hyperfine-level spectroscopy to compensate our residual magnetic field inside the vacuum chamber. The idea is based on the following: The Zeeman levels of the two hyperfine ground states $5^2S_{1/2}F = 1$ and $5^2S_{1/2}F = 2$ can be coupled by using micro wave (MW) transitions. Note that only the magnetic field of the MW radiation drives the transitions with $\Delta l = 0$ (see Sec. 1.5). By scanning the MW transition frequency we can resolve distinct resonances each belonging to one pair of Zeeman

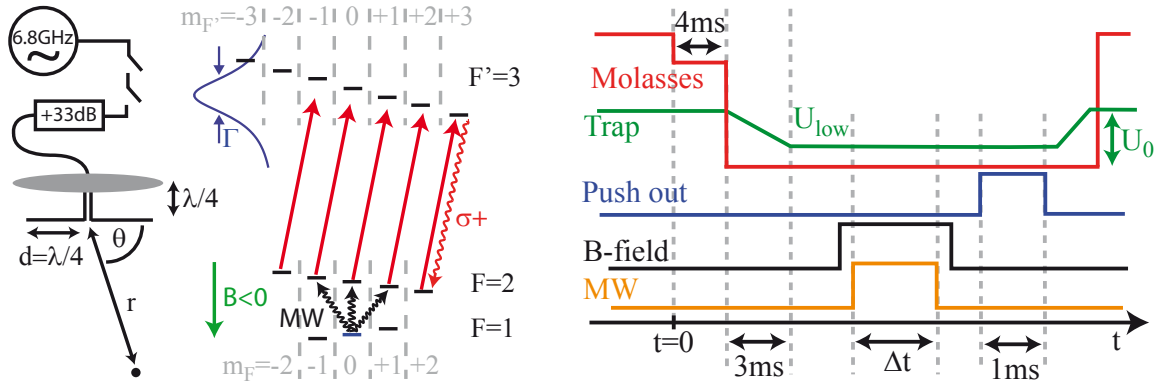

Figure 5.9: Hyperfine-level micro wave spectroscopy. *left*) To drive the hyperfine transitions we use an antenna as a microwave emitter at 6.8 GHz about $r = 12$ cm above the atom outside the vacuum chamber. Two fast switches (10 ns) are used in series to obtain 80 dB attenuation. *middle*) Level scheme of ^{87}Rb with the displacement of the hyperfine levels in an external magnetic field B. *right*) The molasses beams are used to detect and prepare a single atom in the state $5^2S_{1/2}F = 1$ as well as check if it still there in the end of the sequence. Just after its preparation the trap is adiabatically lowered from $U_0/k_B = 2.7$ μK to $U_{low}/k_B = 0.3$ μK. The MW pulse is used to pump the atom into the $5^2S_{1/2}F = 2$ state depending on the magnetic field set by the compensation coils. The "push-out" pulse is used to discriminate the hyperfine level.

states. For the atom in $5^2S_{1/2}F = 1, m_F = 0$ there are three possible transitions that can be driven leading to $5^2S_{1/2}F = 2, m_F = -1$, $m_F = 0$ and $m_F = +1$ for a σ^-, π or σ^+ polarization as illustrated on the left side of Fig. 5.9. The transition frequencies depend on the external magnetic field (see Sec. 1.4). We can now adjust the magnetic compensation field such that all Zeeman levels belonging to the same hyperfine level are degenerate. In this case there is no residual magnetic field left and the transition frequency between any two Zeeman states is the same.

The setup for the MW generation is shown on the left of Fig. 5.9. The micro wave (MW) frequency is delivered by a MW generator around $\nu = 6.835$ GHz to drive the hyperfine-level transition $5^2S_{1/2}F = 1 \rightarrow 5^2S_{1/2}F = 2$ in ^{87}Rb. We control two fast MW switches (2 ns) placed in series and each one having 40 dB attenuation to efficiently turn on and off the MW. Between the switches and the antenna we use a 33 dB amplifier to reach a power of $\sim$30 dBm in the antenna. The antenna has a length of $d = \frac{\lambda}{4} = \frac{c}{4\nu} \sim 1.1$ cm and is placed outside the vacuum chamber about $r = 12$ cm above the position of the atom. It has a metallic back plate attached to redirect some of the power onto the atoms that would otherwise be emitted in the opposite direction. Note that the geometry of the antenna supports a linear MW polarization. Reflections inside the vacuum chamber as well as a missing quantization axis however create a mix of circular and linear components seen by the atom.

To measure the hyperfine transition frequencies we follow the experimental sequence illustrated on the right of Fig. 5.9. We trap a single atom in our optical tweezer at 850 nm with trap depth $U_0/k_B = 2.7$ mK and prepare it in the $5^2S_{1/2}F = 1$

ground state by illuminating it for 4 ms with the MOT lasers only and leaving the repumper MOT lasers switched off. In this case we do not know in which Zeeman sublevel the atom is finally prepared. We will see that on average all sublevels are populated with approximately equal probability. We then ramp down the dipole trap during ~ 3 ms to $U_{low}/k_B \sim 0.3$ mK (1 mW) in order for the "push-out" laser to efficiently discriminate between the occupation of the hyperfine level, see Sec. 5.2.3. Before the "push-out" laser we apply a MW pulse for Δt to drive any transition between two Zeeman states belonging to different hyperfine levels. Having prepared the atom initially in $5^2S_{1/2}F = 1$, we find recapture rates of close to 100 % if the MW frequency is not on resonance with any transition. If however the MW is on resonance the atom can be transferred into $5^2S_{1/2}F = 2$ with high efficiency. In this case the "push-out" leads to the loss of the atom.

We first calibrate the power in the antenna in order to estimate the length of the MW transfer pulse Δt. MW powers of up to $P_{max} = 30$ dBm can be reached corresponding to a current in the cable of $I_0 = \sqrt{\frac{2}{R} P_{max}} = 0.2$ A for a resistance of $R = 50$ Ohm. To measure the magnetic field created by the MW at a distance of 12 cm away from the antenna we use a square antenna as receiver. It has a side length of 5 mm and thus shorter than $\lambda/4$ to avoid that destructive interference influences the measurement. In the far field ($r \gg \lambda$) the averaged magnetic field radiated by an antenna of length $l = 2d$ is described by

$$\langle B \rangle = \frac{1}{\sqrt{2}} \frac{I_0 \sin(\theta)}{2\epsilon_0 c r} \frac{l}{\lambda} , \tag{5.6}$$

where θ is the angle formed by one end of the antenna, its center and the receiver. According to this equation the antenna should be able to create a MW-induced magnetic field of $\langle B \rangle = 52$ mGauss. Experimentally however, we measure a power received by the receiver antenna of 0 ± 1 dBm, which corresponds to a magnetic field of $\langle B \rangle = 3$ mGauss. It is about one order of magnitude smaller than theoretically estimated and probably due to bad impedance matching. We take the measured value and calculate the corresponding MW pulse length to efficiently change the hyperfine level population. The pulse length is given by $\tau = \pi/\Omega$ with the Rabi frequency Ω. We find $\Omega/2\pi = 0.7$ MHz/Gauss $\cdot\, 3 \cdot 10^{-3}$ Gauss $= 2.1$ kHz for the magnetic field $\langle B \rangle = 3$ mGauss, where $g_F = 0.7$ MHz/Gauss is the Landé factor, and thus a pulse length of 238 μs.

MW transitions with $m_F = 0 \rightarrow m_F = 0$

In the beginning we scanned the RF frequency around the clock frequency $\nu_0 =$ 6834682.611 kHz. Here we should be able to drive the $F = 1, m_F = 0 \rightarrow F = 2, m_F = 0$ transition, which depends on the magnetic field in second order as 575.15 Hz/Gauss^2 and is therefore much less sensitive to a residual field. Estimating the residual magnetic field to be on the order of one Gauss this transition is much easier to find as it only shifts by 575 Hz and therefore stays inside the power broadened line width of $\sim \Omega/2\pi$. On the left of Fig. 5.10 the transition encountered around ν_0 is shown, for

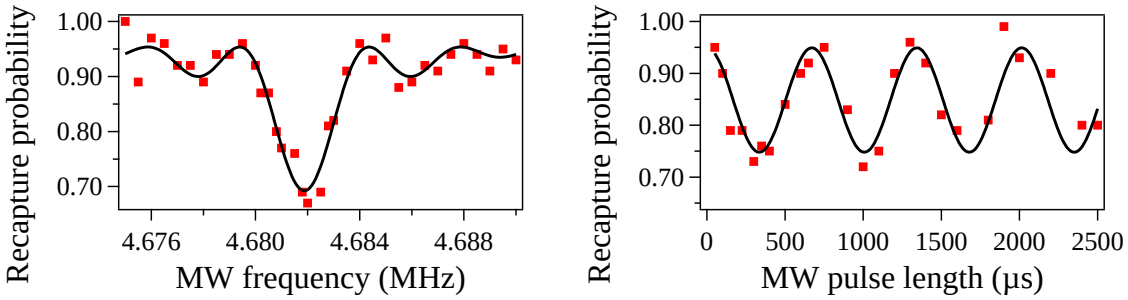

Figure 5.10: MW induced hyperfine transition $\mathbf{F=1, m_F=0 \rightarrow F=2, m_F=0}$. *left*) Dependence of the single atom recapture rate on the MW frequency for a MW pulse duration of 350 μs. The black line is a fit to the hyperfine transition spectral line. *right*) Dependence of the single atom recapture rate on the MW pulse duration for a MW frequency of $\nu_0 =$ 6.834682 GHz.

which we optimized the MW pulse length to $\Delta t = 350$ μs. The pulse length is confirmed by a second measurement for which we fix the frequency to $\nu_0 = 6.834682$ GHz and vary the length of the MW pulse Δt. On the right of Fig. 5.10 we see that the minimal recapture rate is reached for $\Delta t \sim 350$ μs. We note a drop of only ~ 30 %. The reason lies in the fact that only about one third of the atoms are initially in the $\mathrm{F}=1, \mathrm{m_F}=0$ state. The other two thirds are prepared in $\mathrm{F}=1, \mathrm{m_F}=-1$ and $\mathrm{F}=1, \mathrm{m_F}=+1$ which for the chosen MW frequency would only be coupled to the $\mathrm{F}=2$ states for a perfectly compensated magnetic field.

To understand the data we model the MW transitions in analog to the dipolar transitions in Sec. 1.5.4 by using the density matrix approach. The MW couples two hyperfine states g, e which is a special case of App. B. The Hamiltonian H and the decoherence part $\mathcal{L}\rho$ are taken to be

$$\rho = \begin{pmatrix} \rho_{gg} & \rho_{ge} \\ \rho_{eg} & \rho_{ee} \end{pmatrix} \quad , \quad H = \begin{pmatrix} 0 & \frac{\Omega}{2} \\ \frac{\Omega}{2} & -\Delta \end{pmatrix} \quad , \quad \mathcal{L}\rho = \begin{pmatrix} 0 & -\gamma\rho_{ge} \\ -\gamma\rho_{eg} & 0 \end{pmatrix} \quad ,$$

where Ω is the Rabi frequency of the coupling between levels g, e. It is directly proportional to the power of the MW as explained above. Δ is the detuning between the MW frequency and the resonance frequency of the g, e transition. The diagonal entries of the decoherence part are zero, since the lifetime of $g \equiv 5^2\mathrm{S}_{1/2}\mathrm{F}' = 2$ can be assumed to be infinite for all practical purposes described here. The off-diagonal terms γ describe the dephasing of the coherence. An intuitive and easy solution can be found for a dephasing rate $\gamma = 0$ for which the transition probability yields

$$P_{\mathrm{F}=1\rightarrow\mathrm{F}=2} = \rho_{ee} = \frac{\Omega^2}{\Omega^2 + \Delta^2} \sin^2\left(\sqrt{\Omega^2 + \Delta^2}\frac{t}{2}\right) \quad . \tag{5.7}$$

For the transition $5^2\mathrm{S}_{1/2}\mathrm{F}=1, \mathrm{m_F}=0 \rightarrow 5^2\mathrm{S}_{1/2}\mathrm{F}=2, \mathrm{m_F}=0$, the dephasing due to residual magnetic fields can be assumed to be small since this transition is only sensitive to magnetic fields in second order. A fit of Eq. 5.7 to the frequency spectrum gives a Rabi frequency of $\Omega/2\pi = 1.96 \pm 0.2$ kHz and a center frequency of

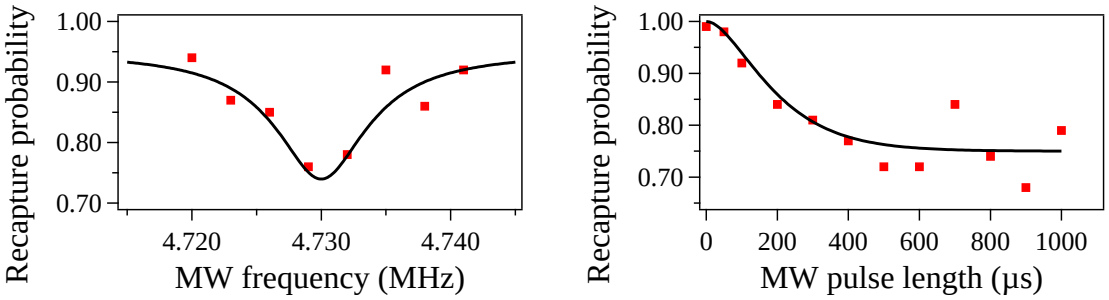

Figure 5.11: Hyperfine transition $\mathbf{F=1 m_F=0 \rightarrow F=2 m_F=+1}$ and $\mathbf{F=1 m_F=+1 \rightarrow F=2 m_F=0}$. *left*) Recapture rate versus MW frequency (MHz). For a unknown mix of σ^+ and σ^- MW radiation this transition line corresponds to the two transitions $\mathrm{F=1 m_F=0 \rightarrow F=2 m_F=+1}$ and $\mathrm{F=1 m_F=+1 \rightarrow F=2 m_F=0}$. *right*) Dependence of the recapture rate on the MW pulse duration for a MW frequency $\nu_0 = 6.834730$ GHz.

6834681.9 ± 0.6 kHz. Compared to the reference value ν_0 the line is shifted by not more than 1.31 kHz. This corresponds to a static residual magnetic field of only 48 mGauss. This value has to be taken with care since the MW generator has an uncertainty of 5 Hz and possibly a non negligible bias 10 years after its last calibration. Fitting the Rabi oscillation on the right of Fig. 5.10 by Eq. 5.7 we extract the Rabi frequency $\Omega/2\pi = 1.5 \pm 0.1$ kHz which is slightly smaller than the first value. The measured Rabi frequency also agrees with the value estimated earlier by using the receiver antenna. Note that observing the Rabi oscillation without observable damping after three cycles justifies the use of a nearly zero dephasing rate $\gamma \sim 0$.

MW transitions including $\mathbf{m_F \neq 0}$

Knowing the Rabi frequency for the linear polarization permits to search for the next linear transition $\mathrm{F=1, m_F=+1 \rightarrow F=2, m_F=+1}$. We set the MW pulse to $\Delta t = 350$ ms and scan the MW in steps of 3 kHz to find the next transition without missing it. We find it at 6.835378 GHz for which the frequency difference with respect to the first transition line is $\Delta\nu = 696$ kHz. We look for other transitions at multiples of $\Delta\nu$ and find all other possible transitions at $\nu_0 \pm 3\Delta\nu$, $\nu_0 \pm 2\Delta\nu$, $\nu_0 \pm 1\Delta\nu$. We conclude that the found transition at $\nu_0 + \Delta\nu$ corresponds to a combination of $\mathrm{F=1, m_F=0 \rightarrow F=2, m_F=+1}$ and $\mathrm{F=1, m_F=+1 \rightarrow F=2, m_F=0}$ for σ^+/σ^- polarization. The frequency difference of $\Delta\nu = 696$ kHz then corresponds to a residual magnetic field of ~ 1 Gauss. Resolving all these transitions also proves that the MW pulses contain all polarizations.

The left graph in Fig. 5.11 shows the transition $\mathrm{F=1 m_F=0 \rightarrow F=2 m_F=+1}$ and $\mathrm{F=1 m_F=+1 \rightarrow F=2 m_F=0}$. We notice that the line is much larger than the previous one which could be due to a much higher Rabi frequency or a dephasing $\gamma \gg 0$. To measure the Rabi frequency we again measure the Rabi oscillations and find a quick suppression of the coherence as can be seen on the right of Fig. 5.11. The broadening of the transition is therefore due to dephasing. This is not very surprising as the Zee-

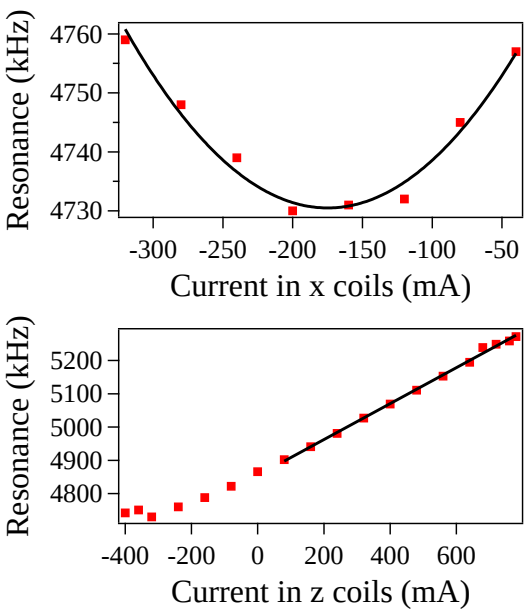

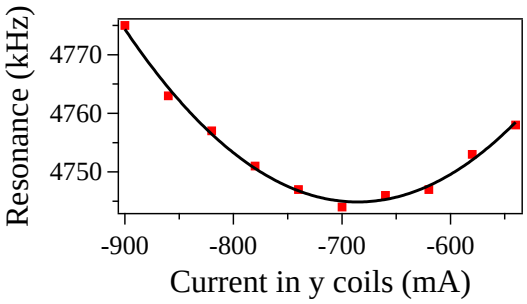

Figure 5.12: Magnetic field compensation. Dependence of the position of the $F=1, m_F=0 \rightarrow F=2, m_F=+1$ transition on the current in the compensation coils x, y, z. Near the minimum we fit a parabola to extract the points of perfect field cancelation. Far away from the minimum we observe a linear dependence.

man considered levels $F=2, m_F=+1/F=1, m_F=+1$ depend on a residual magnetic field in first order 0.7 MHz/Gauss now. Comparing both data sets with a theoretical curve (black curve) obtained by solving the Bloch equations numerically we extract a Rabi frequency of $\Omega/2\pi=1.5$ kHz and a dephasing rate of $\gamma/2\pi=3$ kHz due to fluctuations of the magnetic field (~ 1 mGauss) for example. The Rabi frequency is slightly smaller for this σ^+ or σ^- transition than for a linear polarization. For this transition we therefore have to work with a MW pulse length of 666 μs.

5.4.1 Compensating residual magnetic fields

The compensation coils in the three directions x, y, z (see Fig. 3.2) can now be used to compensate residual fields and level out all Zeeman hyperfine levels. We stick with the $F=1, m_F=0 \rightarrow F=2, m_F=+1/F=1, m_F=+1 \rightarrow F=2, m_F=0$ transition which shifts with the magnetic field as 0.7 MHz/Gauss. We change the current in the coils, which changes the magnetic field and thus the splitting between the hyperfine Zeeman levels, and follow the new position of the transition. The position depends on the magnetic field as the absolute value of the B-field vector $B=\sqrt{B_x^2+B_y^2+B_z^2}$. For e.g. the z-direction we observe that far away from the minimum, the position changes linearly with the current. In this regime we can calibrate the compensation coils and find a slope of 540 kHz/A which corresponds to 0.77 Gauss/A. The geometry of the coils allows a calculation of the magnetic field inside the vacuum chamber. The coils with $n=16$ windings have a square shape with a length and width of $a=17$ cm. The distance between them is $L=16$ cm. Using the Biot-Savart law, we find a magnetic field for one coil

$$B(z)=\frac{\mu_0}{2\pi}\frac{nIa^2}{((\frac{a}{2})^2+z^2)(\frac{a^2}{2}+z^2)^{\frac{1}{2}}}\ , \tag{5.8}$$

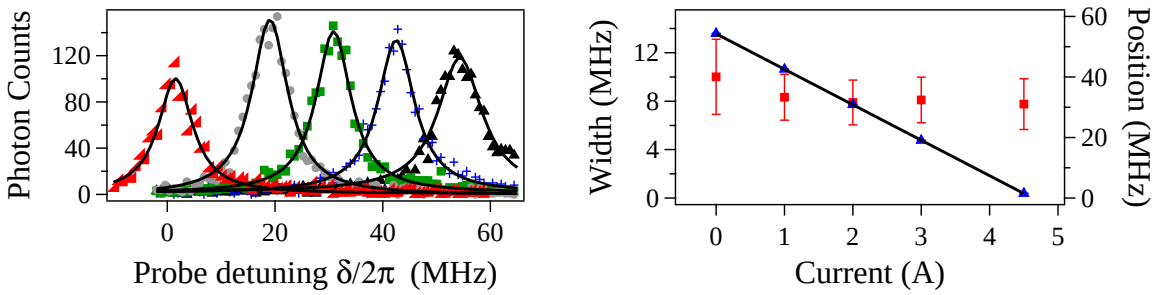

Figure 5.13: MOT coil calibration. *left*) Dependence of the number of detected photons on the probe frequency around the $F = 2, m_F = +2 \rightarrow F' = 3, m'_F = +3$ transition. The dependence is shown for a current of $0, 1, 2, 3, 4.5$ A (from right to left) in the MOT coils. *right*) Center position and width of the atomic distribution versus the MOT current.

where μ_0 is the vacuum magnetic permeability. The equation is valid for positions on the z-axis passing both square coils in their center. We assume the atom to be on axis at $z = 0$ which corresponds to the center between both coils. Both coils can thus be found at $z = \pm L/2$ with respect to the atom. The total magnetic field on the atom is then calculated to be $B_{tot}/I = [B(-L/2) + B(L/2)]/I = 0.94$ Gauss/A and slightly higher than measured.

We find the same behavior for the x and y direction. We finish by measuring the position around the minimum of the magnetic field to make sure that we have found the global minimum. The residual shift of ≈ 50 kHz corresponding to a residual magnetic field $B_{res} \approx 70$ mGauss could be explained by a dynamic rotating magnetic field which can not be compensated with our static compensation coil setup. The actual source of the residual field could not be identified so far. Nevertheless, the compensation directly resulted in a sub-Doppler temperature of the single atom of 35 μK directly after it is loaded from the melasses, see Sec. 9.2.

5.4.2 Calibration of the MOT coils magnetic field

We want to calibrate the MOT coil pair that is aligned in z-direction and which are not limited to 1.54 Gauss as the compensation coils. To calibrate the MOT coils we do spectroscopy on the cycling transition $5^2S_{1/2}F = 2 \rightarrow 5^2P_{3/2}F' = 3$ as performed to measure the trap depth in Sec. 5.2.1. We apply the same sequence and measure how the transition shifts when varying the magnetic field. Note that we now use a σ^+ polarized uni-directional probe with $s \sim 0.4$.

The atomic distributions can be seen on the left of Fig. 5.13. With 0 A in the MOT coils the atom distribution is shifted by 55 MHz due to the light shift induced by the dipole trap. The shift due to the residual magnetic field is negligible here. We see how the distribution center moves to lower frequencies with higher MOT coil currents. The line width of 8.5 MHz does not change with the MOT coil current and is again slightly larger than the natural line width of 6.1 MHz. We show on the

right side of Fig. 5.13 that the position of the distribution varies linearly with the coil current. A fit shows a variation of -11.7 ± 0.02 MHz/A which corresponds to -8.36 Gauss/A. We again estimate the magnetic field using the Biot-Savart law. For round coils the equation is

$$B(z) = \frac{\mu_B}{2} \frac{nIR^2}{(R^2 + z^2)^{\frac{3}{2}}} \ . \tag{5.9}$$

The MOT coils are placed in Helmholtz geometry and have a diameter of $R = 8.5$ cm. The distance between the coils is therefore also $R = 8.5$ cm. Each coil consist of $n = 81$ windings and can carry up to 10 A. We calculate a magnetic field of -8.5 Gauss/A, which is again slightly larger than the measured value of -8.36 Gauss/A.

5.5 Conclusion

This chapter concentrated on a detailed study of important experimental parameters. We discussed a characterization of the optical dipole trap and measured quantities such as the trap lifetime limited by collisions with the background gas. Furthermore, we compensated residual magnetic fields by doing MW hyperfine spectroscopy. The compensation yields a calibration of the magnetic field coils. These measurements are all based on the detection of a single atom by using the APD. The next chapter will show how the CCD camera can also be used to detect single atoms and measure quantities such as its temperature for example.

Chapter 6

Measuring the temperature of the single atom

Contents

This chapter describes two independent techniques that can be used to measure the temperature of a single atom inside the optical dipole trap. The first technique relies on the CCD camera where we perform fluorescence imaging of the atom after its release from the trap. The time-of-flight expansion of the atomic spatial density distribution is observed by accumulating many single atom images. The position of the atom is revealed with a spatial resolution close to 1 μm by a single photon event, induced by a short resonant probe. The expansion yields a measure of the temperature of a single atom. It is in very good agreement with a second independent technique which is based on a release-and-recapture method. The atom is released from the dipole trap and eventually recaptured after a variable period of time depending on its initial energy. We reconstruct the recapture rate as a measure of the temperature by repeating the sequence and checking the presence of the atom each time. Here, the atom detection relies on the APD and is therefore not affected by any bias of

the imaging system which would affect the result of the time-of-flight fluorescence integration method.

The comparison of both methods provides a way of eliminating any possible bias on the imaging system. This calibration is useful for experiments where we study the behavior of a cloud of a few tens or hundreds of cold atoms held in the trap (see part IV). In this regime the cloud can be very dense and light scattering of near-resonant light used for diagnostic purposes may exhibit a collective behavior (see e.g. (Sokolov *et al.*, 2009)). It is therefore important to understand the optical response of the imaging system in the single atom case to interpret the images in the multi-atom regime where collective effects may come into play. Moreover, because the atoms can be illuminated right after their release from the dipole trap, our method allows us to explore the properties of the momentum distribution of such a gas in the near-field regime.

6.1 Résumé

Nous avons réalisé l'imagerie de fluorescence d'un atome en vol libre, en accumulant de nombreuses images contenant un événement photonique unique correspondant à un seul atome. Nous avons utilisé la technique de temps de vol pour mesurer la température de l'atome après extinction du piège optique. Cette mesure de la température a été confirmée par une méthode indépendante basée sur une technique de lâcher-recapture (Fuhrmanek *et al.*, 2010b). La grande ouverture numérique de notre système d'imagerie et le confinement extrême des atomes dans le piège permettent une haute résolution spatiale de l'ordre de ~ 1 μm. Le faible niveau de bruit de notre système d'imagerie donne des images montrant ~ 150 atomes avec un très bon rapport signal sur bruit (~ 20). Ces mesures ont été effectuées dans des conditions où le mouvement des atomes au cours de l'éclairage par la sonde peut être complètement négligé. Nous avons ainsi obtenu une caractérisation très précise de notre système d'imagerie. Enfin, les mesures et l'analyse présentées dans ce chapitre fournissent une calibration utile pour les expériences de temps de vol à plusieurs atomes (cf. chapitres suivants), où les interactions atomiques joueront un rôle central.

6.2 Single-atom temperature measurement by using time-of-flight imaging

Time-of-flight imaging of ultra-cold atomic gases in expansion is a common way to study their properties. It provides a direct measurement of the momentum distribution and is therefore routinely used to extract the temperature of cold thermal samples (Lett *et al.*, 1988). It can also give access to spatial density or momentum correlations in atomic ensembles. While fluorescence imaging is widely used in experiments to detect single trapped atoms ,(Schlosser *et al.*, 2001; Kuhr *et al.*, 2001; Nelson, Li, and Weiss, 2007), and sometimes spatially resolve them (Sortais *et al.*,

2007; Miroschnychenko *et al.*, 2006; Bakr *et al.*, 2009), fluorescence imaging of freely propagating single atoms has been demonstrated only recently (Bücker *et al.*, 2009). In that experiment, cold atoms are released from a trap and fall under the gravity through a sheet of light, which is imaged on an intensified CCD camera using efficient collection optics. The presence of an atom is revealed by an individual spot corresponding to the detection of many fluorescence induced photons. The detection efficiency of a single atom is close to unity and the spatial resolution ($\lesssim 10$ μm) is set by the motion of the atom in the light sheet.

In our setup we can follow a complementary approach where we perform time-of-flight fluorescence imaging of a single Rb atom in free space, based on single photon detection, with a spatial resolution of ~ 1 μm. A single atom is first trapped in a microscopic dipole trap and then released in free space where it evolves with its initial velocity. To detect the atom and locate it with the best accuracy possible, we illuminate it with a very short pulse of resonant light and collect the fluorescence on an image intensifier followed by a CCD camera. The presence of the atom is revealed by a single photon event. We repeat the experiment until the spatial distribution of the atom is reconstructed with a sufficient signal-to-noise ratio; the accumulation of successive single atom images yields an average result that exhibits the same features as would a single experiment with many non-interacting atoms. Average images recorded for increasing time-of-flights allow us to measure the root mean square (abbreviated rms) velocity of the atomic expansion, and thus the temperature of a single atom. This method allows to measure temperatures over a wide range ($\sim$ 50nK-$\sim$ 10K).

6.2.1 Requirements for time-of-flight imaging of a single atom

The principle of a time-of-flight experiment is to measure the position of atoms after a period of free expansion. From the rms positions of the atoms, one extracts the rms velocity σ_v of the atoms. We measure the position of the atom by illuminating it with resonant laser light and collecting its fluorescence. This method requires that the position of the atom changes by less than the resolution of the imaging system during the light pulse. The imaging system is diffraction limited with a resolution $\sigma_{\text{diff}} = 0.5$ μm. This imposes a pulse duration of $\tau < \sigma_{\text{diff}}/\sigma_v$. Typically, for a rubidium atom at the Doppler temperature ($T_{\text{Doppler}} \simeq 150$ μK), this yields probe pulses as short as 4 μs. For a collection efficiency of ~ 1 % and a scattering rate $R \approx \Gamma/2 \simeq 2 \cdot 10^7$ s^{-1}, the number of detected photons per pixel would approach unity in single shot, which is well below the capabilities of the CCD camera.

We solve this issue by inserting the light intensifier described in Ch. 4 in front of the CCD camera. The intensifier acts as a fast shutter (opened during the probe pulse only), and amplifies a single photon event to a level about two orders of magnitude above the noise level of the CCD camera, see Ch. 4. Using this intensifier, the presence of one atom is revealed by one single photon event (the case of detecting more than one photon emitted by a single atom during the probe pulse is very unlikely).

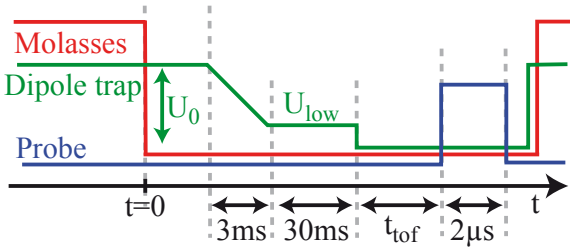

Figure 6.1: Time-of-flight sequence. Time sequence for a time-of-flight experiment. Note that the time axis is not drawn to scale. The loading sequence lasts $\sim 1\,\mathrm{s}$, while the adiabatic cooling, time-of-flight, and probing sequences are much shorter.

6.2.2 Experimental sequence and results

The experimental sequence is summarized in Fig. 6.1. It starts with loading and cooling a single atom in the $U_0/k_\mathrm{B} \sim 2.2$ mK deep dipole trap at 850 nm. The molasses cooling beams are switched off immediately upon detection of the atom. The single atom is kept in the dipole trap for an extra 30 ms where the trapped atom can be further cooled by adiabatically ($\sqrt{U}/T = \mathrm{const}$) ramping down the trap depth to U_{low}. We also use this 30 ms interval to let the atoms in the molasses spread out, with all cooling beams having been switched off. This precaution is taken in order to minimize light scattered by the background molasses during the subsequent probe pulse.

After the single atom is trapped and cooled, the dipole trap is switched off and the single atom time-of-flight experiment takes place. We let the single atom fly for a variable time t_tof and then illuminate it by a 2 μs pulse of probe light. We use the counter-propagating (to avoid radiation pressure force) probe and repumper probe laser (see Sec. 3.3.5). The saturation parameter of the probe light is $s \sim 1$ for each beam. At the same time, the intensifier is switched on for 2 μs and the probe-induced fluorescence is collected by the intensified CCD camera. The loading sequence is then started again, in order to prepare for the next time-of-flight experiment. The acquisition of one image for a given time-of-flight is performed by repeating the experimental sequence described above, with a cycle rate of $\sim 0.5 - 2\ \mathrm{s}^{-1}$ and accumulating the total fluorescence light on the CCD. When a sufficient number of photons have been detected (typically 100), the CCD chip is read out and the image is displayed. Note that, for each sequence, the CCD receives light only during the 2 μs the intensifier is on. In this way the intensifier also serves as a fast switch, preventing stray light from reaching the CCD during the cooling and trapping phases.

Figure 6.2 shows typical images taken for time-of-flights as long as 50 μs. The longer the time-of-flight, the lower the peak signal, and the larger the number of accumulations required. For a measured rms size $\sigma \simeq 1$ μm (corresponding to the time-of-flight $t_{TOF} = 1$ μs of image i)), we perform ~ 3400 sequences, corresponding to 3400 single trapped atoms, and detect 150 photons (this number of photons is extracted from an independent calibration of the intensifier response to a single photon event, see Ch. 4). This means that the probability to detect a single atom in a single realization of the experiment is $4.4 \cdot 10^{-2}$ when using a 2 μs-probe. At $R = \Gamma/2$ this corresponds to a detection efficiency $2.2 \cdot 10^{-3}$ and is well explained by the collection efficiency of 3.8 % up to the PBS of Table 3.2, the PBS transmis-

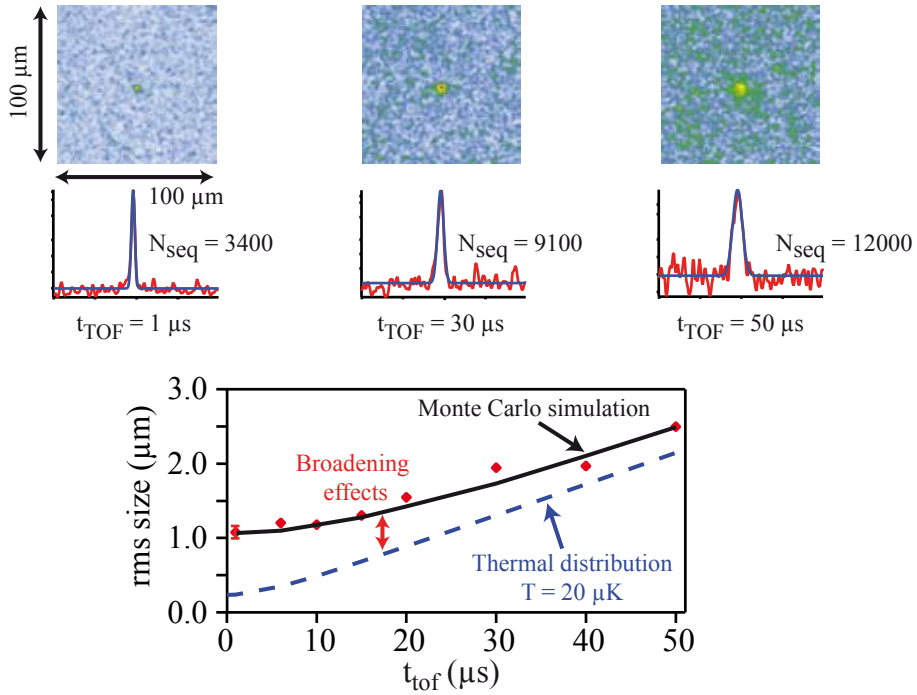

Figure 6.2: Single-atom images in a time-of-flight measurement. Results of a typical single atom time-of-flight experiment. The atom is released from a trap with depth $U \sim 0.08\,\mathrm{mK}$. The rms size of the "cloud" is plotted versus the time-of-flight of the single atom after it is released from the dipole trap. The dashed line is a fit to the data (diamonds), using Eq. (6.1). The solid black line is the result from a Monte-Carlo simulation described in the text. We show a typical error bar (for $t_{\mathrm{tof}} = 1\mu\mathrm{s}$) obtained by repeating the same experiment several times. Insets show images and associated cross-sections of the data for three particular time-of-flights. Each image results from the detection of a large number of successively trapped single atoms. The rms size of the cloud is thus the rms position of a single atom after a given time-of-flight. Image i) corresponds to 3400 sequences and 150 detected photons, and therefore 150 detected atoms. Image iii) corresponds to 12000 accumulations and 520 detected atoms.

sion of 50 % (Sec. 3.3.5) and the quantum efficiency of the intensifier photocathode ($\eta_{\mathrm{intensifier}} \sim 10$ %) (see Sec. 4.6).

The images are well fitted by a 2D Gaussian model, for which we extract the rms width in pixel. The rms size in the plane of the atoms can be evaluated considering that each pixel has a size of 13 μm and the radial magnification of the imaging system is $\sim 26 \pm 2$. One pixel therefore corresponds to 0.5 μm. Within the error bars the images possess symmetry of revolution. We plot the rms size σ of the expanding "cloud" along one axis versus the time-of-flight t_{tof}. We fit the data shown in Fig. 6.2 by the general form

$$\sigma(t_{\mathrm{TOF}}) = \sqrt{\sigma(0)^2 + \sigma_v^2 t_{\mathrm{tof}}^2}\ , \tag{6.1}$$

that gives the rms position of a particle after a time-of-flight t_{tof} when the initial

Effect	rms size (μm)
Intensifier	0.9 ± 0.2
Diffraction (σ_{diff})	0.5 ± 0.1
Atomic thermal distribution ($\sigma_\perp(0)$)	0.3
Depth of focus ($\sigma_\parallel(0)$)	0.1
Atomic displacement during τ ($\sigma_{\tau,\text{thermal}}$)	0.04
Atomic random walk ($\sigma_{\tau,\text{scatter}}$)	0.02
Quadratic sum	1.1 ± 0.2

Table 6.1: Spatial resolution budget of our system, when the light source is a single atom with temperature $T = 20$ μK illuminated by a probe pulse with duration $\tau = 2$ μs (see text). The rms size of the global response is the quadratic sum of the different rms contributions.

position and the velocity are taken from distributions with standard deviations $\sigma(0)$ and σ_v. We find $\sigma(0) = 1.1 \pm 0.1$ μm and $\sigma_v = 45 \pm 2\,\text{mm.s}^{-1}$. The energy distribution of a single atom in the trap being a thermal Maxwell Boltzmann distribution (Sec. 3.4.1) this translates into a temperature $T = m\sigma_v^2/k_\text{B} = 21 \pm 2$ μK.

Let us now compare the result for $\sigma(0)$ to the expected rms radial position of an atom in equilibrium and trapped in a harmonic potential with depth U and transverse size w_0 (at $1/e^2$), i.e.

$$\sigma_\perp(0) = \sqrt{\frac{k_\text{B}T}{m\omega_\perp^2}}\ , \tag{6.2}$$

where $\omega_\perp$ is the radial oscillation frequency of the atom in the trap. With $\omega_\perp \sim 2\pi \cdot 26$ kHz and $T = 20$ μK, we find $\sigma_\perp(0) = 0.3$ μm, below the diffraction limit of the imaging system. Taking the latter into account, we should thus expect a rms size of 0.6 μm at null time-of-flight, i.e. a factor 1.8 below the actual data (0.5 μm).

6.2.3 Spatial resolution of our imaging system

In order to understand the size at $t_\text{tof} = 0$, we investigated experimentally the effects that contribute to the loss in resolution of our imaging system and lead to the measured value $\sigma(0)$. These effects are listed in Table 6.1 and sum up quadratically to yield a value of 1.1 μm, in agreement with the measure of $\sigma(0)$ obtained in Sec. 6.2.2.

The dominant contribution comes from the loss of resolution of the imaging system due to the intensifier as described in Sec. 4. The second largest contribution comes from the diffraction limit of the imaging optics, which is due to the numerical aperture of the aspheric lens, and was tested by removing the intensifier and illuminating a trapped atom for 100 ms. In this case, the atom acts as a point source for the imaging system and the associated response on the CCD is well fitted by a Gaussian shape with a size $\sigma_\text{diff} = 0.5 \pm 0.1$ μm.

The thermal distribution contributes for 0.3 μm due to the transverse size of the

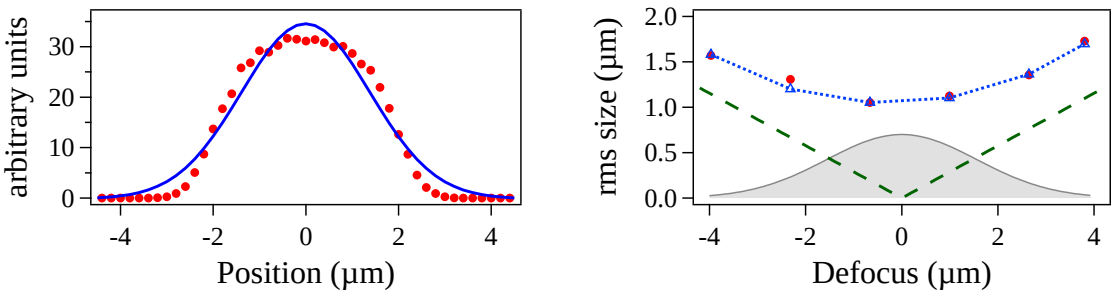

Figure 6.3: Measuring the depth of focus by using a single atom. *left*) The simulated position distribution (red circles) for an atom at 150 μK and a defocus of 4 μm has a rms width of 1.19 μm in agreement with the result of Eq. 6.3. Although a Gaussian fit (blue line) deviates from the simulated result we extract a very close rms value of 1.39 μm. *right*) The measured rms size (red circles) is shown for different defocus. It agrees with a Monte-Carlo simulation (blue dotted line) taking into account the longitudinal profile of the thermal distribution (grey filled curve) with a width $\sigma_{\parallel}(0) = 1.6$ μm. Also shown: Analytical result for the defocus using Eq. 6.3 (dashed green line).

distribution $\sigma_{\perp}(0)$, and 0.1 μm due to the effect of depth of focus associated to the longitudinal size of the distribution $\sigma_{\parallel}(0)$. We measured this effect of the depth of focus by imaging a single trapped atom for various positions of the trap along the optical axis of the imaging system. The right plot in Fig. 6.3 shows the rms size of a Gaussian fit to the data, although for large values of the defocus δz they slightly deviate from a Gaussian (left plot in Fig. 6.3). The results tend asymptotically to the expected rms value σ_{defocus} of a disc with uniform intensity and radius $\delta z \tan\alpha$

$$\sigma_{\text{defocus}} = \frac{1}{2}\,\delta z \cdot \tan\alpha \ , \tag{6.3}$$

where α is related to the numerical aperture by $\sin\alpha = \text{NA}$. For large values of the defocus, the main contribution comes from the depth of focus, which scales linearly with the defocus according to Eq. 6.3 (dashed green line)[1].

Furthermore, we analyze the contribution of the movement of the atom during the probe pulse. Firstly, the photons scattering by the probe induces a random walk of the atom, leading to a rms position in the plane perpendicular to the probe beam

$$\sigma_{\tau,\text{scatter}} = \frac{1}{3} v_{\text{rec}} \sqrt{R}\, \tau^{3/2} \ , \tag{6.4}$$

where v_{rec} is the recoil velocity, R is the spontaneous emission rate, and τ is the duration of the probe pulse (Joffe *et al.*, 1993). Secondly, the atom moves during the probe pulse due to the thermal velocity. The accumulated position distribution for a radially symmetric cloud can be calculated by

[1] The measurement can also be used to measure the axial magnification of the micro trap laser between the fiber and its focal point in the plane of the atom. Moving the fiber by 120 μm we displace the atom by 4 μm resulting in an axial magnification of $g_x^{-2} = 5.5$ comparable to the theoretical result in Sec. 3.3.5.

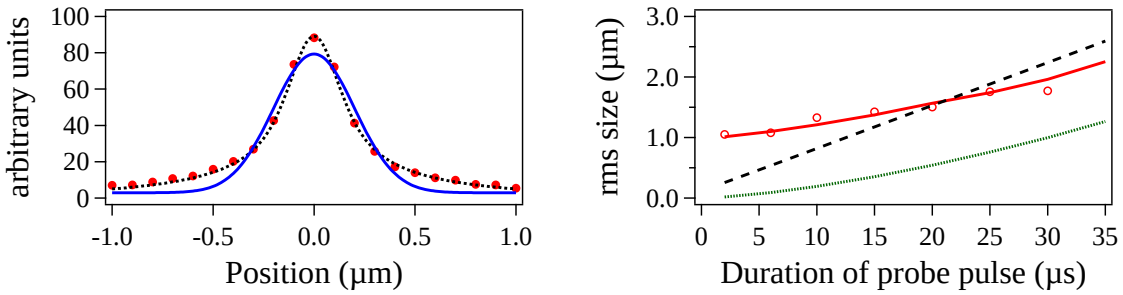

Figure 6.4: Probe-laser effect on the position distribution. *left*) Simulated (red circles) profile of position distribution of a single atom at 150 μK and a probe length of 20 μs. The theoretical result of Eq. 6.5 (black dots) has a rms of 0.9 μm. A Gaussian fit (blue line) with an rms of 0.2 μm is also shown. *right*) rms size of an imaged single atom, versus the duration of the probe pulse. The data (red circles) are in good agreement with the simulation results (blue dotted line). Also shown : analytical rms contributions of Eq. 6.4 (dotted green line) and of Eq. 6.6 (dashed line).

$$P(r) \propto \int_{t_1}^{t_2} \frac{1}{\sigma_\perp^2 + \sigma_v^2 t^2} \exp\left(-\frac{1}{2}\frac{r^2}{\sigma_\perp^2 + \sigma_v^2 t^2}\right) dt \ . \tag{6.5}$$

The left image in Fig. 6.4 shows a simulated position distribution for $\tau = t_2 - t_1 \sim t_2 = 20$ μs that is very well reproduced by Eq. 6.5. An analytical calculation of the associated rms displacement yields

$$\sigma_{\tau,\text{thermal}} = \sigma_v \ \tau/\sqrt{3} \tag{6.6}$$

Both contributions (6.4) and (6.6) broaden the image of a single atom when the duration of the probe τ is increased. We tested this effect by increasing τ up to 30 μs, as shown on the right of Fig. 6.4. Although negligible for 2 μs probe pulses and atoms at 150 μK (as is the case in Fig. 6.4), this effect alone would be comparable to the intensifier response if we were using pulses as long as 20 μs in the perspective of scattering more photons per shot and thus detect single atoms with a larger efficiency.

We confirmed the analysis above by a Monte-Carlo simulation that takes into account all the effects mentioned above. It reproduces accurately our experimental data (see Fig. 6.3 and Fig. 6.4). Here, the simulation indicates a significant deviation from a Gaussian shape for long probe durations or large values of the defocus as shown on the left images in Fig. 6.4 and Fig. 6.3, respectively. This is also the reason why the contribution of Eq. 6.6) is larger than both experimental and simulated results for long probe durations in Fig. 6.4. Because of the presence of noise in our imaging system, see Sec. 6.2.5, we did not consistently observe significant deviations on the real images and could not calculate any reliable value for the rms size of the images. We thus fitted our images with a Gaussian model and compared it to a Gaussian fit of our simulation. The discrepancy between the analytical expression Eq. 6.6 and the results in Fig. 6.4 is an indication of the error that we make by doing so. Note also that we have not included in the model the potential effect of the cooling of the atom

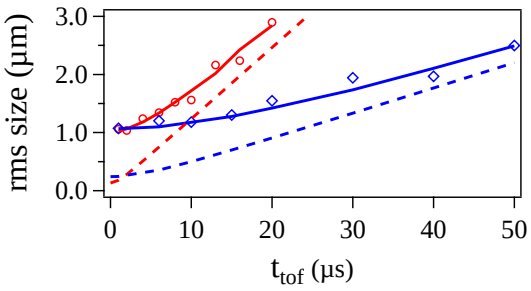

Figure 6.5: Time-of-flight measurement of a single atom. We show the time-of-flight measurements with corresponding simulation for two different temperatures: $T = 20 \pm 2$ μK (blue diamonds) and $T = 150 \pm 16$ μK (red circles). The dashed lines (respectively blue and red) show the results of Eq. 6.1 for the same temperatures and $\sigma_0 = \sigma_\perp(0)$.

by the counter-propagating probe beams.

6.2.4 Temperature results

We now come back to the temperature result obtained by fitting the data using Eq. 6.1. Among all the effects that degrade the resolution, the depth of focus is the only one that varies with the time-of-flight as the atom can fly in the direction parallel to the optical axis. Therefore, Eq. 6.1 is not strictly valid in our case. We now use the Monte Carlo simulation mentioned above to fit the data shown in Fig. 6.2. The starting point of this simulation is a thermal distribution with a temperature that we adjust in order to reproduce the data. We find $T = 20 \pm 2$ μK. Not surprisingly, this result is in good agreement with the rough analysis mentioned in Sec. 6.2.2, since the effect of the depth of focus is small.

Fig 6.5 also shows a measurement for a higher temperature $T \sim 150$ μK, achieved by leaving the dipole trap depth unchanged after loading it with a single atom. This detection method is therefore applicable over a large range of temperatures with no anticipated limitation in the low temperature range. We note that although Eq. 6.1 is not applicable for short time-of-flights, we can however use it for expanded clouds where the size varies linearly with time as $\sigma \sim \sigma_v t$ and is independent of the initial value. Here, only the defocus influences the result. By using the analysis of the last section we find that we overestimate the temperature by ~ 20 % using Eq. 6.1.

6.2.5 Analysis of the noise of the imaging system

We now address the issue of the noise of our imaging system. The peak signal in the time-of-flight image shown in Fig. 6.2(i) is 30600 adu in 1 pixel and corresponds to the detection of ~ 150 single atoms after 3400 shots of 2 μs probe pulses. Normalized to one shot, the mean peak signal is thus 9 adu in 1 pixel. This should be compared to the background noise, which results from three contributions shown in Fig. 6.6: read-out noise from the CCD camera, a background noise contribution from the probe light, and a background noise contribution from spurious light (other than probe light).

We have measured the read-out noise of the CCD camera and found 12 adu in one

image. This noise is independent of the number of shots N_{seq} performed to acquire the image, since the CCD is read out only once after the probe pulses have illuminated the atom and the associated scattered light has fallen on the CCD. Normalized to one shot, the read-out noise of the CCD thus scales as 12 adu/$\mathrm{N_{seq}}$. By contrast, the contributions, per shot, of the probe light and spurious light, scale as $1/\sqrt{N_{\mathrm{seq}}}$. The three contributions were measured independently and add up quadratically to yield the data shown in Fig. 6.6. The signal to noise ratio is by far limited by the probe light contribution, which is due in part to scattering by atoms of the Rb beam intersecting the trapping region, and in part to scattering by the optics mounts under vacuum. We decrease this noise contribution by reducing the waist of the probe beam from 6 mm to 1 mm in all following experiments. A noise calibration for the smaller probe waist is described in Sec. 8.3.4.

Figure 6.6 allows us to extract the number of sequences necessary to reach a given signal-to-noise ratio. As explained at the end of Sec. 6.2.2, the probability to detect one photon (and therefore one atom) in single shot is $4.4 \cdot 10^{-2}$ using a 2 μs-duration probe, meaning that 23 shots are necessary to detect on average one photon. For a time-of-flight image to be correctly fitted, we have found that we need typically 100 detected photons, which implies 2300 sequences. For instance, in the case of the image shown in Fig. 6.2(i), the signal to noise ratio is ~ 20, while it is ~ 9 for Fig. 6.2(iii).

6.3 Measuring the temperature by using a release-and-recapture method

We use the release-recapture technique to cross check the temperature measurements done by the time-of-flight fluorescence integration method. It has been introduced by measuring the temperature of a molasses (Lett *et al.*, 1988) and can easily be applied to a single atom. The experimental sequence is shown on the left of Figure 6.7. We work in the exact same conditions as for the time-of-flight measurement to allow for comparison. The method uses the APD to detect the presence or the absence of the atom in the trap after release for a variable time t_{rel}. Averaging over typically 200 sequences we reconstruct the recapture rate depending on the release time. It is based on the idea that hotter atoms leave the trap region faster than colder ones during the release time. The results obtained by the release-and-recapture method are shown on the right of Fig. 6.7. A fit using a Monte-Carlo simulation (Darquié, 2005; Beugnon, 2007; Tuchendler *et al.*, 2008) to the data yields a temperature $T = 19 \pm 2$ μK and 149 ± 15 μK for an atom in a trap depth of $U_{low}/k_{\mathrm{B}} = U_0/k_{\mathrm{B}} \sim 2.2$ mK and $U_{low}/k_{\mathrm{B}} \sim 0.08$ mK, respectively, and is in good agreement with the results of the time-of-flight method. The agreement is also a confirmation of the calculated radial magnification 26 ± 2 of our imaging system.

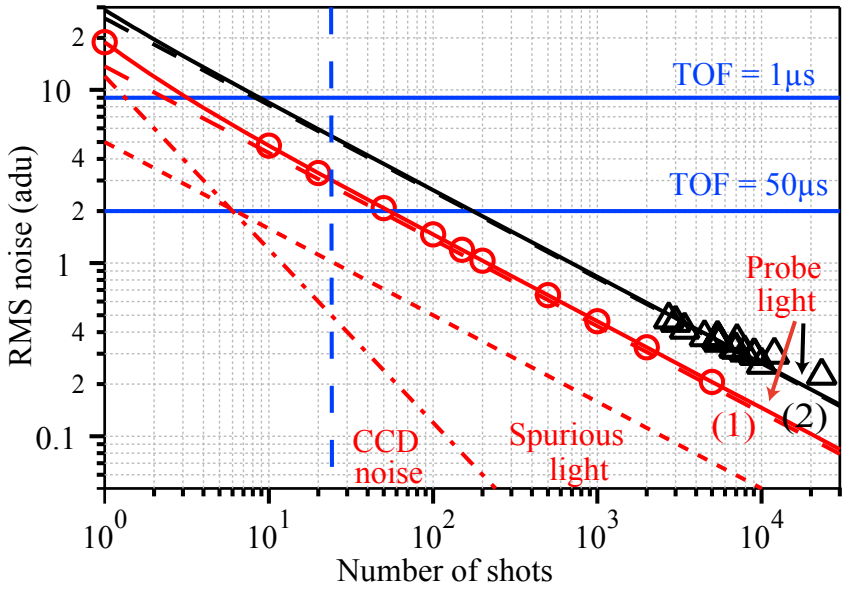

Figure 6.6: Image noise contributions. Noise contributions, normalized to one shot, of our imaging system, versus the number of shots performed to acquire an image. The total rms noise (solid lines) is the quadratic sum of three contributions that were measured independently : the CCD read-out noise (red dash dotted line) and the background contributions due to spurious light (red dotted line) and probe light (dashed lines). The latter is larger when the atomic beam is switched on (case (2): black dashed line) than when it is off (case (1): red dashed line), due to the scattering by atoms of the atomic beam intersecting the probe beam. In both cases, the quadratic sum of the three contributions is in good agreement with the measured rms values of the total noise (black triangles and red circles, respectively). The peak signal, normalized to one shot (blue horizontal lines) is shown for two values of the time-of-flight, $t_{\mathrm{TOF}} = 1$ μs and $t_{\mathrm{TOF}} = 50$ μs, corresponding to images shown in figure 6.2(i) and (iii). The vertical dashed line indicates the minimum number of shots required to detect one atom.

6.4 Conclusion

We have performed fluorescence imaging of a single atom in free flight by accumulating many images containing a single photon event corresponding to a single atom. We used this time-of-flight technique to measure the temperature of the atom after release from the optical dipole trap. This temperature measurement was confirmed by an independent method based on a release-and-recapture technique (Fuhrmanek *et al.*, 2010b). The large numerical aperture of our imaging system and the extreme confinement of the atoms in the trap allow a high spatial resolution on the order of ~ 1 μm. The low noise level of our imaging system yields images showing ~ 150 atoms with a very good signal to noise ratio (~ 20). These measurements have been performed in conditions where the atomic motion during the probe pulse can be completely neglected (see table 6.1). We thus obtained a very accurate characterization of the optical performance of our system. Finally, the measurements and the analysis presented provide a calibration of our imaging system for time-of-flight experiments

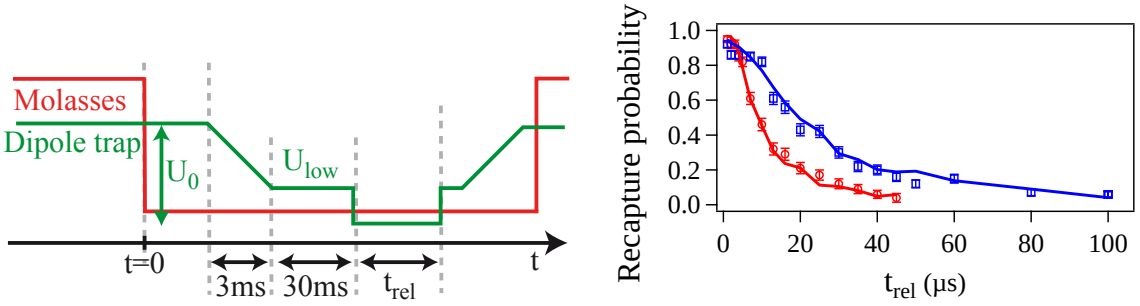

Figure 6.7: Release-and-recapture measurement of a single atom. *left*) Experimental sequence used for the release-recapture method. A single atom is trapped and cooled in the dipole trap U_0. After adiabatic lowering to U_{low} the trap is switched off for t_{rel}. The trap depth is then ramped back up to U_0 and we check for the presence of the atom. *right*) Release-and-recapture measurements of a single atom for the same loading and cooling parameters as in Fig. 6.5. The fit (lines) yields $T = 19 \pm 2$ μK and 149 ± 15 μK (data points are in blue squares and red circles, respectively).

where many atoms are confined in a microscopic dipole trap, and where interactions may play a central role.

Chapter 7

Lossless state detection of a single trapped atom

Contents

In Sec. 5.2.3 we discussed the "push-out" technique to measure the hyperfine state of an atom. Although this technique has been proved to be efficient and quantum projection limited (Jones *et al.*, 2007), it does not discriminate between detection-induced losses from any other unwanted losses[1]. In this chapter we describe the implementation of a state detection that relies on a fluorescence measurement (Wineland *et al.*, 1980) without losing of the atom. The idea is the following: We identify a bright and

[1] This has been a major difficulty for calculating the entanglement fidelities using single neutral Rydberg atoms (Wilk *et al.*, 2010; Isenhower *et al.*, 2010)

a dark state to each hyperfine ground state. The bright state is coupled to an excited state by a closed optical transition. The signature of the bright state population is the emission of fluorescence light by the atom when it is illuminated by a probe laser tuned to this transition. The signature of the dark state population, on the contrary, is the absence of fluorescence due to the large hyperfine splitting of 6.8 GHz. As this method relies on photon scattering, the energy of the probed atom or ion increases with the number of recoils. In the case of e.g. ions, trap depths of several thousands of Kelvins are typical, leading to a very efficient state detection with a negligible loss probability. There, detection fidelities as high as 99.99 % have been reported (Myerson *et al.*, 2008).

However, the detection technique mentioned above, when applied to neutral atoms, is hampered by the small trap depth, typically lower than a few milliKelvins. The heating induced by the probe laser leads more easily to the loss of the atom before one can collect enough photons to decide in which state the atom is. One way to implement lossless and yet efficient detection is to place the trapped atom in an optical cavity. Thanks to the Purcell effect, the fluorescence rate is enhanced in the cavity mode such that enough fluorescence photons can now be collected without losing the atom. Recently, two experiments demonstrated the state selective detection of a single atom using an optical cavity with reported fidelities larger than 99.4 % (Bochmann *et al.*, 2010; Gehr *et al.*, 2010).

In our setup we can simply make use of our aspheric lens with a high numerical aperture to efficiently collect the fluorescence emitted by an atom trapped in an optical dipole trap, without the need for a cavity. We follow this route and demonstrate a single-shot detection of the internal state of a rubidium 87 atom trapped in an optical tweezer. The fidelity of this state selective detection method is 98.6 % in 1.5 ms and the probability to lose the atom during the detection is less than 2 %. Similar results have been found by Gibbons *et al.* (2011).

The bright state used in our experiment is the hyperfine Zeeman state $|\uparrow\rangle = |5S_{1/2}, F=2, m_F=+2\rangle$. It is coupled to the excited state $|e\rangle = |5P_{3/2}, F'=3, m'_F=+3\rangle$ by a closed transition at $\lambda = 780$ nm. The advantage of using a closed transition is that no depumping into other states, e.g. dark states, takes place. The dark state can be any Zeeman state of the $(5S_{1/2}, F=1)$ manifold, including $|\downarrow\rangle = |5S_{1/2}, F=1, m_F=+1\rangle$ [2]. It is separated from the bright state by ~ 6.835 GHz. Let us estimate the feasibility of the state detection, using probe light tuned to the transition between $|\uparrow\rangle$ and $|e\rangle$. To do so, we consider an atom prepared at the bottom of our dipole trap at 850 nm in state $|\uparrow\rangle$ and we estimate the number of absorption-spontaneous emission cycles that elevate the energy of the atom by an amount equal to the trap depth U. For $U/k_B = 2$ mK (typical value for our experiment), this number is on the order of $U/2E_r \sim 5000$ ($E_r = \frac{\hbar^2 k^2}{2m}$ is the recoil energy induced by a photon with a wave vec-

[2] The states $|\downarrow\rangle$ and $|\uparrow\rangle$ are commonly used as qubit states and can be manipulated by microwaves (Kuhr *et al.*, 2003) or Raman lasers (Yavuz *et al.*, 2006).

tor $k = 2\pi/\lambda$, m is the mass of the atom). This number puts constraints on the probe light parameters in order to detect the atom without losing it. Taking for the saturation parameter $s = I/I_{\text{sat}} = 0.1$ and for the probe duration $\Delta t = 1$ ms yields a number of scattered photons $\frac{\Gamma}{2}\frac{s}{1+s}\Delta t \sim 2000$ during the probe pulse, below the 5000 photons calculated above. Using an imaging system with a detection efficiency of 0.6 % (see Sec. 3.3.5), one thus expects to detect ~ 11 fluorescence photons in 1 ms. As our noise level is well below 1 photon during this time, the bright state $|\uparrow\rangle$ should be identified unambiguously. Based on this estimation we implement this method on a single atom.

The first step is to prepare the atom in the qubit states $|\downarrow\rangle$ and $|\uparrow\rangle$. The preparation procedure will be described in the next section. In a second step we want to focus in more detail on the approximation made above that justifies a reliable state read-out without loosing the atom (see Sec. 7.3). Finally, Sec. 7.4 focuses on the read-out of the state and the measure of its fidelity.

7.1 Résumé

Nous avons mis en place une lecture de l'état interne d'un atome unique piégé dans la pince optique sans perte d'atome. Cette méthode est basée sur la détection de la fluorescence induite par la sonde. La fidélité de la détection de l'état atomique est actuellement de 98.6 % sur un coup, avec des améliorations techniques possibles à l'avenir. Combinée à notre capacité à contrôler efficacement les états internes des atomes (Jones *et al.*, 2007; Wilk *et al.*, 2010), cette détection d'état non-destructive complète notre boîte à outils pour l'ingénierie quantique. En outre, l'absence de perte d'atome évite le rechargement de l'atome après chaque mesure, améliorant ainsi le rapport cyclique de nos expériences. Elle évite également des corrections a posteriori lors de l'exécution d'opérations quantiques sur un ensemble de qubits d'atomes neutres (Fuhrmanek *et al.*, 2011).

7.2 State preparation by optical pumping

We want to distinguish between the preparation into a hyperfine level and a specific Zeeman sub-level as their efficiency measurements rely on different experimental techniques.

7.2.1 Hyperfine state preparation

We measure the fidelity of the preparation in $5S_{1/2}, F = 2$ or $5S_{1/2}, F = 1$ by using the "push-out" technique introduced in Sec. 5.2.3. The preparation sequence is shown in Fig. 7.1. We load a single atom in a $U_0/k_B = 2.7$ mK deep trap and ramp down the trap to $U_{low}/k_B = 0.3$ mK corresponding to a light shift of ~ 6 MHz. During the entire sequence the compensation coil currents are set such that the residual magnetic field is minimized to ~ 70 mGauss as described in Sec. 5.4.1. In this configuration the atom is sub-Doppler cooled to 35 μK. It corresponds to the $\frac{k_B T}{h\nu} \sim 4$th vibrational

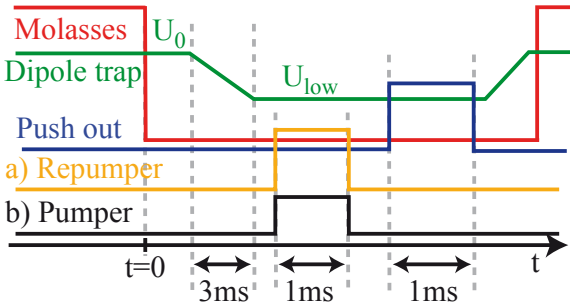

Figure 7.1: Single atom hyperfine state preparation sequence. We load a single atom in a trap with $U_0/k_B = 2.7$ mK and adiabatically ramp it down to $U_{low}/k_B = 0.3$ mK. Here, we prepare the atom in the state a) $5S_{1/2}, F = 2$ by using the repumper probe laser or b) $5S_{1/2}, F = 1$ by using the pumper laser.

level of the trap with its radial oscillation frequency being $\nu = 162$ kHz. We now distinguish between the preparation in a) $5S_{1/2}, F = 2$ and b) $5S_{1/2}, F = 1$:

- **a)$5S_{1/2}, F = 2$** We use the uni-directional σ^+ repumper probe laser to pump the atom into $5S_{1/2}, F = 2$. If the atom is initially in $5S_{1/2}, F = 1$ the atom scatters on average 2 photons before it is pumped into $5S_{1/2}, F = 2$. The probability for the atom to scatter less than two photons for a repumper probe time of only 1 μs is already as low as 10^{-3} for a laser saturation of $s \sim 2$. Once in $5S_{1/2}, F = 2$ the atom does not scatter laser photons any more and remains in the trap unheated. We can therefore choose our repumping interval much larger (1 ms) to increase the preparation probability without extra heating. Afterwards the "push-out" is used to detect the atom hyperfine state. Finally, we ramp back up the dipole trap power to U_0 and check if the atom is still present by using the molasses beams. We find a hyperfine state preparation efficiency of 99.97 %, obtained by recapturing 2 atoms after 6000 cycles[3].

- **b)$5S_{1/2}, F = 1$** We use the uni-directional σ^+ pumper laser for 1 ms to prepare the atom into $5S_{1/2}, F = 1$. The pumper laser is on resonance with the 6 MHz light-shifted transition $5S_{1/2}, F = 2 \rightarrow 5P_{3/2}, F' = 2$ with saturation $s \sim 0.1$. If the atom is initially in $5S_{1/2}, F = 2$ the atom scatters on average 2 photons to be pumped into $5S_{1/2}, F = 1$. We again use the "push-out" beam to detect the atom hyperfine state and find preparation efficiencies similar to case a).

The "push-out" technique is insensitive to the preparation of a particular Zeeman state. The next section will show how the preparation in state $|\uparrow\rangle = |5S_{1/2}, F = 2, m_F = +2\rangle$ is achieved.

7.2.2 Zeeman state preparation

Figure 7.2 illustrates the preparation into state $|\uparrow\rangle$. As before we prepare the atom in a trap with $U_{low}/k_B = 0.3$ mK and a residual magnetic field $B_{res} = 70$ mGauss. Here, we illuminate the atom with the preparation lasers, i.e. the uni-directional σ^+ repumper probe and pumper laser, for a time t_{pump}. Initially we do not know in which

[3]There is a very small probability (< 1 %) that an atom is lost before the "push-out" pulse is applied, which would lead to an overestimation of the preparation efficiency by $< 10^{-5}$.

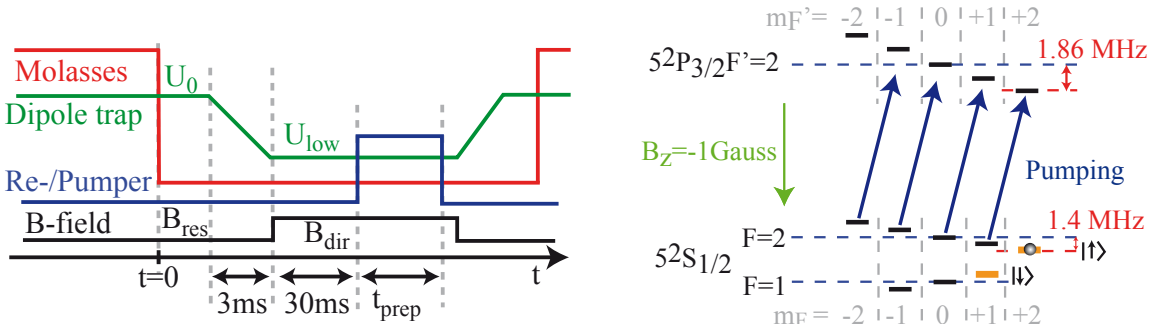

Figure 7.2: Single atom optical pumping sequence. *left*) Experimental sequence used to prepare a single atom in the state $5S_{1/2}F=2, m_F=+2$. *right*) Rb level scheme under a magnetic bias field $B_z=-1$ Gauss. The pumper laser drives the atom into state $|\uparrow\rangle$. The linear trap polarization points in z-direction and is thus parallel to the magnetic bias field.

state the atom has been prepared. The repumping laser is necessary in case the atom was initially in one of the $5^2S_{1/2}F=1$ Zeeman states. The pumping laser is necessary to pump the atom into the state $5^2S_{1/2}F=2, m_F=+2$. Assuming the atom having been prepared in the $5^2S_{1/2}F=2, mf=-2$ state it only takes ~ 20 photons to pump it into $5^2S_{1/2}F=2, mf=+2$ with efficiencies of 99.999 %, which can be calculated by solving the rate equations as given in App. C. For a pumping laser saturation $s\sim 0.1$ we estimate $t_{prep}\sim 20$ μs for the preparation. In a perfect situation the atom would then be pumped into $|\uparrow\rangle$ and would stop scattering more photons even if the laser pulse exceeds 20 μs. In this case the atom would stay unheated in $|\uparrow\rangle$ resulting in a recapture rate ~ 100 %. There are however several experimental issues for which this is never entirely the case and a drop in the recapture rate can be observed:

- **Improper quantization axis** A quantization axis which is not parallel with the preparation laser leads to a improper laser polarization seen by the atom. If the preparation laser polarization is not properly σ^+ polarized, the atom keeps scattering photons since it is never really pumped into the dark state $|\uparrow\rangle$. We can therefore impose a quantization axis by applying a bias magnetic field B_{dir} parallel to the preparation laser in z-direction.

- **Residual magnetic field** Figure 7.3 shows the effect of a residual magnetic field $B_{res,\perp}$ that is perpendicular to the preparation laser direction. This magnetic field depumps an atom prepared in state $m_F=+2$ into $m_F=+1$ at the rate of the Larmor frequency $\Omega_B=\frac{g_F m_F \mu_B}{\hbar}B_{res,\perp}$. The depumping leads to a heating of the atom since it continues to scatter photons from the pump laser field as it is never well prepared in the dark state $m_F=+2$. A bias magnetic field B_{dir} can help here, too. It reduces the depumping rate thanks to the introduced Zeeman level shift $\Delta\propto B_{dir}$ as explained below.

In order to estimate the efficiency of the preparation in the $m_F=+2$ Zeeman state, we calibrate our bias magnetic field and analyze the residual heating rate induced by the preparation lasers.

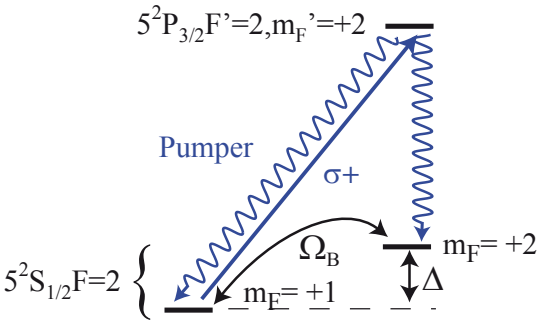

Figure 7.3: Preparation laser heating due to magnetic depumping. We show the main Zeeman sub-levels that participate in the state preparation using the σ^+ pumping laser. A residual magnetic field perpendicular to the pumping laser leads to a coupling Ω_B between the ground Zeeman levels, which have an energy difference Δ induced by the bias magnetic field.

Calibration of the magnetic field director

The first experiment in this context is a fine tuning of the pumper frequency. The magnetic field stays at B_{res} and the preparation laser length at $t_{prep} = 2$ ms. Figure 7.4 shows the recapture rate as a function of the pump laser frequency driving the $5^2S_{1/2}F = 2 \rightarrow 5^2P_{3/2}F' = 2$ transition. If the laser is resonant with the transition the atom keeps scattering photons and is heated out of the trap. The line has a width of $\sim \Gamma/2\pi$ as expected for a cold trapped atom and is shifted by ~ 4 MHz with respect to the vacuum transition frequency, here taken to be 0 MHz. The shift is due to the dipole-trap induced light shift and is slightly smaller than the expected 6 MHz for a trap depth of 0.3 mK. The discrepancy could be due to the acoustic optical modulator that is working at the edge of its radio frequency bandwidth. This is also the reason why we did not scan the transition line entirely.

We continue by adjusting the bias magnetic field strength B_{dir}. On the left side of Fig. 7.5 we change the final value of the bias magnetic field B_{dir} using the $z-$coils and measure the single atom recapture rate. It is very low for no bias field in the $z-$direction. Here, a residual magnetic field perpendicular to the z-direction leads to a mixing of the Zeeman sub-levels and an inhibits the preparation of a proper dark state. Increasing the magnetic field we observe a sharp rise of the recapture rate which already levels off for very small bias fields of $B_{dir} \sim 0.2$ Gauss. For higher fields the atom is more efficiently pumped into the dark state and scatters less photons. It is therefore less likely to lose the atom in this situation.

For a theoretical description we restrict ourselves to states $g \equiv 5^2S_{1/2}F = 2, m_F = +1$ and $e \equiv 5^2P_{3/2}F' = 2, m_{F'} = +2$ to be coupled by the residual magnetic field (in analogy to the micro-wave spectroscopy in Sec. 5.4). The Rabi frequency Ω_B corre-

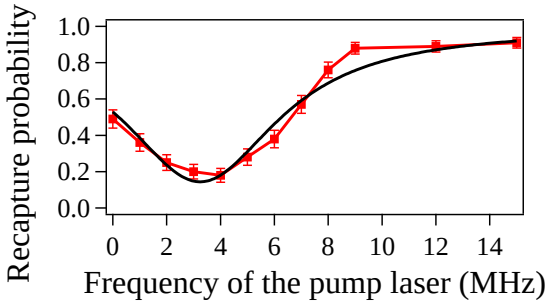

Figure 7.4: Pump laser transition. Single atom recapture rate versus the pumping laser frequency driving the $5S_{1/2}F = 2 \rightarrow 5P_{3/2}F' = 2$ transition. A lorentzian fit (black line) reveals a width of $\sim \Gamma$ at a ~ 4 MHz light-shifted position. The scan is cut to the left due to limitations of the AOM.

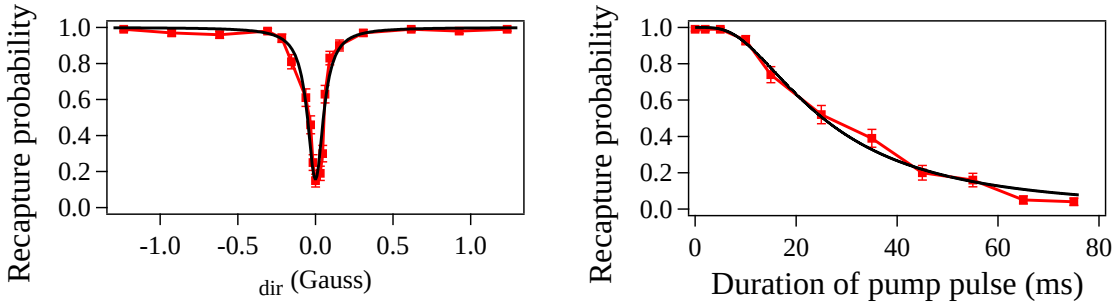

Figure 7.5: Single atom state preparation. *left*) Single atom recapture rate versus the magnetic field imposed by the z-compensation (blue circles) coils for a duration of the pumper pulse of 2 ms. The black line is a lorentzian fit. *right*) Dependence of the recapture rate versus the duration of the pumper pulse for a bias magnetic field $B_{dir} = -1$ Gauss. The black line is a fit of Eq. 5.5.

sponds to the Larmor frequency in this case and the level shift Δ is the Zeeman level shift imposed by the bias field B_{dir} (see Sec. 1.4). We fit Eq. 5.7 and find $\Omega_B/2\pi = 39$ kHz corresponding to a residual magnetic field perpendicular to the z-direction $B_{res,\perp} = 56 \pm 9$ mGauss, which is very close to the value measured in Sec. 5.4 of $B_{res} = 70$ mGauss. This means that ~ 20 % of the residual magnetic field is actually along z, which corresponds to an angle of $\cos^{-1}\left(\frac{56}{70}\right) \sim 38°$ that the B-field vector forms with the $x-y$ plane (see Fig. 3.2).

We want to work at a bias field much higher than 0.2 Gauss but not too high to avoid that the bias field shifts the Zeeman sub-levels out of resonance with the preparation lasers. We choose for the bias field $B_{dir} = -1$ Gauss for which the Zeeman shift is still smaller than the atomic line width $\Gamma/2\pi$ and the lasers stay on resonance with the trapped atom.

Preparation laser heating rate

In order to measure the heating rate we do the following experiment. We change the preparation pulse length t_{prep} and measure the recapture probability shown on the right side of Fig. 7.5 for a bias magnetic field $B_{dir} = -1$ Gauss. We use the model introduced in Sec. 5.3 to extract the heating rate α. A fit of Eq. 5.5 illustrated by the black line on the right side of Fig. 7.5 yields $\alpha = 2.5 \pm 1$ μK/ms and the trap depth $U_{low}/k_B = 0.21 \pm 0.07$ mK, the initial atom temperature being a constraint parameter of the fit at $T_0 \sim 11$ μK. The extracted trap depth is lower than the expected value $U_{low}/k_B = 0.3$ mK obtained by measuring the trap laser power. This is due to the radiation force effect induced by the uni-directional preparation laser in Eq. 1.28. Fig. 7.6 shows how the original trap profile with depth $U_{low}/k_B = 0.3$ mK is inclined due to the radiation pressure force and results in an effectively lower trap $U_{low}/k_B =$ 0.15 mK. This value agrees with the fit result.

The measured heating rate can be used to estimate the population Π in states other than $F = 2, m_F = +2$. We find $\Pi_{F=2 m_F \neq +2} = \frac{\alpha}{2E_{rec}\frac{\Gamma}{2}\frac{s}{1+s}} = 0.4 \pm 0.2$ % with a pump-

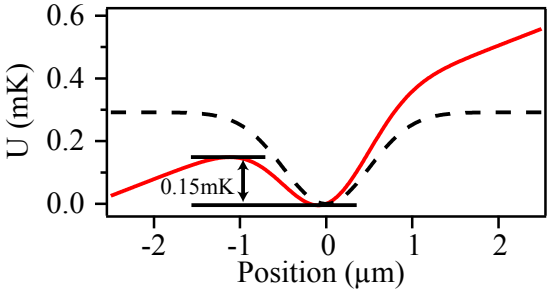

Figure 7.6: Effective trap depth due to radiation pressure. In the absence of any near-resonant light the 0.3 mK deep trap has a Gaussian shape (black dashed curve). Resonant light at e.g. $s \sim 0.1$ creates a radiation force on the atom which produces a tilted Gaussian profile (red curve) with an effectively smaller trap depth 0.15 mK.

ing laser saturation parameter of $s \sim 0.1$. The preparation efficiency into the state $|\uparrow\rangle$ is therefore 99.6 ± 0.2 %.

Note that the measured value agrees within the error bar with the theoretical result of Eq. 5.7. There, we calculate a population in $F = 2, m_F \neq +2$ of 0.3 % for a bias magnetic field of $B_{dir} = -1$ Gauss and a residual magnetic field perpendicular to the z-axis of 55 mGauss.

7.3 Understanding the lossless state read-out

Fig. 7.7 shows the preparation procedure as it is used in the following. We always work with a single atom in a trap $U_{low}/k_B = 0.3$ mK at 11 μK. The repumper laser is switched on for 1.6 ms to ensure a proper preparation in $F = 2$ as discussed in Sec. 7.2.1. 1 ms after switching on the repumper laser, the pumper laser is used for 500 μs to pump the atoms into $|\uparrow\rangle$, while the magnetic field is $B_{dir} = -1$ Gauss. On the right side of Fig. 7.5 we see that for 500 μs the atom stays still trapped with a high probability. On the other hand it is sufficient for a proper preparation as the atom only needs to scatter photons during 20 μs on average to be pumped into $|\uparrow\rangle$. After the preparation we can change the trap depth to U_f and probe the closed transition $|\uparrow\rangle \leftrightarrow |e\rangle$ (see Fig. 1.5). The state read-out must be performed by using the probe laser to conserve a hyperfine-sensitive result. No repumper laser should be used here, otherwise we would lose all information on the initial state since we would detect photons no matter which state the atom has been prepared in.

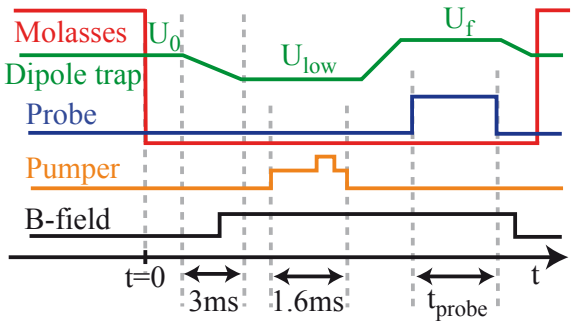

Figure 7.7: State $|\uparrow\rangle$ preparation and read-out sequence. A single atom is prepared in a $U_{low}/k_B = 0.3$ mK deep trap with a temperature of 11 μK by adiabatic lowering from $U_0/k_B = 2.7$ mK in ~ 3 ms. The 1.6 ms repumper pulse is superimposed on a 500 μs long pumping pulse ($s \sim 0.1$) for preparation. The read-out is done at trap depth U_f by using the probe laser. Finally, we check for the presence of the atom.

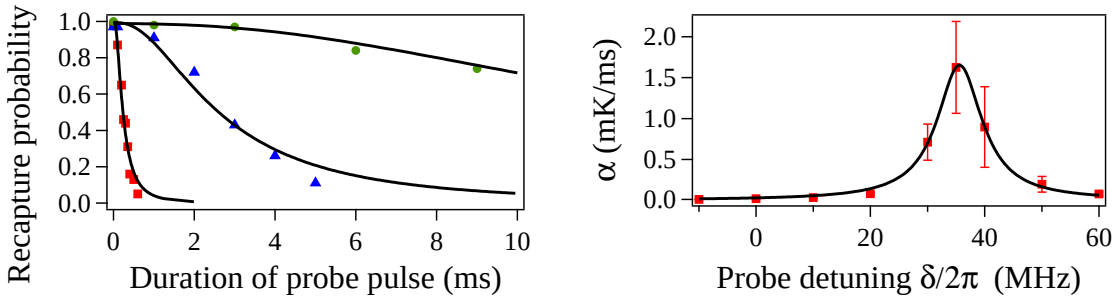

Figure 7.8: Atom heating due to probe laser. *left*) Single atom recapture probability versus the probe duration t_{probe}. The atom is in a trap of $U_f/k_B = 1.7$ mK ($U_f/h = 36$ MHz) and heated by the probe laser with $s \sim 0.3$ and frequencies $10, 35, 50$ MHz (green circles, red squares, blue triangles) blue detuned with respect to the vacuum resonance. A fit of Eq. 5.5 allows to extract the heating rates $\alpha = 0.02 \pm 0.005, 1.6 \pm 0.6, 0.2 \pm 0.1$ mK/ms, respectively. *right*) The heating rate α is shown versus the probe detuning δ. A lorentzian fit (Eq. 7.1) has a width of 8 ± 2 MHz and slightly broader than the natural line width $\Gamma/2\pi$. The center is at 35.6 ± 0.1 MHz and corresponds to the light shift U_f/h.

There are two difficulties in detecting the prepared state without losing the atom. First, we need to make sure that we detect enough photons before the atom is lost. In the introduction we estimated that our collection efficiency is high enough to fulfill this requirement. Second, using the probe laser only, we need to make sure that the atom cycles in the closed transition and is not depumped into the $F = 1$ manifold before or during the readout. In the next section we will take a look at the atom loss due to the probe heating and we will then address the depumping rate.

7.3.1 Probe-induced atom loss

We choose a trap depth of $U_f/k_B = 1.7$ mK and study the heating process of the atom inside the trap illuminated by our uni-directional probe laser. We also use the repumper probe laser to avoid depumping into the $F = 1$ manifold. Depending on the length of the probe interval the recapture rate of the atom changes as can be seen on the left side of Fig. 7.8. Here, we measure the single atom loss for several probe laser frequencies keeping its saturation constant $s \sim 0.3$.

We again use Eq. 5.5 to model the data on the left of Fig. 7.8 and extract the heating rate α considering that the probe laser leads to an effective trap depth smaller than 1.7 mK due to radiation pressure. On resonance for example it decreases the trap depth to 1.3 mK. The heating rate $\alpha = 2E_{rec}R$ is proportional to the fluorescence rate

$$R = \frac{\Gamma}{2} \frac{s}{1 + s + 4\left(\frac{\delta - U_f/\hbar}{\Gamma}\right)^2}, \tag{7.1}$$

which has a lorentzian profile (see Eq. 1.28). A fit with fixed saturation $s = 0.3$ yields a width of 8.5 ± 0.3 MHz again slightly larger than Γ due to the finite temperature

and high saturation parameter. The peak is at 35.7 ± 0.1 MHz and is compatible with the trap depth $U_f/k_\mathrm{B} = 1.7$ mK ($U_f/h = 36$ MHz). The peak height 1.6 ± 0.6 mK/ms is explained by $2E_{rec}\frac{\Gamma}{2}\frac{s}{1+s} = 1.6$ mK/ms.

7.3.2 How closed is the closed transition?

The closed transition is not completely closed due to the residual magnetic fields, improper light polarization and trap-light induced Raman transitions. During or before the read-out interval this can lead to a change in hyperfine level and a loss of information. Let us estimate these contributions.

Raman transitions

The trap-induced Raman transitions have been discussed in Sec. 1.5.7. If a Raman transition occurs between the state preparation and read-out we would measure the bright (dark) state although it has been prepared in the dark (bright) one. We can minimize the Raman transition rate by decreasing the time between preparation and read-out pulses between which we only apply a linear adiabatic ramp from $U_{low}/k_\mathrm{B} = 0.3$ mK to U_f. For a trap depth $U_f/k_\mathrm{B} = 1.7$ mK the ramp has a duration of 3.5 ms. For typical probe time length t_probe of 1 ms the depump rate from $|\uparrow\rangle$ into $|\downarrow\rangle$ is ~ 0.1 % by using Eq. 1.43.

Probe-induced depumping

Due to the large but finite level spacing between $F' = 2$ and $F' = 3$ of 266 MHz there is a small probability $\frac{s}{1+s+4(266/6)^2} \sim 10^{-5}$ ($s \sim 0.1$) to be excited into $5^2\mathrm{P}_{3/2}\mathrm{F}' = 2$ by the probe laser if the atom is in any Zeeman sub-level $5^2\mathrm{S}_{1/2}\mathrm{F} = 2$ except $|\uparrow\rangle$. From the excited state $5^2\mathrm{P}_{3/2}\mathrm{F}' = 2$ it deexcites into $5^2\mathrm{S}_{1/2}\mathrm{F} = 1$ with 50 % chance and does not scatter any probe photons.

We want to estimate the depump rate. No matter in which Zeeman sub-states of $5^2\mathrm{S}_{1/2}\mathrm{F} = 2$ the atom is initially prepared in, it quickly cycles into the closed transition due to the σ^+ polarization of the probe laser. We assume the atom to be in $|\uparrow\rangle$ during the probe interval (probe with $s \sim 0.1$) with the same probability 99.6 % as during the preparation interval (pumper with $s \sim 0.1$). This can be justified by the fact that the probe laser beam has the same polarization characteristics as the pumper laser beam as they pass the exact same optics. Overall the probe-induced depump rate from $|\uparrow\rangle$ into $|\downarrow\rangle$ is estimated to be $\sim 10^{-5} \cdot 0.5 \cdot 0.004 = 2 \cdot 10^{-8}$ and is therefore negligible.

Experimentally we can get an indication of the low depump rate into the dark state by monitoring the scattered photons emitted by the single atom during the probe read-out pulse. After the preparation process the trap is ramped to $U_f/k_\mathrm{B} = 3$ mK and the atom is illuminated with the unidirectional probe for 3 ms. The probe frequency is set to 70 MHz to be resonant with the trapped atom. We perform two measurements where we compare the detected fluorescence in two situations: In the

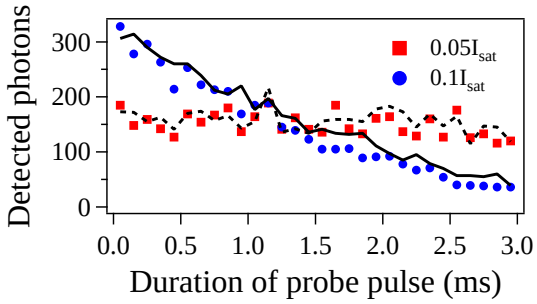

Figure 7.9: Probe-induced depump probability. Fluorescence of a single atom averaged over 500 sequences with two different probe pulse powers of 0.05 I_{sat} and 0.1 I_{sat}. The black curves correspond to the fluorescence when the repumper probe laser is additionally switched on. The recapture rate over 500 sequences is 99 % and 70 %, respectively.

first case we use the probe laser only. Once depumped into $|\downarrow\rangle$ the atom stops fluorescing and we detect a decrease of the fluorescence over time. In a second scenario we additionally use the repumper probe laser in which case a depumping into $|\downarrow\rangle$ should not lead to any decrease of the fluorescence.

Figure 7.9 shows the fluorescence detected by the APD averaged over 500 sequences. For a probe intensity $s = 0.05$ the fluorescence level stays constant and the atom is not heated out of the trap, which is also indicated by the recapture rate which we measure to be 99 %. Adding the repumper laser does not change the amount of detected fluorescence. This means that the atom seems to stay in the cycling transition throughout the probing interval without being depumped into $|\downarrow\rangle$. For a higher probe intensity 0.1 I_{sat} the fluorescence is initially about twice as high but quickly decreases. The decrease can be attributed to the heating and subsequent loss of the atom due to the scattering process. This reasoning would be supported by the recapture rate which decreases to 70 %. A second effect for a decreasing fluorescence may be the changing light shift. In the deep trap the atom will be heated by the probe laser. The hot atom will quickly be driven out of resonance with the probe due to the light shift which changes with temperature via the atomic motion. Again we do not have any indication for a depumping into $|\downarrow\rangle$ since almost the same fluorescence is observed using the repumper probe laser in parallel with the probe.

The result for $s = 0.05$ shows that the atom can scatter at least 1500 photons without being depumped in the state $5^2S_{1/2}F = 1$. And even for $s = 0.1$, corresponding to 3900 photons scattered, the atom does not seem to be considerably depumped in the state $5^2S_{1/2}F = 1$ either. This measurement is unfortunately not sensitive enough to measure the depump probability precisely. It gives however an intuition that the fluorescence is not much influenced by a possible depumping. A more accurate measurement could be done by applying the "push-out" technique after the probe interval.

7.4 State detection of a single atom

We now want to measure the fidelity of the state read-out, i.e. the detection efficiency of the atom in state $|\uparrow\rangle$ and $|\downarrow\rangle$. This can be done by measuring the detected photon

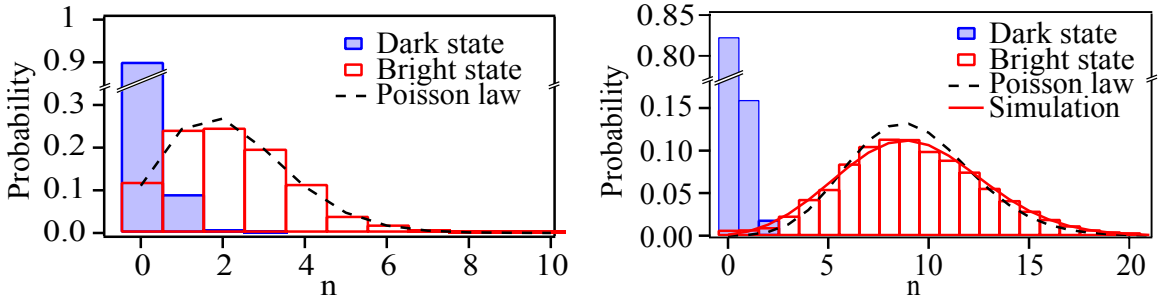

Figure 7.10: Detected photon distribution. *left*) Histogram of the photon detection probability versus the number of detected photons when the atom is in $|\uparrow\rangle$ (red bars) or $|\downarrow\rangle$ (blue bars) for a trap depth of 0.3 mK, a probe pulse length of 0.75 ms and $s \sim 0.01$. The black dashed line is a Poissonian fit to the data. *right*) Same situation as on the left but for an atom in a 1.7 mK trap, a duration of the probe pulse of 1.5 ms and $s \sim 0.06$. The sequence is repeated 10000 times. The red fit is a simulation taking into account shot-to-shot fluctuations of the dipole trap.

distributions of the atom when it is in the dark or bright state. We measure both distributions for several trap depths $U_f/k_B = (0.3; 0.4; 0.9; 1.3; 1.7)$ mK and maximize the collected fluorescence for the atom in the bright state $|\uparrow\rangle$ allowing a maximal atom loss of 2 %. Note that in addition to the probe induced losses, we measure an atom loss probability of 1 % intrinsic to our set up, due to errors when testing for the presence of the atom at the beginning and at the end of the sequence (0.6 %, see Sec. 3.4.1) and to the vacuum limited lifetime $\tau = 24$ s (see Sec. 5.3) of the single atom in the dipole trap (0.4 %). In the results presented below we post-select the experiments where the atom is present at the end of the sequence.

Optimized values are found for the probe length $\tau = (0.7; 0.75; 1; 1.25; 1.5)$ ms, saturation parameter $s = (1; 2; 4; 5; 6) \cdot 10^{-2}$ with ± 30 % uncertainty and the probe frequency close to resonance with the atom for each trap depth. The low saturation is also chosen to avoid radiation pressure effects. We add that the detected fluorescence is constant over the probe interval as shown in Fig. 7.9 for $s = 0.1$. Fig. 7.10 shows the detected photon distributions for two different trap depths 0.3 mK (left image) and 1.7 mK (right image) averaged over several thousand sequences. If the atom is prepared in the $F = 1$ manifold including state $|\downarrow\rangle$ we mainly detect APD dark counts. This clearly changes for a preparation in state $|\uparrow\rangle$. The distribution now contains APD dark counts and the probe-induced fluorescence photon counts. For smaller trap depths the difference between both distributions is less clear since we are limited by a faster atom loss. We will now analyze the distributions in more detail.

7.4.1 Form of the distributions

The dark distributions are well fitted by a Poissonian law. This is supported by calculating the Fano factor $(\Delta n)^2/\overline{n}$, which equals to one for a Poissonian distribution. Figure 7.11 shows the calculated Fano factors for varying trap depth. While

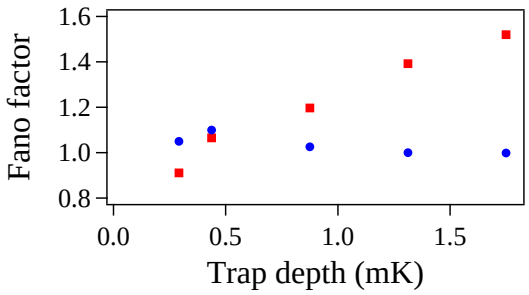

Figure 7.11: Fano factor. Fano factor of the bright (red squares) and dark (blue circles) distribution versus the trap depth. The background Fano factor is close to one and compatible with a Poissonian distribution. For the bright distribution it increases linearly indicating a broadening for higher trap depths.

the dark distribution is clearly Poissonian type (~ 1) the bright one differs from a Poisson distribution for higher trap depths. The Fano factor indicates a broadening which increases linearly with increasing trap depth to $\sim 1.5 > 1$ for 1.7 mK. It is due to fluctuations of the dipole trap of < 10 %. We develop a simulation taking into account these fluctuations by summing many Poisson distributions with mean values proportional to the scattering rate R given in Eq. 7.1. The scattering rate R depends on the trap power and shifts the atomic resonance frequency due to the light shift. For each summand we choose a different light-shift according to a Gaussian law around a mean value U_f/h with a rms width of 10 % of the mean. The normalized sum reproduces well the distribution for 1.7 mK in Fig. 7.10 (red solid curve on bright state distribution).

7.4.2 Dark level distribution and background contribution

The background level is composed of several sources:

- **APD dark counts** The APD dark count rate is measured over a period of 10 sec to be 130 ± 5 counts/sec.
- **Background light** There is a probability to detect photons scattered by the background gas atoms, by the probe laser diffused inside the vacuum chamber or ambient light sources. On the left side of Fig. 7.12 we see however that this contribution is negligible as it is indistinguishable from the APD.
- **Poor atom preparation** The atom preparation into the dark state is not perfect and trap-induced Raman transitions can pump the atom from the dark into the bright state. On the right picture of Fig. 7.12 we compare the background distribution with the one where the atom has been prepared in the dark state. Both distributions are not distinguishable from each other which shows that a poor atom preparation has a negligible contribution.

7.4.3 Bright level distribution

On the left side of Fig. 7.13 the mean detected photon number is shown as a function of the trap depth. The deeper the trap the more photons can be scattered by the atom before being heated out of the trap. The dependence is linear which supports

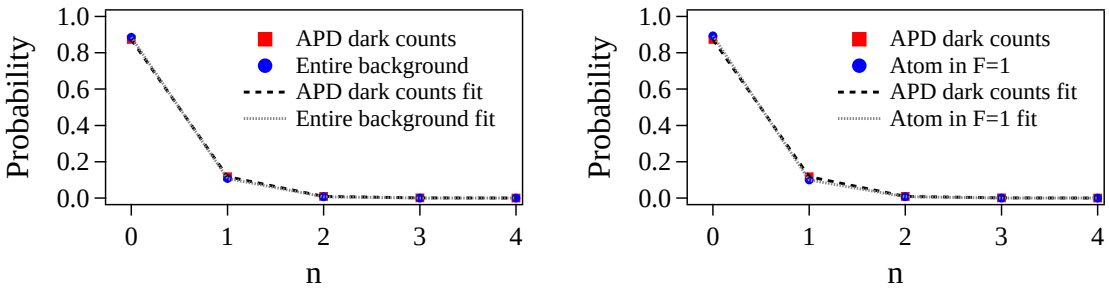

Figure 7.12: APD background levels. *left*) The distribution of all background contributions (red squares) and APD dark counts only (blue circles) are shown. The mean values are 0.1± counts/ms and 0.1± counts/ms, respectively. A fit by a Poissonian distribution to the APD dark counts emphasizes the Poissonian character of the background counts. *right*) The background level on the APD is compared to the distribution obtained for the atom prepared in the dark state $5^2S_{1/2}F=1$.

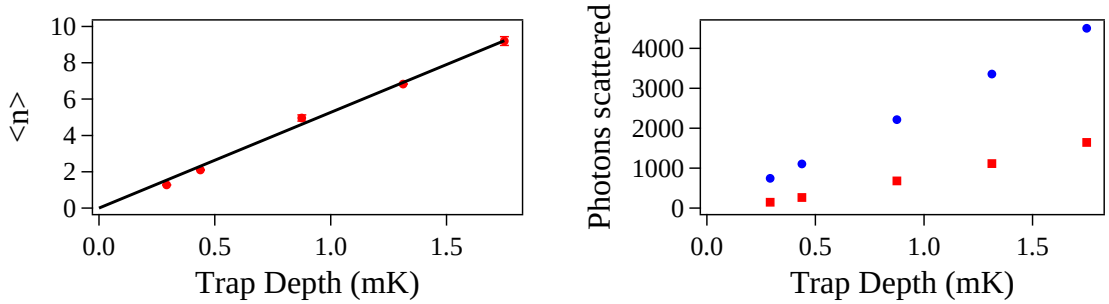

Figure 7.13: Mean detected photon number and probe frequency. *left*) Mean detected photon number versus the trap depth. A linear fit gives a slope of 5.3 ± 0.1 photons/mK. *right*) Dependence of the number of scattered photons by the atom (red squares) on the trap depth. For comparison, the number of photons $U_f/(2E_{rec})$ that can maximally be scattered by the atom before being heated out of the trap is shown as blue circles.

the assumption that the heating process is entirely due to photon scattering. A linear fit to the mean value has a slope of 5.3 ± 0.1 photons/mK.

We can use this measurement to estimate the detection efficiency η of the APD imaging system. For probe pulses with a length τ, the mean number of photons $\langle n \rangle$ scattered by the atom is $R\tau$. The number of photons detected by the APD can then be written as

$$\langle n \rangle = \eta R \tau \ . \tag{7.2}$$

The result at e.g. 1.3 mK with $s = 0.05$ and $\tau = 1.25$ ms yields 5.2 photons/mK and is compatible with the measurement taking a detection efficiency of $\eta = 0.6$. It is also in agreement with the independent measurement of the detection efficiency discussed in Sec. 3.3.5. Up to the separation PBS of Table 3.2 the detection efficiency is 3.8 %. The PBS with 50 %, the APD fiber coupling 60 ± 20 % and APD quantum efficiency 50 % lead to $\eta = 0.6 \pm 0.2$ %.

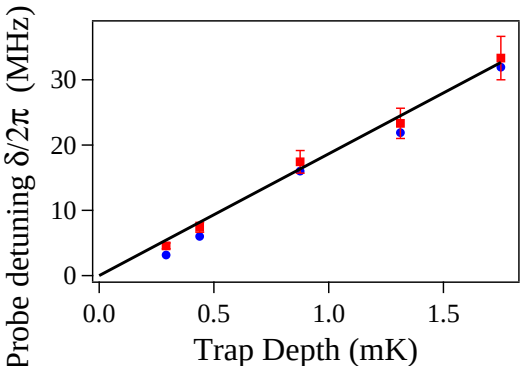

Figure 7.14: Probe laser frequency. We plot the probe laser detuning δ versus the trap depth. For each trap depth the probe laser frequency needs to be adjusted to stay on resonance with the light-shifted atom. The linear fit through the origin has a slope of 18.6 ± 0.4 MHz/mK and indicates that the probe laser is slightly red-detuned with the light-shifted atom, see text.

The number of photons actually scattered by the atom corresponds to the mean value $< n >$ divided by the detection efficiency η. It is plotted as a function of the trap depth on the right side of Fig. 7.13 (red squares). Additionally, the calculated number of photons that can maximally be scattered by the atom inside the trap before being lost $U_f/(2E_{rec})$ is shown as blue circles. We see that we scatter only half as many photons on the atom as it should theoretically be possible to ensure a lossless state detection. We note that for the trap depth of 1.7 mK the atom cycles almost 2000 photons. As discussed at the end of Sec. 7.3.2 a depumping into level $|\downarrow\rangle$ is not expected for these low numbers of scattered photons.

On Fig. 7.14 the optimized probe detuning δ is shown depending on the trap depth. We observe a linear dependence with a slope of 18.6 ± 0.4 MHz/mK. For a probe laser on resonance with the atom we would expect the slope to be $k_B/h = 20.8$ MHz/mK. The probe laser is therefore slightly red-detuned with the atoms at the bottom of the trap.

7.4.4 State detection fidelity

In order to characterize the performance of the state detection we use the state readout fidelity $\mathcal{F}$ defined in (Myerson *et al.*, 2008):

$$\mathcal{F} = 1 - \frac{1}{2}(\epsilon_B + \epsilon_D) \ , \tag{7.3}$$

where ϵ_B is the fraction of experiments in which an atom prepared in the bright state is detected to be dark and, conversely, ϵ_D is the fraction of experiments where an atom prepared in the dark state is found to be bright. To calculate these quantities we define a threshold n_c on the number of detected photons. We consider that an experiment where more (resp. less) than n_c photons are detected during the probe pulse corresponds to an atom prepared in the bright (resp. dark) state. We calculate the errors ϵ_B and ϵ_D using

$$\epsilon_B = \sum_{n=0}^{n_c} P_B(n) \quad \text{and} \quad \epsilon_D = \sum_{n=n_c+1}^{\infty} P_D(n) \ . \tag{7.4}$$

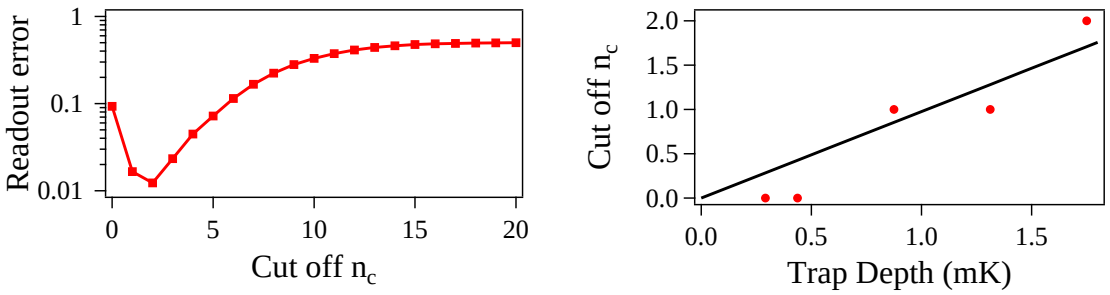

Figure 7.15: Cut off parameter n_c. *left*) Dependence of the state detection fidelity on the cut off parameter n_c for the photons detected by atoms in a 1.4 mK trap depth and a probe pulse length of 1.5 ms. *right*) Cut off parameter $n_{c,min}$ that minimizes the read-out error versus the dipole trap depth.

The left side of Fig. 7.15 shows the readout error $\epsilon = \frac{1}{2}(\epsilon_B + \epsilon_D)$ versus the threshold n_c, for the same set of data ($U_f/k_B = 1.7$ mK) as shown on the right side of Fig. 7.10. The curve shows a minimum for $n_c = 2$. From the data in Fig. 7.15, we extract a minimal readout error of 1.2 % (obtained for $n_c = 2$) i.e. a state detection fidelity $\mathcal{F} = 98.8$ %. We repeated the same experiment 6 times over several days and found an average fidelity $\mathcal{F} = 98.6 \pm 0.2$ % (the error bar is statistical).

We can now study the dependence of the fidelity on the trap depth. We note that for each trap depth a different n_c minimizes the error as can be seen on the right side of Fig. 7.15. Obviously the cut off changes discretely with the distributions. Fig. 7.16 shows the minimal read-out error versus the trap depth. Large values of the trap depth allow us to increase the probe durations to detect more photons. The black line is the simulated result (black line). For the model we use Eq. 7.3 where we assume the bright and dark distributions to be Poissonian. The mean of the bright state distribution is taken to be the mean scattered photon number which increases with the trap depth as shown in Fig. 7.13. For the dark state distribution we assume a mean value increasing with time due to the dark counts as 0.13 counts/ms. Furthermore we assume the cut off parameter n_c to behave as shown in Fig. 7.15. We find good agreement between our data and the model for low trap depths for which the assumption of Poissonian distribution is valid. For higher trap depths the distributions become super-Poisson (see Sec. 7.4.1) leading to a discrepancy between the data and the model. The model in this case indicates the ideal case with no broadening of the distribution. The dips in the black curve are a result of these discrete jumps of the cut off parameter n_c when going to higher trap depths.

7.4.5 Error budget

We discuss the factors that limit our state detection fidelity to 98.6 % and explore the possibilities for improvement. The main contribution to the error budget (see Tab. 7.1) comes from the dark counts of our avalanche photodiode and is ~ 1 %. Using commercially available photodiodes with a lower dark count rate of 25 s^{-1} (Bochmann *et al.*, 2010) would readily bring this error contribution down to 0.3 %. A small

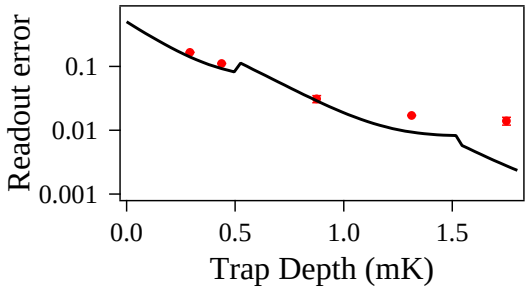

Figure 7.16: State detection fidelity. Dependence of the read-out error on the trap depth. As the trap depth increases we can scatter more photons without losing the atom (The atom loss is held constant at 2 %). The black line corresponds to a theoretical model described in the text.

contribution to the error budget comes from the above mentioned imperfect state preparation in $|\uparrow\rangle$ (0.03 %). Off-resonant Raman transitions induced by the dipole trap light after the preparation phase also contribute for $\sim$0.1 % as they mimic a bad state preparation by coupling the $F=1$ and $F=2$ levels, see Sec. 7.3.2. As this contribution scales approximately as Δ^{-4} (Δ is the trap laser frequency detuning with respect to the fluorescence transitions), we estimate that using a trapping laser with a larger wavelength while maintaining the same trap depth would efficiently reduce this error. The remaining contribution, which is presently 0.27 %, comes mainly from the small number of detected photons $\langle n_B \rangle$ and hence to a non negligible value for $P_{\mathrm{B}}(n \leq n_c)$. This error will be harder to reduce as it implies improving the collection efficiency on our setup. A small part of the 0.27 % ($<$0.1 %) comes from the impurity of the polarization of the probe laser, leading to optical pumping in the $F=1$ manifold.

Source of error	Contribution
Detector dark counts	1 %
Detection inefficiency	0.27 %
Raman transitions	0.1 %
Imperfect preparation	0.03 %
Total error	1.4 %

Table 7.1: Error budget of our lossless state detection.

7.5 Conclusion

We have implemented a lossless internal state readout of a single atom trapped in the optical tweezer. This method is based on the collection of the probe-induced fluorescence. The fidelity of the state detection is presently 98.6 % in single shot, with room for technical improvements in the future. Combined with our ability to efficiently control the internal states of single atoms (Jones *et al.*, 2007; Wilk *et al.*, 2010), this non-destructive state detection completes our toolbox for quantum engineering. Furthermore, the absence of atom loss prevents the reloading of the atom after each measurement, thus improving the duty cycle of the experiments. It also avoids post-detection corrections when performing quantum operations on a set of neutral atom qubits (Fuhrmanek *et al.*, 2011). A demonstration of a possible quantum-projection noise limitation could be for example done by applying the lossless state detection to

measure Rabi oscillations as discussed in Jones *et al.* (2007).

Part III

Going to many atoms

Chapter 8

Measurement of the atom number in the optical tweezer

Contents

So far we concentrated on single atom measurements which served to a great extent as a calibration of our experimental setup. For many atom clouds inside the dipole trap we need to implement techniques to measure their characteristics, too. Most important are the measurement of the atom ensemble temperature and the number of atoms. The temperature can be measured e.g. by using the time-of-flight or release-recapture method (see Ch. 6). Here, we focus on two methods that can independently be used to measure the atom number inside the dipole trap. The first method is analogous to the fluorescence integration measurement used to image a single atom in Sec. 6.2.2. The second method relies on the measurement of the atom number distribution by using single photon counting. Both methods lead to the average number of atoms inside the dipole trap.

8.1 Résumé

Nous avons mis en œuvre deux méthodes qui sont capables de mesurer le nombre moyen d'atomes chargés dans le piège optique. La méthode par intégration de fluorescence est analogue à la mesure par temps de vol décrite dans le Ch. 6 où nous accumulons la fluorescence au cours de nombreuses répétitions. La méthode par comptage d'atomes est basée sur la détection, au niveau du photon unique, des événements de fluorescence diffusés par les atomes lorsqu'ils subissent une marche aléatoire dans la lumière résonante de la sonde. Cette méthode peut être utilisée pour reconstruire la distribution du nombre d'atomes piégés (Fuhrmanek *et al.*, 2010a) et révéle un caractère sub-Poissonien dans le micro piège, même en présence de plusieurs atomes. La méthode permet en outre d'étudier des ensembles d'atomes mésoscopiques, non seulement lorsque les atomes sont confinés par un potentiel de piégeage, mais aussi quand ils se déplacent ou sont libérés du piège, afin d'accéder aux propriétés hors équilibre.

8.2 Fluorescence integration method

This method consists in illuminating the cloud of freely propagating atoms by a 2 μs probe pulse, and accumulating the fluorescence detected on the CCD over many realizations of the experiment. The sequence is similar to the one shown in Fig. 6.1. Once the trap is loaded, either with exactly one atom, or with N atoms, we switch off the cooling and repumping lasers and wait an additional 30 ms before switching off the dipole trap. This waiting period allows enough time for the atoms of the magneto-optical trap to leave the observation region, otherwise they would strongly contribute to the signal observed with the intensifier. We then switch off the dipole trap (in $\sim$200 ns) and, after a time of flight of the atoms of 1 μs in free space, we turn on the resonant probe laser, while gating the intensifier (at gain 9). We use the $\sigma^+ - \sigma^-$ counter-propagating probe ($s \sim 5$) and repumper probe ($s \sim 0.5$) lasers. Finally, the CCD camera is read out once after all repetitions of the sequence are realized. As explained in 6.2.2, after typically several hundreds repetitions of the experiment, the image shows a nearly Gaussian distribution, reconstructed from many individual detected events (see Fig. 8.1). We perform this experiment in the multi-atom regime and then in the single-atom regime for which the fluorescence scattering rates are $R_{tot} = N R_{\text{single}}$ and R_{single}, respectively. We use the latter to extract the number of atoms N in the multi-atom regime, by calculating the ratio of the integrated fluorescence values $N = R_{tot}/R_{\text{single}}$ obtained in the two regimes[1].

Nevertheless, special care must be taken when the number of interacting particles involved is small. For instance, when using fluorescence imaging the small number of atoms combined with the low collection efficiency makes it hard to collect more than a few photons per realization of the experiment, therefore preventing the reliable extraction of the number of atoms in single shot. To circumvent this problem, a

[1] This approach requires all atoms to scatter at the same rate R_{single}, which is not necessarily the case for interacting atoms, see Sec. 2.2.3 and 10.3.1.

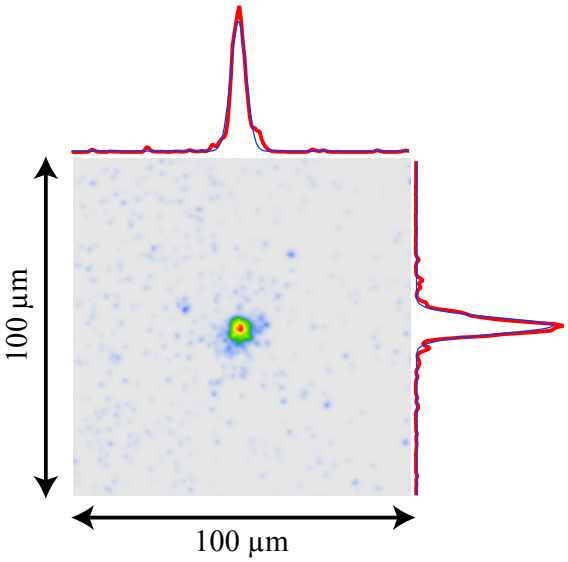

Figure 8.1: Image of a cloud containing 5.3 atoms on average. Result of the accumulation of 600 fluorescence images obtained with an average number of $\bar{N} = 5.3$ atoms released from the micro trap. After a 1 μs time of flight the atoms are illuminated by a 2 μs probe and repumper probe pulse. The CCD camera is read out once after all accumulations are finished. The width of the distribution of ~ 2 μm is extracted from a 2D-Gaussian fit (blue) to the data cross-sections (red).

method was recently demonstrated (Bücker *et al.*, 2009) where freely propagating atoms fall through a sheet of resonant light leading to the detection of many photons per atom. The method described below goes in that direction.

8.3 Measurement of the atom number distribution in an optical tweezer using single photon counting

This method relies on single-photon counting which experimental realization is similar to the integration method: We release the cloud of cold atoms from the dipole trap and let them expand in a resonant light probe for long probe times of several 10 μs. The atoms diffuse in the probe in a Brownian motion and emit photons. Some of the photons are collected by our imaging system and impinge on an image intensifier where we count them. After one shot we observe well separated single photon events on the CCD, which in contrast to the integration method is read out after each realization. By repeating the experiment several times and recording the counting results, we reconstruct the distribution of the number of detected photons. We can again work with exactly one atom, or with a cloud of up to a few tens of atoms. In this way we perform a calibration of the number of detected photon events when a single atom is trapped. In contrast to the integration method we can use the calibration to determine the atom number distribution inside the dipole trap.

8.3.1 Experimental procedure and fluorescence images

The experimental sequence is the same as for the integration method. During the 1 μs time of flight in free space, the atoms start separating from each other. Then

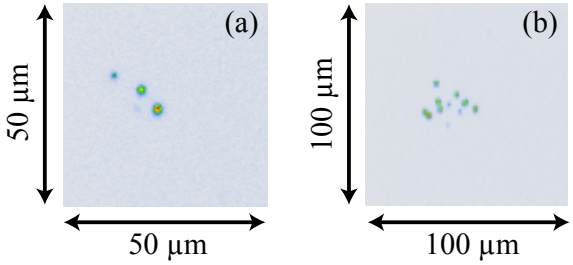

Figure 8.2: Photon events on CCD image. Figure (a) is an image taken for a 40μs-illumination period of a single atom. The region of interest has a size of 50 μm×50 μm in the plane of the atoms. Figure (b) shows an image (100 μm×100 μm) in which about 8 atoms were released from the trap and illuminated with a 20 μs probe pulse.

they walk randomly in the light probe and scatter photons at a rate $R_{\text{single}} \sim \Gamma/2 \simeq 2 \times 10^7\,\text{s}^{-1}$. Some of the scattered photons are collected on the image intensifier and impinge on the CCD at different positions due to the random walk of the atom in the probe light [2]. The total number n of detected events is proportional to the number of atoms N on average. After each sequence we read out the CCD camera, which lasts ∼500ms, while launching the next loading sequence.

The images shown in Fig. 8.2(a) and (b) were obtained after a single realization of the experimental sequence. Figure 8.2(a) corresponds to the time of flight of a single atom ($T \sim 150$ μK) moving randomly in the probe light. Figure 8.2(b) corresponds to the time of flight of about 8 initially trapped atoms at $T \sim 1$ mK. In both cases, the detected photons correspond to a large extent to photons being scattered by the atom and detected by the intensifier and, to a smaller extent, to photons due to spurious laser light or self-induced charges generated inside the intensifier (see more details below). This fact leads us to adjust the size of the region of interest to the measured temperature of the atom(s): for a time of flight of duration Δt, we choose a square with side dimension bigger than $\sim 4\sigma_v \Delta t$, where $\sigma_v = \sqrt{k_\text{B} T/m}$. This choice leads to a negligible probability of missing an atomic event, while reducing the number of background events, which are uniformly distributed on the CCD.

We note that using an image intensifier is crucial for the experiment because it enables our imaging system to detect single photon events. In the absence of the intensifier, single photon events have an amplitude lower than the noise of the CCD camera alone ($6e^-$/pixel). The intensifier amplifies a single photon event to an average amplitude of $822e^-$/pixel at gain 9, well above this noise level (Sec. 4.4).

8.3.2 Procedure for analyzing the images

In order to count the number of events detected on the CCD camera, one has to decide what one calls an event. In order to do so, we apply the counting algorithm described in Sec. 4.3 and recall some important issues:

[2] The detected photon events are distributed around the geometrical images of the atoms according to the point spread function of the imaging system, which includes diffraction, residual aberrations and defocus due to the spatial distribution of the atoms. Given the size of the tweezer and the temperature of the atoms, the aberrations and the defocus are negligible. The collection efficiency therefore does not depend on the position of the atoms.

Firstly, we know the amplitude distribution of single-photon events recorded by the intensifier followed by the CCD camera (see Sec. 4.4). Using this distribution, we find that about 1 % of the events have a peak amplitude smaller than $6\sigma_{\mathrm{CCD}}$ for an intensifier gain 9. Our counting procedure thereby does not underestimate the number of events by more than 1 %. Secondly, we have measured the probability of counting only one event when actually two events impinge on the detector within a separation range corresponding to the full width at half maximum of an individual event. This probability is maximum at the center of the image, where the density of atoms is maximum, and is for example 2.5 % for 9 atoms released from the microscopic dipole trap with a temperature $T \sim 150$ μK (see Sec. 8.3.5). In this case, the number of atoms is thus underestimated by less than 2.5 %. This second source of bias scales quadratically with the number of atoms N, all other parameters being kept constant. Note, however, that this bias can be easily maintained to a low level by letting the atomic cloud expand for more than 1 μs before sending the probe light, as this bias varies approximately as N^2/σ_0^4 (σ_0 is the size of the cloud when we switch the probe light on)[3]. As an example, for our micro trap and typical parameters, this effect can be maintained below the 1 % level up to $N \sim 1100$ atoms, the only limit being the size of our CCD detector (1024×1024 pixels, pixel side length 13 μm).

Finally, we observed that a few events with a large amplitude are surrounded by one (sometimes two) less intense companion peaks, which are indistinguishable from real events, and which we attribute to second order amplification processes in the intensifier micro-channel plates. We evaluated the fraction of such multi-events and found that by taking into account the companion events we overestimate the number of real events by no more than[4] 6 %.

8.3.3 Calibration using a single atom

The first step of the calibration of the imaging system as a counting device was to measure the histogram of the number of background events in one image when no atom is trapped in the dipole trap. The histogram is shown in Fig. 8.3, which results from the analysis of 200 images of the background. The probe pulse duration was $\Delta t = 30$ μs. The data are well fitted by a Poisson distribution with average $\bar{n}_{\mathrm{bg}} = 0.7$.

In a second step, we repeated the same experiment with exactly one atom trapped in the dipole trap. In particular, the probe duration was the same as above ($\Delta t = 30$ μs). As the detection efficiency is small and corresponds to a random collection of photons, we also expect a Poisson distribution for the number of detected photons emitted by the atom. In this case, the distribution of detected events, including the background events, is a Poisson distribution with a mean value:

$$\bar{n}_{\mathrm{single}} = \bar{n}_{\mathrm{at}} + \bar{n}_{\mathrm{bg}} \ . \tag{8.1}$$

[3] This bias actually decreases faster than $1/\sigma_0^4$ due to the depth of focus effect.

[4] In the results presented below we did not use the "sharp" and "round" parameters (see Ch. 4).

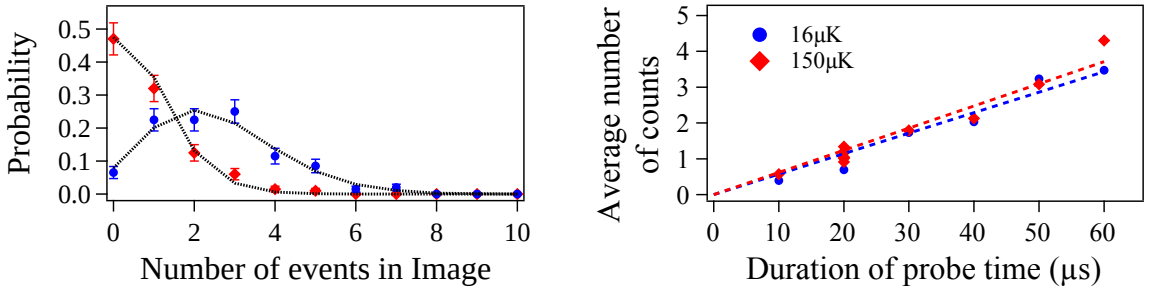

Figure 8.3: Single atom photon event distribution and its calibration. *left*) Probability distribution of the number of detected events in one image. The probe duration is 30 μs. Red diamonds: background events (no atom present in the trap). Blue circles: total number of detected events (including background events) when the dipole trap is filled with exactly one atom. In both cases, the probability p to measure a given number a counts in one image is deduced by analyzing 200 images. The error bar on each data point is calculated by $\sqrt{p(1-p)/200}$, which we tested by repeatability measurements. A Poisson distribution fits the data very well in both cases (dotted lines). *right*) Average number of detected photons after scattering by a single atom with temperature 16 μK (blue circles) or 150 μK (red diamonds), versus the duration of the atom illumination by the probe light. Linear fits to the data (dashed lines) yield a photon detection rate $R_\mathrm{d} = 57200 \pm 3100\ \mathrm{s}^{-1}$ for 16 μK and $R_\mathrm{d} = 61800 \pm 2400\,\mathrm{s}^{-1}$ for 150 μK.

The experimental distribution is shown in Fig. 8.3, together with a fit by a Poisson distribution. We obtain a good agreement for $\bar{n}_\mathrm{single} = 2.5$. This yields an average number of detected photons, emitted by one atom, of $\bar{n}_\mathrm{at} = 1.8$.

Finally, we tested the linearity of our counting system with the duration of the probe pulse. The results are shown in Fig. 8.3, where we plot the average number of detected events due to scattering by a single atom, $\bar{n}_\mathrm{at}$, obtained after subtraction of the average number of background events. We first performed the experiment with a single atom with a temperature $T \sim 150$ μK and observed a linear dependency of $\bar{n}_\mathrm{at}$ with the duration of the probe illumination. A linear fit to the data yields a photon detection rate, for one atom released from the trap, of $R_\mathrm{d} = 57200 \pm 3100\ \mathrm{s}^{-1}$ (the error bar is from the fit). Knowing the detection efficiency of the imaging system ($\sim 3 \cdot 10^{-3}$), see Sec. 3.3.5, we deduce a scattering rate of $1.9 \cdot 10^7\ \mathrm{s}^{-1}$, in agreement with the value calculated for the parameters of our probe.

In order to further test the linearity of our counting system, we also performed the same measurement for an atom adiabatically cooled down to 16 μK (Tuchendler *et al.*, 2008). In this case, the detected events tend to accumulate on a smaller area on the I-CCD, due to the smaller velocity of the atom (the time of flight of the atom is maintained constant and equal to 1 μs with respect to the previous case at $T \sim 150$ μK). In spite of the increase in the surface density of detected events, we were still able to discriminate between individual events and found the same linear dependency as above, with a photon detection rate of $61800 \pm 2400\,\mathrm{s}^{-1}$.

To conclude, we detect on average $\bar{n}_\mathrm{at} = 1.1$ photons scattered by a single atom for a probe duration $\Delta t = 20$ μs. This value will serve as a calibration in the experiments described below, where the average number of atoms is the unknown.

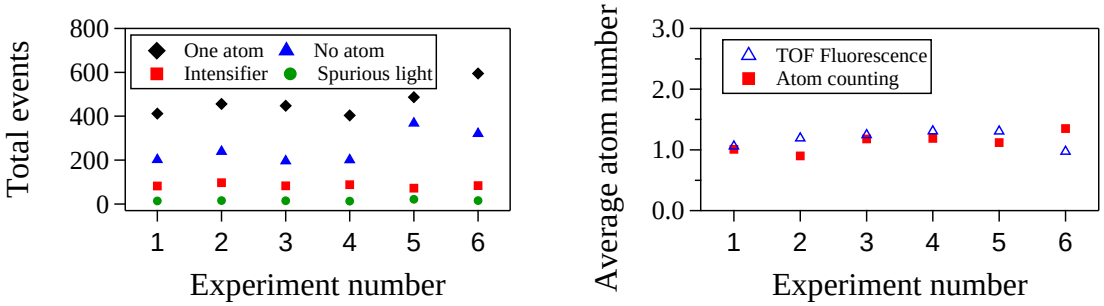

Figure 8.4: Fluctuations of total event number. *left*) We plot the total number of events detected over 200 sequences. The measurement is repeated six times over a period of two weeks. Half of all 467 ± 70 events (black diamonds) coming from a single atom illuminated for 20 μs come from the background 254 ± 73 (blue triangles). The background is composed of spurious light 16 ± 3 (green circles), auto-generated intensifier events 84 ± 8 (red squares) and scattered photons from the background gas. *right*) We compare the atom number extracted by a time-of-flight integration measurement and the atom counting method for a single atom over the same series of six measurements. On average the time-of-flight fluorescence corresponds to 1.07 ± 0.13 atoms and the atom counting method to 1.1 ± 0.1 atoms.

8.3.4 Fluctuations and repeatability

In order to evaluate the noise sources that affect the counting measurement we repeated two measurements six times over a period of two weeks. The first measurement was based on the atom counting method of a single atom for which we chose a probe laser length of 20 μs. The left plot in Fig. 8.4 shows the results. Over 200 sequences we measured 467 ± 70 events when the atom is loaded. Without atom we measured 254 ± 73. The normalized difference between both numbers equals the average number of detected photons per atom $\bar{n}_{\mathrm{at}} = 1.1$ as mentioned above. The background events have three different origins: The largest contribution comes from light scattered by the atoms of the atomic beam that cross the region of observation (61 %). It can be improved by decreasing the oven temperature at the expense of a lower experimental duty cycle and less atoms loaded into the trap. The second largest contribution comes from self-induced events generated by the gated intensifier when the high voltage is switched on and off (33 % of the counts, see Sec. 4.5); finally, a smaller contribution comes from scattering of the probe beams on the surfaces inside the vacuum chamber and ambient light (6 %).

The second measurement that was repeated was the fluorescence integration of Sec. 8.2 on a single atom using a probe of 2 μs. The accumulated fluorescence over 2000 sequences is normalized as follows. First, we divide it by the fluorescence of a Gaussian photon event intensified on the CCD camera at gain 9 ($\sim 8 \pm 3 \cdot 10^3$ adu·pixel^2, see Sec. 4.6). Doing so we find that on average 0.11 ± 0.4 photons impinge on the CCD camera per sequence. Next, we divide it $\Gamma/2 \cdot 0.003 \cdot 2$ μs, i.e. the fluorescence rate multiplied by the detection efficiency of the imaging system and the duration of the probe pulse. We thus extract the average number of atoms inside the trap to be 1 ± 0.4. The right plot in Fig. 8.4 compares the two measurement techniques

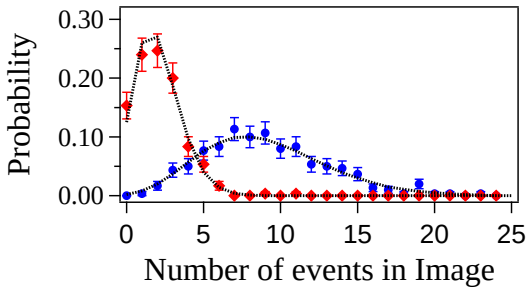

Figure 8.5: Event histogram for ~ 6 atoms on average. Probability distribution of the number of detected events when the dipole trap is filled with 6.3 atoms on average (blue circles). It is well fitted by Eq. 8.2 for a probe duration of 20 μs corresponding to an average number of detected photons scattered per atom $\bar{n}_{\mathrm{at}} = 1.1$. The background distribution (red diamonds) is of Poisson type ($\bar{n}_{\mathrm{bg}} = 2.1$).

and shows that both techniques are compatible with having loaded a single atom into the trap. We note that the experimental fluctuations on the fluorescence integration of a single atom are 11 % and much less than the 40 % above, which originate from the uncertainty on the fluorescence of the intensified Gaussian photon events.

8.3.5 Atom number distribution in the multi-atom regime

We now operate in the regime where more than one atom are loaded in the dipole trap. We repeat the same experimental procedure and extract the histogram of the number of detected events for a probe duration $\Delta t = 20$ μs. Figure 8.5 shows the histogram of the background events as well as the probability distribution of the total number of detected events (including the background events) when about 6.3 atoms are loaded in the dipole trap of ~ 15 mK on average. The background gives an average number of events $\bar{n}_{\mathrm{bg}} = 2.1$, larger than in Sec. 8.3.3, as we needed to increase the flux of the atomic beam in order to load more than one atom in the trap.

To fit the distribution of events in the multi-atom regime, we consider the distribution of the number of atoms N in the dipole trap, $P_N(\bar{N})$, with $\bar{N} = \sum_{N=0}^{\infty} N P_N$ the mean atom number. The probability to detect n photon events is then given by the composed law (Schlosser, Reymond, and Grangier, 2002):

$$p(n) = \sum_{N=0}^{\infty} P_N(\bar{N}) \times \Pi(n, N \times \bar{n}_{\mathrm{at}} + \bar{n}_{\mathrm{bg}}) \tag{8.2}$$

with $\Pi(n, \alpha)$ the Poisson distribution of mean α. Even in the case when $P_N(\bar{N})$ is a Poisson law, the distribution $p(n)$ is not Poissonian. Nevertheless, for any distribution $P_N(\bar{N})$, the mean value of this composed law is given by:

$$\bar{n}_{\mathrm{multi}} = \bar{N} \times \bar{n}_{\mathrm{at}} + \bar{n}_{\mathrm{bg}} \ . \tag{8.3}$$

A direct calculation of the mean of the data shown in Fig. 8.5 yields $\bar{n}_{\mathrm{multi}} = 9$. Taking into account that the probe duration has been chosen to detect $\bar{n}_{at} = 1.1$ events per atom and that $\bar{n}_{\mathrm{bg}} = 2.1$, equation (8.3) yields an average number of atoms $\bar{N} = 6.3$. Taking a Poisson distribution for $P_N(\bar{N})$, a fit of the data by the composed law (8.2) leads to the same result. The result of the fit is shown in Fig 8.5.

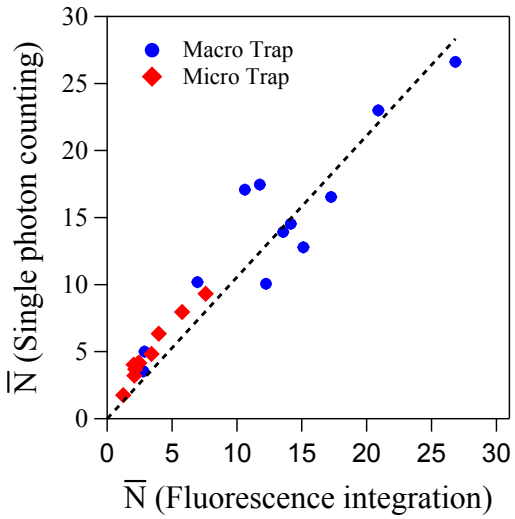

Figure 8.6: Comparison between the fluorescence integration and atom counting method. The average number of atoms $\bar{N}$ obtained by direct counting (vertical) is compared to the number extracted by fluorescence integration (horizontal). The experiments were performed in two configurations: with a microscopic dipole trap (red diamonds, $w = 1$ μm) or with a larger dipole trap (blue dots, waist $w = 3.8$ μm). A linear fit through the origin has a slope of 1.1 ± 0.1.

8.4 Comparison with fluorescence integration

We check that the average number of atoms extracted by the counting method is consistent with the number of atoms extracted by the fluorescence integration method described in the beginning. The comparison between the two results was done in two trap configurations that we now describe. As already explained, a significant fraction of the background events come from photons being scattered when the atomic beam interacts with the probe light. To minimize this effect, we decreased the flux of the beam by reducing the temperature of the oven. This is at the expense of the loading rate of the dipole trap: in this first configuration, we could not load more than ~ 10 atoms in the micro trap. In order to calibrate our detection scheme with a larger number of atoms, we use the macro trap with a larger waist $w = 3.8$ μm. In this second configuration, the atomic density is smaller and the light-assisted collisions limit the number of atoms to a larger value than in the microscopic dipole trap (Kuppens *et al.*, 2000), typically 30. The results of the experiment are shown in Fig. 8.6 where we plot the average number of atoms obtained from the counting method versus the average number of atoms obtained by fluorescence integration. The numbers of atoms obtained by the two methods are compatible : a linear fit to the data yields a slope of 1.1 ± 0.1 which is compatible with 1, as the statistical uncertainty on the slope is 0.05 and we evaluate the bias uncertainties attached to each method to less than 6 % for the counting method, and 11 % for the integrated-fluorescence based method. The compatibility also shows that interaction between the atoms, which can be neglected when applying the atom counting method, are neither playing a role when using the integration method in this case.

8.5 Sub-Poissonian dipole trap loading

We now discuss the Poissonian assumption mentioned above for the atom number distribution $P_N(\bar{N})$. For a single atom the loading is clearly sub-Poissonian as dis-

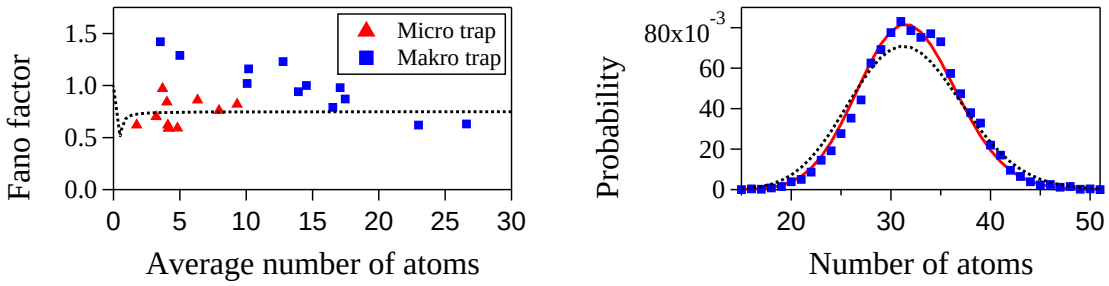

Figure 8.7: Sub-Poissonian dipole trap loading. *left*) We show the Fano factor versus the number of atoms in the micro (red triangles) and macro (blue squares) trap. A theoretical model (black dotted line) with $\gamma = 0.2\ \mathrm{s}^{-1}$ and $\beta' = 0.5\ \mathrm{ms}^{-1}$ is compared to the micro trap data. *right*) Numerically calculated probability (red curve) to have a certain number of atoms in the micro trap ($\gamma = 0$, $\beta' = 1\ \mathrm{ms}^{-1}$, $R = 1000\ \mathrm{ms}^{-1}$). A Monte-Carlo simulation (blue squares) yields the same distribution with $\Delta N^2/\bar{N} = 0.73$. Black dotted line: Poissonian fit of the numerically calculated sub-Poissonian distribution.

cussed in Sec. 3.4.1. We want to see if this is also true when loading more than one atom and extract from the data the variance of the number of detected events, $\Delta n^2_{\mathrm{multi}} = \overline{n^2_{\mathrm{multi}}} - \bar{n}^2_{\mathrm{multi}}$. This variance is related to the variance of the number of atoms ΔN^2 by the following expression, calculated using the probability $p(n)$ of equation (8.2), and valid for any distribution $P_N(\bar{N})$:

$$\Delta n^2_{\mathrm{multi}} = \bar{n}^2_{\mathrm{at}} \times \Delta N^2 + \bar{n}_{\mathrm{multi}} \ . \tag{8.4}$$

Taking again $\bar{n}_{\mathrm{at}} = 1.1$, we find for the data of e.g. Fig. 8.5 a ratio $\Delta N^2/\bar{N} = 0.86 \pm 0.13$ (the error bar is statistical). The left side of Fig. 8.7 shows the Fano factor $(\Delta N^2/\bar{N})$ versus the number of atoms in the micro or macro trap. For the micro trap the average Fano factor of all measurements is 0.72 ± 0.13, which clearly indicates a sub-Poissonian behavior $\Delta N^2/\bar{N} < 1$[5]. The macro trap shows a monotonously decreasing Fano factor, which becomes slightly sub-Poissonian for $\bar{N} > 15$. For low atom numbers it is even super-Poissonian probably due to trap power fluctuations.

8.5.1 Theoretical considerations on the atom number distribution

In order to model the atom number distribution we set up differential equations that describe the evolution of $P_N(t)$ with time t. To do so we calculate the probabilities for an atom to enter or leave the trap during the time interval τ. The probability for an atom to enter the trap during τ is $R\tau$ with R being the loading rate. We will further differentiate between one- and two-body losses.

[5]Note that any kind of fluctuations on the trap depth, loading rate etc. broadens the actual distribution and would lead to Poissonian or super-Poissonian distributions. This reinforces our statement of sub-Poissonian dipole trap loading even for $\bar{N} > 1$.

One-body loss

The probability during τ to undergo a one-body loss is $-N\dot{P}(t)/P(t)\tau$ (see Sec. 9.3.2), which for an exponential loss $P(t) = N(t)/N_0 = \exp(-\gamma t)$ becomes $N\gamma\tau$ with γ being the one-body loss constant. It corresponds to the probability for one atom to undergo a loss $\gamma\tau$ during time τ multiplied by the number of atoms in the sample N. We derive the probability to have N atoms inside the trap at instant $t+\tau$ to be

$$\begin{aligned} P_N(t+\tau) = & P_N(t)(1-R\tau)(1-N\gamma\tau) + P_{N-1}(t)R\tau(1-(N-1)\gamma\tau) + \\ & P_{N+1}(t)(1-R\tau)(N+1)\gamma\tau + P_N(t)(R\tau)(N\gamma\tau) + \dots \ . \end{aligned} \tag{8.5}$$

The first term describes the probability to have already N atoms inside the trap at time t and neither loading another atom $(1-R\tau)$ nor losing one $(1-N\gamma\tau)$ during τ. The second term represents the case having $N-1$ atoms at time t and loading one atom into the trap $R\tau$ without losing one $(1-(N-1)\gamma\tau)$ during τ. The next terms are build up analogously. It is then straight forward to derive the differential equations for one-body loss in the limit $\tau \to 0$ and taking only first order terms in τ

$$\frac{\partial P_0(t)}{\partial t} = -RP_0(t) + \gamma P_1(t) \qquad , \quad N=0 \tag{8.6a}$$

$$\frac{\partial P_N(t)}{\partial t} = -(R+N\gamma)P_N(t) + RP_{N-1}(t) + (N+1)\gamma P_{N+1}(t) \qquad , \quad N \geq 1 \ . \tag{8.6b}$$

Considering Eq. 8.6 we find a Poisson distribution $P_N(t\to\infty) = \frac{(R/\gamma)^N}{N!}\exp(-R/\gamma)$ in steady state[6] by solving the set of equations recursively and imposing the normalization $\sum_{N=0}^{\infty} P_N = 1$. Replacing N by $N+1$ in Eq. 8.6b, multiplying it by N and subsequently summing N from 0 to ∞ on both sides yields

$$\dot{\bar{N}} = R - \gamma\bar{N} \ . \tag{8.7}$$

Here, we explicitly used for the mean value $\bar{N} = \sum_{N=0}^{\infty} NP_N$ and $\dot{\bar{N}} = \sum_{N=0}^{\infty} N\dot{P}_N$. Eq. 8.7 is equivalent to Eq. 3.6 neglecting two-body losses and identifying N as the average atom number $\bar{N}$. In steady state we find a Poissonian distribution with mean $\bar{N}_{\mathrm{st}} = R/\gamma$.

Two-body loss

The probability to undergo a two-body loss is $\frac{N(N-1)}{2}\beta'\tau$, where β' is the two-body loss constant. The two-body loss probability corresponds to the number of atom pairs $\frac{N(N-1)}{2}$ multiplied by the probability $\beta'\tau$ to lose one pair during time τ. Differential equations in the case for one- plus two-body loss can be derived from a set of equations similar to Eq. 8.5, which has been set up for one-body loss only

[6] With the steady state solution in hand one can also derive an analytical solution for the general case $P_N(t) = \frac{\left(\frac{R}{\gamma}\left(1-e^{-\gamma t}\right)\right)^N}{N!}\exp\left(-\frac{R}{\gamma}\left(1-e^{-\gamma t}\right)\right)$.

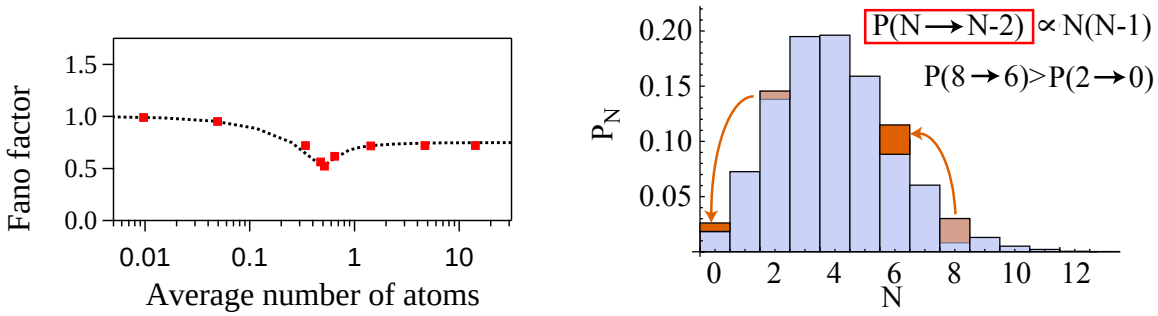

Figure 8.8: Explanation of sub-Poissonian atom number distribution. *left*) We show the Fano factor versus the number of atoms and the loading rate R calculated by using a Monte-Carlo method (red squares) and the numerical solution of the set of differential equations (black dotted line). We fix the values for $\gamma = 0.2$ s^{-1} and $\beta' = 0.5$ ms^{-1}. *right*) The Poissonian distribution (blue) can lead to a sub-Poisson distribution in the presence of two-body loss. For two-body loss it is more probable to eject atom pairs at the high probability tail.

$$\frac{\partial P_0(t)}{\partial t} = -RP_0(t) + \gamma P_1(t) + \beta')P_2(t) \quad , \quad N = 0 \tag{8.8a}$$

$$\frac{\partial P_N(t)}{\partial t} = -(R + N\gamma + \frac{N(N-1)}{2}\beta')P_N(t) + RP_{N-1}(t) + (N+1)\gamma P_{N+1}(t) + \frac{(N+2)(N+1)}{2}\beta' P_{N+2}(t) \quad , \quad N \geq 1\ . \tag{8.8b}$$

Note that Eq. 8.8 and the probability to have N atoms inside the trap $P_N(t)$ at time t is the basis of Eq. 3.6 (see App. D).

Considering two-body loss the equation can be solved numerically. In order to calculate the infinite set of equations 8.8 we restrict ourselves to the first N_{max} equations and make sure that higher populations $P_{N>N_{max}}$ become negligibly small. In the case of the micro trap data in Fig. 8.7 we compare the data with the numerical result for $\gamma = 0.2$ s^{-1} and $\beta' = 0.5$ ms^{-1} ($N_{max} \sim 100$). The one-body loss is chosen very small and mainly due to light scattering from the molasses lasers and background gas collisions. The two-body loss rate is chosen as measured in Sec. 9.2.

The distribution is Poisson for very low average atom numbers. Here, the loading rate is so small that the probability to have two atoms inside the trap and a two-body loss to occur is negligibly small. Following Eq. 8.6 we then find a Poisson distribution in steady state. The onset of two-body collisions for an increasing loading rate governs the single atom regime with the lowest Fano factor $\Delta N^2/\bar{N} = 0.5$. For even higher loading rates and thus higher atom numbers the distribution stays sub-Poissonian. Such a distribution is shown on the right side of Fig. 8.7. We check the result obtained by numerically solving the set of differential equations and by performing a Monte-Carlo simulation which will be described in Sec. 9.3.2. Fig. 8.8 compares the Fano-factor calculated by the two methods and shows that both methods agree well.

The Fano factor converges to $\Delta N^2/\bar{N} \sim 0.75 = 3/4$ in agreement with our measurements in the micro trap. This factor also arises from an analytical stochastic

treatment involving the Fokker-Planck equation (van Kampen, 2007) which furthermore reveals that the atom number distribution in steady state has a Gaussian shape. Note that the Fano factor in the limit of large atom number does neither depend on the origin of two-body inelastic collision (light-assisted collisions, hyperfine changing collisions etc.) nor on its loss constant β'. It depends however on the type of inelastic collision, i.e. two-, three-, or higher order body collisions. A general expression for the Fano factor can be found using the analytical treatment of van Kampen (2007). If a loading process competes with ρ-body inelastic collisions the Fano factor in steady-state behaves as $\frac{1}{2}\left(1+\frac{1}{\rho}\right)$. In the absence of atom loading the atom number distribution is narrower than in the case where atom loading is present and the Fano factor becomes $\rho/(2\rho-1)$. For three-body inelastic collisions in the absence of a loading process this has experimentally been shown by Whitlock, Ockeloen, and Spreeuw (2010).

Analog to the one-body loss case we can derive (see App. D)

$$\dot{\bar{N}} = R - \gamma\bar{N} - \beta'\left(\overline{N^2} - \bar{N}\right) = R - \gamma\bar{N} - \beta'\bar{N}(\bar{N}-1) - \beta'\Delta N^2 \ , \tag{8.9}$$

with the variance $\Delta N^2 = \overline{N^2} - \bar{N}^2$. Note that in contrast to one-body losses Eq. 8.9 is not equivalent to Eq. 3.6 by simply replacing N by $\bar{N}$ in Eq. 3.6 due to the extra term containing the variance ΔN^2 (see discussion in App. D).

An intuitive explanation of sub-Poissonian loading can be given by looking at the right graph in Fig. 8.8. Two-body loss leads to the ejection of both collision partners. The probability for a loss to occur increases with increasing atom number. This means that the higher atom number side of the distribution is decreased much faster than the lower atom number side. This can lead to a narrowing of the atom number distribution and thus a sub-Poissonian character. Such a sub-Poissonian character as observed here could be useful for atomic interferometry below the standard quantum limit (Wineland *et al.*, 1994) as mentioned earlier.

8.6 Conclusion

We have implemented two methods that are capable of measuring the average number of atoms loaded into the optical dipole trap. The fluorescence integration method is analogous to the time-of-flight measurement in Ch. 6 where we accumulate atom fluorescence over many repetitions. The atom counting method is based on the detection, at the single photon level, of fluorescence events scattered by the atoms when they undergo a random walk in the resonant probe light. It can be used to reconstruct the loaded atom number distribution (Fuhrmanek *et al.*, 2010a) revealing a sub-Poissonian micro trap loading behavior even when passing the single-atom regime and going to many atoms. The method additionally allows to study mesoscopic atom ensembles, not only when the atoms are confined by a trapping potential but also when they move or are released from the trap in order to access out-of-equilibrium properties.

Chapter 9

Light-assisted collisions

Contents

Light-assisted collisions play an important role in our experiment for several reasons: First, they govern the loading process described by Eq. 3.6 and fix together with the loading rate R the average number of atoms in the dipole trap. In this context they are also responsible for sub-Poissonian single atom loading.

Second, they hamper Doppler cooling of atom ensembles as observed for a single atom in the microscopic dipole trap $U \sim 3$ mK. We discuss this observation in Sec. 9.2.

Third, important properties such as the temperature (Sec. 6) or the atom number (Sec. 8) are measured using near-resonant light. Being interested in the study of very dense atomic clouds (density $> 10^{14}$ at/cm^{-3}) light-assisted collisions can prevent a reliable measurement.

Finally, light-assisted collisions may introduce fundamental differences in the light scattering process when dealing with small atom samples in contrast to single atoms or non-interacting gases. Collective effects such as the excitation blockade mentioned in Sec. 2.2.3 may come into play.

In this chapter we focus on the measurement of light-assisted collisions in the micro trap triggered by the presence of near-resonant light for which radiative escape (see Sec. 2.2.3) is the dominant loss channel. In a first step we will discuss the major

implications of light-assisted collisions on the trap loading process and we will present a detailed study of the collision rates later on.

9.1 Résumé

Nous présentons dans ce chapitre une série de mesure des collisions assistées par la lumière dans un piège dipolaire microscopique, lorsque l'échantillon atomique est excité par une sonde quasi-résonante. Nous avons mesurés des taux étonnamment élevés de pertes à deux corps. Nous avons également constaté une dépendance du taux de collision avec le nombre d'atomes piégés, non expliquée à ce jour. Ce comportement peut être une signature d'effets collectifs liées à la petite taille du nuage atomique, qui est de l'ordre de la longueur d'onde de la lumière de la sonde. D'autres études expérimentales et des efforts théoriques importants sont nécessaires afin de comprendre nos résultats. Toutefois, le taux élevé de pertes induites par la lumière quasi-résonante implique de trouver de nouvelles techniques afin de charger le micro-piège de manière efficace en l'absence de lumière quasi-résonante (cf.chapitre suivant).

9.2 Trap loading in the presence of near-resonant light

The optimized experimental sequence to directly load atoms into the dipole trap by using the molasses or MOT has been described in Sec. 3.4. Here, we want to discuss some important properties of the trapped atom samples such as its temperature and the maximal number of atoms.

Temperature of loaded sample

We have seen in part II that the single atom temperature inside the dipole trap of ~ 3 mK right after the loading process usually lies within the typical range of Doppler $\frac{\hbar\Gamma}{2k_B} = 145\mu$K and sub-Doppler temperatures. For compensated magnetic fields (70 mGauss) we obtain sub-Doppler temperatures as low as ~ 35 μK by directly loading the atom from the molasses and without further detunings of the molasses frequency as done by Tuchendler *et al.* (2008). It has been experimentally verified by using the release-and-recapture method on a single atom shown on the left side of Fig. 9.1. To investigate if this is still true when loading more than one atom into the trap we apply the same experimental sequence as for a single atom (see Sec. 3.4). The loading rate R into the $U_0/k_B \sim 3$ mK deep micro trap at 850 nm is varied with the atom flux from the oven. The right graph in Fig. 9.1 shows the ensemble temperature depending on the atom number 30 ms after being loaded into the trap. The temperature has been measured by a time-of-flight method described on a single atom basis in Sec. 6.2. Already for 1.5 atoms on average the sub-Doppler temperature of 35 μK increases to 144 μK. Going to four atoms it increases again by a factor 3 and reaches its maximum at ~ 520 μK for eight atoms. For even higher atom numbers

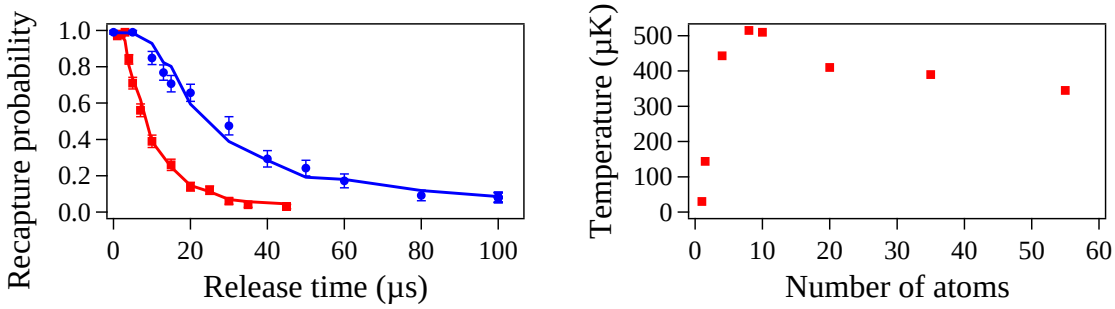

Figure 9.1: Atom number dependent temperature. *left*) We compare the temperature of a single atom loaded into a 2.7 mK deep dipole trap for compensated (red squares) and uncompensated (blue circles) magnetic fields. A simulation leads to temperatures of 150 μK and 35 μK for uncompensated and compensated magnetic fields, respectively. *right*) We show the ensemble temperature versus the loaded atom number. The atom number is changed by varying the oven temperature for a fixed trap depth of $\sim$3 mK.

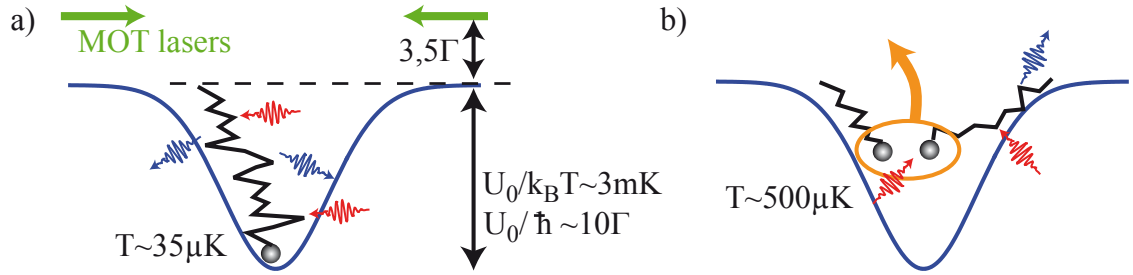

Figure 9.2: Atom cooling inside the dipole trap. a) A single atom can be laser-cooled to the bottom of the trap U_0. Temperatures as low as 35 μK have been measured for $U_0/k_B = 2.7$ mK. b) Cooling of many atoms is hampered by light-assisted collisions. Before being cooled to the bottom of the trap both atoms are ejected from the trap.

the temperature decreases slightly due to higher atomic densities. Higher densities lead to a faster thermalization of the gas during the 30 ms interval (see Sec. 2.3.1) which on long time scales results in $\eta = U_0/k_B T \sim 10$ (see below).

One way to think about this behavior is that atom pairs are lost from the trap due to light-assisted collisions before being cooled to the bottom of the trap ($U_0/k_B \sim$ 3 mK) as it would be the case for a single atom (see Fig. 9.2). The trap depth corresponds to $U_0/\hbar \sim 10\Gamma$ and the MOT lasers are 3.5Γ red-detuned to the atom transition in free space (see Sec. 3.4.1). We therefore assume the atom to see an average laser detuning of $3.5 + 10/2 = 8.5\ \Gamma$. The time for the atom to be MOT-laser cooled to the bottom of the trap would be $t_{cool} = \frac{\hbar}{E_{rec}} \frac{1+s+4(8.5)^2}{s} \sim 1.7$ ms, where we used the estimated MOT laser saturation intensity $s \sim 50$. If during that time another atom enters, both can be ejected from the trap due to light-assisted collisions. The atoms do not have time to reach the bottom of the trap before they are ejected from the trap resulting in a much higher temperature than reached with a single atom. Knowing that this is the case we estimate the two-body loss rate to be higher than t_{cool}^{-1}.

Radiative escape induced by the loading beams prevents the atom sample to have

the same initial temperature as a single atom. Note that thermalization in the absence of any near-resonant light can reduce the temperature and leads to atom sample temperatures of around $T_{th} \sim U_0/k_B/10 = 300$ μK. Beyond this point the thermalization practically stops as mentioned earlier.

Atom number of loaded sample

Light-assisted collisions not only limit the initial temperature but also the total number of atoms to $N_{st} \sim \sqrt{\frac{R}{\beta'}}$ according to Eq. 3.6. To estimate the number of atoms that can maximally be loaded into the trap we start by measuring β'. We work in a regime where three atoms are initially trapped and illuminate the atom cloud with the six molasses beams for a variable time[1]. The atoms have a temperature of ~ 390 μK in a $U_0/k_B = 2.6$ mK deep trap. Fig. 9.3 shows how the atom number quickly decreases and flattens at 0.55 ± 0.05 after ~ 5 ms. The initial decay has a rate of $\beta' \sim 0.5$ ms^{-1} extracted using the simulation of Sec. 9.3.2. It is completely due to two-body loss for two reasons. First, we verify that one-body loss is not important by loading a single atom and illuminating it the same way as the many atom sample. The scaled single atom result (black circles) shows no significant decay over the first 50 ms assuring that one-body loss is negligible.

Second, the reason for the plateau at one-half is due to the nature of two-body loss and a second strong indication for this loss to be dominant in the beginning. For an odd number of atoms, the two-body losses expel all but one atom while for an even number of atoms all atoms are expelled. The one atom that is eventually left in the trap is then lost due to one-body loss at a much longer time scale ($\sim 1 - 24$ s), governed by molasses laser heating and collisions with the background gas. Besides the long lifetime, an indication of single atom preparation is also the temperature of the atom sample which becomes sub-Doppler ~ 40 μK again after ~ 5 ms.

The height of the plateau of 0.55 ± 0.05 also gives information about the atom number distribution inside the trap. If we would have loaded a completely sub-Poissonian distribution with $\bar{N} = 3$ and $\Delta N = 0$ (δ-distribution) we would always measure one atom in the end since always exactly one atom pair is expelled from the trap. The height of the plateau would then be equal to one. For a perfectly Poissonian distribution on the other hand we expect it to be one-half. For the sub-Poissonian atom distribution with $\Delta N^2/\bar{N} = 0.7$ as found in Sec. 8.5 the actual value lies very close to one-half and is in good agreement with the measured value. Note that here the two-body losses are at the heart of sub-Poissonian single atom loading as described in Sec.3.4.1: 50 % of the time one atom is present, 50 % of the time zero atoms are present.

Having extracted the loss constant β' associated to molasses loading we can now estimate the expected average atom number $N_{st} \sim \sqrt{\frac{R}{\beta'}}$ that can maximally be loaded into the trap. We assume our trap loading rate $R \sim n_0 w_x z_R \bar{v}$ to be the product of the MOT density n_0, the trap waist in radial and the Rayleigh length in axial direction

[1] A detailed description of the experimental sequence is given in Sec. 9.3

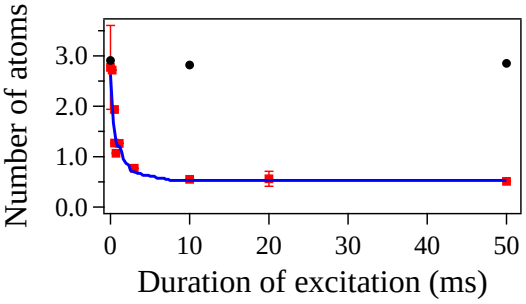

Figure 9.3: MOT-induced two-body loss. Atom number versus excitation light duration for which the MOT lasers have been used. The collisional loss rate $\beta' = 0.5\ \mathrm{ms}^{-1}$ is extracted from a simulation. The black circles indicate the one-body losses.

w_x, z_R and the thermal velocity $\bar{v} = \sqrt{\frac{8k_\mathrm{B}T}{\pi m}}$ (Kuppens *et al.*, 2000). For typical MOT densities $n_0 \sim 10^{10}\ \mathrm{cm}^{-3}$ (Sec. 3.3.4) at the Doppler temperature $T = 150\ \mu\mathrm{K}$ and $w_x \sim 1\ \mu\mathrm{m}$, $z_R \sim 4\ \mu\mathrm{m}$ we find $R \sim 7 \cdot 10^3 \mathrm{at/s}$ and estimate a maximal atom number $N_{st} \sim \sqrt{\frac{R}{\beta'}} = 4$ in steady state. This is much smaller to the actual measured maximal atom number of ~ 100 (see Ch. 10) measured by using the compressed MOT (see Sec. 3.4.2). This incompatibility could be explained by the fact that β', which has been measured in a configuration with constant MOT beam frequency, decreases when loading the trap in the compressed MOT phase, during which the frequency of the MOT beams is varied. It could also arise from an underestimation of the loading rate of the micro trap from the MOT due to an increased MOT density during the compressed MOT phase.

9.3 Measurement of light-assisted collisions

The basic idea of the measurement of light-assisted collisions is the following: We illuminate trapped atoms with near-resonant light and monitor the atom loss over time. The atom number decay can have two principal causes:

- **One-body loss.** The trapped atoms scatter laser photons which leads to a heating and subsequent loss of atoms. The heating rate can be uniquely measured using a single atom as described in Sec. 7.3.1 since no two-body losses are present. The experimental sequence for these measurements is shown on the left of Fig. 9.4. We trap a single atom in our 850 nm trap with $U_0/k_\mathrm{B} = 2.7$ mK. Subsequently, the trap depth is ramped to U_f and illuminated by the probe laser. Finally, the trap is ramped back to its initial value where we check for the presence of the atom. The recapture rate as a function of illumination duration is a measure of the heating rate α. The lifetime of the atom when no near-resonant light is present is ~ 24 s (see Sec. 5.3). Any faster loss can then be attributed to light scattering from the probe laser.

- **Two-body loss.** In samples with many atoms light-assisted collisions can also lead to atom loss. This loss mainly has a two-body nature. A direct measurement cannot always be done since heating due to photon scattering is always present as well. We will show that there are parameter regimes for which the

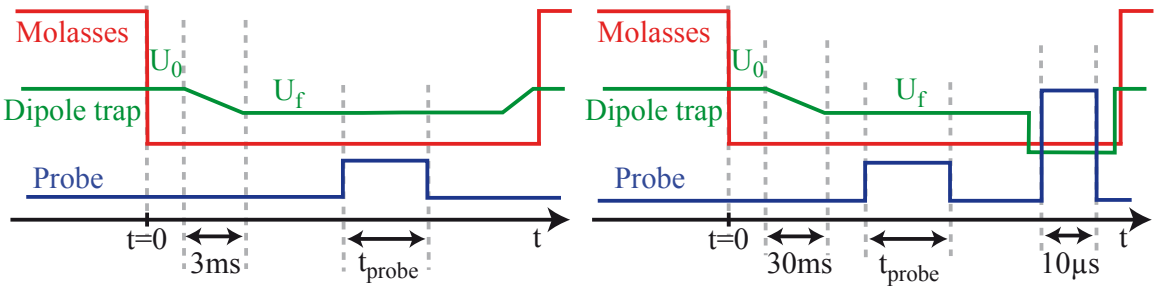

Figure 9.4: Single and many atom experimental sequences. *left*) We prepare a single atom in a U_f deep dipole trap. Afterwards the atom is illuminated by near-resonant light for a variable period of time t_{probe}. The sequence is repeated 200 times to build up the recapture rate. *right*) We prepare ~ 3 atoms in a U_f deep trap by adiabatically ramping from 20 mK in 30 ms. The atoms then thermalize for 50 ms and are afterwards illuminated by near-resonant probe light. Afterwards we switch off the trap to measure the atom number with a 10 μs probe and repumper pulse on resonance with the atom.

one-body loss rate can be held smaller than the two-body one enabling an unbiased measurement of the two-body loss rate. The experimental sequence for the measurement is shown on the right of Fig. 9.4. We load the dipole trap at $U_0/k_{\mathrm{B}} = 20$ mK and adiabatically ramp it down to its final value U_f. After the ramp we wait for 50 ms for the gas to thermalize. It is then illuminated by the probe laser for a variable time period t_{probe}. Subsequently, we switch off the trap and measure the atom number after a 1 μs time of flight. We apply the fluorescence integration method using the probe and repumper probe at resonance for 10 μs (see Sec. 8.2). The loading procedure prepares about 90 % of the atoms in $5^2\mathrm{S}_{1/2}\mathrm{F} = 1$ without control on their Zeeman state. Without any near-resonant light present the lifetime of the atoms is about ~ 200 ms (measured in Sec. 9.3.3) due to hyperfine spin-relaxation two-body losses (Sec. 2.2.2). The atom number can be assumed constant over typical time scales of light-induced losses measured here.

The near-resonant light is provided by the counter-propagating (to avoid radiation pressure) $\sigma^+ - \sigma^-$ probe and repumper probe laser. The repumper laser with $s \sim 5$ stays on resonance with the atom vacuum transition. A magnetic field of ~ 1 Gauss comprises a 45° angle with the probe laser z-direction and defines the quantization axis. This leads to a nearly isotropic probe laser polarization seen by the atom[2]. We study the collision rates over a wide range of probe and trap parameters by applying the following procedure to distinguish between one- and two-body losses: For a given set of probe and trap parameters we first measure the heating rate α of the probe laser on a single atom (Sec. 9.3.1). For the same parameters[3] we then perform the measurement with more than one atom (Sec. 9.3.2). Since both loss mechanisms

[2]Note that the magnetic bias field introduces radiation pressure even for balanced counter-propagating lasers. The effective imbalance has a small effect $\lesssim 10$ % on the actual trap depth.

[3]The only parameter which cannot be adjusted is the temperature which is usually higher for an atom ensemble than for the single atom. We will discuss the effect of a different temperature later on.

compete in this case, we fit the obtained curve by a numerical simulation. In this model the two-body loss rate β' is the only free parameter while the one-body loss rate α is constrained by the single-atom result.

9.3.1 Single atom losses

Typical loss curves for a single atom obtained by varying the probe laser duration and measuring the recapture rate have been shown in Fig. 7.8. We again fit Eq. 5.5 to the data whilst keeping the trap depth U_f constant and allowing the temperature to vary by no more than 10 %. The left and right side of Fig. 9.5 show the extracted heating rates α (blue circles) versus the probe laser detuning for $U_f/k_\mathrm{B} = 0.9$ mK and $U_f/k_\mathrm{B} = 1.8$ mK, respectively. The probe laser saturation was constant $s \sim 0.5$.

For $U_f/k_\mathrm{B} = 1.8$ mK we also plot the data (red squares) of Fig. 7.8, for which the magnetic field was aligned with the probe laser (z-direction). This led to a proper σ^+-polarization of the probe laser and constrained the laser field to drive the closed transition $5^2\mathrm{S}_{1/2}\mathrm{F} = 2, \mathrm{m_F} = +2 \leftrightarrow 5^2\mathrm{P}_{3/2}\mathrm{F}' = 3, \mathrm{m}'_\mathrm{F} = +3$ only. The dashed fit of the data (red squares) is a Lorentzian (Eq. 7.1) with width ~ 8 MHz slightly larger than the natural line width due to temperature broadening.

We see that the curve is much broader when using an isotropic probe laser polarization containing all polarizations ϵ. Also, the form does not resemble a Lorentzian any more. This is due to the fact that for isotropic light probe laser photons are absorbed between all light-shifted Zeeman states $5^2\mathrm{S}_{1/2}\mathrm{F} = 2 \leftrightarrow 5^2\mathrm{P}_{3/2}\mathrm{F}' = 3$ as illustrated in Fig. 1.7. The Zeeman states for e.g. $F' = 3, m_{F'} = 0$ is much more light-shifted than the Zeeman states belonging to the closed transition $F' = 3, m_{F'} = \pm 3$ leading to a larger absorption and thus heating spectrum. A second important broadening effect is the finite temperature of the atom as discussed above. The onset of probe heating appears in both cases when the probe laser detuning starts to reach the trap depth $U_f/k_\mathrm{B} = 0.9$ mK ($U_f/h = 18$ MHz) and $U_f/k_\mathrm{B} = 1.8$ mK ($U_f/h = 36$ MHz).

For a proper treatment of an isotropic probe one needs to solve the optical Bloch equations in Sec. 1.5.4 taking into account all Zeeman levels. Here, we want to simplify the problem by neglecting all non-diagonal elements corresponding to the coherence parts. The set of equations is called rate equations and leads to the steady state populations of each Zeeman level Π_{m_F} for given probe and trap parameters as shown in App. C. Analogous to Sec 7.3.1 we can calculate the heating rate as

$$\alpha = 2E_{rec}\frac{\Gamma}{2}\sum_{m_F}\Pi_{m_F}\sum_{\epsilon}C'^{1/2,3/2,3/2}_{2,m_F,3,m_F+\epsilon}\frac{s}{1+s+4\left(\frac{\Delta_{\mathrm{m_{F'}}}}{\Gamma}\right)^2}\,. \tag{9.1}$$

It contains all possible combinations to excite the atom from any ground Zeeman level into an excited one. We only sum over the ground Zeeman states since the population in the excited states is very small $\sum_{m_{F'}}\Pi_{m_{F'}} \sim 0$ due to the low probe saturation. $\Delta_{\mathrm{m_{F'}}} = \delta - (\Delta_{5^2\mathrm{S}_{1/2}} - \Delta_{5^2\mathrm{P}_{3/2}\mathrm{F}'=3,\mathrm{m_{F'}}})$ is the difference between the probe frequency and the atom transition frequency between the light-shifted ground (Eq. 1.39) and excited states[4] (Eq. 1.37), as illustrated in the figure in App. C. Note that the

[4] For the states $\mathrm{m_{F'}} = \pm 3$ belonging to the cycling transition we simply find $\Delta_{m_{F'}=\pm 3} = \delta - U_f/\hbar$

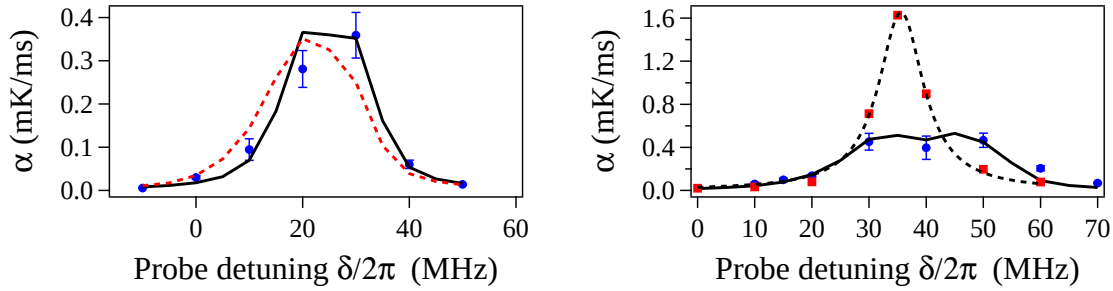

Figure 9.5: Probe-induced atom heating. *left*) Heating rate α (blue circles) versus the probe laser detuning ν_{probe} ($s \sim 0.5$) for a single atom having a temperature of 100 μK in a $U_f/k_B = 0.9$ mK ($U_f/h = 18$ MHz) deep trap. The rate equations result (black line) fits the data well. For a higher temperature of 200 μK the rate equations result (red dashed line) slightly broadens and shifts to lower probe frequencies. *right*) We plot the measured heating rate for a single atom at 200 μK in a trap of depth $U_f/k_B = 1.8$ mK ($U_f/h = 36$ MHz) when illuminated by isotropic probe light (blue circles) and for changing probe frequency. Again the result of the rate equations (black line) reproduces the data. We also show the measured data for a σ^+-polarized probe (red squares). Here, the lorentzian function of Eq. 7.1 (dashed line) explains the data. The probe saturation is kept constant at $s \sim 0.5$.

weights on each sum are normalized $\sum_{m_F} \Pi_{m_F} \sim 1$ and $\sum_\epsilon C'^{1/2,3/2,3/2}_{2,m_F,3,m_F+\epsilon} = 1$, where we used the normalized Clebsch-Gordon coefficients $C'^{1/2,3/2,3/2}_{2,m_F,3,m_F+\epsilon} = C^{1/2,3/2,3/2}_{2,m_F,3,m_F+\epsilon}/W$ with $W = \sum_\epsilon C^{1/2,3/2,3/2}_{2,m_F,3,m_F+\epsilon}$. Additionally, we convolute the heating rate with the position distribution of the atom inside the trap to account for temperature-dependent broadening as introduced in Sec. 5.2.1. The black line in Fig. 9.5 corresponds to the result of the rate equations and generally reproduces the measured data. To indicate the broadening due to higher atom temperatures we show the calculated result for $U_f/k_B = 0.9$ mK and an atom temperature of 200 μK which is twice as high as the measured temperature of 100 μK. The higher temperature result is shifted to smaller detunings and deviates from the measured values slightly.

9.3.2 Two-body losses

We now repeat the same measurements using three atoms on average instead. The left graph in Fig. 9.6 shows one example decay curve for three atoms on average compared to the case of a single atom for a trap depth of $U_f/k_B = 1.8$ mK and the probe detuning $\delta/2\pi = 10$ MHz. While the single atom stays trapped for over 10 ms, this is no longer true when several atoms are simultaneously in the trap. In the multi-atom case light-assisted collisions lead to a rapid loss of the atoms. We see that a one-body loss process (exponential decay, dashed green curve) does not describe the data correctly as the loss is now mainly of two-body nature. Note that the atom number decays to zero and does not level off as when using the molasses lasers. The reason is that the probe lasers do not Doppler-cool the atom in all three dimensions leading to a higher heating than the molasses beams.

In order to extract the two-body loss constant β', we start from the phenomeno-

logical equation 2.12 ruling the variation of the number of atoms $N(t)$ in the presence of one- and two-body losses:

$$\frac{dN(t)}{dt} = -\gamma(t)N(t) - 2\beta'\frac{N(t)(N(t)-1)}{2} \ . \tag{9.2}$$

In this equation, the two-body loss rate is proportional to the number of atom pairs $N(N-1)/2$. The factor 2 in front of the two-body term stems from the fact that one collision between a pair of atoms leads to the loss of the two atoms, as the energy released is usually on the order of hundreds of milliKelvin, much larger than the trap depth. The one-body loss rate $\gamma(t)$ accounts for the heating that eventually leads to the loss of the atoms. It is related to the probability $P_1(t)$ in Eq. 5.5 to lose the atom through $\gamma(t) = -\dot{P}_1(t)/P_1(t)$.

Equation 9.2 with no one-body loss ($\gamma = 0$)

$$\frac{dN(t)}{dt} = -2\beta'\frac{N(t)(N(t)-1)}{2} \ . \tag{9.3}$$

has the analytical solution

$$N(t) = \frac{N_0 \exp \beta' t}{1 - N_0 + N_0 \exp \beta' t} \tag{9.4}$$

and allows the number of atoms to vary continuously. For larger atom number Eq. 9.2 can be simplified to

$$\frac{dN(t)}{dt} = -\gamma(t)N(t) - 2\beta'\frac{N(t)^2}{2} \ , \tag{9.5}$$

which has the solution for $\gamma = 0$

$$N(t) = \frac{N_0}{1 + N_0\beta' t} \ . \tag{9.6}$$

The half lifetime is in this case given by $N_0\beta'$.

In our case however, the small atom number (~ 3) requires a discrete treatment of the atom number. It makes the use of Eq. 9.4 impossible to fit the data even in cases for which the one-body loss is negligibly small. For example Eq. 9.4 leads to a constant steady state atom number of 1 which clearly disagrees with the observed value. Also, $N(t)$ cannot be directly associated with the actual measured average atom number $\bar{N}$, as discussed in Sec. 8.5. We can account for the discretization and the average mean atom number and extract β' by numerically solving Eq. 8.8 or by using a Monte-Carlo simulation.

Monte-Carlo simulation

The starting point of the algorithm is to pick up an initial number of atoms N out of a Poissonian distribution with mean $\bar{N}$. The simulation routine evolves this atom number by time steps Δt. At each step we calculate the probability for atom i out of $N(t)$ atoms to be lost between t and $t + \Delta t$. For one-body loss this probability can be

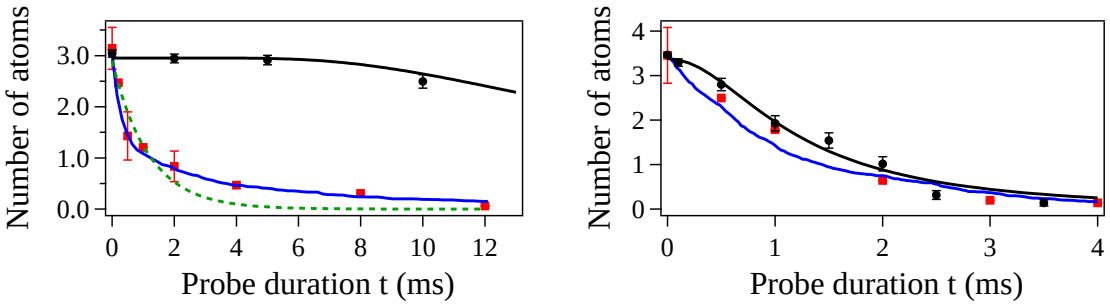

Figure 9.6: Atom loss curves due to one- and two-body loss. Average atom number (red squares) that remains in the $U_f/k_B = 1.8$ mK deep dipole trap after illumination of the probe laser with $s \sim 0.5$ for a duration t. The single atom result (black circles) is also shown with Eq. 5.5 as a fit. *left*) The probe laser detuning is $\delta/2\pi = 10$ MHz and red-detuned to the by 36 MHz light-shifted atomic transition. The simulation result (blue line) yielding $\beta' = 0.6 \pm 0.1\text{ms}^{-1}$ and an exponential fit (green dashed line) are compared. *right*) The probe laser detuning is $\delta/2\pi = 40$ MHz and nearly on resonance with the atom. Here, only the upper-bound value can be given for $\beta' < 0.1 \pm 0.08\text{ms}^{-1}$.

derived as follows. The left graph in Fig. 9.7 shows how $(N(t) - N(t+\Delta t))/N(t) = 1 - N(t+\Delta t)/N(t)$ corresponds to the relative atom loss during the interval Δt. We also know the probability $P(t) = N(t)/N_0$ for the fraction $N(t)/N_0$ of atoms to be left inside the trap after time t. We then find the probability for one atom to be lost during Δt to be $1 - N(t+\Delta t)/N(t) = 1 - P(t+\Delta t)/P(t)$ which we can Taylor expand to $-\dot{P}(t)/P(t)\Delta t$. The probability for a one-body loss to occur in the $N(t)$ atom ensemble is therefore

$$\chi_1 = -N(t)\dot{P}_1(t)/P_1(t)\Delta t \ , \tag{9.7}$$

where $P_1(t)$ is the recapture probability given by Eq. 5.5. Note that $\chi_1 \geq 0$ as $P_1(t)$ is a monotonically decreasing function and thus $\dot{P}_1(t) < 0$. The probability to lose one atom pair by a two-body light-assisted collision per time interval Δt is given by:

$$\chi_2 = \beta' \frac{N(t)(N(t)-1)}{2} \Delta t \ . \tag{9.8}$$

Here $\frac{N(t)(N(t)-1)}{2}$ corresponds to the number of atom pairs in the atom ensemble (see Sec. 8.5).

These probabilities χ_1 and χ_2 allow us to set up the composed probabilities for each of the following three measurement outcomes to happen after the time interval Δt: First, the probability for no losses to occur is $P_{\text{no}} = (1-\chi_1)(1-\chi_2)$. Second, the probability that only a one-body loss happens is $P_{\text{one}} = \chi_1(1-\chi_2)$. The same is true for, third, the probability that a two-body loss takes place $P_{\text{two}} = \chi_2(1-\chi_1)$. All other possible outcomes are proportional to Δt^k with $k > 1$. Their contributions are held small by fulfilling the condition $\chi_1, \chi_2 \ll 1$. Note, that in this case the sum $P_{\text{no}} + P_{\text{one}} + P_{\text{two}} \sim 1$.

At each step we just need to choose a random number ξ from a uniform distribution between 0 and 1 to decide between the three outcomes as illustrated on the

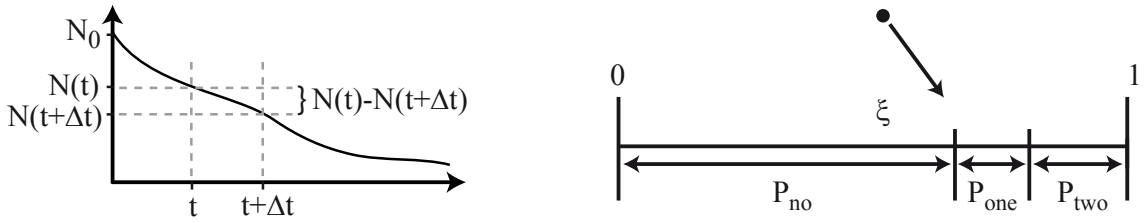

Figure 9.7: Simulation procedure. *left*) Atom number $N(t)$ versus time. During the time step Δt the atom number decreases from $N(t)$ to $N(t+\Delta t)$. *right*) The decision of how to proceed with the atom depends on which case the random number ξ falls in. One- and two-body as well as no loss are possible outcomes, each having probabilities $P_{\text{one}}, P_{\text{two}}$ and P_{no}.

right graph in Fig. 9.7. If, e.g., the random number is smaller than P_{no}, we choose the atoms to stay in the trap. If the random number is bigger than P_{no} but smaller than $P_{\text{no}} + P_{\text{one}}$, the atoms undergo a one-body loss and we decrease N by one. The last possibility arises for a random number greater than $P_{\text{no}} + P_{\text{one}}$ but smaller than $P_{\text{no}} + P_{\text{one}} + P_{\text{two}} = 1$ in which case a two-body loss leads to a decrease of the atom number N by two. We then move forward in time steps Δt until no atom is left. The routine is repeated typically 200 times to average out any numerical noise. Each time we pick the initial atom number out of a Poissonian distribution with mean $\bar{N}$. We also check that the Monte-Carlo simulation gives the same results as numerically integrating the differential equations Eq. 8.8.

We fit the loss curve by this simulation to extract β'. The one-body loss rate as measured on a single atom can be used to constrain χ_1. This is possible as the single atom measurement has been carried out for the same set of parameters. Attention has to be payed to a possible difference in temperature for single atom and many atoms which can result in different heating rates as seen in the last section. In the simulation we therefore use the calculated result for which the single atom temperature has been adjusted to the many atom one. For the data at $U_f/k_{\text{B}} = 1.8$ mK discussed above we find $\beta' = 0.6 \pm 0.1$ ms^{-1} with an atom ensemble temperature of 292 μK, which is slightly higher than the single atom temperature measured to be 200 μK.

Regimes of one- and two-body loss

The example loss curve on the left of Fig. 9.6 showed one example with a two-body loss much faster than the one-body loss. In this case the probe detuning at 10 MHz is red-detuned with respect to the light-shifted atom transition ($U_f/h \sim 36$ MHz). On the right of Fig. 9.6 we show an example for which the probe laser at 40 MHz is close to resonance with the atom inside the trap. Here, the decay is the same for a single atom and for three atoms on average. It is dominated by the probe heating measured on a single atom. In these situations we can only extract an upper-bound value for β', which in this case is $\beta' < 0.1 \pm 0.08$ ms^{-1}.

Fig. 9.8 compares the inverse half-maximum decay time of the initial atom number between a single atom and three atoms for different probe detunings and trap depths $U_f/k_{\text{B}} = 0.9$ mK and $U_f/k_{\text{B}} = 1.8$ mK. We note that the numerically extracted inverse

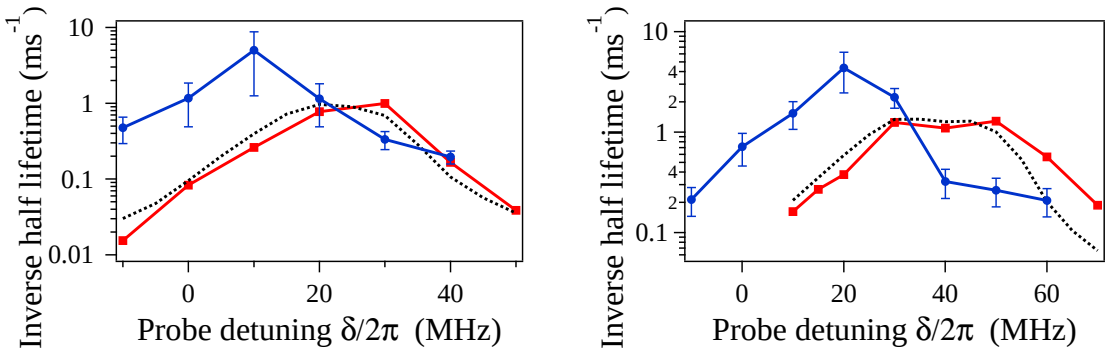

Figure 9.8: Half life time dependent on the probe frequency. We compare the inverse half lifetime of a single atom (red squares) and of three atoms (blue circles) versus the probe detuning for a fixed probe saturation $s \sim 0.5$. The black dotted line is the single atom result adjusted to the many atom ensemble temperature. The trap depth is *left*) 0.9 mK and *right*) 1.8 mK.

half lifetime for the many atom case agree within ~ 20 % with $N(0)\beta'$ as the inverse half lifetime of Eq. 9.6. Although Eq. 9.6 is not completely valid in our case it seems however to be close to the inverse half lifetime which we extract numerically.

We see that two-body losses become dominant for probe detunings smaller than the light-shifted atom transition frequency of 18 MHz for $U_f/k_B = 0.9$ mK and 36 MHz for $U_f/k_B = 1.8$ mK. The probe laser is red-detuned with the atom in this case. For values of the probe detuning on resonance or larger than the light-shifted atom transition, i.e. for an effectively blue-detuned probe, one-body loss due to probe laser heating becomes the dominant loss channel. The measured one-body rates cannot be directly compared to the two-body rates as the single atom temperature is different to the one measured with three atoms on average. We show the calculated one-body rates for which the single atom temperatures have been adjusted to the multi-atom temperatures 198 μK and 292 μK for $U_f/k_B = 0.9$ mK and $U_f/k_B = 1.8$ mK, respectively. A small shift to lower probe detunings is observable for the one-body loss rates. For the simulation we therefore use the temperature-adjusted calculated one-body loss rates although the difference does not affect any conclusions made in the following.

Calculation of the two-body loss rate β

In order to calculate the two-body loss rate $\beta = \beta' V$, we need to know the volume V occupied by the cloud (see Eq. 2.11). In our experiment, the direct measurement of the in-situ density is hard as the size of the cloud is smaller than the diffraction limit of the imaging system and we have to rely on a calculation. We assume thermal equilibrium at the temperature T_0 before the excitation. In this case $V = (\frac{2\pi k_B T_0}{m\bar{\omega}^2})^{3/2}$ (see Sec. 2.3.1). In thermal equilibrium the density has a Gaussian shape and the two-body loss rate follows from the loss constant as[5]

[5]When transforming $n(r) = -\beta n(r)^2$ into $N = -\beta' N^2$ by assuming a thermal and thus Gaussian density profile $n(r)$, we find the conversion factor $2\sqrt{2}$.

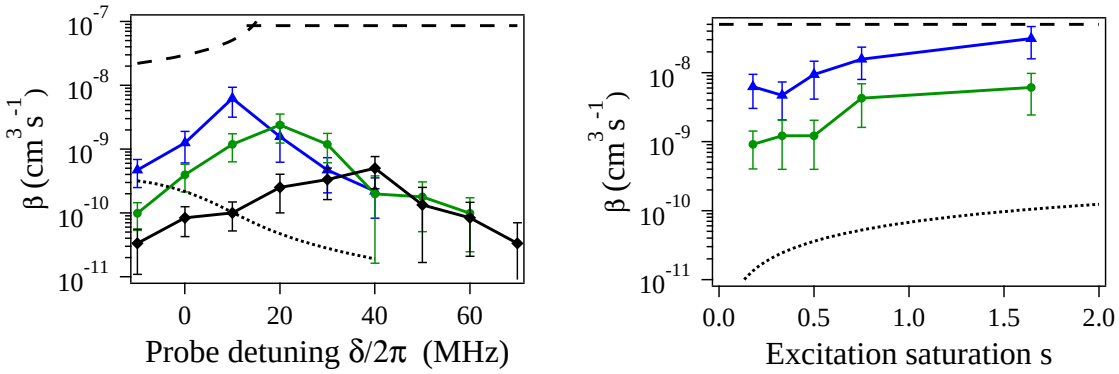

Figure 9.9: Probe frequency and intensity dependence of β. *left*) We show the dependence of β on the probe detuning for different trap depths $U_f/k_B = 0.9$ mK ($U_f/h =$ 18 MHz) (blue triangles), 1.8 mK (36 MHz) (green circles) and 2.6 mK (55 MHz) (black diamonds). The probe saturation is constant $s \sim 0.5$. The dotted black line is the result from the Gallagher-Pritchard model and the dashed line is the Langevin limit (see text). *right*) β versus the probe saturation parameter. The probe frequency is 10 MHz for $U_f/k_B = 0.9$ mK (blue squares) and $U_f/k_B = 1.8$ mK (green triangles).

$\beta = 2\sqrt{2}\beta' V$. Under this assumption we calculate V and find the peak atomic densities $n_0 = (2.7, 4.3, 5.1)\cdot 10^{12}$ cm^{-3} for trap depths $U_f/k_B = (0.9; 1.8; 2.6)$ mK and initial temperatures $(198, 292, 391) \pm (60, 88, 117)$ μK. We also assume that V remains constant during the decay, which implies that the temperature of the sample is constant during the laser excitation. Clearly this assumption cannot be true for the entire range of the excitation parameters, as the influence of the heating is comparable to the light-assisted loss when the probe is close to the atomic resonance. However, the assumption is true for the largest value of the two-body loss rate, as in this regime the heating becomes negligible (see Fig. 9.8). As an example, for the data of the left graph in Fig. 9.6 the temperature of the cloud varies by only ~ 0.3 % during the first 10 ms of the decay. In this case we have checked that by allowing the volume to vary does not change significantly (< 1 %) the value of β.

Under the assumption of thermal equilibrium, we calculate the two-body loss rate β from the measured β' for various excitation parameters. Its dependence on the probe detuning δ is summarized on the left of Fig. 9.9 for three different trap depths. The right side of Fig. 9.9 shows the variation of β with the saturation parameter s for a detuning $\delta/2\pi = 10$ MHz for two trap depths.

9.3.3 Discussion of the results

The general feature of light-assisted collisions can be understood using a semi-classical picture, such as the one proposed by Gallagher and Pritchard discussed in Sec. 2.2.3. Near-resonant light excites a pair of atoms from the ground state $5S_{1/2}$ (neglecting the hyperfine structure) to the molecular, attractive, potential curve $5S_{1/2}+5P_{3/2}$. There, two mechanisms can lead to atom loss. The first one, called fine-structure changing collisions, consists in the pair of atoms to change from the molecular potential curve $5S_{1/2} + 5P_{3/2}$ to $5S_{1/2} + 5P_{1/2}$ before it decays back to the ground state. In this

process the pair of atoms gains ~ 170 K of kinetic energy and therefore escapes the trap. In the second mechanism, called radiative escape, the atoms are accelerated along the attractive $5S_{1/2}+5P_{3/2}$ potential curve and decay back to the ground state molecular curve $5S_{1/2}+5S_{1/2}$ having gained a kinetic energy larger than the depth of the trap. The average time to decay back can be approximated by half the atomic lifetime ($\Gamma^{-1}=26$ ns) (Weiner *et al.*, 1999). In our case where the excitation is nearly resonant, the atoms are excited at long interatomic distance and therefore decay back to the ground state before reaching the region where fine-structure changing collisions occur. The dominant loss mechanism should therefore be radiative escape. Also, hyperfine-structure changing collisions are negligible in the presence of near-resonant light since their loss rates $\beta_{\mathrm{HF}} \sim 10^{-11}$ cm^{3}s^{-1} (Gensemer *et al.*, 2000) are much lower than the loss rates observed in our case. We note however that this model, as well as more developed ones (Weiner *et al.*, 1999) ignore the hyperfine structure in the excited state, an assumption probably inaccurate in our experiment. We are not aware of any theoretical prediction for the light-assisted loss rate in our conditions of a low trap depth and a near-resonant excitation.

The result from the Gallagher/Pritchard model of Eq. 2.17 in Sec. 2.2.3 is exemplary shown for 0.9 mK (dotted black curve) on the left graph of Fig. 9.9 and does not reproduce the data. The general behavior of the data can however be understood. Starting with a very blue detuned laser (see Fig. 9.10) the excitation probability and consequently the loss of the atom is small. The further we tune the laser on resonance with the transition, the more photons the atom scatters, which increases the probability to deexcite in the escape region and therefore also the loss rate. Note that in this region one-body loss dominates and only an upper-bound value for the loss rate can be given. Passing the transition to the red a tradeoff between several mechanisms governs the losses. First, less photons are scattered when the probe detuning becomes off resonant. On the other hand the excitation takes place closer to the escape radius so that the loss rate increases even further. For further red-detuned frequencies the excitation probability decreases significantly. This is due to the probe laser becoming further off resonant. Additionally, the excitation probability decreases as the excitation occurs at interatomic distances much smaller than typical interatomic distances between two atoms. This leads to a decrease in the loss rate.

The Gallagher/Pritchard model captures the main evolution of the loss rate β with varying probe saturation s for 1.8 mK on the right graph of Fig. 9.9 (dotted black curve). The measured loss rate mainly follows the dependence $\beta \propto \frac{s}{1+s}$ but is again much larger than predicted by the model.

The first striking feature observed in Fig. 9.9 lies in the strong dependence of the two-body loss rate on the trap depth. A variation of a factor 3 in the trap depth leads to a 20-fold increase in β. The shift of the resonances is due to the different light shifts experienced by the atom. Even more remarkably, the measured loss rates can be extremely large, much higher than any predictions we could find in the literature. The theoretical maximum collision rate of the light-assisted collision is given by the Langevin limit (Julienne and Vigué, 1991). This Langevin cross-section is obtained from Eq. 2.5 by setting all partial waves $\mathrm{l} \leq \mathrm{l}_{\max}$ contributing to the collision to one $\sin^2 \delta_{\mathrm{l}}(k_{at}) = 1$. For a given collision energy E this yields

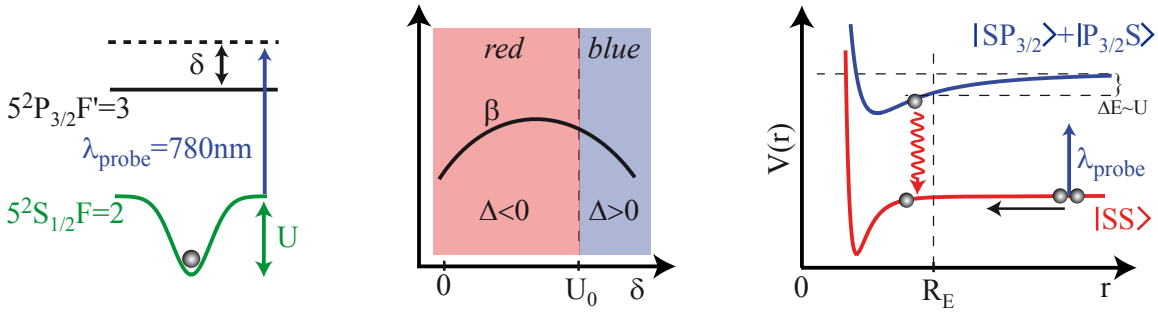

Figure 9.10: Definition of the probe laser detuning. We define the probe detuning δ with respect to the atomic transition $F=2 \rightarrow F'=3$ in free space. We define blue-detuned probe light by $\delta > U/\hbar$ ($\Delta = \delta - U/\hbar > 0$) and red-detuned probe light by $\delta < U/\hbar$ ($\Delta = \delta - U/\hbar < 0$).

$$\sigma_{\text{Langevin}} = \frac{4\pi\hbar^2}{2mE}(l_{\max}+1)^2 \ . \tag{9.9}$$

For the case of the resonant dipole-dipole interaction considered here, the potential [6] when the pair of atoms is excited is $V(r) = -3\hbar\Gamma/4(kr)^3$ (see Sec. 2.2.3). We calculate $l_{\max}$ by imposing two conditions. The first one is that the center of kinetic energy E of the center of mass must be larger than the height of the centrifugal barrier for the collision to take place at short inter-atomic distance. This condition yields

$$l_{\max}(l_{\max}+1) = \left(\frac{3^5(\hbar\Gamma)^2 E}{8^3 E_{rec}^3}\right)^{\frac{1}{3}} \ , \tag{9.10}$$

with $E_{rec} = \hbar^2k^2/2m$ the recoil energy. For a collision energy $E = 3k_BT/2$, we find a Langevin collision rate according to Eq. 2.13

$$\beta_L = 2\pi\left(\frac{\lambda}{2\pi}\right)^2\left(\frac{27}{2}\left(\frac{\hbar\Gamma}{k_BT}\right)^2\right)^{\frac{1}{3}}\bar{v} \ , \tag{9.11}$$

with the average velocity of the center of mass of the atoms $\bar{v} = \sqrt{\frac{16k_BT}{\pi m}}$. For a typical temperature $T = 0.3$ mK we find $\beta_L \sim 8.6 \cdot 10^{-8}$ cm^{3}s^{-1}. The second condition is the following: Julienne and Vigué (1991) show that for the range of temperatures explored in our case, $l_{\max}$ is calculated by imposing that the height of the centrifugal barrier in the S+S potential is small enough to allow a pair of atoms with energy E to be excited before they reach their minimal approach distance, i.e. $l_{\max}(l_{\max}+1)\hbar^2/(mr_{ex}^2) = E$. This yields $\sigma_{\text{Langevin}} = 4\pi r_{ex}^2$, where $kr_{ex} = (-3\Gamma/4\Delta)^{\frac{1}{3}}$, is the interatomic distance at which the atom pair can be excited. The Langevin collision rate is in this case

$$\beta_{L'} = 4\pi\left(\frac{\lambda}{2\pi}\right)^2\left(-\frac{3\Gamma}{4\Delta}\right)^{\frac{2}{3}}\bar{v} \ , \tag{9.12}$$

[6] We note that in our setup, the size of the trap (~ 1 μm) is small enough to influence the interaction between the atoms at distances on the order of a few $\lambda/2\pi$.

which in contrast to the first rate β_L depends on the laser detuning Δ. The bounding Langevin collision rate is then given by $\min(\beta_L, \beta_{L'})$. For atoms at $T = 0.3$ mK in a $U/\hbar = 18$ MHz trap both are indicated on the left of Fig. 9.9 (black dashed line). We see how $\beta_{L'}$ becomes the bounding rate when the laser frequency is smaller than $\delta/2\pi \leq (U - \sqrt{1/3}k_B T)/h = 14.6$ MHz. As both limits do not depend on the probe saturation s we find a constant limit when varying the probe saturation as shown on the right graph of Fig. 9.9. In this case the probe detuning is set to $\delta/2\pi = 10$ MHz, for which $\beta_{L'} \sim 5 \cdot 10^{-8}$ cm^{3}s^{-1} is the limiting collision rate. With increasing probe saturation we see that our measured values reach this limit. It is quite surprising since usually, the survival probability to reach the escape region is small for alkalis. The two-body loss rate is then smaller than the Langevin limit by one or two orders of magnitude (Julienne and Vigué, 1991). We suspect that it is the small trapping volume that leads to this fact.

We compare our findings to the results already published by several groups. Kuppens *et al.* (2000) operate a dipole trap of 26 μm waist, with depth and temperature comparable to ours. The spatial density is also in the 10^{12} cm^{-3} range, but with more than 10^6 atoms. They measure β' in the presence of near-resonant light in the range of $\beta' = 10^{-5} - 10^{-4}$ s^{-1} from which they extract a light-assisted two-body collision rate $\beta \sim 10^{-9}$ cm^{3}s^{-1}, about one order of magnitude smaller than in our case. Kulatunga, Blum, and Olek (2010) work in a dipole trap with a waist of 5 μm. The trap depth, temperature, and densities are also comparable to ours. They measure two-body constants as large as $\beta' \sim 10^{-2}$ s^{-1}, still small with respect to our results, but larger than the Kuppens' one, probably due to the smaller trapping volume. Estimating the volume in their case assuming thermal equilibrium, we find that this corresponds to $\beta \sim 10^{-11}$ cm^{3}s^{-1}.

Finally, Schlosser, Reymond, and Grangier (2002) explain the loading of at most one atom in their sub-micrometer size dipole trap taking $\beta' \sim 1000$ s^{-1}. Estimating the volume either assuming a one-atom thermal distribution or taking reference Kuppens *et al.* (2000), we find a two-body loss rate as high as $\beta \sim 3 \cdot 10^{-9}$ cm^{3}s^{-1}, not surprisingly as large as what we measure here. The comparison between these results tends to suggest that the sub-micrometer size of the potential may play a role in the collision, as for example the size of the trap is not negligible with respect to the range of the dipole interaction between the atoms.

9.3.4 Assumption of thermal equilibrium

The large values of β could also be explained by an overestimation of the volume or underestimation of the density. In order to estimate independently the density, we have measured the rate of the ground-state collisions (see Sec. 2.2.2) between trapped atoms in our sample in the absence of resonant light. The atom losses result from the hyperfine changing collisions between the F = 1 and the F = 2 atoms, which release ~ 300 mK of kinetic energy. The losses should stop when all F = 2 atoms have undergone a collision. Due to spontaneous trap-induced Raman transitions however (rate 0.7 s^{-1}, see Sec. 1.5.7), a fraction of the atoms is steadily transferred to the F = 2 manifold. A steady state population of F = 2 atoms builds up as a compromise

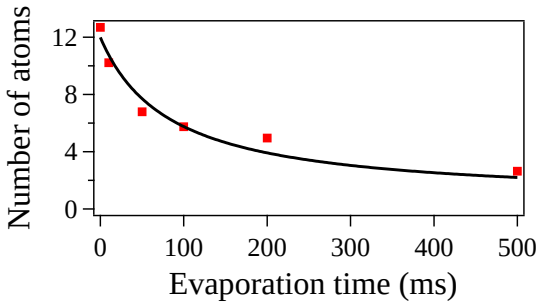

Figure 9.11: Hyperfine changing collisions. We show the atom number versus the holding time at a fixed trap depth of 1.8 mK. The atoms have an initial temperature of 400 μK. The 10 % population in $F=2$ as well as the trap-induced Raman transitions lead to a constant loss due to hyperfine changing collisions. A fit of Eq. 9.4 yields a loss constant $\beta'_{\mathrm{dark}}=1\mathrm{s}^{-1}$.

between the Raman pumping and the collision hyperfine changing losses.

Figure 9.11 shows the atom number as a function of the waiting time in the dark. We start from 12 atoms on average in a 1.8 mK deep trap at a temperature of ~ 400 μK and measured the remaining average number of atoms for various holding times in the trap. We fit the data by a two-body loss process of the form $\dot{N}=-\beta'_{\mathrm{dark}}N(N-1)$ (Eq. 9.4) and extract β'_{dark}. By assuming a thermal volume $V=(\frac{2\pi k_{\mathrm{B}}T_0}{m\bar{\omega}^2})^{3/2}$ we find the loss rate $\beta_{\mathrm{dark}}=2\sqrt{2}\beta'_{\mathrm{dark}}V=3\pm 1\cdot 10^{-12}$ cm^{3}s^{-1}. Gensemer *et al.* (2000) have measured the rate for the hyperfine changing collisions, which varies rapidly with the temperature. At our temperature this rate is around $\beta_{\mathrm{HF}}=3\cdot 10^{-11}$ cm^{3}s^{-1}. The ratio between β_{dark} and β_{HF} is 0.1 and corresponds to the fraction of atoms in the $F=2$ level $\Pi_{F=2}$. We measure $\Pi_{F=2}\sim 10$ % of the atoms in F = 2 by taking a time-of-flight image leaving the repumper probe laser switched off which proves the compatibility of the results. Also, this fraction is compatible with a rate equation model taking into account the spontaneous Raman scattering (see Sec. 5.2.3) and the collision hyperfine changing loss. It therefore seems that the assumption of a thermal volume without the presence of near-resonant light is valid in our case.

However, it may be possible that during the excitation period in the presence of near-resonant light, the density changes and is not constant as assumed in the simulation:

- **Decrease in density.** An increase of the volume V would lead to an even larger value of β. We found two sources for an increase of the volume. First, probe laser photon scattering can lead to an increase in temperature and thus in volume. For the highest loss rates however a temperature increase due to probe laser photon scattering is small as mentioned in Sec. 9.3.2. Second, the density of the few atom cloud is about $n_0=3\cdot 10^{12}$ cm^{-3} and the mean free path of a resonant photon is $1/(n_0\sigma_L)\sim 1.1$ μm, with $\sigma_L\sim 3\lambda^2/2\pi$ the cross-section for the absorption of laser light, much larger than the size of the cloud. We therefore do not expect any influence of photon re-absorption or radiation pressure to decrease the density either.

- **Increase in density.** We do not have any realistic mechanism to explain an increase of the density. The attractive dipole force $9k\hbar\Gamma/4(kr)^4$ seems too weak to pull the atoms together. This however is hard to verify experimentally.

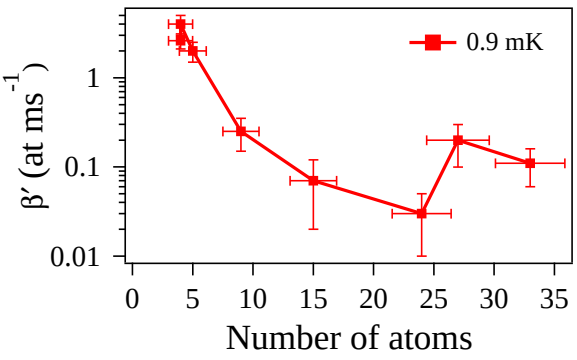

Figure 9.12: Atom number dependent loss rate constant in a $U_f/k_B = 0.9$ mK deep trap. Loss rate constant β' versus the average atom number. The probe saturation is $s = 0.5$ and the probe laser detuning is $\delta/2\pi = 10$ MHz. The loss rate constants are all extracted by applying the simulation.

9.3.5 Evidence of collective behavior

In this section, we investigate the behavior of the loss rate with respect to the number of atoms in the trap. For this measurement the trap depth is $U_f = 0.9$ mK, the saturation of the excitation light is $s \sim 0.5$ and the probe laser detuning is $\delta/2\pi =$ 10 MHz. We vary the average number of atoms in the trap by adjusting the MOT trigger level as mentioned in Sec. 3.4. This allows us to vary the number of atoms in the trap from 3 to 33 on average. We maintain the temperature, and thus the thermal volume roughly constant. It decreases from 192 μK down to 140 μK going from 3 to 33 atoms due to a faster free evaporation process. Fig. 9.12 shows the two-body loss constant β' as a function of the initial average atom number. We observe a very strong and unexpected dependence of this loss rate with respect to the number of atoms: β' varies by almost two orders of magnitude when the average atom number varies from 3 to 33. We have checked that the global dependence of β' on the probe frequency does not change as the number of atoms varies. This means that the plotted loss constants always correspond to the peak values for $U_f = 0.9$ mK for any number of atoms. In the following we discuss some possible mechanisms that could lead to a decrease of the two-body loss rate β' with increasing atom number.

Photon re-absorption and radiation pressure

Following the approach outlined in reference Walker, Sesko, and Wieman (1990), we estimate the density n_{max} of the cloud in the dipole trap, for which re-absorption should become important, to be

$$n_{max} = \frac{c \cdot m \cdot \bar{\omega}^2}{2\sigma_L(\sigma_R - \sigma_L)sI_{sat}} \ , \tag{9.13}$$

where $\sigma_L = (3\lambda^2/2\pi)\frac{1}{1+s}$ is the cross-section for absorption of the laser light and σ_R the cross-section for the absorption of the scattered light, whose ratio σ_R/σ_L is estimated in Steane, Chowdhury, and Foot (1992). We find for our trap parameters $\sigma_R/\sigma_L - 1 \sim$ 0.5 which leads to $n_{max} = 6 \cdot 10^{14}\text{cm}^{-3}$. This density is a factor 10 larger than our highest atom density for 33 atoms of around $4{\cdot}10^{13}$ cm^3 assuming thermal equilibrium. This means that re-absorption of photons should not play a significant role during the excitation of the atoms. This result is also supported by calculating the optical

thickness of the sample.

Optically thick sample

In a second scenario, the relative decrease of the two-body loss rate with increasing atom number comes from an increasing optical thickness of the sample. As the optical thickness becomes higher, the atoms at the center of the cloud see a lower intensity, and therefore have a lower probability to be excited. As the two-body loss rate β depends on the intensity (see Fig. 9.9), the loss rate of the atoms at the center of the cloud will be lower. We have calculated for our densest sample ($N = 33$, $n = 4 \cdot 10^{13}$ cm^{-3}, $T_0 = 165$ μK) a resonant optical thickness along the propagation of the excitation laser of $\mathrm{OD} = n_0 \sigma_L \sigma_\perp = 0.3$. This means that the saturation parameter at the center of the cloud is only $1 - \exp(-OD) \sim 26$ % smaller than in the outer shell. According to Fig. 9.9 a change of ~ 26 % results in a change in β by not more than a factor $1 - 2$ which is far away from explaining a decrease of more than a factor 10.

The low optical thickness also rules out a rather fancy scenario: It could be that the red-shifted photon emitted by the atom excited to the molecular attractive curve is re-absorbed by another atom pair having the right inter particle distance to be excited and to undergo a light-assisted collision. In this scenario, the absorption of only one photon from the laser beams by an atom pair is enough to trigger an avalanche of two-body collisions. It seems to us however that this mechanism would only increase the light-induced loss rate rather than decrease it as observed.

Super-radiance effects

Another mechanism involves the resonant dipole-dipole interaction between the atoms induced by the near-resonant excitation light. The dipole-dipole interaction between two atoms has a magnitude (Weiner *et al.*, 1999)

$$V(r) \sim \frac{\hbar \Gamma}{(kr)^3} \ . \tag{9.14}$$

If the average distance between the atoms is smaller than $1/k = \lambda/2\pi$, the strength of the dipole-dipole interaction is larger than the line width of the transition (see Sec. 2.2.3). In this regime, each pair of atoms has a different resonance frequency. The excitation laser can only excite a fraction of the pairs, thus reducing the two-body loss rate. This situation is reminiscent of the Rydberg blockade observed in atomic ensembles (Urban *et al.*, 2009; Gaëtan *et al.*, 2009). However, for our largest density of $4 \cdot 10^{13}$ at/cm^3, the average inter atomic distance is $2.4 \cdot \lambda/2\pi$ and the dipole-dipole interaction seems too weak to explain our findings.

Breakdown of two-body collision assumption

Finally, the observed dependence of the loss rate could also mean a breakdown of the two-body collision approach. Two scenarios are possible. In the first one the losses are not dominated by two-body collisions but instead by three or more body

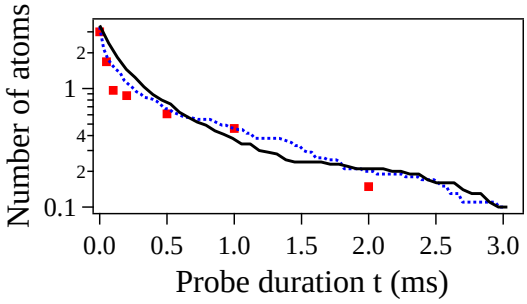

Figure 9.13: Comparison between two- and three-body light-assisted collisions. Atom number (red squares) versus duration of probe pulse for $U_f/k_B = 0.9$ mK, $\delta/2\pi = 10$ MHz and $s \sim 0.5$. A two- (black line) and three-body (blue dotted line) simulation fit are compared.

processes for increasing atom numbers. We simulated the data by using a three-body loss process and could not make a clear difference between two- and three-body losses as shown in Fig. 9.13. In any case we could not find any theoretical prediction for three-body light-assisted collisions.

In the second scenario, a single two-body event triggers the expulsion of more than two atoms. This would be the case if the sample was collisionally thick: the two atoms with large kinetic energy after the spontaneous decay collide with neighboring atoms and expel them from the trap. Although it is not clear what cross section to use to calculate the collisional rate when the kinetic energy of the energetic atoms corresponds to ≥ 0.1 K, we take the largest cross-section possible, that is the s-wave cross section. The mean free path of an atom is then ~ 80 μm, much larger than the size of the cloud. It does not seem that this scenario is likely either.

The conclusion of this section is that we do not have any satisfactory model to explain the dependence of the loss rate with the number of atoms.

9.4 Conclusion

As a conclusion, we have presented a series of measurement of light-assisted collisions in a microscopic dipole trap, when the sample is excited by a near-resonant probe. We have found surprisingly large two-body loss rates, not reported so far, to the best of our knowledge. We have also found an intriguing dependency of the collisional rate with the number of trapped atoms. This behavior may be a signature of collective effects due to the small size of the atomic cloud, on the order of the wavelength of the probing light. Further experimental studies and significant theoretical efforts are needed in order to understand our findings. However, the high loss rates induced by near-resonant light imply new techniques to more efficiently load the micro trap other than by using the molasses. We will present such a technique in the next chapter.

Part IV

Many atom experiments

Chapter 10

Using the micro trap as a dimple

Contents

So far we concentrated on measurements with single atoms or very small atom clouds $N < 10$. The next two chapters will focus on the use of the micro trap in a regime of up to 1000 atoms. The high number of atoms is crucial for forced evaporation experiments reaching ultra-cold and degenerate atom clouds. The last chapter already indicated some limitations that light-assisted collisions impose on the micro trap loading from the molasses or MOT. We will first show the limitations on the number of atoms that can maximally be loaded into the trap and thus motivate the use of another loading technique for the micro trap. Afterwards we describe the technique of using the micro trap in a dimple configuration.

10.1 Résumé

Le chargement du micro-piège directement à partir du MOT est très affectée par les collisions assistées par la lumière. Elles conduisent à une perte d'atomes et à une température élevée. Nous contournons ce problème en utilisant un piège macroscopique

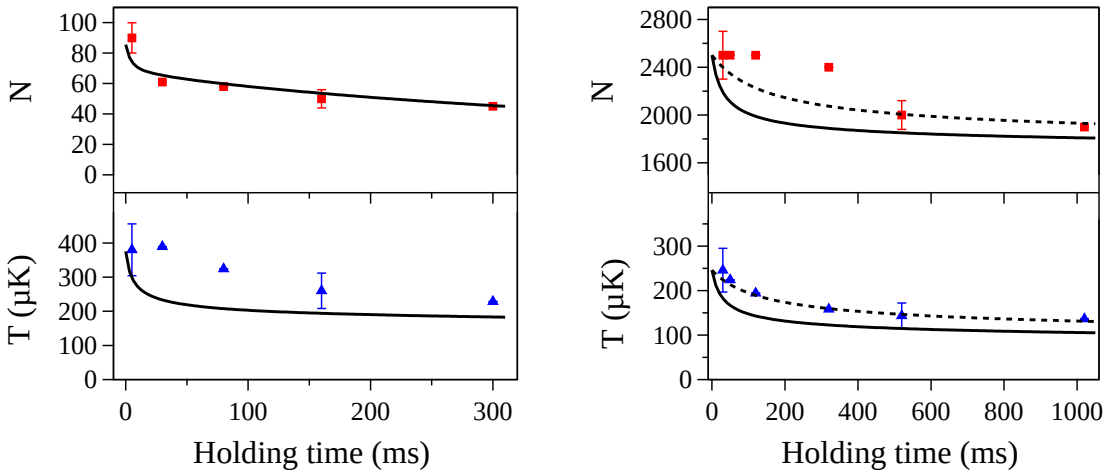

Figure 10.1: Free evaporation in micro and macro trap. We show the evolution of the average atom number N and temperature T of the atom ensemble loaded directly from the MOT into the *left*) 2.7 mK deep micro and *right*) 1.4 mK deep macro trap. The black solid and dotted curves are a simulation described in the text.

comme réservoir d'atomes. Les atomes sont transférés du macro-piège au micro-piège par collisions élastiques en l'absence de toute lumière proche de résonance. Le nombre d'atomes ainsi chargés dans le micro-piège est augmenté d'un ordre de grandeur par rapport au cas du chargement direct par le MOT. La température obtenue est également inférieure.

10.2 Free evaporation in the micro and macro trap

We load the micro (945 nm, $w_x \sim 1$ μm) and macro (850 nm, $w_x \sim 3.8$ μm) trap directly from the MOT as described in Sec. 3.4 and measure the number of atoms N and temperature T as a function of the time the atoms are held in the trap after the loading. For all following measurements we apply the fluorescence integration method discussed in Sec. 8.2 to count the atom number. If not otherwise written the probe ($s \sim 5$) and repumper probe illuminate the free-flying atoms on resonance for 2 μs. The temperature is measured by using the time-of-flight method (Sec. 6.2). For the trap depths used here (< 3 mK) we achieve to prepare 97 % of all atoms in the $5^2S_{1/2}F = 1$ ground state. Additionally the micro trap at 945 nm reduces the Raman-induced hyperfine transitions with respect to the macro trap at 850 nm by a factor ~ 10. Spin-changing collisions therefore do not play a role in the following experiments.

Fig. 10.1 shows the results for the 2.7 mK deep micro trap (left side) and 1.4 mK deep macro trap (right side). While the micro trap can only be loaded with maximally 100 atoms the macro trap contains up to 2500 atoms[1]. The steady-state atom number

[1]The loaded atom number depends on the MOT alignment and the atom flux from the oven. Here, we operate the oven at $T \sim 115°C$.

in both cases follows from Eq. 3.6 and is given by $N_{st} \sim \sqrt{\frac{R}{\beta'}} = \sqrt{\frac{R \cdot V}{\beta}}$. The loading rate R scales with $w \cdot z_R \propto w^3$ (w =waist of the trap laser at the focus, z_R =Rayleigh length) while the atom volume inside the trap scales as $V \propto w^4$. Assuming β to be constant we expect an increase of the atom number of $\sim (w_{\mathrm{macro}}/w_{\mathrm{micro}})^{3.5} \sim 90$, a factor 3.5 larger than measured. This could be due to the different trap depth as the micro trap is almost twice as deep as the macro trap or a higher β for smaller trap sizes.

Leaving the atoms in the trap without any other light present we see a loss of atoms coming along with a decrease in temperature. This behavior is typical for a thermalization process due to elastic collisions introduced in Sec.2.2.1. For the micro trap the thermalization stagnates after $200 - 300$ ms. The temperature decreases by almost a factor two to 200 μK at the expense of a decrease in number of atoms. The stationary regime corresponds to $\eta = U/Tk_{\mathrm{B}} \sim 13.5$ according to Sec. 2.3.1. Here, the thermal atom density is $n_0 = 2 \cdot 10^{14}$ cm^{-3} and the phase-space density from Eq. 2.32 around $\rho = 10^{-4}$ far away from the degenerate regime of < 1. The elastic collision rate $\gamma_{el} = 1.5 \cdot 10^4$ s^{-1} is strikingly high due to the high trap frequencies. Again we find that light-assisted collisions not only limit the initial atom number but also their temperature to values three times larger than the Doppler-limit for a single atom. For the macro trap we find a density $n_0 = 2 \cdot 10^{13}$ cm^{-3} and a calculated elastic collision rate of $\gamma_{el} = 1 \cdot 10^3$ s^{-1}. Due to the larger trapping volume the values are smaller than for the micro trap.

To model the evaporation process we follow the procedure by Luiten, Reynolds, and Walraven (1996) and numerically solve the equations

$$\dot{T} = \frac{\dot{E}_{ev} - \mu \dot{N}}{C} \quad , \quad \dot{N} = -n_0^2 \sigma_{el} \bar{v} e^{-\eta} V_{ev} \ , \tag{10.1}$$

where $\bar{v} = \sqrt{\frac{8k_{\mathrm{B}}T}{\pi m}}$ is the average thermal velocity, μ the chemical potential and $C = (\partial E/\partial T)_N$ is the heat capacity. The effective evaporation volume and the change of internal energy

$$\begin{aligned} V_{ev} &= \frac{\lambda_{th}^3}{k_{\mathrm{B}}T} \int_0^U D_s(E) \left[(U - E - k_{\mathrm{B}}T) e^{-E/k_{\mathrm{B}}T} + k_{\mathrm{B}}T e^{-\eta} \right] dE \ , \\ \dot{E}_{ev} &= \int_U^\infty E D_s(E) \dot{f}(E) dE \ , \end{aligned} \tag{10.2}$$

with the density of states $D_s(E)$ and the Boltzmann distribution function $f(E)$ are similar to the quantities in Sec. 2.3. The basic idea is that hot atoms carry away energy leaving behind colder atoms with a lower internal energy. The black curves in Fig. 10.1 correspond to the solution of the Eq. 10.1. For the micro trap we find good agreement for the evolution of the number of atoms but a theoretically faster expected decrease in temperature. The deviation could be due to the fact that the micro trap is completely filled with atoms from the MOT in which case the harmonic limit (see Sec. 1.5.8) is not valid any more. Also, atoms in the axial direction where the trap has a Lorentzian shape need much more time than predicted to undergo elastic collisions

and to thermalize. We find an even larger deviation between experiment and theory for the macro trap (black curve). Using again the numerical result of Eq. 10.1 we fit the macro trap data for an effective elastic collision rate 5 times smaller than expected (dotted black curve).

High initial temperatures as well as rather low atom numbers ~ 100 that are limited by light-assisted collisions are unfavorable on the way to ultra-cold and dense samples as well as small Bose-Einstein condensates (see below). There are however some possibilities to reduce light-assisted collisions in order to increase the atom number and decrease the temperature when loading the micro trap directly from the MOT. One makes use of the repulsive dipolar potential in the excited state in which case one avoids an increase in kinetic energy due to the attractive potential in the excited state (Dürr, Miller, and Wieman, 2000). In another approach one loads the dipole trap by using a so called dark-SPOT (Ketterle *et al.*, 1993). We also want to mention a technique of a time-averaged trap that has been applied to increase the atom number by a factor two (Ahmadi, Timmons, and Summy, 2005). Here however, we discuss another approach by using the macro trap as an atom reservoir from which the micro trap can be loaded in the absence of any near-resonant light.

10.3 Using the micro trap in a dimple configuration

The results presented so far show that a loading of the micro trap from the MOT is hampered by light-assisted collisions. A widely used technique to go around this is to use the macro trap as an atom reservoir for the micro trap. The idea is to load the macro trap from the MOT. The MOT is then switched off and the micro trap, which is superimposed onto the macro trap, is switched on. Atoms initially inside the macro trap will eventually go into the micro trap without being subject to near-resonant light. For the atoms to stay inside the micro trap we need a dissipative force which has so far been created by the near-resonant light. Now, elastic collisions with the atoms already inside the micro trap will lead to a loss of energy for the entering atoms.

We expect a higher steady state atom number $N_{st} \sim \sqrt{\frac{R}{\beta'}}$ inside the micro trap due to two reasons. First, the loading in the absence of any near-resonant light avoids the atom loss due to light-assisted collisions, thus decreasing β'. Second, the density of the atom reservoir surrounding the micro trap is a factor 1000 larger when using the macro trap instead of the MOT with density $n_{MOT} \simeq 10^{10}$ cm^{-3}. This increases the loading rate as it is proportional to the surrounding atom reservoir density.

Depending on the relative position of both traps we study the number of atoms loaded from the macro into the micro trap. We load the $U_{\mathrm{macro}}/k_{\mathrm{B}} = 1.4$ mK deep macro trap from the MOT with about 2500 atoms (see experimental sequence in Fig. 10.3). After having switched off the MOT we suddenly switch on the $U_{\mathrm{micro}}/k_{\mathrm{B}} =$ 2.7 mK deep micro trap and wait for $t_{\mathrm{transfer}} = 300$ ms for the transfer to be realized. We then switch off the macro trap and wait for 50 ms after which all atoms in the macro trap have flown away. Finally, we switch off the micro trap to measure the number of atoms after 50 μs of free flight by using a 2 μs probe and repumper probe

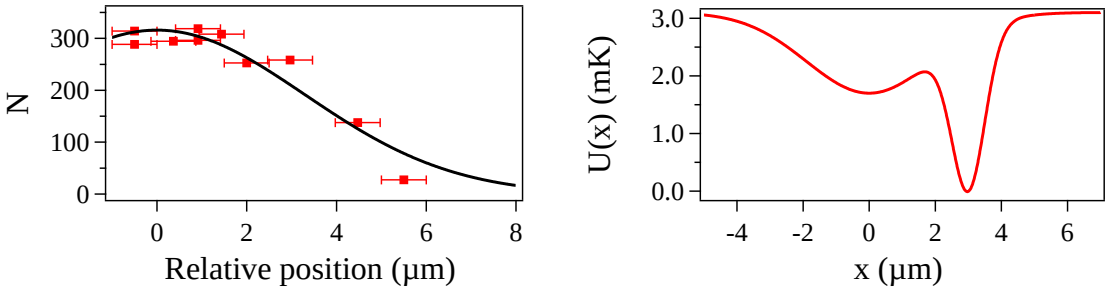

Figure 10.2: Position dependent macro-micro trap atom transfer. *left*) Number of atoms in the micro trap (2.7 mK) versus the relative position between both traps. A Gaussian fit (black curve) yields a rms width of 3.3 ± 0.3 μm. *right*) Trap profile for a combination of the 1.4 mK deep macro and 2.7 mK deep micro trap displaced by 3 μm from each other.

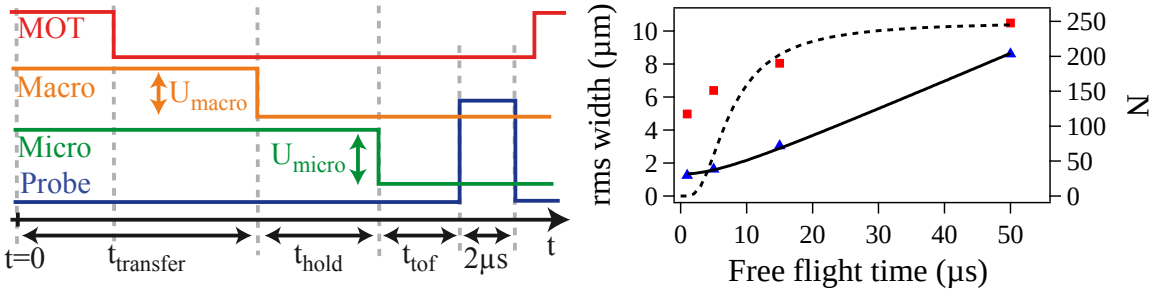

Figure 10.3: Time-of-flight measurement of a dense cloud. *left*) Experimental sequence for loading the $U_{\mathrm{micro}}/k_{\mathrm{B}} = 2.7$ mK deep micro trap from the $U_{\mathrm{macro}}/k_{\mathrm{B}} = 1.4$ mK deep macro trap reservoir. Both traps overlap in time for $t_{\mathrm{transfer}} = 300$ ms. We switch off the micro trap $t_{\mathrm{hold}} = 50$ ms afterwards to measure the atom number and temperature in a time-of-flight experiment. *right*) We plot the atom number N (red squares) and rms width (blue triangles) of the atom sample versus free flight time. The atom fluorescence is induced by a 2 μs probe pulse. The solid and dashed black curves are theoretical models explained in the text.

pulse. The graph on the left in Fig. 10.2 shows the number of atoms inside the micro trap versus the relative position between both traps. When both traps are superimposed the atom number reaches 300, three times as high as by using the MOT to load from. We fit the form of the decrease with a Gaussian function and find a rms width of 3.3 ± 0.3 μm. The graph on the right in Fig. 10.2 shows the radial profile of the trap for a fixed distance of 3 μm between the micro and the macro trap. Increasing the distance lowers significantly the transfer efficiency.

10.3.1 Probing dense atom clouds

Loading the micro trap from the macro trap can lead to high atom densities in the micro trap. A first indication is the enhancement in the number of atoms with respect to the loading from the MOT. Special care has to be taken when probing dense clouds with near-resonant light, as collective effects (see Sec. 9.3.5) can bias the measurement

of the temperature or the number of atoms.

The graph on the right in Fig. 10.3 shows a typical time-of-flight measurement to extract the temperature T and atom number N using the probe laser at resonance ($s \sim 3$). A first striking feature is the increasing number of atoms for longer times of flight. The number of atoms is actually $N \sim 260$, measured at the largest time-of-flight of 50 μs. For the measured temperature and number of atoms $N \sim 260$ we find an atom density exceeding $n_0 = 10^{15}$ cm^{-3}. The optical thickness along the laser propagation in this case is initially $OD = n_0 \sigma_L \sigma_\perp = 11 \gg 1$ with $\sigma_L = (3\lambda^2/2\pi)\frac{1}{1+s}$ showing that not all atoms can scatter light at $\Gamma/2$, thus biasing the fluorescence integration method. For increasing time of flight t the density $n_0(t) = (2\pi)^{3/2} N/(\sigma_\perp^2(t)\sigma_\parallel(t))$ quickly decreases as the size of the atom cloud increases as $\sigma_\parallel(t) = \sqrt{\sigma_\parallel^2 + (vt)^2}$ and $\sigma_\perp(t) = \sqrt{\sigma_\perp^2 + (vt)^2}$ according to Eq. 6.1. This leads to a decrease of the optical thickness as $OD(t) \propto N/(\sigma_\perp(t)\sigma_\parallel(t))$. The function $N\exp(-OD(t))$ with the maximal number of atoms $N = 250$ is comparable to the data for the atom number only for longer flight times ($t \sim 15$ μs). For shorter time-of-flights we detect much more fluorescence than it should be the case theoretically and we thus overestimate the initial optical density. This could for example be explained by radiation pressure, which quickly ($\sim \mu$s for our parameters) increases the initial size of the cloud (see below). This rapid increase in volume leads to a quick decrease in density and a much lower optical thickness, thus detecting more fluorescence.

A second striking feature is the initial rms width of 1.3 ± 0.1 μm exceeding the expected resolution limit $\sigma_{res} = 1.1$ μm (Sec. 6.2.3). We attribute the explosion of the dense cloud to radiation pressure. Considering a radial acceleration due to radiation pressure, the measured rms width would be $\sqrt{\sigma_{res}^2 + \sigma_{\mathrm{rp}}^2}$, where σ_{rp} is the average rms position of the accelerated atom during the probe pulse due to radiation pressure. We estimate σ_{rp} following Steane, Chowdhury, and Foot (1992) and assume a radially symmetric cloud. For full-saturating ($s \sim 3$) resonant light the radial force acting on atom j is

$$F_j(r_j) = m\ddot{r}_j = \int_\omega \int_{r_l} \hbar k \frac{\Gamma}{2} \frac{\sigma_R}{4\pi |r_j - r_l|^2} n(r_l) \ , \tag{10.3}$$

where $n(r)$ is the atom density of Eq. 2.19 and $\sigma_R \sim (3\lambda^2/2\pi)\frac{1}{1+s}$ the cross-section for the absorption of the scattered light. According to Gauss's law this can be written as

$$\nabla_r F_j(r) = \hbar k \frac{\Gamma}{2} \sigma_R n(r) \ . \tag{10.4}$$

We now numerically[2] solve the equation of motion $F(r) = m\ddot{r}$ for an atom initially at the rms position $\sigma_\perp \sim 150$ nm (Eq. 6.2) associated to a temperature of 250 ± 50 μK, which we measure by fitting Eq. 6.1 to the rms width and accounting for a 20 % effect

[2]For a spherical symmetric Gaussian density distribution $n(r)$ the radiation pressure force in Eq. 10.4 has the analytical solution $F(r) = N\frac{\hbar k \Gamma \sigma_L}{2\sqrt{2\pi^3}} \left(\frac{1}{r^2}\sqrt{\frac{\pi}{2}}\mathrm{Erf}\left(\frac{r}{\sqrt{2}\sigma_\perp(t)}\right) - \frac{\exp\left(-\frac{r^2}{2\sigma_\perp^2(t)}\right)}{r\sigma_\perp(t)} \right)$.

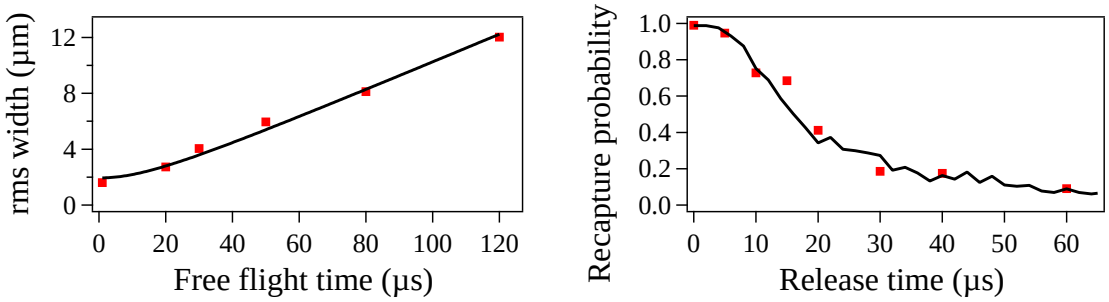

Figure 10.4: Time-of-flight vs release and recapture method for dense clouds. *left*) We show the evolution of the atom cloud rms width with the time in free flight. A fit of Eq. 6.1 yields 87.5 ± 5 μK. *right*) We plot the atom recapture probability versus the release time. A Monte-Carlo simulation to fit the data yields a temperature 80 ± 10 μK.

due to the depth of focus (Sec. 6.2.4). After the probe duration of 2 μs the atom has moved to 1.3 μm taking into account that the density decreases as well during the probe pulse. The rms position averaged over the pulse duration is therefore $\sigma_{rp} \sim 0.65$ μm leading to an overall rms width of $\sqrt{\sigma_{res}^2 + \sigma_{rp}^2} = 1.3$ μm compatible with the measured result[3]. The radiation pressure does not affect the rms width of expanded clouds and does therefore not bias the temperature measurement.

We check that the temperature measurement with the time-of-flight method gives a reliable result by comparing it to the release-recapture technique introduced in Sec. 6.3. Figure 10.4 shows the two methods for an atom cloud in a 1.2 mK deep micro trap. We again fit Eq. 6.1 to the data and find 87.5 ± 5 μK. Again note the initial cloud size $\sigma(0) = 1.6$ μm exceeding the resolution limit due to radiation pressure. This result is compared to the one of the release-recapture technique. We fit the data by using the Monte-Carlo simulation already applied to the single atom measurements and find 80 ± 10 μK, which nicely agrees with the time-of-flight result. We assume here that the atoms are independent so that the ensemble average in the many atom case is equivalent to repeating the simulation using a single atom.

Considering these observations we always measure the number of atoms for long time of flights, for which the cloud is sufficiently dilute and all atoms scatter photons at the same rate. For these dilute clouds the temperature measurement is not biased by e.g. radiation pressure effects either.

10.3.2 Three-body losses in the dense atom cloud

We saw that it takes ~ 250 ms to reach the thermodynamic equilibrium around 250μK when loading the micro trap from the MOT. Furthermore it leads to a reduction in atom number from initially ~ 100 to ~ 50. Loading the micro from the macro trap not only boosts the number of atoms in the micro trap to nearly 300 but also sets their temperature close to the thermal equilibrium temperature $U_0/k_B/10 \sim 250$ μK. Note that this avoids a loss of atoms due to free evaporation. Being at thermal equilibrium

[3]Besides the radiation pressure there exists an attenuation force which compresses the cloud (Dalibard, 1988). Since we do not observe any compression we assume this force to be negligible.

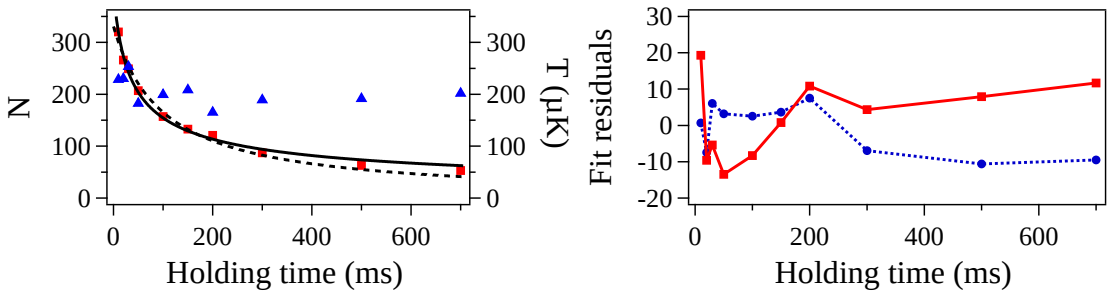

Figure 10.5: Three body loss rate. *left*) We plot the number of atoms N (red squares) and temperature T (blue triangles) versus the holding time in the micro trap. A two-body (dashed black line) and three-body (solid black line) fit are compared to the data. *right*) We plot the difference between the data and the two-body (red squares) and three-body (blue circles) fit result versus the holding time.

and having prepared 97 % of the atoms in the F = 1 ground state we would thus expect the lifetime of the atoms to be limited by background gas collisions. Figure 10.5 nevertheless shows that atoms are lost from the trap at a high rate. At our high densities of $n_0 = 10^{15}$ cm^{-3} the loss could be due to three-body recombination.

To extract the loss rates we fit the data with the three-body loss function

$$N(t) = \frac{N_0}{\sqrt{1 + 2L' \cdot N_0^2 \cdot t}} \tag{10.5}$$

resulting from solving Eq. 2.10 with $\gamma = \beta' = 0$ to the data. We find $L' = 1.8 \cdot 10^{-4}$ s^{-1}. Assuming a constant thermal volume[4] this converts to the loss rate $L = 3\sqrt{3}L'V^2 = 4 \pm 3 \cdot 10^{-29}$ cm^{6}s^{-1} comparable to the value found by Burt *et al.* (1997). The agreement between our measurement and Burt *et al.* (1997) supports the assumption of three-body loss although it is difficult in our case to exclude a two-body loss. The graph on the right in Fig. 10.5 shows the deviation of the fit from the data for a two- and three-body model. Here, the first 200 ms show a better fitting result for a three-body model of Eq. 10.5. For longer holding times the deviations for both models are similar.

10.4 Characterizing the atom transfer to the dimple trap

The transfer of atoms from the macro to the micro trap depends on many parameters. In the following we explore its dependence on the transfer time t_{transfer}, the micro U_{micro} and macro U_{macro} trap depths[5]. To do so we apply the experimental sequence

[4] The temperature and thus the volume are assumed to be constant. However, free evaporation decreases the temperature from 250 μK to 200 μK, thus slightly changing the volume of the cloud in the beginning.

[5] The micro trap waist is $w_0 = 1.5$ μm for these experiments. The reason for going to a larger trap waist is discussed in the next chapter.

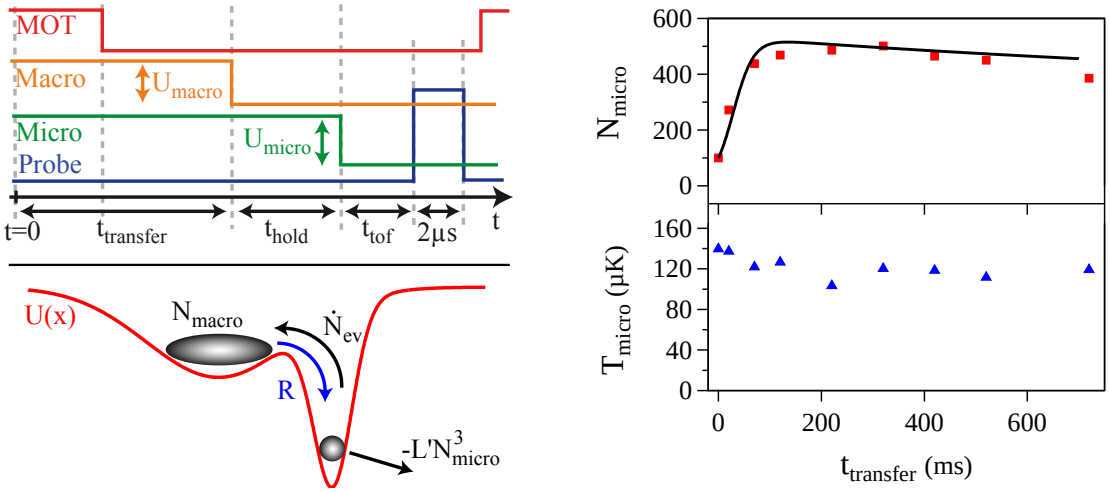

Figure 10.6: Position dependent macro to micro trap atom transfer. *left top*) Experimental sequence used to align the micro onto the macro trap. We start by loading the macro trap from the MOT for 20 ms. We switch off the macro trap after the transfer time t_{transfer}. We then measure the atoms inside the micro trap t_{hold} after switching off the macro trap by illuminating the atoms in free flight with a 2 μs probe pulse. *left bottom*) The macro trap serves as an atom reservoir from which the micro trap is loaded at a rate R. Atoms in the micro trap are evaporated back into the macro trap ($\dot{N}_{\mathrm{ev}}$) or they are lost due to three-body recombination ($L' N^3_{\mathrm{micro}}$). *right*) We show the number of atoms in the micro trap N_{micro} (red squares) and their temperature (blue triangles) versus the transfer time t_{transfer}. The theoretical result (black curve) discussed in the text is used to fit the number of transferred atoms.

shown on the upper graph on the left in Fig. 10.6. We start at $t = 0$ by loading the superimposed macro and micro trap using the MOT for 20 ms. In fact, for the optimized transfer parameters we do not find any significant difference whether we switch on the micro trap before or after having loaded the macro trap from the MOT. The MOT is then switched off and the transfer takes place. After the transfer time t_{transfer} the macro trap is switched off. We then wait for $t_{\mathrm{hold}} = 50$ ms to let the atoms of the macro trap fly away so that only atoms remaining in the micro trap are left. The number of atoms is measured after a time-of-flight of typically $t_{\mathrm{tof}} = 80$ μs which is enough for the atom cloud to be sufficiently dilute. It is then illuminated by a 2 μs probe and repumper probe pulse. The induced fluorescence is detected on the CCD camera.

10.4.1 Measuring the transfer time

We first study the dynamics for the micro trap loading. On the right side of Fig. 10.6 we show how the number of atoms N_{micro} and their temperature T_{micro} inside the micro trap vary as the transfer time t_{transfer} is changed. In this particular case the $U_{\mathrm{macro}}/k_{\mathrm{B}} = 1.4$ mK deep macro trap was loaded with 1500 atoms and was superimposed by the $U_{\mathrm{micro}}/k_{\mathrm{B}} = 1.2$ mK deep micro trap. The atom number inside the micro trap increases sharply by a factor 5 to ~ 500 during the first 100 ms. It then

decreases slowly by 20 % over the next 600 ms mainly due to three-body losses. Note that the maximal atom transfer efficiency here is $500/1500 = 33$ %.

The variation in temperature on the other hand is much less pronounced. It is due to the thermalization of the gas. Its value is set by the depth of the micro trap as the thermalization process leads to $T \sim U_{\mathrm{micro}}/k_{\mathrm{B}}/10$ (see Sec. 10.2). We will now describe the model used to describe the atom transfer between the macro and micro trap.

10.4.2 Atom transfer model

We set up a model to describe the evolution of the atom number in both traps. The temperature is considered to be constant during the process. As can be seen in Fig. 10.6 the temperature T_{micro} of the micro trap atoms N_{micro} is nearly constant during the loading process. The same is true for the temperature of the atoms in the macro trap T_{macro} considering Fig. 10.1. We therefore believe that the assumption of constant temperature is not completely unreasonable[6]. The model is based on the following rate equations

$$\dot{N}_{\mathrm{macro}} = -R + \dot{N}_{\mathrm{ev}} \quad , \quad \dot{N}_{\mathrm{micro}} = R - \dot{N}_{\mathrm{ev}} - L' N_{\mathrm{micro}}^3 \ . \tag{10.6}$$

It treats the loading rate R from the macro into the micro trap, the rate at which atoms evaporate from the micro back into the macro trap as well as three-body loss from the micro trap. We discuss each process illustrated on the bottom left graph of Fig. 10.6 in the following:

- **Loading rate R.** We follow the idea outlined in Kuppens *et al.* (2000) to derive an equation of the loading rate R. The number of atoms passing a certain area per unit time is $n_{0,\mathrm{macro}}\bar{v}$, where $n_{0,\mathrm{macro}}$ is the atom density in the macro trap and $\bar{v}$ is the average thermal velocity (see Sec. 10.2). We assume entering atoms to be sufficiently slowed down due to elastic collisions with the micro trap having a Gaussian density profile $n_{\mathrm{micro}} \propto \exp\left(-\frac{r^2}{2\sigma_\perp^2}\right) \exp\left(-\frac{z^2}{2\sigma_\parallel^2}\right)$. The entering atoms therefore need to cross the surface A enclosing the cigar with axis $\sigma_\perp$ and $\sigma_\parallel$ inside which they undergo elastic collisions. Furthermore, we assume that atoms from the macro reservoir that enter the micro trap are trapped in the micro trap when they collide at least once on average with an atom inside the micro trap[7]. The probability for one collision $P_{\mathrm{trap}} = \sigma_{\mathrm{el}} n_{0,\mathrm{micro}} (\sigma_\perp^2 \sigma_\parallel)^{1/3}$ can be estimated assuming s-wave collisions. The final loading rate then reads

$$R = \frac{1}{4} n_{0,\mathrm{macro}} \bar{v} A P_{\mathrm{trap}} \ . \tag{10.7}$$

- **Free evaporation $\dot{N}_{\mathrm{ev}}$.** The evaporation rate $\dot{N}_{\mathrm{ev}}$ from atoms of the micro into the macro trap is taken directly from Eq. 10.1. We assume that all evaporating

[6] The temperature measurement is taken $t_{\mathrm{hold}} = 50$ ms after the macro trap has been switched off. During this time free evaporation leads to a slightly (~ 20 %) lower temperature as present.

[7] Note that the micro trap is initially filled with ~ 100 atoms.

atoms are not lost but rather caught by the macro trap potential. We neglect free evaporation of the macro trap atoms as the atom transfer process typically takes place on much faster time scales than the free evaporation process from the macro trap.

- **Three-body loss.** The three body loss $L'N_{\mathrm{micro}}^3$ becomes important only for the micro trap where the atom densities can reach $\sim 10^{15}$ cm^{-3}. Here we use the value for L' measured in Sec. 10.3.2.

To fit the data we set all parameters to their measured values, especially the atom temperatures T_{macro} and T_{micro}. However, to obtain satisfactory results we needed to do two changes. First, the optimized value of the loading rate R is a factor ~ 10 smaller than expected from Eq. 10.7 for our parameters $R = 2 \cdot 10^5$ s^{-1}. We attribute this to the fact that the actual trap is not harmonic and that this induces a lower elastic collision rate than expected in our case. This is actually the same argument as encountered in Sec. 10.2, which led to a slower evaporation time in the macro trap. Second, the calculated atom transfer efficiency is a factor 1.5 higher than measured due to the following: We measure the atom number $t_{\mathrm{hold}} = 50$ ms after the transfer during which atoms are lost due to free evaporation and three-body losses. Considering these variations the model does well reproduce the atom number evolution in the micro trap as shown by the black curve in Fig. 10.6.

There are other possibilities to model the trap loading from an atom reservoir. One possibility to qualitatively better model the data would imply a numerical simulation as e.g. done for a crossed dipole trap on a single-particle basis by Schulz *et al.* (2007). Another approach emphasizes on thermodynamic properties such as e.g. entropy and energy of an adiabatic (Stamper-Kurn *et al.*, 1998) and diabatic (Comparat *et al.*, 2006) trap loading process.

10.4.3 Trap depth dependence of the atom transfer

We now fix the transfer time to $t_{\mathrm{transfer}} = 220$ ms and vary the macro and micro trap depths. The left graph of Fig. 10.7 shows the micro trap atom number and temperature versus the macro trap depth U_{macro} while the micro trap depth is held constant at $U_{\mathrm{micro}}/k_{\mathrm{B}} = 1.2$ mK. The atom number increase for macro trap depths below 1 mK is a result of an increasing atom number in the macro trap[8] and an increasing loading rate R. For macro trap depths exceeding ~ 1 mK the atom number stagnates. This is due to the fact that with increasing atom number in the micro trap, also an increasing number of atoms evaporates back into the macro trap. Additionally, three-body losses start to limit the total number of atoms inside the micro trap. The competition of these processes with an increasing loading rate leads to a saturation of the atom number in equilibrium. The temperature of the atoms in the micro trap is constant at $T_{\mathrm{micro}} \sim U_{\mathrm{micro}}/k_{\mathrm{B}}/10 \sim 115$ μK and imposed by the depth of the micro trap as already observed in the previous sections.

[8] We check experimentally that the atom number varies linearly with the trap depth.

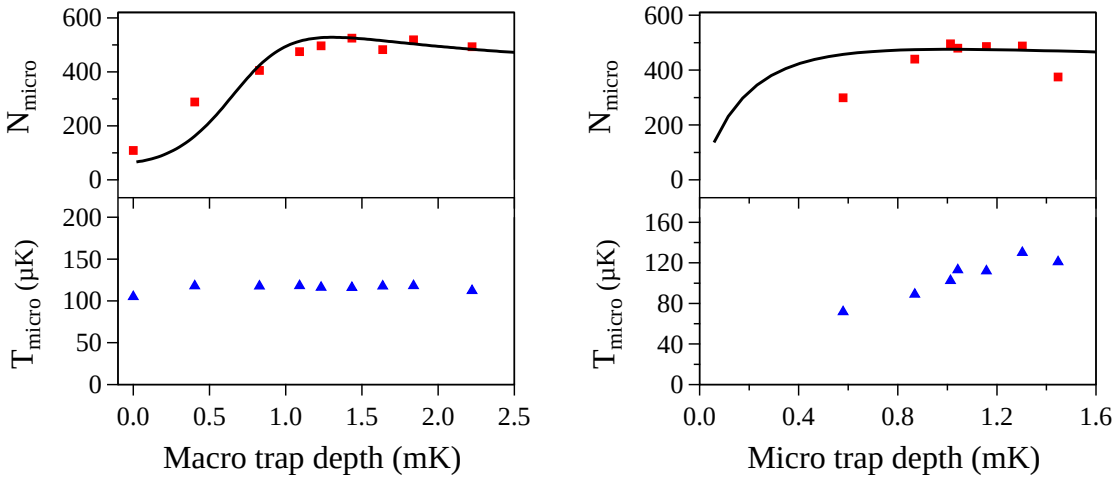

Figure 10.7: Macro-micro trap atom transfer depending on macro and micro trap depth. We plot the number of atoms (red squares) inside the micro trap and the atom temperature (blue circles) versus the *left*) macro trap depth U_{macro} (keeping $U_{\mathrm{micro}}/k_{\mathrm{B}} = 1.2$ mK fixed) and *right*) and micro trap depth U_{micro} (keeping $U_{\mathrm{macro}}/k_{\mathrm{B}} = 1.4$ mK fixed). The measured atom number is compared to the theoretical result (black curve) of the model described in the text. For these measurements the macro and micro trap have been superimposed for $t_{\mathrm{transfer}} = 220$ ms and the micro trap has been switched of $t_{\mathrm{hold}} = 50$ ms after the macro trap.

We repeat the measurements changing the micro trap depth U_{micro} by keeping the macro trap depth fixed at $U_{\mathrm{macro}}/k_{\mathrm{B}} = 1.4$ mK. The right graph of Fig. 10.7 again shows the micro trap atom number and temperature versus the micro trap depth U_{micro}. The best atom transfer is obtained for micro trap depths around 1.2 mK. With lower trap depths less atoms can be held inside the micro trap region. This lowers the elastic collision probability and the atom transfer decreases. For higher trap depths the transfer should increase due to higher atom densities inside the micro trap. Elastic collisions on the other hand become less effective as the scattering cross-section may decrease due to higher partial waves participating in the collision process. The model does not take this into account and the atom number saturates at ~ 500 due to three-body losses. The temperature of the atoms in the micro trap increases linearly from 70 μK at 0.58 mK to 130 μK at 1.3 mK. Again the temperature is imposed by the depth of the micro trap where we confirm the dependence $T_{\mathrm{micro}} \sim U_{\mathrm{micro}}/k_{\mathrm{B}}/10$.

10.5 Conclusion

Loading the micro trap directly from the MOT is highly affected by light-assisted collisions. They lead to a loss of atoms and a high temperature. We circumvent these collisions by using the macro trap as an atom reservoir. Atoms pass from there into the micro trap region and are trapped due to elastic collisions in the absence of any near-resonant light. This increases the number of atoms as well as it leads to a lower temperature than if loaded by the MOT.

Chapter 11

Evaporation

Contents

We saw in the last chapter that we are able to produce small ($N < 1000$) and dense atom clouds in the microscopic dipole trap with temperatures around 100 μK. In order to further cool the gas to reach ultra-cold temperatures and the degenerate regime we apply the technique of evaporative cooling. We will first introduce the principle of evaporative cooling and try to elaborate efficient initial conditions for the cooling process. Afterwards, we present the preliminary results towards small Bose-Einstein condensates and discuss the difficulties in their observation.

11.1 Résumé

Les résultats présentés dans ce chapitre montrent que la production de petits condensats de Bose-Einstein contenant environ 10 atomes dans un piège dipolaire microscopique est possible. Nous avons créé de petits nuages d'atomes ultra-froids $T \sim 100$ nK atteignant des densités dans l'espace des phases de l'ordre de l'unité. Jusqu'à présent, une signature claire de la condensation dans ce régime particulier n'a pas été observée. La poursuite de l'évaporation pour encore augmenter la densité

dans l'espace des phases a été difficile en raison du nombre limité d'atomes présents dans le piège. L'utilisation d'une technique d'évaporation accélérée maintenant la fréquence d'oscillation du piège constante devrait permettre d'améliorer cette limitation.

11.2 Principle of evaporative cooling

Evaporative cooling has been the main ingredient for the realization of Bose-Einstein condensates. A review on the evaporative cooling can be found in e.g. Ketterle and van Druten (1996a). Here, we just want to outline the basic principle and discuss some important theoretical aspects. Figure 11.1 shows a typical forced evaporation cycle. We start with an atom cloud in thermal equilibrium $\eta = U_i/k_\mathrm{B}T_i \gg 1$ inside a dipole trap which energy distribution is of Boltzmann type (see Sec. 2.3.1). If we lower the trap depth to U_f atoms belonging to the high energy tail of the distribution leave the trap. The remaining cold atoms thermalize until approximately the same $\eta = U/k_\mathrm{B}T$ is established. But the gain in temperature of $T_i/T = U_i/U$ is at the expense of an atom loss. If we assume that during the lowering process the gas stays in thermal equilibrium with $k_\mathrm{B}T \ll U$ and $\eta = \mathrm{const}$ it can be shown (O'Hara *et al.*, 2001) that the final atom number N evolves as

$$\frac{N}{N_i} = \left(\frac{U}{U_i}\right)^{3/[2(\eta'-3)]} = \left(\frac{T}{T_i}\right)^{3/[2(\eta'-3)]} , \tag{11.1}$$

where we use $\eta' = \eta + \frac{\eta-5}{\eta-4}$. For the atom density $n \propto N(\hbar\bar{\omega})^3/(k_\mathrm{B}T)^{3/2} \propto N\eta^{3/2}$ (Eq. 2.19), the elastic collision rate $\gamma_{el} = \sigma_{el} n \bar{v}$ (Eq. 2.8) and the phase space density $\rho = N(\hbar\bar{\omega})^3/(k_\mathrm{B}T)^3$ (Eq. 2.32) follow equivalent relationships

$$\begin{aligned} \frac{n}{n_i} &= \frac{N}{N_i} \quad , \quad \frac{\gamma_{el}}{\gamma_{el,i}} = \left(\frac{U}{U_i}\right)^{\eta'/[2(\eta'-3)]} \\ \frac{\rho}{\rho_i} &= \left(\frac{U_i}{U}\right)^{3(\eta'-4)/[2(\eta'-3)]} = \left(\frac{N_i}{N}\right)^{\eta'-4} , \end{aligned} \tag{11.2}$$

considering that the trap oscillation frequency decreases with the trap depth as $\omega \propto \sqrt{U}$. However, the equations do not tell anything about the dynamics of the evaporation process. Intuitively it is clear that the dynamics are governed by the elastic collision rate as indicated in Eq. 10.1. Under the constraint that η stays constant during the ramping, the trapping potential depends on time as

$$\frac{U(t)}{U_i} = \left(1 + \frac{t}{\tau_{ev}}\right)^{-2(\eta'-3)/\eta'} \quad \text{with} \quad \frac{1}{\tau_{ev}} = \frac{2}{3}\eta'(\eta-4)\exp(-\eta)\gamma_{el,i} . \tag{11.3}$$

This equation can be used to derive the time dependence of any other variable as we expressed them as a function of $U(t)/U_i$ in Eq. 11.1 or 11.2.

Let us use typical values for the micro trap when loaded directly from the MOT (see Sec. 10.2). We prepared 50 atoms at $U_i = 2.7$ mK with $\eta \sim 10$ resulting in a peak atom density $n_0 = 2 \cdot 10^{14}$ cm^{-3} and an elastic collision rate $\sigma_{el} = 1.4 \cdot 10^4$ s^{-1}.

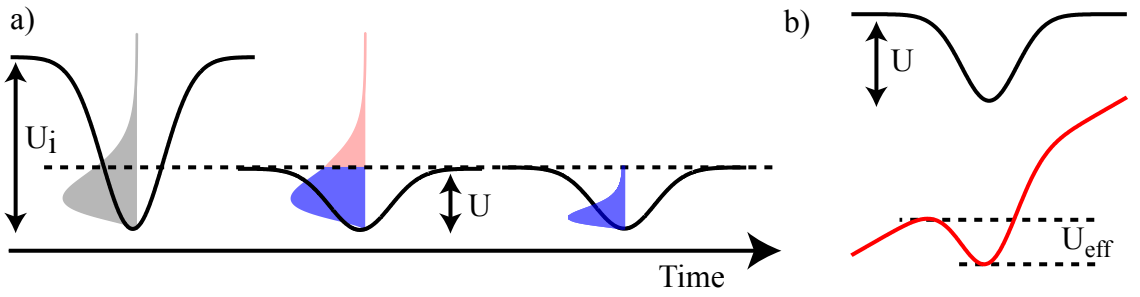

Figure 11.1: Evaporative cooling. *a*) The atoms occupy the trap energy levels according to a Boltzmann distribution for temperatures $T_i \gg 0$. Lowering the trap depth from U_i to U all atoms belonging to the grey shaded part of the distribution are lost and colder atoms remain trapped. After thermalization, the temperature of the gas is lowered to $T = T_i \cdot U/U_i$. *b*) A possibility to lower the effective trap depth without changing the oscillation frequency.

According to these equations a phase space density of one would be reached in 3 s by lowering the trap depth by a factor 700 and finishing with ~ 10 atoms at ~ 400 nK. The atom density n drops by a factor 3 and the elastic collisions rate σ_{el} by ~ 120. These estimations show up two major difficulties: First, the large drop in the elastic collision rate slows down the evaporation as the elastic collision rate defines the speed of this process. Here, we find an evaporation time of 3 s allowing any loss processes to further reduce the atom number. Second, the BEC would contain about 10 atoms only. Any losses would lead to even less atoms and smaller densities slowing down the BEC production time even more (Miesner *et al.*, 1998). In the next section we will discuss these issues.

11.3 Optimizing the evaporative cooling process

In our case it is difficult to say what initial parameters are best for evaporative cooling. This becomes clear from the following considerations: Eq. 11.2 indicates that the higher the initial phase-space density ρ_i the less we have to lower the potential and the faster the evaporation process will be. To increase ρ_i we can load more atoms into the trap as it is proportional to the number of atoms $\rho_i \propto N_i$. It also varies with the temperature as $\rho_i \propto T_i^{-3}$ so that is seems more efficient to reduce the initial temperature than to increase the number of atoms. Lower temperatures are possible for lower initial trap depths U_i as in thermal equilibrium $k_B T_i = U_i/\eta$ with $\eta \sim 10$. A lower trap depth however has a major drawback: We cannot neglect the fact that we are working with low atom numbers $N_i \ll 1000$. It is therefore not possible to arbitrarily reduce the trap depth to minimize the temperature because this would lead to a significant reduction of the number of atoms. And a lack of atoms results in the termination of the evaporation process. We will discuss three possible approaches to improve the evaporative cooling scheme.

11.3.1 Going to a 1.5 micrometer trap waist

We need to avoid any atom losses that are faster than or comparable to the evaporation time. We briefly discuss possible effects of one-, two- and three-body losses.

- **One-body loss** We know that the one-body loss decay due to background gas collisions is $\sim 1/24$ s^{-1} (see Sec. 5.3), much longer than typical evaporation times.

- **Two-body loss** We avoid hyperfine changing collisions by preparing 97 % of all atoms in the $F=1$ ground state. Trap-induced Raman transitions are as low as 0.1 s^{-1} for the $U/k_B = 2.7$ mK deep trap at 945 nm. On the other hand Zeeman-changing collisions can also lead to losses. The energy released in a collision depends on the Zeeman shift, which is proportional to the residual magnetic field according to Eq. 1.8. These collisions may become important when the trap depth is on the order of the released energy, which is 2.4 μK for our residual magnetic field of 70 mGauss. But typical loss rates are estimated to be very low $\beta_{\text{Zeeman}} = 10^{-17}$ cm^{3}s^{-1} (Hensler *et al.*, 2003) and this loss therefore negligible in our case.

- **Three-body loss** The high three-body collision rate measured in Sec. 10.3.2 can be hazardous for a further forced evaporation (Sebby-Strabley *et al.*, 2005) towards ultra-cold and degenerate atom samples as it can lead to rapid atom loss and anti-evaporation (Comparat *et al.*, 2006). We can lower the probability of three-body recombination by increasing the trap waist from $w_0 = 1$ μm to $w_0 = 1.5$ μm. We do so by clipping the trap laser before the aspheric lens[1]. As the density scales as w_0^{-4} with the trap waist we expect a decrease in density by a factor 5 whilst keeping η and the number of atoms constant. The larger trap waist and lower density is at the expense of a lower elastic collision rate ($\gamma_{el} \propto w_0^{-4}$) which increases the evaporation time. In the absence of losses however this does not put any restriction on the evaporative cooling.

11.3.2 Evaporative cooling keeping the oscillation frequency fixed

One can evaporate atoms from an optical dipole trap by keeping the oscillation frequency ω constant. This can be done by following Hung *et al.* (2008). The dipole trap potential is deformed by a magnetic or optical force gradient resulting in an effective trap depth $U_{\text{eff}} < U_i$ as illustrated on the right of Fig. 11.1. The curvature at the bottom of the trap and thus the oscillation frequency ω stays constant whatever the magnetic or optical force gradient. The atom density $n_0 \propto \omega^3$ as well as the elastic collision rate $\gamma_{el} \propto \omega^3$ do therefore not decrease due to a decreasing oscillation

[1] Note that the clipping of the trap beam does increase the height of the Airy rings with respect to the center peak by a factor ~ 4 (see Sec. 3.3.5). But the optical potential created by the Airy rings is still too small to be considerable for trapping atoms that could disturb the main center trap.

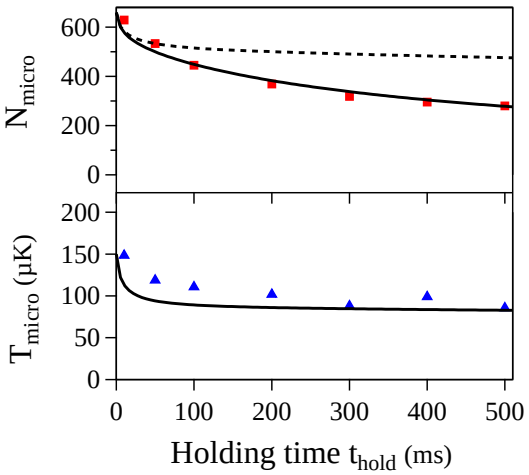

Figure 11.2: Optimized micro trap loading from macro trap reservoir. We plot the number of atoms N (red squares) and temperature T (blue triangles) versus the holding time in the micro trap with depth $U_{\mathrm{micro}}/k_{\mathrm{B}} = 1.2$ mK. The decrease in the number of atoms is due to free evaporation as well as three-body losses. A numerical result (black curve) taking into account both effects reproduces the data well. Without three-body losses the atom number would not decrease as rapidly (dashed black curve).

frequency when lowering the potential for evaporation. This could help to decrease the evaporation times and increase the final condensate atom number.

So far a force gradient has not been implemented. A magnetic gradient would not be favorable in our case since a potential difference of only ~ 10 μK applied over our trap of ~ 2 μm diameter already requires magnetic fields of ~ 5 T/cm. This demands the use of optical fields to create the force gradient.

11.3.3 Maximizing the initial phase-space density

As the loss processes can be sufficiently reduced, we decided to optimize the initial phase-space density for the evaporation starting point. Note that even in the larger trap three-body losses can be present when the densities clearly pass 10^{14} cm^{-3}. We increase the phase-space density by loading the micro from the macro reservoir as explained in Sec. 10.3. We scan the parameter space by varying the micro U_{micro} and macro U_{macro} trap depths as well as the transfer time t_{transfer}. We maximized the initial phase-space density for $U_{\mathrm{micro}}/k_{\mathrm{B}} = 1.2$ mK and $U_{\mathrm{macro}}/k_{\mathrm{B}} = 1.4$ mK together with a transfer time $t_{\mathrm{trans}} = 220$ ms.

Figure 11.2 shows the evolution of the number of atoms N and of the temperature T directly after the trap is loaded. Initially we measure $N_i = 650 \pm 25$ atoms at $T_i = 150$ μK which results in a peak atomic density $n_i = 3 \cdot 10^{14}$ cm^{-3} and a phase-space density $\rho = 10^{-3}$. The atom loss seen here is partially due to free evaporation of the gas as indicated by the initial decrease in temperature and partially due to losses. A simulation taking into account both effects yields the three-body loss rate $L = 3 \pm 2 \cdot 10^{-29}$ cm^{6}s^{-1} in agreement with the previously measured value in Sec. 10.3.2. Without three-body loss the atom number evolution is expected to take the form of the black dashed line.

Under these initial conditions we would achieve a phase-space density of one in ~ 0.5 s by applying the scaling laws. The gas would then contain ~ 140 atoms at a temperature of 560 nK. However, due to the increased atom number there are still three-body losses present but at a much reduced rate as compared to Fig. 10.5 due to

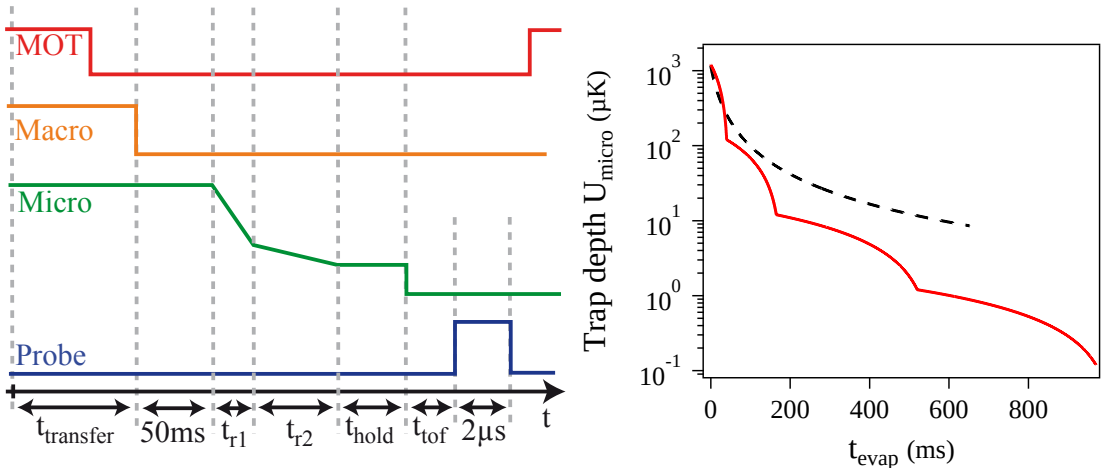

Figure 11.3: Experimental sequence and ramp for forced evaporation. *left*) The micro trap at 1.2 mK is directly loaded from the macro trap during $t_{\text{transfer}} = 220$ ms. After 50 ms of free evaporation its trap depth is lowered in a sequence of linear ramps each having a length of $t_{r,i}$. The atoms are then left to thermalize during typically $t_{\text{hold}} = 200$ ms before measuring the number of atoms and temperature. *right*) We plot the micro trap depth U_{micro} versus the forced evaporation time t_{evap}. The ramp is built up of several linear ramps with decreasing slope (Here in lin-log scale). The theoretical result of Eq. 11.3 is shown (black dashed curve).

the lower density. These lower three-body losses do not affect the evaporative cooling for two reasons. First, the loss rate is acceptable for an evaporation time of only ~ 0.5 s and second, during forced evaporation the trap depth is quickly (factor 10 in ~ 50 ms) lowered in the beginning. This decreases the density and thus makes the losses due to three-body recombination negligible.

11.4 Evaporation results

We pursue evaporation ramps as it is usually done to obtain all-optical BECs (Barrett, Sauer, and Chapman, 2001) by lowering the dipole trap power. We choose the starting point of the forced evaporation 50 ms after the 1.2 mK deep micro trap has been loaded from the macro reservoir as indicated in the experimental sequence in Fig. 11.3. This ensures the atoms to be thermalized as shown in Fig. 11.2. We find $N_i = 530$ atoms at $T_i = 120\ \mu$K (see Fig. 11.2) with $\eta = 10$. The peak density is $n_i = 3{\cdot}10^{14}$ cm^{-3} and the phase-space density reads $\rho = 2 \cdot 10^{-3}$.

Evaporation ramps

With the initial values in hand we can calculate the theoretical form of the evaporation ramp given by Eq. 11.3 and shown on the right graph of Fig. 11.3 (black dashed curve). A phase-space density of unity is reached after ramping down the trap depth by a factor ~ 300 to $\sim 4\ \mu$K over ~ 0.7 s. We want to approximate the optimal form by

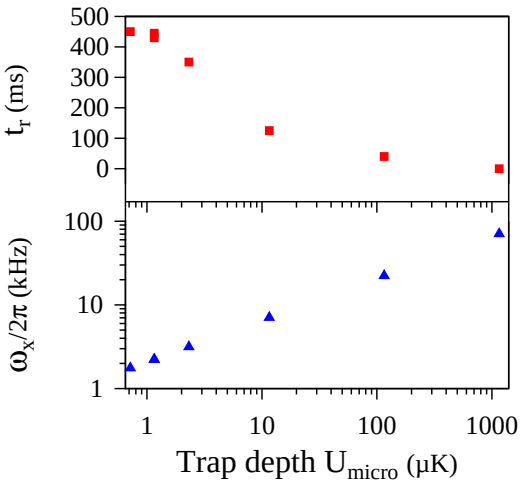

Figure 11.4: Trapping frequency and ramp length versus the trap depth. *top*) We show the length of the evaporation ramp pieces t_r (red squares) versus the micro trap depth. *bottom*) The radial trap oscillation frequency $\omega_x/2\pi$ (blue triangles) is also shown versus the micro trap depth. The decreasing trap depth lowers the oscillation frequency and requires longer evaporation ramps.

linearly ramping down the trap depths by factors of $5-10$. We vary the length of the ramps to maximize the phase-space density ρ. The phase-space density ρ as well as all other quantities such as the atomic density or the elastic collision rate for example are deduced from the measured number of atoms N and their temperature T assuming a thermal energy distribution.

A typical optimized ramp is also shown in Fig. 11.3 (red curve). It shows one disadvantage of lowering the trapping potential for forced evaporation as the oscillation frequency shown in Fig. 11.4 decreases, too. The decreasing oscillation frequency leads to a lower elastic collision rate and requires longer ramps for the gas to evaporate to thermal equilibrium. The increasing ramp lengths for smaller trap depths are also shown in Fig. 11.4. Taking one series of ramps from 1.2 mK to, successively ~ 120 μK, ~ 12 μK, and finally ~ 1.2 μK takes about 0.9 s of total evaporation time. It is longer than the theoretical estimated length of ~ 0.7 s which we can explain in the following.

We find that η does not stay constant during the ramp but decreases by a factor ~ 2 when dividing the trap by a factor 10. The result is that the implemented ramp is less efficient than theoretically predicted in the sense that the temperature after the ramp is two times higher than expected. We studied the behavior of smaller discretization steps (factors of $2-5$) and found no significant difference of this behavior. We conclude that ramping down the trap by a factor of up to 10 does not deteriorate the evaporation efficiency and is not the reason for an increasing η. The increase of η has not unambiguously been identified but could be due to a heating introduced by fluctuations of the trap laser for example. It could also be due to the Lorentzian trap shape in axial direction as it already led to a lower thermalization rate as discussed in Sec. 10.2. And lower thermalization rates lead to higher temperatures as the gas needs more time to attend thermal equilibrium.

General results of forced evaporative cooling

The number of atoms as well as the temperature are measured $t_{\mathrm{hold}} = 200$ ms after the ramps are finished as illustrated in Fig. 11.3 to reestablish thermal equilibrium

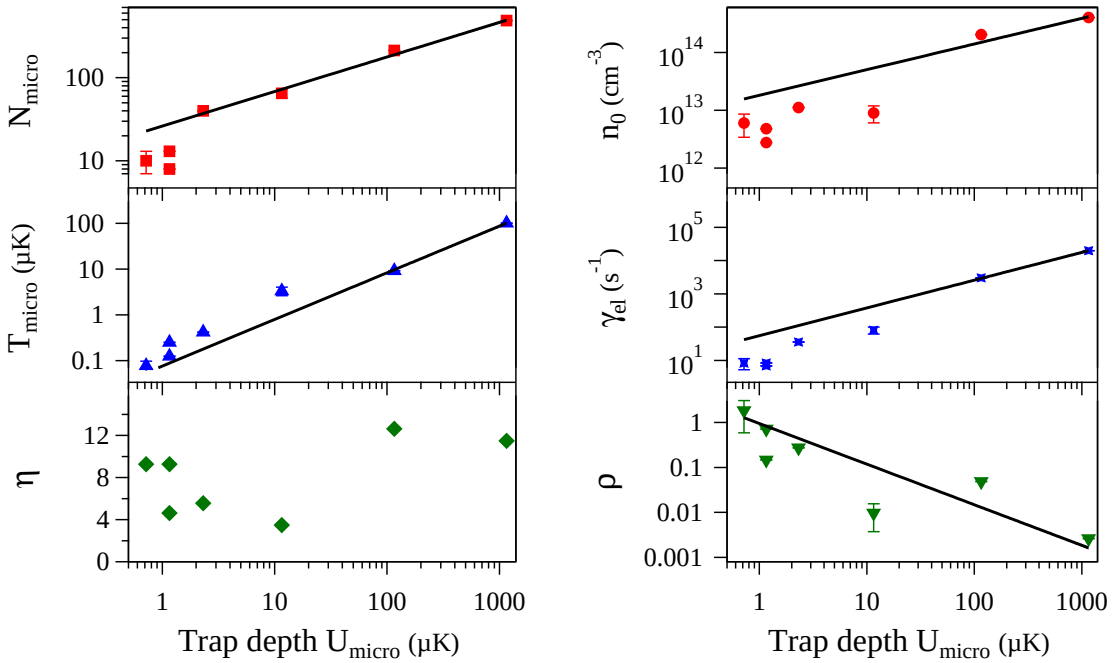

Figure 11.5: Forced evaporation results. We plot the number of atoms N (red squares), the temperature T (blue triangles), η (green diamonds), the atom peak density n_0 (red cirles), the elastic collisions rate γ_{el} (blue stars) and the phase space density ρ (green downward triangles) versus the micro trap depth.

with $\eta \sim 10$. All images are well-fitted by a $2D$-Gaussian model. This is in particular the case for ultra-cold atom clouds in the quasi-degenerate regime, which profiles are different to Gaussians and are described by Eq. 2.25.

The main results are summarized in Fig. 11.5. The data are compared to the scaling laws of Eqs. 11.1 and 11.2 by using the function

$$\frac{x}{x_i} = \left(\frac{U}{U_i}\right)^{\alpha_x} , \tag{11.4}$$

where x is replaced by the considered quantity. We fix the initial trap depth to $U_i/k_B = 1.2$ mK and extract the exponent α_x. When ramping down the trap depth we see that the number of atoms N and the temperature T decrease. The fit yields $\alpha_N = 0.42 \pm 0.03$ and $\alpha_T = 1.02 \pm 0.05$ for the atom number and temperature, respectively. The scaling laws in Eq. 11.1 predict 0.35 and 1 assuming $\eta = 8$ indicating a slightly faster atom loss than expected.

The decrease in atom number and temperature lead overall to a decrease of the peak density n_0 and elastic collision rate γ_{el} but an increase of the phase-space density ρ. We extract the exponents $\alpha_{n_0} = 0.44 \pm 0.07$, $\alpha_{\gamma_{el}} = 0.83 \pm 0.02$ and $\alpha_\rho = -0.9 \pm 0.05$ and compare them to the theoretical result 0.35, 0.85 and -1.15, respectively. Again we find a faster drop in density than expected which goes along with the faster loss of atoms as mentioned above. The exponent for the elastic collision rate is in good agreement with the theory. On the other hand we find a less rapid increase in phase-

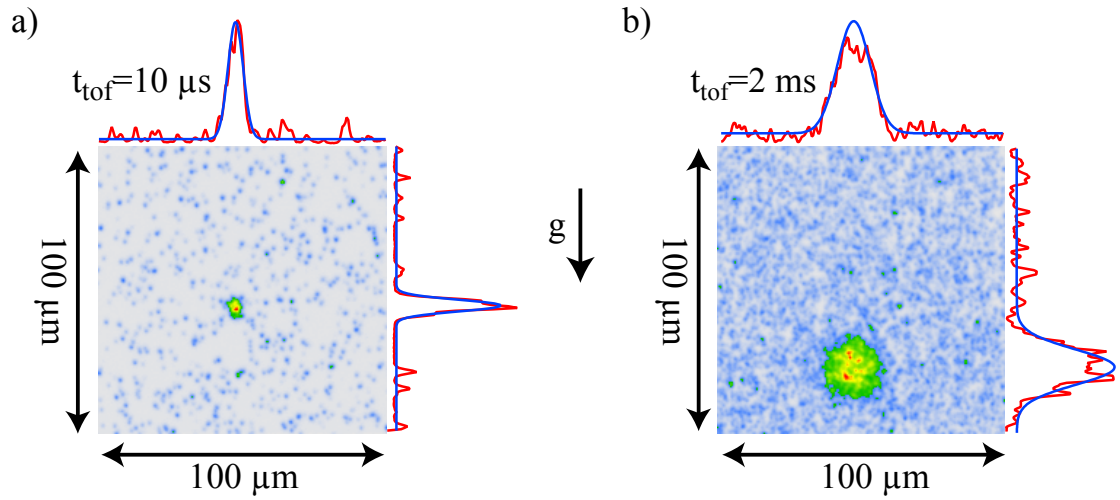

Figure 11.6: Raw images of cold atom cloud. We show raw images of an ultra-cold atom cloud containing 8 atoms on average. The cloud is imaged using the probe and repumper probe laser for 10μs with $s \sim 5$ after a time of flight of *a*) 100 μs and *b*) 2 ms. The cross-sections (red lines) are fitted by using a Gaussian model (blue lines). For long time of flights gravity leads to a shift of the atom cloud center.

space density than calculated. Note that for the values N, n_0 and γ_{el} the measured values start to deviate from the linear dependence for lower trap powers. This can be an indication of Zeeman-changing collisions or an actually smaller trap depth due to gravity. We calculate the effect of gravity for a trap depth of 1.2 μK to be ~ 20 %.

Ultra-cold small atom clouds

The evaporation sequence leads to ultra-cold atom samples containing ~ 10 atoms. Figure 11.6 shows typical images taken in time of flight after a) 100 μs and b) 2 ms. For time-of-flight images as long as 2 ms gravity leads to a displacement of the cloud. The extracted rms width of the cloud is shown versus the time of flight on the left side of Fig. 11.7 from which we extract a temperature of 80 ± 24 nK. For such long time of flights the cloud significantly shifts away from the center position due to gravity. The z-position of the cloud is plotted as a function of time on the right graph in Fig. 11.7. We fit the function $z = -\frac{1}{2} g \cdot t^2$ to the data and find $g = 10.1 \pm 0.3$ m/s^2 compatible with Newton's heritage within the error bar. The slightly elevated measured result implies an underestimation of the transverse magnification of our imaging system as calibrated in Ch. 6 by $2 - 3$ %.

For the shown images the cloud containing $N = 10 \pm 3$ atoms has a temperature of $T = 80 \pm 24$ nK in a 0.7 μK deep trap. The peak density is $n_0 = 6 \pm 2 \cdot 10^{12}$ cm^{-3} and the phase-space density $\rho = 1.8 \pm 1.2$. The measured phase-space density passes unity and indicates that we reached the quasi-degenerate or even degenerate regime.

To check whether the ultra-cold cloud is in the degenerate regime we tried to observe a clear signature of condensation such as a double-structure or an ellipticity in the cloud expansion (Dalfovo *et al.*, 1999). So far we did not observe any clear signature of condensation (see Fig. 11.6 b)) maybe due to the following reasons:

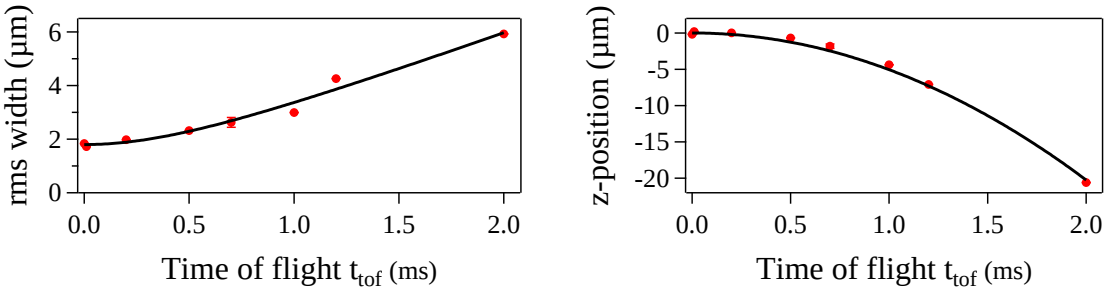

Figure 11.7: Time-of-flight experiment with an ultra-cold atom cloud. *left*) We plot the rms width of the cloud dependent of the flight time. We extract a temperature of $T = 80 \pm 24$ nK. *right*) The cloud center position in $z-$direction is shown versus the flight time. We fit the parabola $z = -\frac{1}{2} g \cdot t^2$ to the data and extract an earth acceleration of $g = 10.1 \pm 0.3$ m/s^2.

First, the calculated phase-space density relies on the measured values for the atom number and the temperature. It is possible that the calibrations done in Ch. 8 and Ch. 6 are inaccurate. Second, there are indications for a saturation of the phase-space density for dense atom clouds in tight traps (Sebby-Strabley *et al.*, 2005). Although it is not clear what mechanism prevents a condensation in this case we do not believe this limitation to be present in our case since our ultra-cold atom cloud has rather low atomic densities $10^{12} - 10^{13}$ cm^{-3}. Third, we work in a single focused dipole trap. Most other groups creating all-optical BECs work in crossed dipole traps (Barrett, Sauer, and Chapman, 2001; Kinoshita, Wenger, and Weiss, 2005; Hung *et al.*, 2008; Clément *et al.*, 2009). There are however a few BECs that were also produced in single focused laser beams so that our configuration does not seem to put any constraint on the production of BECs (Gericke *et al.*, 2007). Fourth, it is possible that the resonant light inducing the atom fluorescence at full saturation ($s \sim 5$) does destroy the condensate. The study in Ch. 6 however shows that short probe pulses < 10 μs should not affect the atom distribution, especially when dealing with dilute atom clouds after long time of flights. Fifth, the results are still preliminary and a more detailed study is necessary. For example, we would need to advance to even smaller trap depths and thus lower temperatures in order to reach higher phase-space densities. At this point a further evaporation is limited by the small atom number keeping in mind that a possible condensate would be divided into three Zeeman sublevels $m_F = (-1, 0, +1)$ decreasing the number of atoms per Zeeman state to $N/3$ on average. Further increasing the waist of the trapping beam or implementing the techniques mentioned in Sec. 10.2 could help to increase the initial atom number. Finally, the observation of such a small condensate is quite delicate which will be the subject of the next section.

11.5 Observing small Bose-Einstein condensates

There are many ways of distinguishing thermal and condensed atom clouds. We want to discuss a few techniques in the context of small atom clouds where the small number

of atoms can put major constraints on their application. The following calculations are performed for a non-interacting gas as the interaction energy is calculated to be much smaller than the potential energy in Eq. 2.28. The condensed cloud then has a Gaussian profile given by Eq. 1.48.

Observing the BEC double structure

The onset of the degenerate regime is characterized by a macroscopic atom occupation of the trap ground state. In a time-of-flight experiment the condensed fraction expands with velocity $v = \sqrt{\frac{\hbar\bar{\omega}}{m}}$. A thermal gas however expands with velocity $v = \sqrt{\frac{k_B T_C}{m}}$ for a temperature close to the condensation threshold T_C. For long time of flights the rms width of the cloud is given by $\sigma = v \cdot t$ and the ratio between the thermal and condensed cloud size follows as $\sqrt{\frac{k_B T_C}{\hbar\bar{\omega}}}$. We replace T_C by the value from Eq. 2.30 and obtain $\sqrt{0.94 N^{1/3}} \sim 1.4$ for $N = 10$ atoms. A double structure is therefore much less pronounced as for high atom number BECs.

To get an intuition about typical cloud profiles we use a sum of two Gaussians, one for the thermal and the other for the condensed part, to model the overall shape. Figure 11.8 a) shows an example of a cross-section of a partially condensed cloud with 80 atoms in the ground and 80 in higher states. The ratio between both rms widths is ~ 2. Even in this case, where the ratio is larger than 1.4 (obtained for $N = 10$) the overall result can hardly be distinguished from a single Gaussian curve (red dashed line).

Anisotropic expansion

A markable difference between the thermal and condensed part is their expansion characteristic. Looking from the side the atom cloud initially has a radially symmetric cigar shape[2]. The condensed part does expand with a direction-dependent velocity $v_i = \sqrt{\frac{\hbar\omega_i}{m}}$ with $i \in (x, y, z)$. The cloud confined in the radial directions x or y therefore expands with a velocity greater than in the axial direction z. After long time of flights the ratio between the rms widths becomes $v_i / v_j = \sqrt{\frac{\omega_i}{\omega_j}} = \sqrt{\frac{w_j}{w_i}}$ by using the result from Eq. 1.46. This leads to an inversion of the cigar and clearly identifies the condensed fraction from a thermal one for long time of flights as a thermal gas expands uniformly in all directions with the same velocity $v = \sqrt{\frac{k_B T}{m}}$ (see Fig. 11.8 b)). The rms width ratio for the axial z and radial (x or y) directions is $\sqrt{\frac{z_R}{w_{x,y}}} = 2.2$ in our case and should be clearly visible. Unfortunately our setup does not allow to image the trap from the side. We can only image the radial directions onto the CCD camera for which the rms ratio is close to one. One could however introduce a radial ellipticity on the trap to apply this technique.

[2] We would not be able to image the initial cigar-shape position distribution since the atom cloud is smaller than the imaging resolution of 1.1 μm.

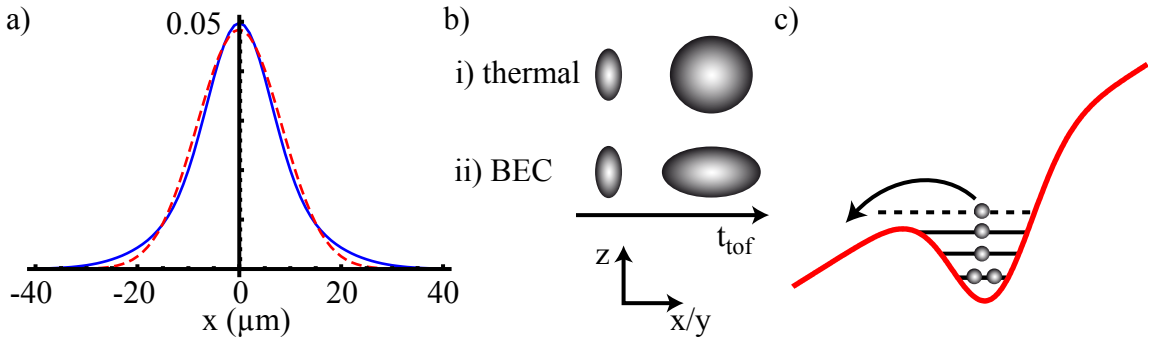

Figure 11.8: Observing small BECs. *a*) We show the cross-section (blue curve) of an image corresponding to an atom cloud with 50 % of all (160) atoms in the ground state. The result is the sum of two Gaussian distributions having a rms width ratio of ~ 2. *b*) Initially the trapped cloud has a cigar shape. In a time-of-flight expansion i) a thermal cloud expands isotropically while ii) a condensed cloud inverses its axes and keeps a fixed axes ratio at long time of flights. *c*) Gravity can tilt the potential and lead to unbound energy states. This could be used to probe the occupation number.

Comparing losses of thermal and condensed gas

Another signature for a condensed gas can be found in the loss characteristics. For n-body loss, the decay rate is reduced by a factor $1/n!$ if the atoms are degenerate. It comes from the fact that the probability to be at the same position for n atoms is $n!$ less likely for a condensed gas than for a thermal gas due to its higher-order coherence properties. This has been experimentally observed by Burt *et al.* (1997). This technique however requires an accurate measurement technique for the atom density. Although the number of atoms can be precisely measured, their volume can only be deduced indirectly by assuming thermal equilibrium for example (see Ch. 9).

Measuring the energy level occupation probability

For a single atom (Tuchendler *et al.*, 2008) as well as for many atom systems (Brantut *et al.*, 2008) an indirect measurement of the energy distribution has been performed. It may be possible to apply similar techniques to measure the occupation number of the trap vibrational levels and distinguish between a thermal and condensed energy distribution. Figure 11.8 c) shows how tilting the dipole trap leads to unbound energy states. Any atoms occupying this state are then spilled from the trap and lost. Measuring the losses from the dipole trap depending on the trap depth could be used as a measure of the occupation probability (Serwane *et al.*, 2011). In analogy to tilting the trap depth also Raman transitions between trapped and untrapped states could be used to measure the occupation probability.

11.6 Conclusion

The results presented in this chapter show that the production of small Bose-Einstein condensates containing about 10 atoms in a microscopic dipole trap is feasible. We

created small ultra-cold atom clouds $T \sim 100$ nK reaching phase-space densities above unity. So far a clear signature of condensation has not been observed also because it is not completely evident in which way one could prove the existence of a condensate in such a particular configuration. A further evaporation to go to even higher phase-space densities has been difficult due to the limited number of atoms present inside the trap. Using an accelerated evaporation technique by keeping the trap oscillation frequency constant or loading more atoms inside the trap will certainly improve this limitation.

General conclusion and perspectives

The work presented in this thesis reveals the versatility of the introduced experimental setup. The high numerical aperture aspheric lens can be used to create microscopic optical dipole traps which can operate in two distinct regimes: A single atom regime where exactly one atom is loaded into the trap and a many atom regime where up to 1000 atoms are loaded on average. The high imaging resolution of the lens allows the imaging of a single atom and is also helpful for the study of the small atom samples. Together both regimes offer unique possibilities to study mesoscopic systems containing only a few tens of interacting atoms. Furthermore, they provide ideal conditions for quantum information science using neutral atoms.

In this context we demonstrated in this thesis the use of a single atom as a quantum bit. Preparation fidelities of 99.97 % and read-out fidelities of 98.6 % were measured without losing the atom. The results further motivate the use of neutral atoms as candidates for quantum computing. Single atoms also manifest their capabilities as a calibration tool that we use to measure important quantities such as the trap depth, trap lifetime and residual magnetic fields.

It became apparent in this thesis that the direct comparison of single atom and many atom measurements is particularly powerful. This led to understand the time-of-flight temperature measurements of many atoms, which are biased when interactions between the atoms become important. Also, a precise measurement of the atom number distribution inside the dipole trap was possible using the comparison of single and many atom results. In this context the demonstration of sub-Poissonian trap loading even for atom numbers exceeding the single atom regime is remarkable. The sub-Poissonian regime is identified to originate from two-body light-assisted collisions. A deeper analysis of the collision process reveals extremely high collision rates close to the Langevin limit for only three trapped atoms on average. Again a comparison of the single from the many atom losses allowed to unambiguously identify the two-body loss nature.

The microscopic dipole trap configuration also allowed to study dense ultra-cold atom gases. Up to thousands of atoms were loaded into the microscopic trap by using a superimposed larger optical dipole trap as atom reservoir. This produces highly dense atom clouds that are subject to fast three-body recombination losses. Forced evaporation was then applied to cool down the dense sample to nano Kelvin

temperatures. We achieved phase-space densities exceeding unity for atom ensembles containing ten atoms on average. The observation of Bose-Einstein condensation is in this case complicated by the small atom number, which also prevents further evaporation to even higher phase-space densities.

This work sets the beginning for a study of the mesoscopic atom ensembles. The control over the atoms' internal degrees together with the possibility to cool small atom samples close to degeneracy opens new ways for the study of a variety of physical phenomena. The study of small atom clouds has so far not been intensified but bears interesting features as the breakdown of the thermodynamic limit for small atom numbers for example. Reaching a degenerate gas with only ten atoms could be used to measure the smearing out of the condensation phase transition. Also, the study of atom ensembles much smaller than the wavelength of the laser light used for their manipulation is possible. Interesting collective effects such as super-radiance or the dipole-dipole interaction blockade in small atom ensembles is now within reach.

Part V

Appendices

Appendix A

Physical properties of rubidium 87

A short summary of the most important definitions and physical properties of rubidium 87 are listed below. More information can be found in Ref. (Steck, 2008).

ϵ_0	$8.854\,18 \cdot 10^{-12}$ As/Vm	vacuum permittivity
μ_0	$4\pi \cdot 10^{-7}$ H/m	vacuum permeability
c_0	$2.997\,92 \cdot 10^{8}$ m/s	speed of light in the vacuum
e	$1.602\,189\,2 \cdot 10^{-19}$ C	electron charge
h	$6.626\,068\,96 \cdot 10^{-34}$ Js	Planck's constant
k_B	$1.380\,6504 \cdot 10^{-23}$ J/K	Boltzmann's constant
μ_B	h $1.399\,624\,604 \cdot 10^{-19}$ MHz/Gauss	Bohr magneton
m	$1.443\,160 \cdot 10^{-25}$ kg	mass of rubidium 87
λ_1	794.978 nm	Wavelength for $5^2\mathrm{S}_{1/2} \leftrightarrow 5^2\mathrm{P}_{1/2}$
λ, λ_2	780.245 nm	Wavelength for $5^2\mathrm{S}_{1/2} \leftrightarrow 5^2\mathrm{P}_{3/2}$
Γ	$2\pi \cdot 6.066$ MHz	$5\mathrm{P}_{3/2} \leftrightarrow 5\mathrm{S}_{1/2}$ decay rate
ω_1	$2\pi \cdot c/\lambda_1 = 377.107\,463$ THz	$5^2\mathrm{S}_{1/2} \leftrightarrow 5^2\mathrm{P}_{1/2}$ frequency
ω_2	$2\pi \cdot c/\lambda_2 = 384.230\,484$ THz	$5^2\mathrm{S}_{1/2} \leftrightarrow 5^2\mathrm{P}_{3/2}$ frequency
$\bar{\omega}$	$(\omega_x\omega_y\omega_z)^{1/3}$	geometric average of trap frequencies
Δ_1	$\omega_{dip} - \omega_1$	trap laser detuning
Δ_2	$\omega_{dip} - \omega_2$	trap laser detuning
k	$2\pi/\lambda$	wave number of probe laser
v_{rec}	$\hbar k/m = 5.8845$ m/s	recoil velocity due to probe laser
E_{rec}	$1/2mv_{rec}^2/h = 3.78$ kHz	recoil energy due to probe laser
g_I	0.000 559 141	nuclear g-factor
g_S	2.002 319	electron spin g-factor
g_L	0.999 994	electron orbital g-factor
I_{sat}	16.693 W/m^2	Saturation intensity of $5^2\mathrm{S}_{1/2}\mathrm{F} = 2, \mathrm{m_F} = \pm 2 \leftrightarrow 5^2\mathrm{P}_{3/2}\mathrm{F}' = 3, \mathrm{m_{F'}} = \pm 3$
λ_{th}	$\frac{h}{\sqrt{2\pi m k_\mathrm{B} T}}$	thermal de Broglie wavelength
ρ	$n\lambda_{th}^3$	phase-space density

Table A.1: Physical constants, rubidium 87 properties and definitions used along this thesis.

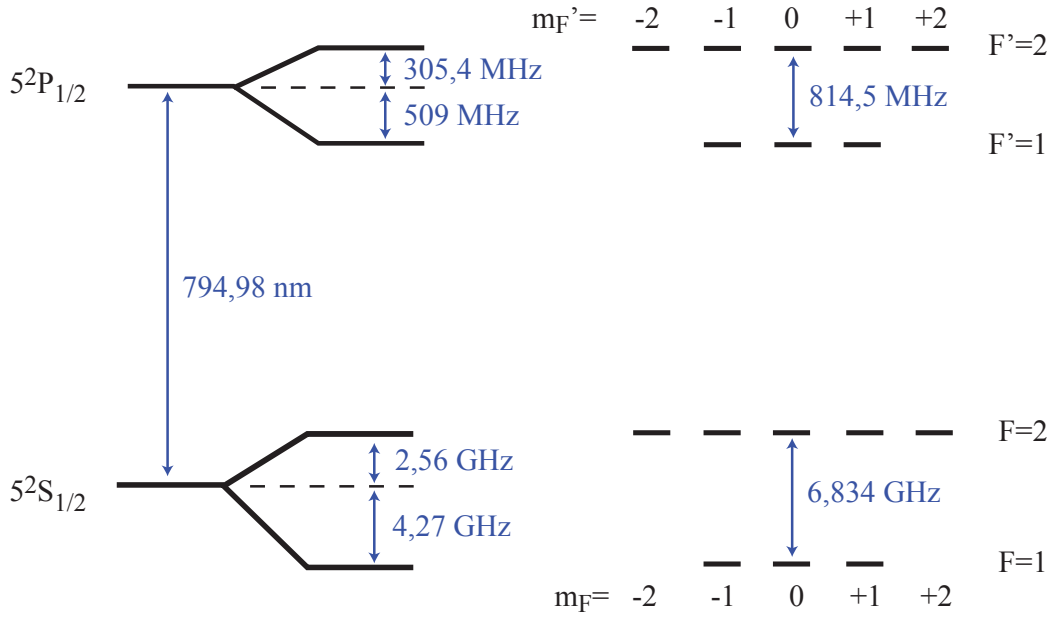

Figure A.1: Rubidium D_2 transition ($5^2S_{1/2} \rightarrow 5^2P_{1/2}$). Hyperfine structure of the rubidium ground state $5^2S_{1/2}$ and the excited state $5^2P_{1/2}$ with its magnetic components m_F.

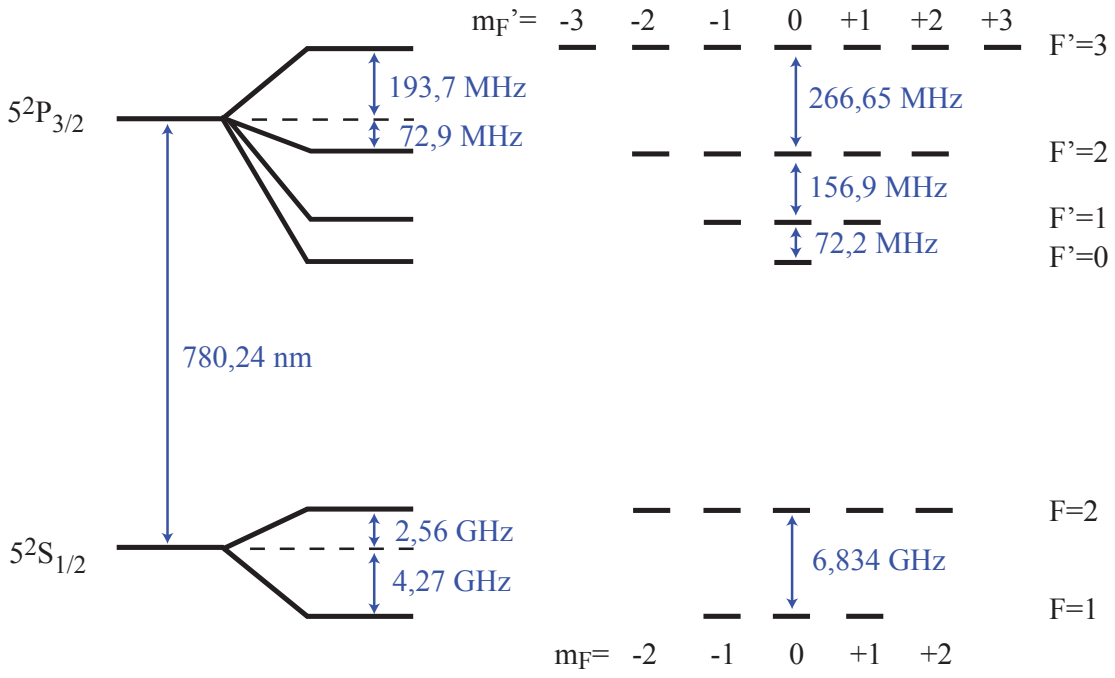

Figure A.2: Rubidium D_2 transition ($5^2S_{1/2} \rightarrow 5^2P_{3/2}$). Hyperfine structure of the rubidium ground state $5^2S_{1/2}$ and the excited state $5^2P_{3/2}$ with its magnetic components m_F.

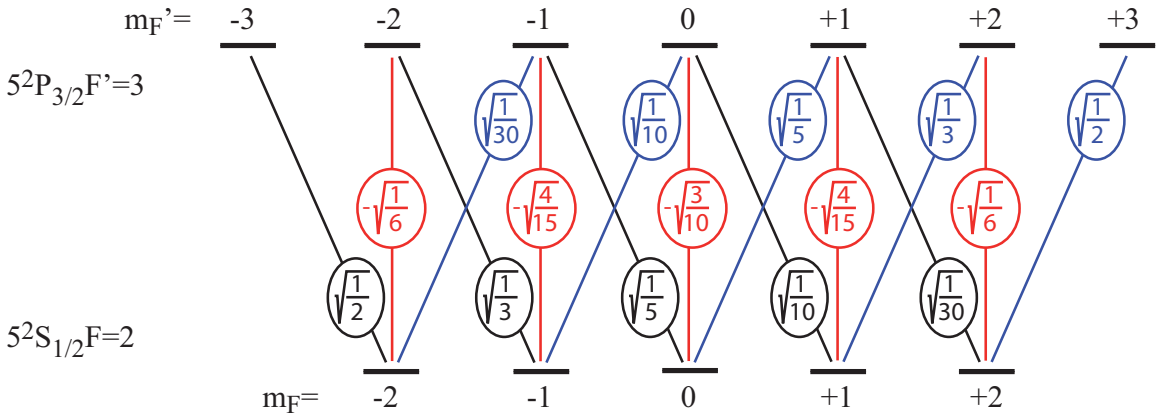

Figure A.3: Clebsch-Gordon coefficients $C^{J,J',I}_{F,m_F,F',m_{F'}}$ for the transition $5^2S_{1/2}F=2 \rightarrow 5^2P_{3/2}F'=3$. Coefficients $C^{1/2,3/2,3/2}_{2,m_F,3,m_{F'}}$ for the σ^+ transition $m_{F'}=m_F+1$ (blue), π transition $m_{F'}=m_F$ (red) and σ^- transition $m_{F'}=m_F-1$ (black).

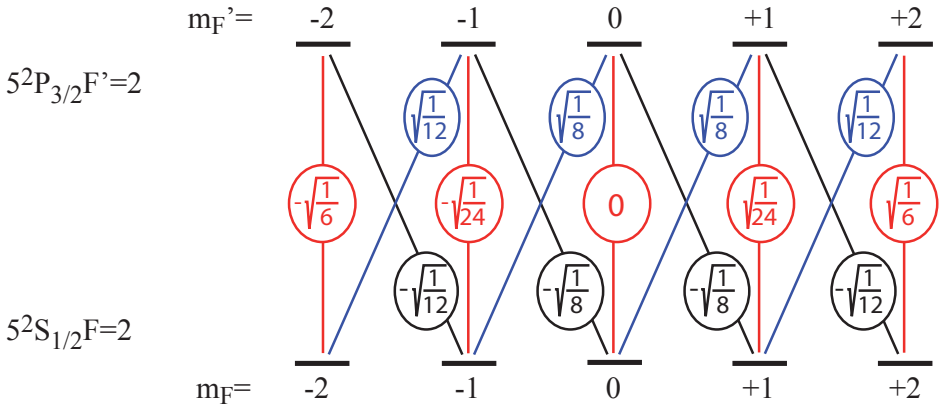

Figure A.4: Clebsch-Gordon coefficients $C^{J,J',I}_{F,m_F,F',m_{F'}}$ for the transition $5^2S_{1/2}F=2 \rightarrow 5^2P_{3/2}F'=2$. Coefficients $C^{1/2,3/2,3/2}_{2,m_F,2,m_{F'}}$ for the σ^+ transition $m_{F'}=m_F+1$ (blue), π transition $m_{F'}=m_F$ (red) and σ^- transition $m_{F'}=m_F-1$ (black).

Appendix B

Optical Bloch equations for one ground and N_e excited states

We calculate the optical Bloch equations for the four level system, comprised of the ground state $|g\rangle$ and N_e excited states $|e_1\rangle, \ldots, |e_{N_e}\rangle$. The density matrix reads

$$\boldsymbol{\rho} = \begin{pmatrix} \rho_{gg} & \rho_{ge_1} & \cdots & \rho_{ge_{N_e}} \\ \rho_{e_1 g} & \rho_{e_1 e_1} & \cdots & \rho_{e_1 e_{N_e}} \\ \vdots & \vdots & \ddots & \vdots \\ \rho_{e_{N_e} g} & \rho_{e_{N_e} e_1} & \cdots & \rho_{e_{N_e} e_{N_e}} \end{pmatrix} . \tag{B.1}$$

Electrical dipole transitions between the ground and each excited state $|e_j\rangle$ are driven by a light field $\propto e^{i(\omega_j t - \boldsymbol{k}_j \boldsymbol{r})}$. Between two excited levels the dipole matrix element is zero so that the Hamiltonian in matrix form can be written as

$$\boldsymbol{H} = \begin{pmatrix} \hbar\omega_g & \frac{1}{2}\hbar\Omega_{ge_1} e^{(i\omega_1 t - \boldsymbol{k}_1 \boldsymbol{r})} & \cdots & \frac{1}{2}\hbar\Omega_{ge_{N_e}} e^{i(\omega_{N_e} t - \boldsymbol{k}_{N_e} \boldsymbol{r})} \\ \frac{1}{2}\hbar\Omega_{ge_1} e^{-i(\omega_1 t - \boldsymbol{k}_1 \boldsymbol{r})} & \hbar\omega_{e_1} & 0 & 0 \\ \vdots & 0 & \ddots & 0 \\ \frac{1}{2}\hbar\Omega_{ge_{N_e}} e^{-i(\omega_{N_e} t - \boldsymbol{k}_{N_e} \boldsymbol{r})} & 0 & 0 & \hbar\omega_{e_{N_e}} \end{pmatrix} \tag{B.2}$$

with real Rabi frequencies $\Omega_{ge_i} = \Omega^*_{ge_i}$ and the loss part as

$$\boldsymbol{\mathcal{L}}_{loss} \cdot \boldsymbol{\rho} = \begin{pmatrix} \sum_{j=1}^{N_e} \Gamma_{e_j e_j} \rho_{e_j e_j} & -\frac{\Gamma_{ge_1}}{2}\rho_{ge_1} & \cdots & -\frac{\Gamma_{ge_3}}{2}\rho_{ge_3} \\ -\frac{\Gamma_{e_1 g}}{2}\rho_{e_1 g} & -\Gamma_{e_1 e_1}\rho_{e_1 e_1} & \cdots & -\frac{\Gamma_{e_1 e_{N_e}}}{2}\rho_{e_1 e_{N_e}} \\ \vdots & \vdots & \ddots & \vdots \\ -\frac{\Gamma_{e_{N_e} g}}{2}\rho_{e_{N_e} g} & -\frac{\Gamma_{e_{N_e} e_1}}{2}\rho_{e_{N_e} e_1} & \cdots & -\Gamma_{e_{N_e} e_{N_e}}\rho_{e_{N_e} e_{N_e}} \end{pmatrix} . \tag{B.3}$$

For the density matrix $\sum_{j=1}^{N_e} \rho_{e_j e_j} = 1 - \rho_{gg}$ and $\rho_{jl} = \rho^*_{lj}$ with $j \neq l$ hold. The differential equations resulting from the Liouville equation have the form

$$
\begin{aligned}
\dot{\rho}_{gg} &= i\sum_{j=1}^{N_e}\frac{\Omega_{ge_j}}{2}\left(e^{-i(\omega_j t-\boldsymbol{k}_j\boldsymbol{r})}\rho_{ge_j}-e^{i(\omega_j t-\boldsymbol{k}_j\boldsymbol{r})}\rho_{e_j g}\right)+\sum_{l=1}^{N_e}\Gamma_{e_l e_l}\rho_{e_l e_l}\\
\dot{\rho}_{e_je_j} &= i\frac{\Omega_{ge_j}}{2}\left(e^{i(\omega_j t-\boldsymbol{k}_j\boldsymbol{r})}\rho_{e_j g}-e^{-i(\omega_j t-\boldsymbol{k}_j\boldsymbol{r})}\rho_{ge_j}\right)-\Gamma_{e_je_j}\rho_{e_je_j}\\
\dot{\rho}_{ge_j} &= -\left(\frac{\Gamma_{ge_j}}{2}+i(\omega_g-\omega_{e_j})\right)\rho_{ge_j}+i\frac{\Omega_{ge_j}}{2}\left(e^{i(\omega_j t-\boldsymbol{k}_j\boldsymbol{r})}\rho_{gg}-e^{i(\omega_j t-\boldsymbol{k}_j\boldsymbol{r})}\rho_{e_je_j}\right)\\
&\qquad -i\sum_{\substack{l=1\\ l\neq j}}^{N_e}\frac{\Omega_{ge_l}}{2}e^{i(\omega_l t-\boldsymbol{k}_l\boldsymbol{r})}\rho_{e_le_j}\\
\dot{\rho}_{\substack{e_je_l\\ j<l}} &= -\left(\frac{\Gamma_{e_je_l}}{2}+i\left(\omega_{e_j}-\omega_{e_l}\right)\right)\rho_{e_je_l}-i\frac{\Omega_{ge_j}}{2}\left(e^{-i(\omega_j t-\boldsymbol{k}_j\boldsymbol{r})}\rho_{ge_l}-e^{i(\omega_j t-\boldsymbol{k}_j\boldsymbol{r})}\rho_{e_j g}\right)
\end{aligned}
\tag{B.4}
$$

with $\dot{\rho}^*_{e_je_l}=\dot{\rho}_{e_le_j}$. We can transform the matrices in the slow-rotating reference frame

$$
\rho_{ge_j}=\tilde{\rho}_{ge_j}e^{i(\omega_j t-\boldsymbol{k}_j\boldsymbol{r})}\qquad,\qquad \rho_{e_je_l}=\tilde{\rho}_{e_je_l}e^{i((\omega_l-\omega_j)t-(\boldsymbol{k}_l-\boldsymbol{k}_j)\boldsymbol{r})}
\tag{B.5}
$$

and obtain

$$
\dot{\rho}_{gg}=i\sum_{l=1}^{N_e}\frac{\Omega_{ge_l}}{2}\left(\tilde{\rho}_{ge_l}-\tilde{\rho}_{e_l g}\right)+\sum_{l=1}^{N_e}\Gamma_{e_le_l}\rho_{e_le_l}
\tag{B.6a}
$$

$$
\dot{\rho}_{e_je_j}=-i\frac{\Omega_{ge_j}}{2}\left(\tilde{\rho}_{ge_j}-\tilde{\rho}_{e_j g}\right)-\Gamma_{e_je_j}\rho_{e_je_j}
\tag{B.6b}
$$

$$
\dot{\tilde{\rho}}_{ge_j}=-\left(\frac{\Gamma_{ge_j}}{2}+i\Delta_{ge_j}\right)\tilde{\rho}_{ge_j}+i\frac{\Omega_{ge_j}}{2}\left(\rho_{gg}-\rho_{e_je_j}\right)-i\sum_{\substack{l=1\\ l\neq j}}^{N_e}\frac{\Omega_{ge_l}}{2}\tilde{\rho}_{e_le_j}
\tag{B.6c}
$$

$$
\dot{\tilde{\rho}}_{\substack{e_je_l\\ j<l}}=-\left(\frac{\Gamma_{e_je_l}}{2}+i\left(\Delta_l-\Delta_{ge_j}\right)\right)\tilde{\rho}_{e_je_l}+i\frac{\Omega_{ge_j}}{2}\left(\tilde{\rho}_{ge_l}-\tilde{\rho}_{e_j g}\right)\ ,
\tag{B.6d}
$$

where we use $\Delta_{ge_j}=\omega_j-\left(\omega_{e_j}-\omega_g\right)=\omega_j-\delta\omega_{e_jg}$ as the detuning between the laser and the atomic resonance. The transformed matrices then read

$$
\boldsymbol{\rho}=\begin{pmatrix}\rho_{gg} & \tilde{\rho}_{ge_1} & \tilde{\rho}_{ge_2} & \tilde{\rho}_{ge_{N_e}}\\ \tilde{\rho}_{e_1 g} & \rho_{e_1e_1} & \tilde{\rho}_{e_1e_2} & \tilde{\rho}_{e_1e_{N_e}}\\ \vdots & \vdots & \ddots & \vdots\\ \tilde{\rho}_{e_{N_e}g} & \tilde{\rho}_{e_{N_e}e_1} & \cdots & \rho_{e_{N_e}e_{N_e}}\end{pmatrix}\quad,\quad \boldsymbol{H}=\begin{pmatrix}0 & \frac{1}{2}\hbar\Omega_{ge_1} & \cdots & \frac{1}{2}\hbar\Omega_{ge_{N_e}}\\ \frac{1}{2}\hbar\Omega_{ge_1} & -\hbar\Delta_{ge_1} & 0 & 0\\ \vdots & 0 & \ddots & 0\\ \frac{1}{2}\hbar\Omega_{ge_{N_e}} & 0 & 0 & -\hbar\Delta_{ge_{N_e}}\end{pmatrix}\ ,
$$

$$
\boldsymbol{\mathcal{L}}_{loss}\boldsymbol{\rho}=\begin{pmatrix}\sum_{j=1}^{N_e}\Gamma_{e_je_j}\rho_{e_je_j} & -\frac{\Gamma_{ge_1}}{2}\tilde{\rho}_{ge_1} & \cdots & -\frac{\Gamma_{ge_{N_e}}}{2}\tilde{\rho}_{ge_{N_e}}\\ -\frac{\Gamma_{e_1g}}{2}\tilde{\rho}_{e_1g} & -\Gamma_{e_1e_1}\rho_{e_1e_1} & \cdots & -\frac{\Gamma_{e_1e_{N_e}}}{2}\tilde{\rho}_{e_1e_{N_e}}\\ \vdots & \vdots & \ddots & \vdots\\ -\frac{\Gamma_{e_{N_e}g}}{2}\tilde{\rho}_{e_{N_e}g} & -\frac{\Gamma_{e_{N_e}e_1}}{2}\tilde{\rho}_{e_{N_e}e_1} & \cdots & -\Gamma_{e_{N_e}e_{N_e}}\rho_{e_{N_e}e_{N_e}}\end{pmatrix}\ .
\tag{B.7}
$$

Appendix C

Rate equations

We set up the rate equations that can be solved to obtain the Zeeman level populations Π_{m_F} in $5^2\mathrm{S}_{1/2}\mathrm{F}=2$ and $\Pi_{m_{F'}}$ in $5^2\mathrm{P}_{3/2}\mathrm{F}'=3$, respectively, see Fig. C.1. The coupling from $5^2\mathrm{S}_{1/2}\mathrm{F}=2,\mathrm{m_F}$ to $5^2\mathrm{P}_{3/2}\mathrm{F}'=3,\mathrm{m_{F'}}$ is denoted as $F_{m_F\to m_{F'}}=\frac{s}{1+s+4\left(\frac{\Delta_{\mathrm{m_{F'}}}}{\Gamma}\right)^2}$. Here, s is the probe saturation and $\Delta_{\mathrm{m_{F'}}}=\delta-(\Delta_{5^2\mathrm{S}_{1/2}}-\Delta_{5^2\mathrm{P}_{3/2}\mathrm{F}'=3,\mathrm{m_{F'}}})$ the difference between probe detuning and the light shifted atom transition. The coefficients as weights on the populations are the Clebsch-Gordon coefficients in Fig. A.3.

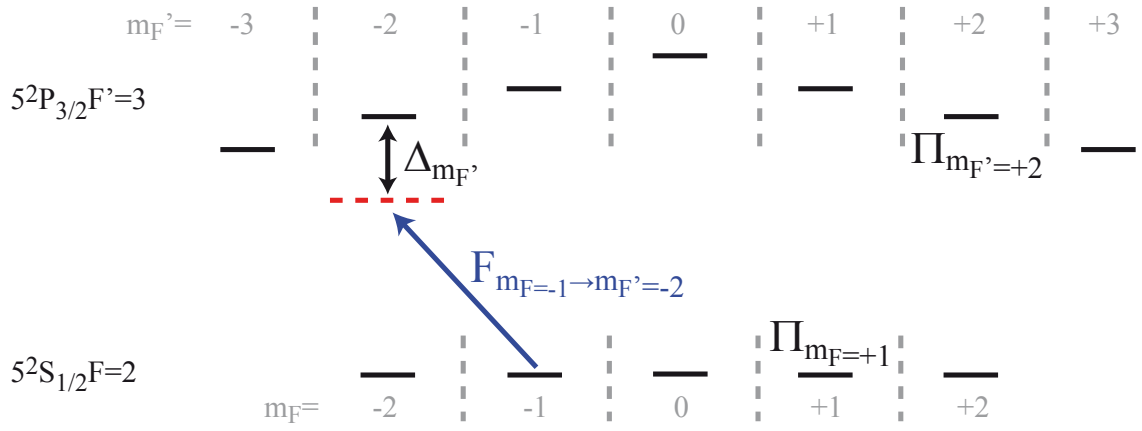

Figure C.1: Off-resonant probe laser driving the transition $5^2S_{1/2}F=2\to 5^2P_{3/2}F'=3$. The probe laser (blue arrow) drives any transition between $5^2\mathrm{S}_{1/2}\mathrm{F}=2\to 5^2\mathrm{P}_{3/2}\mathrm{F}'=3$ with coupling $F_{m_F\to m_{F'}}$ and alters the population in each level Π_{m_F}. Its frequency detuning with respect to a certain Zeeman level $5^2\mathrm{P}_{3/2}\mathrm{F}'=3\mathrm{m_{F'}}$ is denoted as $\Delta_{\mathrm{m_{F'}}}$.

$$
\begin{aligned}
\dot{\Pi}_{m_F=-2} &= \Gamma\left(\Pi_{m_{F'}=-3} + \frac{1}{3}\Pi_{m_{F'}=-2} + \frac{1}{15}\Pi_{m_{F'}=-1}\right) - \\
&\qquad \frac{\Gamma}{2}\left(F_{-2\to-3} + \frac{1}{3}F_{-2\to-2} + \frac{1}{15}F_{-2\to-1}\right)\Pi_{m_F=-2} \ , \\
\dot{\Pi}_{m_F=-1} &= \Gamma\left(\frac{2}{3}\Pi_{m_{F'}=-2} + \frac{5}{18}\Pi_{m_{F'}=-1} + \frac{1}{5}\Pi_{m_{F'}=+1}\right) - \\
&\qquad \frac{\Gamma}{2}\left(\frac{2}{3}F_{-1\to-2} + \frac{8}{15}F_{-1\to-1} + \frac{2}{3}F_{-1\to0}\right)\Pi_{m_F=-1} \ , \\
\dot{\Pi}_{m_F=0} &= \Gamma\left(\frac{2}{5}\Pi_{m_{F'}=-1} + \frac{6}{10}\Pi_{m_{F'}=0} + \frac{2}{5}\Pi_{m_{F'}=+1}\right) - \\
&\qquad \frac{\Gamma}{2}\left(\frac{2}{5}F_{0\to-1} + \frac{6}{10}F_{0\to0} + \frac{2}{5}F_{0\to+1}\right)\Pi_{m_F=0} \ , \\
\dot{\Pi}_{m_F=+1} &= \Gamma\left(\frac{1}{5}\Pi_{m_{F'}=0} + \frac{8}{15}\Pi_{m_{F'}=+1} + \frac{2}{3}\Pi_{m_{F'}=+2}\right) - \\
&\qquad \frac{\Gamma}{2}\left(\frac{1}{5}F_{+1\to0} + \frac{8}{15}F_{+1\to+1} + \frac{2}{3}F_{+1\to+2}\right)\Pi_{m_F=+1} \ , \\
\dot{\Pi}_{m_F=+2} &= \Gamma\left(\frac{1}{15}\Pi_{m_{F'}=0} + \frac{1}{3}\Pi_{m_{F'}=+1} + \Pi_{m_{F'}=+2}\right) - \\
&\qquad \frac{\Gamma}{2}\left(\frac{1}{15}F_{+2\to0} + \frac{1}{3}F_{+2\to+1} + F_{+2\to+2}\right)\Pi_{m_F=+2} \ , \\
\dot{\Pi}_{m_{F'}=-3} &= -\Gamma\Pi_{m_{F'}=-3} + \frac{\Gamma}{2}F_{-2\to-3}\Pi_{m_f=-2} \ , \\
\dot{\Pi}_{m_{F'}=-2} &= -\Gamma\Pi_{m_{F'}=-2} + \frac{\Gamma}{2}\left(\frac{1}{3}F_{-2\to-2}\Pi_{m_f=-2} + \frac{2}{3}F_{-1\to-2}\Pi_{m_f=-1}\right) \ , \\
\dot{\Pi}_{m_{F'}=-1} &= -\Gamma\Pi_{m_{F'}=-1} + \frac{\Gamma}{2}\left(\frac{1}{15}F_{-2\to-1}\Pi_{m_f=-2} + \frac{8}{15}F_{-1\to-1}\Pi_{m_f=-1} + \frac{2}{5}F_{0\to-1}\Pi_{m_f=0}\right) \ , \\
\dot{\Pi}_{m_{F'}=0} &= -\Gamma\Pi_{m_{F'}=0} + \frac{\Gamma}{2}\left(\frac{1}{5}F_{-1\to0}\Pi_{m_f=-1} + \frac{6}{10}F_{0\to0}\Pi_{m_f=0} + \frac{1}{5}F_{+1\to0}\Pi_{m_f=+1}\right) \ , \\
\dot{\Pi}_{m_{F'}=+1} &= -\Gamma\Pi_{m_{F'}=+1} + \frac{\Gamma}{2}\left(\frac{2}{5}F_{0\to+1}\Pi_{m_f=0} + \frac{8}{15}F_{+1\to+1}\Pi_{m_f=+1} + \frac{1}{15}F_{+2\to+1}\Pi_{m_f=+2}\right) \ , \\
\dot{\Pi}_{m_{F'}=+2} &= -\Gamma\Pi_{m_{F'}=+2} + \frac{\Gamma}{2}\left(\frac{2}{3}F_{+1\to+2}\Pi_{m_f=+1} + \frac{1}{3}F_{+2\to+2}\Pi_{m_f=+2}\right) \ , \\
\dot{\Pi}_{m_{F'}=+3} &= -\Gamma\Pi_{m_{F'}=+3} + \frac{\Gamma}{2}F_{+2\to+3}\Pi_{m_f=+2} \ .
\end{aligned}
\tag{C.1}
$$

Appendix D

Sub-Poissonian dipole trap loading

We concentrate on two-body losses and will set $\gamma = 0$ in Eq. 8.8b. We replace N by $N+1$ and find

$$\frac{\partial P_{N+1}(t)}{\partial t} = -(R + \frac{N(N+1)}{2}\beta')P_{N+1}(t) + RP_N(t) + \frac{(N+3)(N+2)}{2}\beta' P_{N+3}(t) \ . \tag{D.1}$$

Multiplying this equation by N and subsequently summing N from 0 to ∞ on both sides yields

$$\dot{\bar{N}} = R - \beta'\left(\overline{N^2} - \bar{N}\right) = R - \beta'\bar{N}(\bar{N}-1) - \beta'\Delta N^2 \ , \tag{D.2}$$

where the mean value is $\bar{N} = \sum_{N=0}^{\infty} NP_N$ and the variance is $\Delta N^2 = \overline{N^2} - \bar{N}^2$. This equation resembles Eq. 9.2 ($\gamma = 0$), if taking the average value of Eq. 9.2. Note that both equations do not match if we associate N in Eq. 9.2 to be the mean atom number $\bar{N}$ inside the trap, because of the additional term $-\beta'\Delta N^2$. This term is responsible for describing the width of the atom distribution and thus describes if its type is Poissonian, sub-Poissonian or super-Poissonian. The term can however be neglected when calculating the average number of atoms as we will see now by considering three special cases:

- $\boldsymbol{\Delta N^2 = \bar{N}}$ This case corresponds to a Poissonian distribution and leads to

  $$\dot{\bar{N}} = R - \beta'\bar{N}^2 \ , \tag{D.3}$$

  equivalent to Eq. 3.6 in the large atom number regime ($N(N-1) \to N^2$) and neglecting one-body losses ($\gamma = 0$) if additionally we assume N in Eq. 3.6 to be the mean atom number $\bar{N}$. The average atom number in steady state is $\bar{N}_{st} = \sqrt{R/\beta'}$.

- $\boldsymbol{\Delta N^2 = 0}$ This case corresponds to the maximally sub-Poissonian distribution and leads to

$$\dot{\bar{N}} = R - \beta' \bar{N}(\bar{N} - 1) \ , \tag{D.4}$$

equivalent to Eq. 3.6 with $\gamma = 0$ and associating N in Eq. 3.6 with the mean atom number $\bar{N}$. The average atom number in steady state is $\bar{N}_{st} = 1/2 + \sqrt{1/4 + R/\beta'}$ and converges to $\bar{N}_{st} = \sqrt{R/\beta'}$ for $R/\beta' \gg 1/4$ (large atom numbers), the average value found in the Poisson case.

- $\boldsymbol{\Delta N^2 = 3/4\bar{N}}$ This case corresponds to the distribution that has been calculated numerically (or by means of a Monte-Carlo simulation). It is also the value that is closest to the in Sec. 8.5 measured one. An analytical derivation of the factor 3/4 can be found following the approach in van Kampen (2007).

  The atom number evolves in this case as

$$\dot{\bar{N}} = R - \beta' \bar{N}(\bar{N} - \frac{1}{4}) \ . \tag{D.5}$$

  The average atom number in steady state is $\bar{N}_{st} = 1/2 + \sqrt{R/\beta' - 1/2}$ and also converges for $R/\beta' \gg 1/2$ to $\bar{N}_{st} = \sqrt{R/\beta'}$, the value found in the Poisson case.

The calculations show that the average atom number depends on the variance of the atom distribution ΔN^2. Note that Eq. D.3, D.4 and D.5 can be used to model the evolution of the average atom number $\bar{N}$ in the limit $R/\beta' \gg 0$ (large atom numbers), for which they yield the same result. This is due to the fact that the equations do not significantly depend on the width of the distribution ΔN^2 for $R/\beta' \gg 0$. However, the equations do not give any information about the form of the distributions.

Bibliography

Adams, C. S., Lee, H. J., Davidson, N., Kasevich, M., and Chu, S., *"Evaporative Cooling in a Crossed Dipole Trap,"* Phys. Rev. Lett. **74**, 3577–3580 (1995).

Ahmadi, P., Timmons, B. P., and Summy, G. S., *"Geometrical effects in the loading of an optical atom trap,"* Phys. Rev. A **72**, 023411 (2005).

Albiez, M., Gati, R., Fölling, J., Hunsmann, S., Cristiani, M., and Oberthaler, M., *"Direct observation of tunneling and nonlinear self-trapping in a single bosonic josephson junction,"* Phys. Rev. Lett. **95**, 010402 (2005).

Bakr, W., Gillen, J., Peng, A., Fölling, S., and Greiner, M., *"A quantum gas microscope for detecting single atoms in a hubbard-regime optical lattice,"* Nature **462**, 74 (2009).

Bali, S., O'Hara, K. M., Gehm, M. E., Granade, S. R., and Thomas, J. E., *"Quantum-diffractive background gas collisions in atom-trap heating and loss,"* Phys. Rev. A **60**, R29–R32 (1999).

Barrett, M. D., Sauer, J. A., and Chapman, M. S., *"All-Optical Formation of an Atomic Bose-Einstein Condensate,"* Phys. Rev. Lett. **87**, 010404 (2001).

Basden, A., Haniff, C., and Mackay, C., *"Photon Counting Strategies with low light level CCDs,"* Mon. Not R. astro. Soc. **345**, 985–991 (2003).

Beterov, I., Tretyakov, D., Entin, V., Yakshina, E., Ryabtsev, I., MacCormick, C., and Bergamini, S., *"Deterministic single-atom excitation via adiabatic passage and Rydberg blockade,"* arXiv:1102.5223v4 (2011).

Beugnon, J., Thèse de doctorat, Ph.D. thesis, Université Paris XI (2007).

Beugnon, J., Jones, M. P. A., Dingjan, J., Darquié, B., Messin, G., Browaeys, A., and Grangier, P., *"Quantum interference between two single photons emitted by independently trapped atoms,"* Nature **440**, 779 (2006).

Beugnon, J., Tuchendler, C., Marion, H., Gaëtan, A., Miroshnychenko, Y., Sortais, Y., Lance, A., Jones, M., Messin, G., Browaeys, A., and Grangier, P., *"Two-dimensional transport and transfer of a single atomic qubit in optical tweezers,"* Nature Physics **3**, 696 (2007).

Bloch, I., Dalibard, J., and Zwerger, W., *"Many-body physics with ultracold gases,"* Rev. Mod. Phys. **80**, 885–964 (2008).

Bochmann, J., Mücke, M., Guhl, C., Ritter, S., Rempe, G., and Moehring, D., *"Lossless state detection of single neutral atoms,"* Phys. Rev. Lett. **104**, 203601 (2010).

Brantut, J. P., Clément, J. F., de Saint Vincent, M. R., Varoquaux, G., Nyman, R. A., Aspect, A., Bourdel, T., and Bouyer, P., *"Light-shift tomography in an optical-dipole trap for neutral atoms,"* Phys. Rev. A **78**, 031401 (2008).

Brink, D. and Satchler, G., Angular Momentum (Oxford University Press, USA, 1994).

Bücker, R., Perrin, A., Manz, S., Betz, T., Koller, C., Plisson, T., Rottmann, J., Schumm, T., and Schmiedmayer, J., *"Single atom sensitive flouresence imaging of ultracold quantum gases,"* New J. Phys. **11**, 103039 (2009).

Burt, E. A., Ghrist, R. W., Myatt, C. J., Holland, M. J., Cornell, E. A., and Wieman, C. E., *"Coherence, Correlations, and Collisions: What One Learns about Bose-Einstein Condensates from Their Decay,"* Phys. Rev. Lett. **79**, 337–340 (1997).

C.-S. Chuu,, Schreck, F., Meyrath, T., Hanssen, J., Price, G., and Raizen, M., *"Direct observation of sub-poissonian number statistics in a degenerate bose gas,"* Phys. Rev. Lett. **95**, 260403 (2005).

Clément, J.-F., Brantut, J.-P., Robert-de Saint-Vincent, M., Nyman, R. A., Aspect, A., Bourdel, T., and Bouyer, P., *"All-optical runaway evaporation to Bose-Einstein condensation,"* Phys. Rev. A **79**, 061406 (2009).

Cline, R., Miller, J., Matthews, M., and Heinzen, D., *"Spin relaxation of optically trapped atoms by light scattering,"* Optics Letters **19**, 207–209 (1994).

Cohen-Tannoudji, C., Dupont-Roc, J., and Grynberg, G., Processus d'interaction entre photons et atomes (InterEditions, Paris, 1988).

Comparat, D., Fioretti, A., Stern, G., Dimova, E., Tolra, B. L., and Pillet, P., *"Optimized production of large Bose-Einstein condensates,"* Phys. Rev. A **73**, 043410 (2006).

Condon, E. and Shortley, G., The theory of atomic spectra (Ellipses, Paris, 1997).

Dalfovo, F., Giorgini, S., Pitaevskii, L. P., and Stringari, S., *"Theory of bose-einstein condensation in trapped gases,"* Rev. Mod. Phys. **71**, 463–512 (1999).

Dalibard, J., *"Laser cooling of an optically thick gas: The simplest radiation pressure trap?"* Optics Communications **68**, 203 – 208 (1988).

Dalibard, J. and Cohen-Tannoudji, C., *"Laser cooling below the doppler limit by polarization gradients: simple theoretical models,"* J. Opt. Soc. Am. B **6**, 2023 (1989).

Darquié, B., Thèse de doctorat, Ph.D. thesis, Université Paris XI (2005).

Darquié, B., Jones, M. P. A., Dingjan, J., Beugnon, J., Bergamini, S., Sortais, Y., Messin, G., Browaeys, A., and Grangier, P., *"Controlled Single-Photon Emission from a Single Trapped Two-Level Atom,"* Science **309**, 454–456 (2005).

DePue, M. T., McCormick, C., Winoto, S. L., Oliver, S., and Weiss, D. S., *"Unity occupation of sites in a 3d optical lattice,"* Phys. Rev. Lett. **82**, 2262–2265 (1999).

Dumke, R., Volk, M., Müther, T., Buchkremer, F., Birkl, G., and Ertmer, W., *"Micro-optical realization of arrays of selectively addressable dipole traps: A scalable configuration for quantum computation with atomic qubits,"* Phys. Rev. Lett. **89**, 097903 (2002).

Dürr, S., Miller, K. W., and Wieman, C. E., *"Improved loading of an optical dipole trap by suppression of radiative escape,"* Phys. Rev. A **63**, 011401 (2000).

Engler, H., Weber, T., Mudrich, M., Grimm, R., and Weidemüller, M., *"Very long storage times and evaporative cooling of cesium atoms in a quasielectrostatic dipole trap,"* Phys. Rev. A **62**, 031402 (2000).

Esteve, J., Gross, C., Weller, A., Giovanazzi, S., and Oberthaler, M., *"Squeezing and entanglement in a bose-einstein condensate,"* Nature **455**, 1216–1219 (2008).

Fedichev, P. O., Reynolds, M. W., and Shlyapnikov, G. V., *"Three-Body Recombination of Ultracold Atoms to a Weakly Bound s Level,"* Phys. Rev. Lett. **77**, 2921–2924 (1996).

Foot, C., Atomic Physics (Oxford University Press, USA, 2005).

Frese, D., Ueberholz, B., Kuhr, S., Alt, W., Schrader, D., Gomer, V., and Meschede, D., *"Single Atoms in an Optical Dipole Trap: Towards a Deterministic Source of Cold Atoms,"* Phys. Rev. Lett. **85**, 3777–3780 (2000).

Förster, L., Alt, W., Dotsenko, I., Khudaverdyan, M., Meschede, D., Miroschnychenko, Y., Reick, S., and Rauschenbeutel, A., *"Number-triggered loading and collisional redistribution of neutral atoms in a standing wave dipole trap,"* New J. Phys. **8**, 259 (2006).

Fuhrmanek, A., Bourgain, R., Sortais, Y. R. P., and Browaeys, A., *"Free-Space Lossless State Detection of a Single Trapped Atom,"* Phys. Rev. Lett. **106**, 133003 (2011).

Fuhrmanek, A., Lance, A., Tuchendler, C., Grangier, P., Sortais, Y., and Browaeys, A., *"Imaging a single atom in a time-of-flight experiment,"* New J. Phys. **12**, 053028 (2010a).

Fuhrmanek, A., Sortais, Y., Grangier, P., and Browaeys, A., *"Measurement of the atom number distribution in an optical tweezer using single-photon counting,"* Phys. Rev. A **82**, 023623 (2010b).

Gallagher, A. and Pritchard, D. E., *"Exoergic collisions of cold Na*-Na,"* Phys. Rev. Lett. **63**, 957–960 (1989).

Gaëtan, A., Miroshnychenko, Y., Wilk, T., Chotia, A., Viteau, M., Comparat, D., Pillet, P., Browaeys, A., and Grangier, P., *"Observation of collective excitation of two individual atoms in the Rydberg blockade regime,"* Nature Phys. **5**, 115–118 (2009).

Gehr, R., Volz, J., Dubois, G., Steinmetz, T., Colombe, Y., Lev, B. L., Long, R., Estève, J., and Reichel, J., *"Cavity-Based Single Atom Preparation and High-Fidelity Hyperfine State Readout,"* Phys. Rev. Lett. **104**, 203602 (2010).

Gensemer, S. D., Gould, P. L., Leo, P. J., Tiesinga, E., and Williams, C. J., *"Ultracold ^{87}Rb ground-state hyperfine-changing collisions in the presence and absence of laser light,"* Phys. Rev. A **62**, 030702 (2000).

Gensemer, S. D., Sanchez-Villicana, V., Tan, K. Y. N., Grove, T. T., and Gould, P. L., *"Trap-loss collisions of ^{85}Rb and ^{87}Rb: Dependence on trap parameters,"* Phys. Rev. A **56**, 4055–4063 (1997).

Gericke, T., Würtz, P., Reitz, D., Utfeld, C., and Ott, H., *"All-optical formation of a Bose-Einstein condensate for applications in scanning electron microscopy,"* Applied Physics B: Lasers and Optics **89**, 447–451 (2007).

Gerritsma, R., Kirchmair, G., Zähringer, F., Solano, E., Blatt, R., and Roos, C. F., *"Quantum simulation of the Dirac equation,"* Nature **463**, 68–71 (2010).

Gibbons, M. J., Hamley, C. D., Shih, C.-Y., and Chapman, M. S., *"Nondestructive Fluorescent State Detection of Single Neutral Atom Qubits,"* Phys. Rev. Lett. **106**, 133002 (2011).

Grebenev, S., Toennies, J., and Vilesov, A., *"Superfluidity Within a Small Helium-4 Cluster: The Microscopic Andronikashvili Experiment,"* Science **279**, 2083–2086 (1998).

Grimm, R., Weidemüller, M., and Ovchinnikov, Y., *"Optical Dipole Traps for Neutral Atoms,"* Adv. At. Mol. Opt. Phys. **42**, 95 (2000).

Grünzweig, T., Hilliard, A., McGovern, M., and Andersen, M., *"Near-deterministic preparation of a single atom inan optical microtrap,"* Nat. Phys. **6**, 951–954 (2010).

Gross, M. and Haroche, S., *"Superradiance: An essay on the theory of collective spontaneous emission,"* Physics Reports **93**, 301 – 396 (1982).

Grossmann, S. and Holthaus, M., *"On bose-einstein condensation in harmonic traps,"* Physics Letters A **208**, 188 – 192 (1995).

Hansch, T. and Schawlow, A. L., *"Cooling of gases by laser radiation,"* Opt. Commun. **13**, 68–69 (1975).

Haugerud, H., Haugset, T., and Ravndal, F., *"A more accurate analysis of bose-einstein condensation in harmonic traps,"* Physics Letters A **225**, 18 – 22 (1997).

Hensler, S., Werner, J., Griesmaier, A., Schmidt, P., Görlitz, A., Pfau, T., Giovanazzi, S., and Rzazewski, K., *"Dipolar relaxation in an ultra-cold gas of magnetically trapped chromium atoms,"* Applied Physics B: Lasers and Optics **77**, 765–772 (2003).

Hollenhorst, J., *"A theory of multiplication noise,"* IEEE Transactions on Electron Devices **37**, 781 (1990).

Hroch, F., *"Noise Properties and Time Response of the Staircase Avalanche Photodiode,"* Experimental Astronomy. **9**, 251–259 (1999).

Hung, C.-L., Zhang, X., Gemelke, N., and Chin, C., *"Accelerating evaporative cooling of atoms into Bose-Einstein condensation in optical traps,"* Phys. Rev. A **78**, 011604 (2008).

Isenhower, L., Urban, E., Zhang, X. L., Gill, A. T., Henage, T., Johnson, T. A., Walker, T. G., and Saffman, M., *"Demonstration of a Neutral Atom Controlled-NOT Quantum Gate,"* Phys. Rev. Lett. **104**, 010503 (2010).

Itah, A., Veksler, H., Lahav, O., Blumkin, A., Moreno, C., Gordon, C., and Steinhauer, J., *"Direct observation of a sub-poissonian number distribution of atoms in an optical lattice,"* Phys. Rev. Lett. **104**, 113001 (2010).

Joffe, M., Ketterle, W., Martin, A., and Pritchard, D., *"Transverse cooling and deflection of an atomic beam inside a zeeman slower,"* J. Opt. Soc. Am. B **10**, 2257–2262 (1993).

Jones, M. P. A., Beugnon, J., Gaëtan, A., Zhang, J., Messin, G., Browaeys, A., and Grangier, P., *"Fast quantum state control of a single trapped neutral atom,"* Phys. Rev. A **75**, 040301 (2007).

Julienne, P. S. and Vigué, J., *"Cold collisions of ground- and excited-state alkali-metal atoms,"* Phys. Rev. A **44**, 4464–4485 (1991).

van Kampen, N., Stochastic Processes in Physics and Chemistry (Elsevier, Amsterdam, 2007).

Ketterle, W., Davis, K. B., Joffe, M. A., Martin, A., and Pritchard, D. E., *"High densities of cold atoms in a dark spontaneous-force optical trap,"* Phys. Rev. Lett. **70**, 2253–2256 (1993).

Ketterle, W. and van Druten, N., *"Evaporative cooling of atoms,"* Advances in Atomic, Molecular, and Optical Physics **37**, 181–236 (1996a).

Ketterle, W. and van Druten, N. J., *"Bose-einstein condensation of a finite number of particles trapped in one or three dimensions,"* Phys. Rev. A **54**, 656–660 (1996b).

Kinoshita, T., Wenger, T., and Weiss, D. S., *"All-optical Bose-Einstein condensation using a compressible crossed dipole trap,"* Phys. Rev. A **71**, 011602 (2005).

Kuhr, S., Alt, W., Schrader, D., Dotsenko, I., Miroshnychenko, Y., Rosenfeld, W., Khudaverdyan, M., Gomer, V., Rauschenbeutel, A., and Meschede, D., *"Coherence Properties and Quantum State Transportation in an Optical Conveyor Belt,"* Phys. Rev. Lett. **91**, 213002 (2003).

Kuhr, S., Alt, W., Schrader, D., Müller, M., Gomer, V., and Meschede, D., *"Deterministic delivery of a single atom,"* Science **293**, 278 (2001).

Kulatunga, P., Blum, T., and Olek, D., *"Loading characteristics of a microscopic optical dipole trap,"* arXiv[physics.atom-ph]:1009.2544 (2010).

Kuppens, S., Corwin, K., Miller, K., Chupp, T., and Wieman, C., *"Loading an optical dipole trap,"* Phys. Rev. A **62**, 013406 (2000).

Ladd, T. D., Jelezko, F., Laflamme, R., Nakamura, Y., Monroe, C., and O'Brien, J. L., *"Quantum computers,"* Nature **464**, 45–53 (2010).

Lamb, W. E. and Retherford, R. C., *"Fine structure of the hydrogen atom by a microwave method,"* Phys. Rev. **72**, 241–243 (1947).

Landau, L. and Lifshitz, L., Quantum Mechanics Non-Relativistic Theory (Butterworth-Heinemann, 1981).

Leanhardt, A. E., Pasquini, T. A., Saba, M., Schirotzek, A., Shin, Y., Kielpinski, D., Pritchard, D. E., and Ketterle, W., *"Cooling Bose-Einstein Condensates Below 500 Picokelvin,"* Science **301**, 1513–1515 (2003).

Lett, P., Watts, R., Westbrook, C., Phillips, W., Gould, P., and Metcalf, H., *"Observation of atoms laser cooled below the doppler limit,"* Phys. Rev. Lett. **61**, 169 (1988).

Loudon, R., The Quantum Theory of Light (Oxford University Press, USA, 2000).

Luiten, O. J., Reynolds, M. W., and Walraven, J. T. M., *"Kinetic theory of the evaporative cooling of a trapped gas,"* Phys. Rev. A **53**, 381–389 (1996).

Mandel, O., Greiner, M., Widera, A., Rom, T., Hänsch, T., and Bloch, I., *"Controlled collisions for multi-particle entanglement of optically trapped atoms,"* Nature **425**, 937–940 (2003).

Marte, A., Volz, T., Schuster, J., Dürr, S., Rempe, G., van Kempen, E. G. M., and Verhaar, B. J., *"Feshbach Resonances in Rubidium 87: Precision Measurement and Analysis,"* Phys. Rev. Lett. **89**, 283202 (2002).

Matsuo, K., Teich, M., and Saleh, B., *"Noise Properties and Time Response of the Staircase Avalanche Photodiode,"* IEEE Trans. Elect. Dev. **ED-32**, 2615–2623 (1985).

McGovern, M., Hilliard, A., Grünzweig, T., and Andersen, M., *"Counting atoms in a deep optical microtrap,"* Optics Letters **36**, 1041–1043 (2011).

Messiah, A., Quantum Mechanics Volume II (Dover Publications, Mineola, 1999).

Miesner, H.-J., Stamper-Kurn, D., Andrews, M., Durfee, D., Inouye, S., and Ketterle, W., *"Bosonic stimulation in the formation of a Bose-Einstein condensate,"* Science **279**, 1005–1007 (1998).

Miller, J. D., Cline, R. A., and Heinzen, D. J., *"Photoassociation spectrum of ultracold Rb atoms,"* Phys. Rev. Lett. **71**, 2204–2207 (1993).

Miroschnychenko, Y., Alt, W., Dotsenko, I., Förster, L., Khudaverdyan, M., Meschede, D., Schrader, D., and Rauschenbeutel, A., *"Quantum engineering: An atom-sorting machine,"* Nature **442**, 151 (2006).

Mohring, B., Bienert, M., Haug, F., Morigi, G., Schleich, W. P., and Raizen, M. G., *"Extracting atoms on demand with lasers,"* Phys. Rev. A **71**, 053601 (2005).

Morice, O., Castin, Y., and Dalibard, J., *"Refractive index of a dilute Bose gas,"* Phys. Rev. A **51**, 3896–3901 (1995).

Myerson, A., Szwer, D., Webster, S., Allock, D., Curtis, M., Imreh, G., Sherman, J., Stacey, D., Steane, A., and Lucas, D., *"High-Fidelity Readout of Trapped-Ion Qubits,"* Phys. Rev. Lett. **100**, 200502 (2008).

Nelson, K., Li, X., and Weiss, D., *"Imaging single atoms in a three-dimensional array,"* Nat. Phys. **3**, 556 (2007).

O'Hara, K. M., Gehm, M. E., Granade, S. R., and Thomas, J. E., *"Scaling laws for evaporative cooling in time-dependent optical traps,"* Phys. Rev. A **64**, 051403 (2001).

Orzel, C., Tuchman, A., Fenselau, M., Yasuda, M., and Kasevich, M., *"Squeezed states in a bose-einstein condensate,"* Science **291**, 2386–2389 (2001).

Parkins, A. S. and Zoller, P., *"Laser cooling of atoms with broadband real Gaussian laser fields,"* Phys. Rev. A **45**, 6522–6538 (1992).

Petrich, W., Anderson, M., Ensher, J., and Cornell, E., *"Behavior of atoms in a compressed magneto-otpical trap,"* J. Opt. Soc. Am. B **11**, 1332–1335 (1994).

Phillips, W. and Metcalf, H., *"Laser deceleration of an atomic beam,"* Phys. Rev. Lett. **48**, 596–599 (1982).

Puppe, T., Schuster, I., Grothe, A., Kubanek, A., Murr, K., Pinkse, P. W. H., and Rempe, G., *"Trapping and Observing Single Atoms in a Blue-Detuned Intracavity Dipole Trap,"* Phys. Rev. Lett. **99**, 013002 (2007).

Ramsey, N., Molecular Beams (Oxford University Press, USA, 1990).

Roos, C., Chwalla, M., K.Kim,, Riebe, M., and Blatt, R., *""Designer atoms" for quantum metrology,"* Nature **443**, 316–319 (2006).

Saffman, M. and Walker, T. G., *"Creating single-atom and single-photon sources from entangled atomic ensembles,"* Phys. Rev. A **66**, 065403 (2002).

Saffman, M., Walker, T. G., and Mølmer, K., *"Quantum information with Rydberg atoms,"* Rev. Mod. Phys. **82**, 2313–2363 (2010).

Sakurai, J., Modern Quantum Mechanics (Addison Wesley, 1993).

Savard, T. A., O'Hara, K. M., and Thomas, J. E., *"Laser-noise-induced heating in far-off resonance optical traps,"* Phys. Rev. A **56**, R1095–R1098 (1997).

Schlosser, N., Reymond, G., and Grangier, P., *"Subpoissonian loading of a microscopic dipole trap,"* Phys. Rev. Lett. **89**, 023005 (2002).

Schlosser, N., Reymond, G., Protsenko, I., and Grangier, P., *"Subpoissonian loading of a microscopic dipole trap,"* Nature **411**, 1024 (2001).

Schulz, M., Crepaz, H., Schmidt-Kaler, F., Eschner, J., and Blatt, R., *"Transfer of trapped atoms between two optical tweezer potentials,"* Journal of Modern Optics **54**, 1619 – 1626 (2007).

Söding, J., Guéry-Odelin, D., Desbiolles, P., Chevy, F., Inamori, H., and Dalibard, J., *"Three-body decay of a rubidium Bose-Einstein condensate,"* Applied Physics B: Lasers and Optics **69**, 257–261 (1999).

Sebby-Strabley, J., Newell, R. T. R., Day, J. O., Brekke, E., and Walker, T. G., *"High-density mesoscopic atom clouds in a holographic atom trap,"* Phys. Rev. A **71**, 021401 (2005).

Serwane, F., Zürn, G., Lompe, T., Ottenstein, T., Wenz, A., and Jochim, S., *"Deterministic preparation of a tunable few-fermion system,"* Science **332**, 336–338 (2011).

Sokolov, I., Kupriyanova, M., Kupriyanov, D., and Havey, M., *"Light scattering from a dense and ultracold atomic gas,"* Phys. Rev. A **79**, 053405 (2009).

Sortais, Y., Marion, H., Tuchendler, C., Lance, A., Lamare, M., P.Fournet,, Armellin, C., Mercier, R., Messin, G., Browaeys, A., and Grangier, P., *"Diffraction-limited optics for single-atom manipulation,"* PRA **75**, 013406 (2007).

Stamper-Kurn, D. M., Miesner, H.-J., Chikkatur, A. P., Inouye, S., Stenger, J., and Ketterle, W., *"Reversible formation of a bose-einstein condensate,"* Phys. Rev. Lett. **81**, 2194–2197 (1998).

Steane, A., Chowdhury, M., and Foot, C., *"Radiation force in the magneto-optical trap,"* J. Opt. Soc. Am. B **9**, 2142–2158 (1992).

Steck, D. A., *"Rubidium 87 d line data,"* available online at http://steck.us/alkalidata (2008).

Stetson, P., *"A computer program for crowded-field stellar photometry,"* Publ. Astron. Soc. Pac. **99**, 191–222 (1987).

Tubbs, R., Dissertation, Ph.D. thesis, University of Cambridge (2003).

Tuchendler, C., Lance, A. M., Browaeys, A., Sortais, Y. R. P., and Grangier, P., *"Energy distribution and cooling of a single atom in an optical tweezer,"* Phys. Rev. A **78**, 033425 (2008).

Tulloch, S. and Dhillon, V., *"On the use of electron-multiplying CCDs for astronomical spectroscopy,"* Monthly Notices of the Royal Astronomical Society , no. doi: 10.1111/j.1365–2966.2010.17675.x (2010).

Urban, E., Johnson, T. A., Henage, T., Isenhower, L., Yavuz, T., Walker, T. G., and Saffman, M., *"Observation of Rydberg blockade between two atoms,"* Nature Phys. **5**, 110–114 (2009).

Walker, T., Sesko, D., and Wieman, C., *"Collective behavior of optically trapped neutral atoms,"* Phys. Rev. Lett. **64**, 408–411 (1990).

Weiner, J., Bagnato, V. S., Zilio, S., and Julienne, P. S., *"Experiments and theory in cold and ultracold collisions,"* Rev. Mod. Phys. **71**, 1–85 (1999).

Whitlock, S., Gerritsma, R., Fernholz, T., and Spreeuw, R., *"Two-dimensional array of microtraps with atomic shift register on a chip,"* New J. Phys. **11**, 023021 (2009).

Whitlock, S., Ockeloen, C., and Spreeuw, R., *"Sub-poissonian atom-number fluctuations by three-body loss in mesoscopic ensembles,"* Phys. Rev. Lett. **104**, 120402 (2010).

Wilk, T., Gaëtan, A., Evellin, C., Wolters, J., Miroshnychenko, Y., Grangier, P., and Browaeys, A., *"Entanglement of Two Individual Neutral Atoms Using Rydberg Blockade,"* Phys. Rev. Lett. **104**, 010502 (2010).

Wineland, D., Bollinger, J., Itano, W., and Heinzen, D., *"Squeezed atomic states and projection noise in spectroscopy,"* Phys. Rev. A **50**, 67–88 (1994).

Wineland, D. and Dehmelt, H., *"Proposed $10^{14}\Delta\nu < \nu$ laser fluorescence spectroscopy on TI^{+} mono-ion oscillator III,"* Bull. Am. Phys. Soc. **20**, 637 (1975).

Wineland, D. J., Bergquist, J. C., Itano, W. M., and Drullinger, R. E., *"Double-resonance and optical-pumping experiments on electromagnetically confined, laser-cooled ions,"* Optics Letters **5**, 245–247 (1980).

Yavuz, D. D., Kulatunga, P. B., Urban, E., Johnson, T. A., Proite, N., Henage, T., Walker, T. G., and Saffman, M., *"Fast Ground State Manipulation of Neutral Atoms in Microscopic Optical Traps,"* Phys. Rev. Lett. **96**, 063001 (2006).

Résumé

Cette thèse traite de la manipulation d'atomes de rubidium 87 piégés dans un piège optique dipolaire microscopique. Les expériences sont réalisées dans divers régimes de chargement du piège allant d'un atome unique à quelques milliers d'atomes en moyenne.

Le régime à un seul atome permet de calibrer le dispositif expérimental. Nous utilisons l'atome unique comme bit quantique dont nous pouvons préparer et lire l'état avec une efficacité de 99.97 % et 98.6 %, respectivement. Lorsque plusieurs atomes sont chargés dans le piège microscopique, nous observons une distribution sub-Poissonienne du nombre d'atomes, liée aux collisions assistées par la présence de lumière quasi résonante. Une étude de ces collisions dans notre cas particulier (piège microscopique) révèle des taux de pertes extrêmement élevés, proches de la limite théorique de Langevin. Enfin, nous montrons que le chargement du piège microscopique avec plusieurs atomes est plus efficace lorsque nous superposons sur ce piège un deuxième piège, macroscopique, qui joue le rôle de réservoir d'atomes. Ce réservoir permet de charger le micro-piège à partir du macro-piège en l'absence de lumière quasi résonante et donc d'éviter les collisions assistées par la lumière.

Le chargement du micro-piège à partir du macro-piège conduit à des conditions initiales optimales pour l'évaporation forcée dans la perspective d'atteindre la condensation de Bose-Einstein avec seulement une dizaine d'atomes. Après évaporation du gaz nous atteignons des densités dans l'espace des phases proches du régime de dégénérescence.

Mots-clés: physique atomique, information quantique, atomes uniques, systèmes mésoscopiques, pinces optiques, condensation de Bose-Einstein, collisions assistées par la lumière, piège dipolaire

Summary

This thesis focuses on the manipulation of rubidium 87 atoms in a microscopic optical dipole trap. The experiments are performed in various regimes where the number of atoms in the microscopic trap ranges from exactly one atom to several thousands on average.

The single atom regime allows us to calibrate the experimental setup. We use it as a quantum bit, which state we can prepare and read out with efficiencies of 99.97 % and 98.6 %, respectively. When several atoms are loaded in the microscopic trap we observe a sub-Poissonian distribution of the number of atoms due to light-assisted collisions in the presence of near-resonant light. A study of these collisions in our particular case (microscopic trap) reveals extremely high loss rates approaching the theoretical Langevin limit. Finally, we demonstrate that the loading of the microscopic trap is more efficient when we superimpose on this trap a second macroscopic trap, which we use as an atom reservoir. This reservoir allows us to load the micro trap from the macro trap in the absence of any near-resonant light, thus avoiding light-assisted collisions.

The loading of the micro trap from the macro trap leads to optimal initial conditions for forced evaporation towards Bose-Einstein condensation with about ten atoms only. After evaporation we reach phase-space densities approaching the degenerate regime.

Key words: atomic physics, quantum information, single atoms, mesoscopic systems, optical tweezers, Bose-Einstein condensation, light-assisted collisions, dipole trap